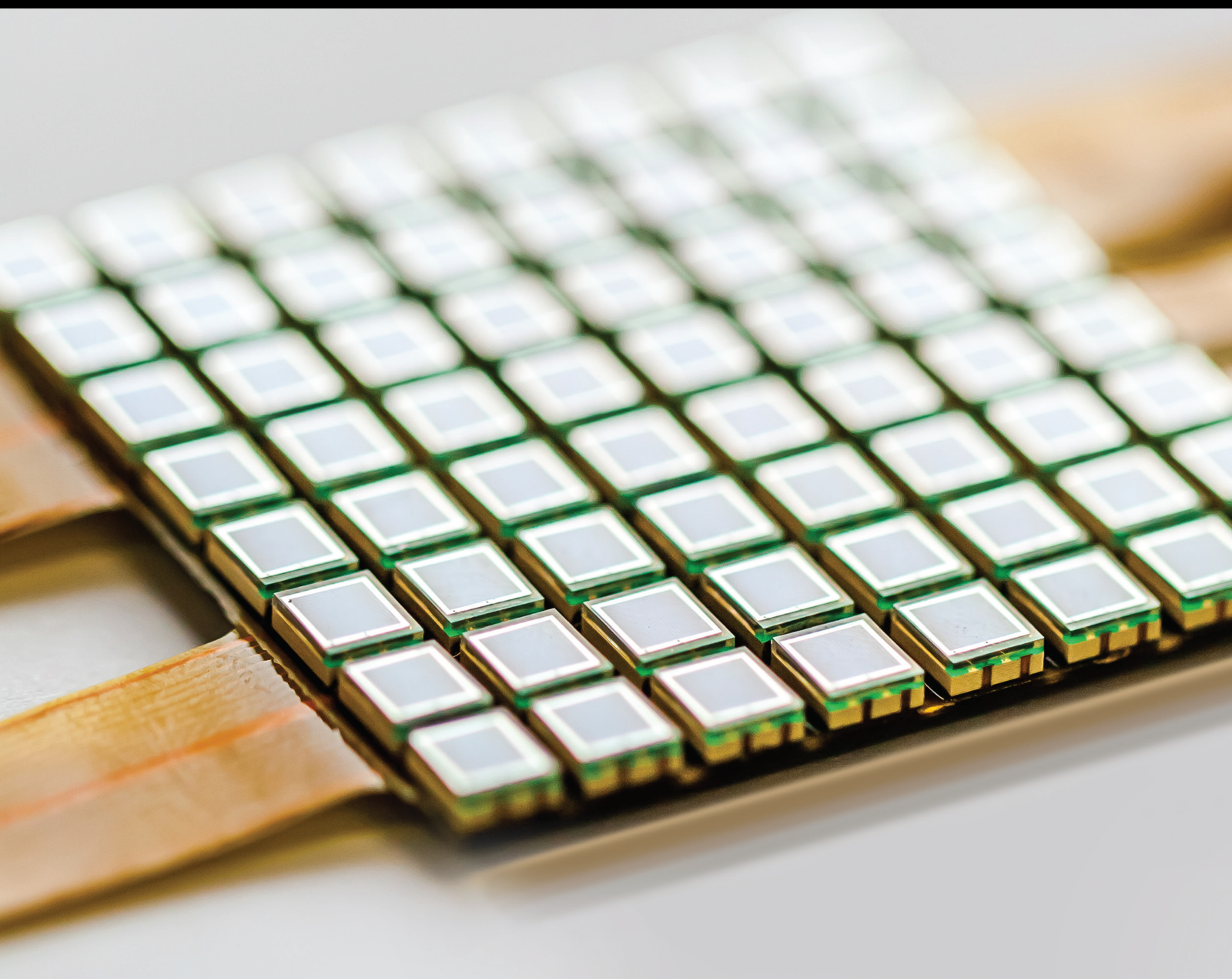


# Artificial and Computational Intelligence Utilizing Multi-Sensor Fusion Data in Forest Management

Lead Guest Editor: Bahareh Kalantar

Guest Editors: Alfian A. Halin and Shattri Bin Mansor





---

**Artificial and Computational Intelligence  
Utilizing Multi-Sensor Fusion Data in Forest  
Management**

**Artificial and Computational  
Intelligence Utilizing Multi-Sensor  
Fusion Data in Forest Management**

Lead Guest Editor: Bahareh Kalantar

Guest Editors: Alfian A. Halin and Shattri Bin  
Mansor



---




Copyright © 2022 Hindawi Limited. All rights reserved.

This is a special issue published in "Journal of Sensors." All articles are open access articles distributed under the Creative Commons Attribution License, which permits unrestricted use, distribution, and reproduction in any medium, provided the original work is properly cited.

# Chief Editor

Harith Ahmad , Malaysia

## Associate Editors

Duo Lin , China  
Fanli Meng , China  
Pietro Siciliano , Italy  
Guiyun Tian, United Kingdom

## Academic Editors

Ghufran Ahmed , Pakistan  
Constantin Apetrei, Romania  
Shonak Bansal , India  
Fernando Benito-Lopez , Spain  
Romeo Bernini , Italy  
Shekhar Bhansali, USA  
Matthew Brodie, Australia  
Ravikumar CV, India  
Belén Calvo, Spain  
Stefania Campopiano , Italy  
Binghua Cao , China  
Domenico Caputo, Italy  
Sara Casciati, Italy  
Gabriele Cazzulani , Italy  
Chi Chiu Chan, Singapore  
Sushank Chaudhary , Thailand  
Edmon Chehura , United Kingdom  
Marvin H Cheng , USA  
Lei Chu , USA  
Mario Collotta , Italy  
Marco Consales , Italy  
Jesus Corres , Spain  
Andrea Cusano, Italy  
Egidio De Benedetto , Italy  
Luca De Stefano , Italy  
Manel Del Valle , Spain  
Franz L. Dickert, Austria  
Giovanni Diraco, Italy  
Maria de Fátima Domingues , Portugal  
Nicola Donato , Italy  
Sheng Du , China  
Amir Elzawwy, Egypt  
Mauro Epifani , Italy  
Congbin Fan , China  
Lihang Feng, China  
Vittorio Ferrari , Italy  
Luca Francioso, Italy






Libo Gao , China  
Carmine Granata , Italy  
Pramod Kumar Gupta , USA  
Mohammad Haider , USA  
Agustin Herrera-May , Mexico  
María del Carmen Horrillo, Spain  
Evangelos Hristoforou , Greece  
Grazia Iadarola , Italy  
Syed K. Islam , USA  
Stephen James , United Kingdom  
Sana Ullah Jan, United Kingdom  
Bruno C. Janegitz , Brazil  
Hai-Feng Ji , USA  
Shouyong Jiang, United Kingdom  
Roshan Prakash Joseph, USA  
Niravkumar Joshi, USA  
Rajesh Kaluri , India  
Sang Sub Kim , Republic of Korea  
Dr. Rajkishor Kumar, India  
Rahul Kumar , India  
Nageswara Lalam , USA  
Antonio Lazaro , Spain  
Chengkuo Lee , Singapore  
Chenzong Li , USA  
Zhi Lian , Australia  
Rosalba Liguori , Italy  
Sangsoon Lim , Republic of Korea  
Huan Liu , China  
Jin Liu , China  
Eduard Llobet , Spain  
Jaime Lloret , Spain  
Mohamed Louzazni, Morocco  
Jesús Lozano , Spain  
Oleg Lupan , Moldova  
Leandro Maio , Italy  
Pawel Malinowski , Poland  
Carlos Marques , Portugal  
Eugenio Martinelli , Italy  
Antonio Martinez-Olmos , Spain  
Giuseppe Maruccio , Italy  
Yasuko Y. Maruo, Japan  
Zahid Mehmood , Pakistan  
Carlos Michel , Mexico  
Stephen. J. Mihailov , Canada  
Bikash Nakarmi, China

Ehsan Namaziandost , Iran  
Heinz C. Neitzert , Italy  
Sing Kiong Nguang , New Zealand  
Calogero M. Oddo , Italy  
Tinghui Ouyang, Japan  
SANDEEP KUMAR PALANISWAMY ,  
India  
Alberto J. Palma , Spain  
Davide Palumbo , Italy  
Abinash Panda , India  
Roberto Paolesse , Italy  
Akhilesh Pathak , Thailand  
Giovanni Pau , Italy  
Giorgio Pennazza , Italy  
Michele Penza , Italy  
Sivakumar Poruran, India  
Stelios Potirakis , Greece  
Biswajeet Pradhan , Malaysia  
Giuseppe Quero , Italy  
Linesh Raja , India  
Maheswar Rajagopal , India  
Valerie Renaudin , France  
Armando Ricciardi , Italy  
Christos Riziotis , Greece  
Ruthber Rodriguez Serrezuela , Colombia  
Maria Luz Rodriguez-Mendez , Spain  
Jerome Rossignol , France  
Maheswaran S, India  
Ylias Sabri , Australia  
Sourabh Sahu , India  
José P. Santos , Spain  
Sina Sareh, United Kingdom  
Isabel Sayago , Spain  
Andreas Schütze , Germany  
Praveen K. Sekhar , USA  
Sandra Sendra, Spain  
Sandeep Sharma, India  
Sunil Kumar Singh Singh , India  
Yadvendra Singh , USA  
Afaque Manzoor Soomro , Pakistan  
Vincenzo Spagnolo, Italy  
Kathiravan Srinivasan , India  
Sachin K. Srivastava , India  
Stefano Stassi , Italy

Danfeng Sun, China  
Ashok Sundramoorthy, India  
Salvatore Surdo , Italy  
Roshan Thotagamuge , Sri Lanka  
Guiyun Tian , United Kingdom  
Sri Ramulu Torati , USA  
Abdellah Touhafi , Belgium  
Hoang Vinh Tran , Vietnam  
Aitor Urrutia , Spain  
Hana Vaisocherova - Lislalova , Czech  
Republic  
Everardo Vargas-Rodriguez , Mexico  
Xavier Vilanova , Spain  
Stanislav Vitek , Czech Republic  
Luca Vollero , Italy  
Tomasz Wandowski , Poland  
Bohui Wang, China  
Qihao Weng, USA  
Penghai Wu , China  
Qiang Wu, United Kingdom  
Yuedong Xie , China  
Chen Yang , China  
Jiachen Yang , China  
Nitesh Yelve , India  
Aijun Yin, China  
Chouki Zerrouki , France




# Contents

## **Application and Potential of Drone Technology in Oil Palm Plantation: Potential and Limitations**

Zailani Khuzaimah , Nazmi Mat Nawi , Siti Nooradzah Adam , Bahareh Kalantar , Okoli Jude Emeka , and Naonori Ueda

Review Article (18 pages), Article ID 5385505, Volume 2022 (2022)

## **Fire-Net: A Deep Learning Framework for Active Forest Fire Detection**

Seyd Teymoor Seydi, Vahideh Saeidi , Bahareh Kalantar , Naonori Ueda, and Alfian Abdul Halin 

Research Article (14 pages), Article ID 8044390, Volume 2022 (2022)

## **Evaluating the Street Greening with the Multiview Data Fusion**

Lishuang Sun , Jianing Wang , Zhiwei Xie , Ruren Li , Xinyu Wu , and Yifan Wu 



Research Article (15 pages), Article ID 2793474, Volume 2021 (2021)

## **A Method to Locate Tree Positions Using Ultrawideband Technology**

Fangxing Yuan, Sheng Chen, Luming Fang , Siqing Zheng, Yuzhen Liu, and Junjun Ren

Research Article (14 pages), Article ID 5539302, Volume 2021 (2021)

## **Canopy Extraction and Height Estimation of Trees in a Shelter Forest Based on Fusion of an Airborne Multispectral Image and Photogrammetric Point Cloud**

Xuwen Wang , Qingzhan Zhao , Feng Han, Jianxin Zhang, and Ping Jiang

Research Article (13 pages), Article ID 5519629, Volume 2021 (2021)

## **Application of an Ensemble Statistical Approach in Spatial Predictions of Bushfire Probability and Risk Mapping**

Mahyat Shafapour Tehrany, Haluk Özener, Bahareh Kalantar , Naonori Ueda, Mohammad Reza Habibi, Fariborz Shabani, Vahideh Saeidi, and Farzin Shabani 

Research Article (31 pages), Article ID 6638241, Volume 2021 (2021)

## Review Article

# Application and Potential of Drone Technology in Oil Palm Plantation: Potential and Limitations

Zailani Khuzaimah <sup>1</sup>, Nazmi Mat Nawi <sup>1</sup>, Siti Nooradzah Adam <sup>1</sup>,  
Bahareh Kalantar <sup>2</sup>, Okoli Jude Emeka <sup>3</sup>, and Naonori Ueda<sup>2</sup>

<sup>1</sup>*Institute of Plantation Studies, Universiti Putra Malaysia, 43400 Selangor Darul Ehsan, Malaysia*

<sup>2</sup>*RIKEN Center of Advanced Intelligence Project, The Goal-Oriented Technology Research Group, Disaster Resilience Science Team, Tokyo, Japan*

<sup>3</sup>*Department of Civil Engineering, Faculty of Engineering, Universiti Putra Malaysia, Serdang 43400, Malaysia*

Correspondence should be addressed to Bahareh Kalantar; bahareh.kalantar@riken.jp

Received 3 September 2021; Accepted 1 August 2022; Published 1 September 2022

Academic Editor: Davide Palumbo

Copyright © 2022 Zailani Khuzaimah et al. This is an open access article distributed under the Creative Commons Attribution License, which permits unrestricted use, distribution, and reproduction in any medium, provided the original work is properly cited.

Oil palm has become one of the largest plantation industries in Malaysia, but the constraints in terms of manpower and time to monitor the development of this industry have caused many losses in terms of time and expense of oil palm plantation management. The introduction to the use of drone technology will help oil palm industry operators increase the effectiveness in the management of oil palm cultivation and production. In addition, knowledge gaps on drone technology were identified, and suggestions for further improvement could be implemented. Therefore, this study reviews the application and potential of drone technology in oil palm plantation, and the limitation and potential of the methods will be discussed.

## 1. Introduction

Oil palm has become one of the country's main sources of income apart from rubber and paddy cultivation. It has also dominated the world's vegetable oil producers such as soybean, rapeseed, and sunflower by more than 35%. At the present time, Malaysia and Indonesia have become the world's leading oil palm growing countries [1]. Furthermore, Malaysia has become the second largest exporter of palm oil and its related products. In 2020, Malaysia's palm oil production was projected to reach about 20 million tonnes (350,000 barrels per day) with total export revenue about RM72.30 billion. In terms of planting, oil palm is suitable for planting in areas that have sunlight between 5 and 7 hours every day. They required temperature as above as 18 Celsius with an optimum temperature between 28 and 32 Celsius [2], while the optimal rainfall distribution is between 2000 mm and 3000 mm [3].

However, an increase in demand requires more modern approaches and technologies to be adopted in a sustainable

manner to increase the production. The development of information and communication technology (ICT), especially the Internet of things (IoT) including drone technology which provides mapping and data analysis services, can provide more accurate and effective information for precision agriculture technology. In general, IoT technology, especially drones, can collect and process information obtained from various sources and can help in collecting weather information, soil profile, and drainage, and at the same time, manage all crops in a more efficient way [4–7]. In plantation, drone technology is being utilized to monitor large plantation area due to its success in photography, aerial mapping, and surveillance [8, 9].

Drone which is also known as unmanned aerial vehicle (UAV) is an aircraft that has no human pilot on board to navigate the vehicle [10, 11]. Despite not having a pilot, it still can fly thousands of kilometers, into confined space, and fly remotely and autonomously [12]. It can carry lethal or nonlethal payloads [13]. Drone technologists classified drones based on its aerial platform. There are four major



types of drones such as multicopter [14–19], fixed-wing [20–22] single rotor helicopter [23], and fixed-wing hybrid VTOL (vertical take-off and landing) [24]. Drones were first made by the Austrians in 1849 using explosive-filled balloons for military use which has been well known for nearly 150 years [25].

The first civilian drone was produced in the 80s in Japan at the request of the Minister of Agriculture, Forestry, and Fisheries [26]. The difference between civilian and military drones can be seen in terms of the size of the engine and its capability where civilian drones are powered by electric motors while military drones are powered by internal combustion engines. Most public drones are used for mapping and imaging [27].

Drones with specialized sensors (Figure 1), or drones that work in tandem with IoT, can record high-resolution photographs and help monitor a variety of vegetation properties. Aside from that, many sensors might be used in the agricultural sector [28]. However, the selection of type of sensors to be incorporated into the drone or UAV highly depends on the low payload capacity and the usage of minor platforms. Commonly, the main criteria that a sensor must meet to capture high resolution image are an acceptable weight with appropriate size and to utilize enough energy. In addition, different types of sensors can monitor specific parameters such as the color and texture of vegetation and the geometric outline of agriculture crops. Furthermore, certain sensors can monitor plant biomass, vegetation health, and other critical agricultural properties at various phases of plant development. This data can also be utilized to monitor utilizing certain wavelengths of radiation [29].

The function of each sensor is depending on the function of its thermal sensor to obtain data on the relative temperature of a surface and is widely used for the purpose of designing irrigation and drainage systems in the plantation sector. Multispectral sensors are usually used to produce normalized difference vegetation index (NDVI) images that help to distinguish between cultivated areas and vacant land [30]. It can also detect crops that are under pressure by obtaining data on plant fertility levels. On the other hand, hyperspectral sensors have several hundred bands that are commonly used to obtain and process information from the electromagnetic spectrum in each pixel of the image taken. However, for light detection and ranging (LiDAR) sensor, it was usually utilized to obtain the slope elevation and structural data [31].

This article was written to highlight an overview of the use of drones' technology in the oil palm industry its weaknesses and recommend further research to enhance the capabilities of more effective drone technology in the oil palm industry. The following section reviewed a list of drone applications in a wide range of oil palm management and monitoring, accompanied by its lapses or gaps and recommendation for improvement of the drone technology in the oil palm industry.

## 2. Drone Capabilities: Endurance and Range

Drone configurations and features are varying according to the platform and mission requirements. There are various

classifications for drones that focus on different parameters that can be found in the literature reported by Hassanalian and Abdelkefi [36]. The advantages of each drone always depend on the user demand. For instance, in scientific research, the drone was classified based on characteristics such as size, duration, range, and durability [37]. According to Arjomandi [38], drones are also classified according to weight, flight distance, wingspan, maximum altitude, and engine capability. For example, heavy drones are for those over 2000 kg, heavy with a weight between 200 kg and 2000 kg, medium with a weight between 50 kg and 200 kg, and light (5 kg-50 kg) and minidrones with weight less than 5 kg as shown in Table 1.

Drone endurance is described as the total duration during take-off. For an electric fixed-wing helicopter or quadrotor, this is primarily associated with the battery's capacity as well as the ability of the motor to produce current to keep the helicopter on air. There are several factors that can be used to determine the endurance; however, a simple endurance computation can be estimated using the below equation [39].

$$\text{Endurance (hrs)} = \frac{\text{Battery Capacity (Ah)}}{\text{Current (Amps)}}. \quad (1)$$

The endurance of the helicopter depends largely on its size, weight, and the weight of the payload. For instance, a macrofixed-wing aircraft with a large wingspan will have longer endurance compared to a miniquadrotor. Another key point is that the endurance also will have a factor on the range of the aircraft. The distance with an uncrewed aerial vehicle can go is known as its range. Furthermore, the range of the aircraft is dependent on the amount of current that is being applied for the aircraft to be lifted, the endurance itself, flight speed, and the aerodynamic performance which can be determined by using the range of a drone. Meanwhile, the range can be calculated by calculating the fixed-wing and quadrotor by the equation below [39].

$$\text{Range (miles)} = \frac{kV \cdot V \cdot 60 \cdot \text{Pitch}}{12.5260} \text{Endurance (hrs)}, \quad (2)$$

where kV is the amount of revolutions per minute, the motor will turn when 1 V was applied to the motor, pitch is the pitch (in inches) of the propeller on the UAV, and the endurance is the amount of time in hours the aircraft can stay in the air.

This equation will enable a rough calculation of the total UAV's range. However, to effectively estimate the range, factors like wing area, weight, and the coefficient of lifting of the air foil used on the helicopter will be crucial.

## 3. Application of Drone in Oil Palm Plantation

Malaysia is the world's second largest exporter after Indonesia with about 5.08 million ha of oil palm plantations. Most of the plantations are owned by private farmers who work on a small scale [41]. They desperately need an autonomous platform with an affordable price for the use of monitoring, inventory, crop yield assessment, spraying, health assessment, and disease detection. The capability of drone technology in



FIGURE 1: Examples of sensors used by UAVs for PA: (a) thermal sensor [32], (b) RGB sensor [33], (c) multispectral sensor [34], and (d) hyperspectral sensor [35].

TABLE 1: The proposed drones' categorization by [38] based on their weight.

Designation	Weight range
Extremely heavy	> 2000 kg
Heavy	200 kg ≤ 2000 kg
Medium	>50 kg ≤ 200 kg
Light	>5 kg ≤ 50 kg
Mikro	≤ 5 kg

taking high-resolution aerial photographs has changed the way oil palm cultivation into more economical [42]. Conventional methods have been replaced with the use of drone tech-

nology [43, 44] that can provide more quick and accurate information to help in making smart decisions. Drone technology which is an emerging technology is capable of providing significant functions in precision agriculture and smart farming, to enable the increases in long-term production [45] by the acquisition of real-time environmental data. Drone is one of the breakthroughs for smart and precision agriculture farming, which is utilized for monitoring vast and cultivated lands and provides practical solutions for precision farming [5, 29]. With that, the main purpose of precision farming to optimize yields and maintain sustainable crop production capacity based on crop monitoring and crop health assessment [44] can be effectively achieved.

By recording high spatial and temporal resolution photos, drone can be vastly utilized in a wide range of

applications, including crop management. Through photographs, it can intelligently, simply, and cost-effectively monitor crop and vegetation factors. UAVs for crop monitoring and management will provide opportunities for the farmers to monitor, map, and survey a diverse range of crops, located in many countries around the world [46]. Recently, globally, many have been considering using drone for agriculture purposes for crop irrigation [47] and growth for yield estimation, health determination, disease detection [47], and for spraying [48].

Drone technology has bridged the gap between ground base observation and satellite data, and it has increased its capabilities in terms of crop monitoring, yield mapping, soil profile and soil property mapping, crop health, and disease monitoring and spraying [40]. This technology is easy-to-operate, flexible, and in addition, low-cost drone has greatly revolutionized smart farming technology from the beginning of the planting process up to the harvesting. Drones can also provide live data from various types of sensors as shown in Figure 2 (multispectral, near infrared reflectance (NIR), LiDAR etc.), with high resolutions imagery up to less than one centimeter per pixel. With this information, it can help a lot in replanting planning, oil palm data census for inventory data, calculation of land use, distance between crops, canopy size, oil palm height, and crop density. With all the data and information, it is very useful in the development of support systems in decision-making and estimating plantation management-based results. Figure 3 suggests the suitability of each sensor usage at various stages of cultivation in order to obtain relevant data and information, and Table 2 shows summary of drone application in plantation.

**3.1. Oil Palm Plantation Inventory.** In most underdeveloped countries, land registration is a big problem such as in Malaysia. Failures in land registration caused many difficulties such as title disputes, control, and distribution of aid such as pesticides and fertilizers. Land registration in the form of terrestrial measurements is projected to be addressed in the next decades. For urban planners, monitoring urban development has become a vital issue. Drone technology is an alternative step to speed both processes because it is a unique instrument that can fly without a human operator on board and conduct sophisticated and viable duties such as monitoring, cadastre, and earthwork analysis. The photogrammetry method used in drone is to obtain an ortho map.

3D mapping is an integral part of geological surveying [61]. Recently, drone usage for visual surveying through the generation of 3D images of sites has become a necessity [62]. Drone's technologies can acquire high-resolution images converted into 3D surface models used for topographic mapping, volumetric calculations, or showing the site in the 3D format [63].

Drone technology for the oil palm plantation industry includes all relevant information, including crop density, drainage, crop area, and basic infrastructure information such as plantation road network, and crop yield estimates. Figure 4 shows the images and information on the inventory using drone technology.

Drone is capable of capturing the crown formation of palm trees images by using high spatial resolution images. Here, it uses the template matching algorithms to detect the object's boundary of the image as a criteria [64]. In some instances, the problem of image distortion or occlusion can be overcome by using the method of object base analysis to reduce the influence of scale and geometry of objects through segmentation [56]. However, parameter selection will result in inaccurate detection in trees. To obtain the best inventory information, the use of satellite images with fine resolution is particularly suitable for large areas of oil palm [57].

Nevertheless, the limitations of satellite data such as frequency of public coverage, cost, and time make it less suitable for the estimation of structural parameters. In order to improve accessibility, low operating costs, and enhance usage, the development of lightweight drone platforms was developed as an effective mechanism in oil palm plantation management. For this development, the UAV teams had been established by major commercial oil palm companies for a routine acquisition of aerial imagery [65].

**3.2. Tree Counting.** Tree counting is vital for estimation of yield, observation, replanting, and layout preparation. Nevertheless, it is costly, labor-intensive, and prone to human error when done in the field. Furthermore, due to the variability of the plantations, most plantations used to estimate cost estimates by multiplication of the total location by the amount of palms per hectare, which is inaccurate because of the diverse land mass such as hilly, undulating, or flat and presents of natural features such as river, land, or forest. Remote sensing was a possible option for seeing the plantation area and automatically counting the trees to solve this problem.

In the mid-1980s, studies into automatic detection of trees and feature extraction from digital imagery began. Pinz [66] offered aerial imaging utilizing a vision expert system; although, various detection methods have been proposed. This system powers the centrifuge. The center of the tree crown was successfully detected using this approach, and the radius was estimated using local brightness, followed by the valleys between the tree crowns using ground sampled distance digital aerial images.

Individual trees, on the other hand, were detected using software. To distinguish individual trees, Woodham and Pollock [67] use model-based template matching approaches. Kattenborn et al. [59] proposed a method for automatically detecting single palm trees using photogrammetric point clouds (Figure 5).

VisualSFM was used to process single camera images with a structure from a motion tool chain. Each image was divided into three categories: palms, shrubs/trees, and the ground. A multiscale dimensionality criterion were utilized to train and evaluate the data set for classification purposes, in which the classifier was set in a separate scale factor. Palm trees and their ground soil were classified using point cloud local dimensionality features. Algorithms are limited while training a classifier for a dataset. Because training a classifier takes time and requires more computer resources for each

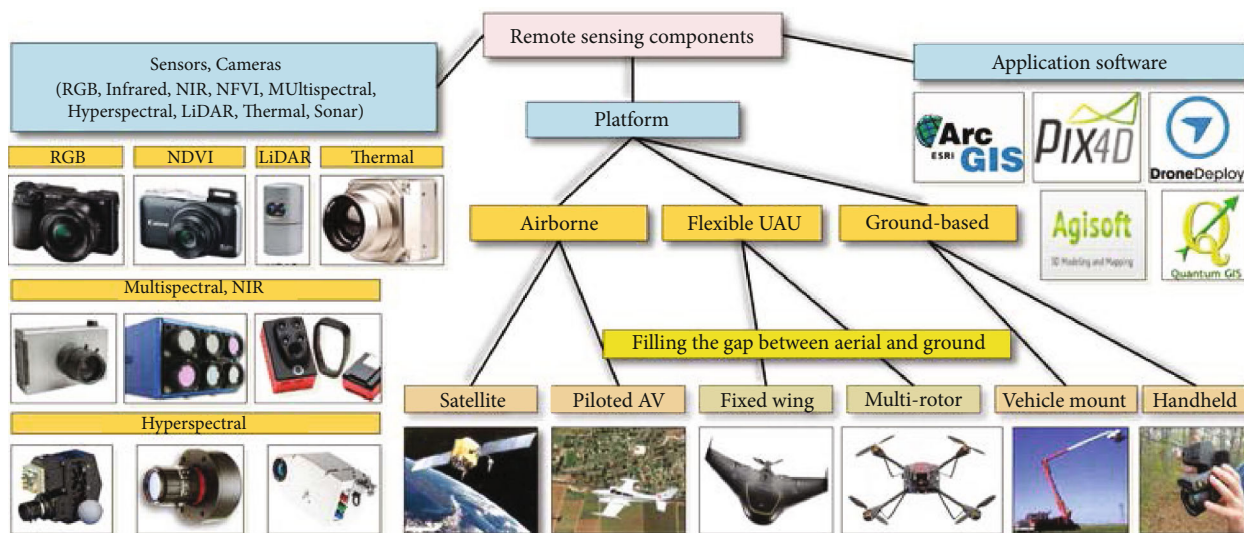


FIGURE 2: Typical components of a UAV-based remote sensing platform for precision agriculture in oil palm [40].

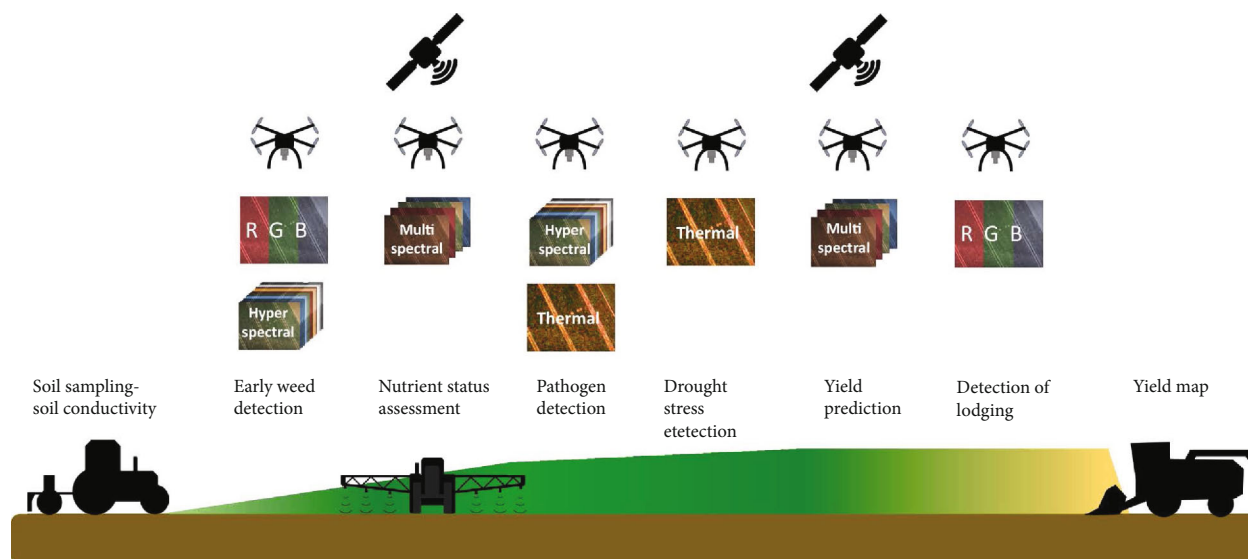


FIGURE 3: Schematic overview showed the different ways to extract spatial information in the areas, the useful platforms and the optimal UAV sensors, throughout a growing season of a crop. The optimal sensors for UAVs were also shown. Abbreviations: RGB: red-green-blue [60].

type of tree species, the classifier must be coached before detecting trees.

For this study, a structure from the motion toolchain with VisualSFM was used to process single-camera images. The images were classified into three classes: palm, shrubs/trees, and ground. For classification, a multiscale dimensionality criterion was used whereby the classifier was set to a different scale factor that trained and tested the data set. Local dimensionality characteristics of point clouds were applied to classify palm trees and their ground soil. Training a classifier for a dataset leads to a constraint for algorithms. Since training a classifier is time-consuming and needs more computational power for each tree species, one must coach the classifier before detecting trees.

Mansur et al. [68] utilized drone data capture and spatial filtering to acquire data for counting oil palm tree using ground control points. They used the concept of crown geometry and vegetation response to radiation in their research. A spatial convolution processing approach, such as a low pass filter, was used to detect the tree crown in the enlarged image. After applying a spatial filter to the data set, morphological analysis was used to perform object extraction, image filtering, and image segmentation processes.

Wang et al. [69] improved on Brandtberg and Walter [70] work by first using edge detection methods to detect the boundaries of tree crowns, then intersecting the results of local nonmaximum suppression on grey level images and local maximum values of morphological transformed

TABLE 2: Summary of drone application in plantation.

Literature work	Objective	Task	Technical characteristics and payload
[49] [50]	To detect the drainage pipe	For a monitoring purposes	VIS-C, MS, and TIR camera
[51]	To monitor the vegetation level	For a monitoring purposes	Camera GNSS IMU LiDAR Multispectral Compass First person view platform
[52]	Monitoring vegetation state	For a monitoring purposes	FlightCTRL GPS system GSM modem Magnetic Multispectral NaviCTRL 3-axis accelerometer 8 GPS system Digital compass
[53]	Evaluation water stress	For a monitoring purposes	FlightCtrl NaviCtrl Pressure sensor Storing device Thermal sensor IMU
[54]	Monitoring vegetation state	For a monitoring purposes	LiDAR Multispectral sensor Single-board computer
[55]	Spraying with consideration of climate conditions	For a spraying process	Spraying device Barometer IMU
[56]	Spraying fruits and trees	For a spraying process	Magnetometer Multispectral sensor Servos Spraying device Autonomous power supply Control switches
[57]	Estimating chlorophyll density	For a monitoring purposes	GPS system Hyperspectral sensor LCD screen Storing device
[58]	Oil palm harvest prediction	For a data acquisition	20.2 mega pixel digital camera
[59]	Palm tree detection	For a data acquisition	Panasonic Lumix G3 with a 20 mm lens

distance between pixels. By combining the two methods, a decent estimate of the treetops was obtained, which were subsequently tallied using contour-based methods. The presence of background objects, such as buildings and roads, however, causes this method to fail.

*3.3. Drone for Spraying.* In the present era, various developments in precision agriculture are being carried out to increase the crop productivity. For example, in the developing countries like India, over 70% of the rural people who depends upon the agriculture fields need to be feed. However, their agriculture fields often face dramatic losses due to the plant diseases. These diseases either come from the pests or insects, which have possibilities to reduce the produc-

tivity of the crops. Pesticides and fertilizers were used to kill the insects and pests to enhance the crop quality. Hence, the WHO (World Health Organization) has estimated one million cases of ill caused by the pesticides spraying activity in the field. Therefore, precision agriculture to cater the growing population is so demanding. In precision agriculture, the drone's technology is being utilized to spray the pesticides to avoid the health problems of the users when they spray manually. Drones can be operated easily for this purpose [71]. This system was first developed in Japan in the 1980s, by the combination of unmanned aircraft with small pesticide tanks [72]. Today's drones were developed to be able to lift big tanks with up to 10 liters of capacity. Furthermore, the rate of liquid discharge could be set to

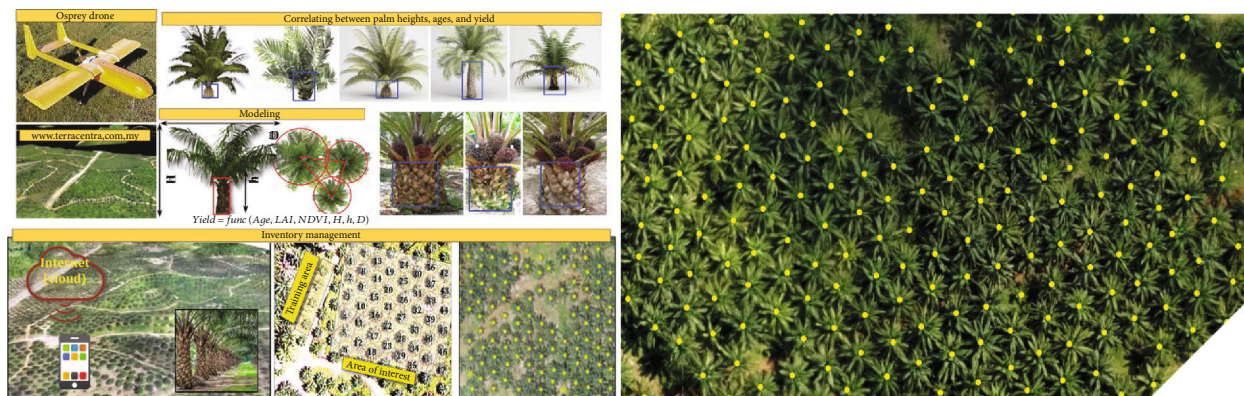


FIGURE 4: Mapping and inventory of oil palm plantation tree counting analysis [40].

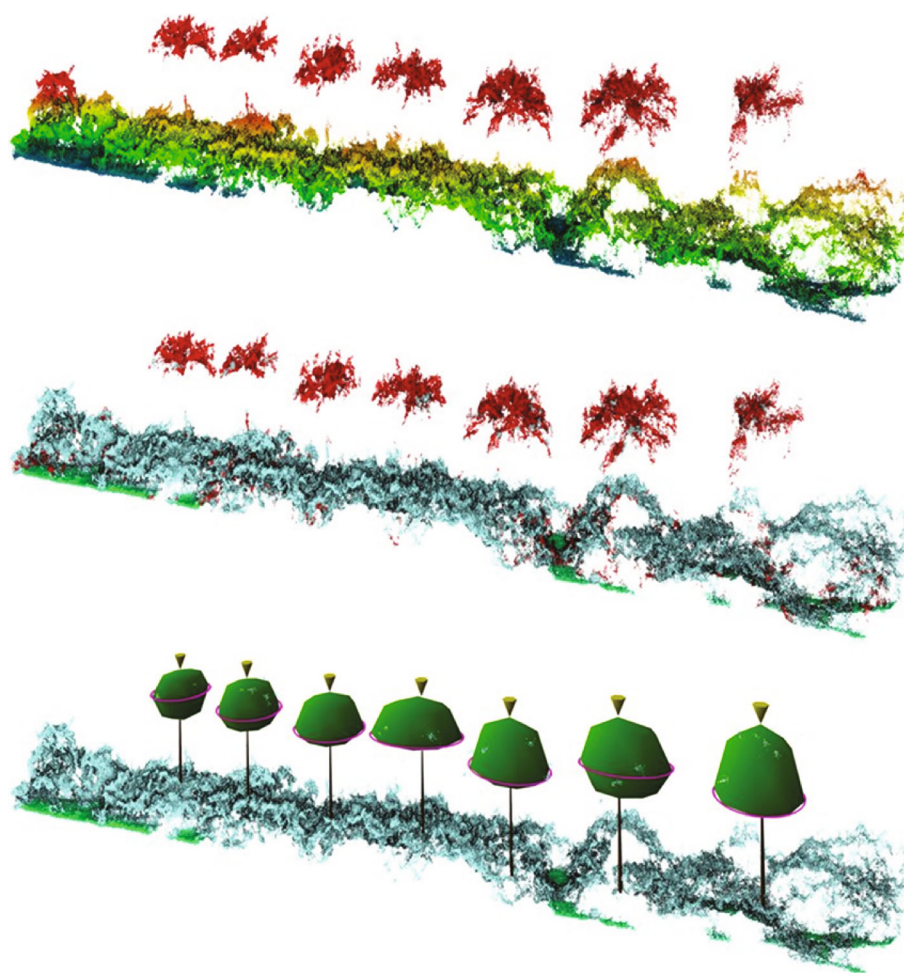


FIGURE 5: Automatic single palm tree detection using photogrammetric point clouds [59]. Palm: red; other vegetation: blue; ground: green (center) with modeled palms (bottom). Green shapes represent the convex hull of the crown, vertically surrounded by crown margins (purple). Yellow cones represent the top ( $z$ ) and the position ( $x, y$ ).

one liter per minute that makes it possible to cover a large area in 10 minutes. Also, drone-based spraying platform integrated with an aerial crop monitoring process will be able to provide efficient and accurate use of the agrochemical products. This will reduce the number of agrochemical products usage and is also a part of environmental protections. According to Zhang et al. [73], drones using M-18B

and Thrust 510G model can fly at heights of five meters and four meters, respectively. He found that height differences had a significant effect for effective and uniformity spray on crops. Meanwhile, Kurkute et al. [74] used a quadcopter (4 rotor drone), which uses a universal spraying mechanism to spray liquid and solid contents. The author reported different control systems for agricultural purposes



FIGURE 6: Drone for crop spraying [76].

and found that the Atmega 644PA model is the most suitable and efficient drone. Meanwhile, Sadhana et al. [75] used a different approach in developing drone modules for simpler pesticide spraying mechanisms in improving yields as well as crop protection. By using a quadcopter drone, the author identified it that it was able to carry a load of 1 kg and use to spray pesticides at a height as shown in Figure 6. In this study, the author detected that the quadcopter drone was operated by Arduino UNO AT mega328 system and brushless direct current (BLDC), electronic speed control (ESC), MPU-6050 consisting of MEMS accelerometer, and MEMS gyro in one chip, radio receiver, and LiPo battery.

Kedari et al. [77], also used quadcopter drones that is suitable for indoor and outdoor crops. It is an autonomous flight that sprays pesticides as well as fertilizers using Android devices as well as Bluetooth that operates in real time. It can be used in agricultural sectors to reduce the time and the hazardous effects that can present during spraying of pesticides and fertilizers.

**3.4. Biomass Estimation.** A major requirement for precision farming is to monitor biomass which is an important step throughout the oil palm tree life circle [5, 78]. However, due to the presence of natural influences, precision farming must be modeled to determine the level of nutrient supply, water availability, soil quality, and healthiness because these parameters will contribute to the oil palm biomass. In precision farming, an effective management of the oil palm biomass need to be considered. Modeling the yield of a field through a satellite image by stratification often turns out to be mostly outdated, too cloudy, and not available for specific dates as of when needed. Another downside of the method is in field measurements, as it is hard to replicate and to cover wide plantation area that has too many plots. Besides that, it can hardly take care of small segment of the field apart from the cost and labor-intensive that is required for the whole process. Conclusively, it is an expensive venture that does not bring a perfect solution in biomass modeling. However, dynamic progression of drone systems enables to join airborne surveying with precision and resolution of terrestrial methods [63, 79, 80]. With this, drones became advantageous in biomass monitoring for oil palm modelling assessments via photos taken by consumer-grade RGB camera

mounted on a small octocopter [81]. Further, some scholars use multispectral cameras, e.g., near-infrared in addition to RGB [82].

Tree geometric parameters from an orchard can also be estimated from data collected from the drone [83, 84]. By using an information collected from the drone, one acquired the crop parameters such as biomass that plays a significant part in yield forecast and in optimizing plantation management. Biomass can be assessed through spectral reflectance measurements [85] from space [86, 87] and from the air [88, 89]. Nevertheless, these measurements frequently consist of refined and costly apparatus that necessary for vigilant standardization. Drones occasionally denoted as remotely piloted aerial systems (RPAS) or unmanned aerial systems (UAS) actually are the evolving implements to be used for small-scale remote sensing [78, 89, 90]. UAVs can be used for oil palm biomass modeling, for instance, crop status investigation using near-infrared or thermal data. Figure 7 below shows the research methods that was summarized with reference to some previous research.

**3.5. Crop Growth Monitoring and Yield Estimations.** The combination of real-time remote sensing images and information from related sensors can provide information that can increase plantation productivity through the mapping of spatial information changes in the field. Information on the status of the cultivation area such as soil profile and crop fertility can help in fertilization planning, watering schedule, weather analysis data, and also crop yield estimates. The collection of all this information by using drone technology can provide a more effective management plan [86].

Bura et al. [58] used drone technology in predicting the yield of oil palm harvest, by dividing the study into two stages, namely, by the configuration of the drone system and in the image processing for predicting the yield of oil palm harvest. The drone system configuration included the use of an X-8 airframe with Pixhawk control system, electric motor, and 20.2 mega pixel digital camera RGB (red, green, and blue) sensor. High-resolution images were once taken at a 6-year-old oil palm plantation in North Sumatra. The resulting image was used to calculate the forecast of crop yield by using the number of crops. The estimated harvest for that particular area was detected as an average of 50.5 tonnes per hectare per year, which is more than the management company's estimation at 23 tonnes per hectare per year.

An accurate early yield prediction is beneficial to farmers as well as the plantation industry. With drone technology, the use of high-resolution sensors can map accurate crop information such as crop height, canopy cover, and crop distribution, which can be used to predict crop yields. Distribution using RGB sensors [92, 93] and multispectral sensors [94, 95] is used to predict crop yields.

Drones can be used to observe the crop with different indices. It can also cover large parcel of land in a single flight using either thermal or multispectral cameras [79, 96]. It will capture the reflectance of the vegetation canopy mounted beneath the quadcopter. The camera captures one image per second and records it in the memory and transferred

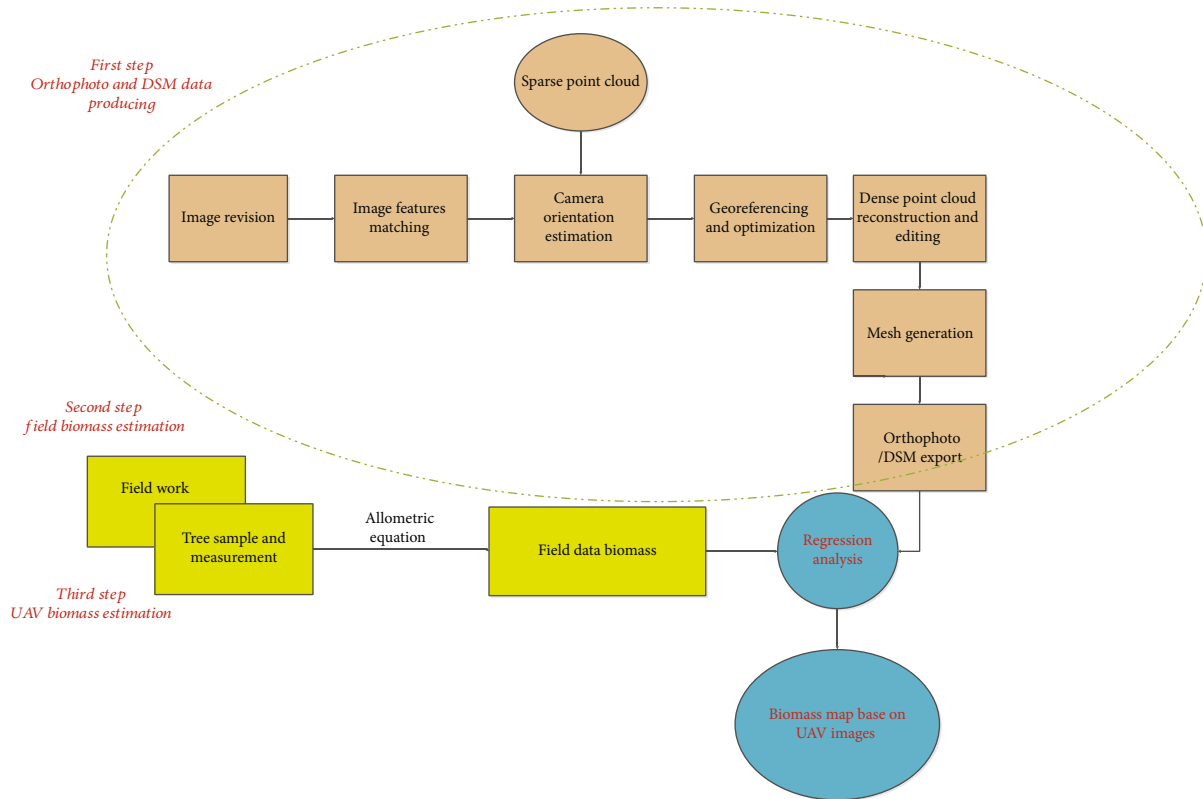


FIGURE 7: Biomass mapping flow chart.

to the ground station via wireless telemetry that uses MAV-LINK protocol. The images were recorded in visible five bands with contradicting wave lengths, for example, blue wavelength 440-510 nm, (ii) green wavelength 520-590 nm, (iii) red-wavelength 630-685 nm, (iv) red-edge wavelength 690-730 nm, and (v) near-infrared wavelength 760-850 nm. The data retrieved from the multispectral camera through telemetry was analyzed using the geographic indicator NDVI [97–99] that was represented in the equation below.

$$\text{NDVI} = \frac{(R_{\text{NIR}} - R_{\text{RED}})}{(R_{\text{NIR}} + R_{\text{RED}})}, \quad (3)$$

where  $R_{\text{NIR}}$  represents the reflectance of the near-infrared band, and  $R_{\text{RED}}$  is the reflectance of the red band. A computation value of -1 to +1, or close to 0 (zero), means that there is no vegetation on the crop, and a value close to +1 (0.8 to 0.9) signifies that the highest density of green leaves was grown on the crops. For these results, farmers can effectively point out the spot to spray pesticides and fertilizer. The equipped GPS (Global Positioning System) module will manage the GPS coordinates of each acquired image. The GPS coordinates of the image are then saved in the UAV to pesticides or fertilizer spraying simultaneously without control.

There are various types of drone that were invented for agriculture purposes. Drones such as the DJI Agras MG-1 [100] were designed to apply liquid pesticides, fertilizers, and herbicides. On the other hand, multispectral and hyper-

spectral aerial and satellite imagery used to create NDVI maps will help differentiate the soil from grass or forest and detect plants under stress and differentiate between crops and plant growth stages. There are strong correlations between NDVI data measured at certain point with the crop yield and plant growth stages [101]. Hence, tracking the plant growth will help provide an accurate estimation of the crop yield and address any plant growth issues earlier. For the purpose of obtaining soil profile and plant fertility by using drones, suitable sensors used are multispectral, hyperspectral, and infrared sensors. Agricultural information with a combination of NDVI data with crop-water stress index (CWSI) and canopy-chlorophyll content index (CCCI) can provide more accurate results. The response of the plant leaf reflection to the sensor can provide information on the fertility level of the plant whether it is a state of dehydrate or stress (Figure 8). The information can also distinguish between cultivated areas and non-crops.

Forecasting plantation production is something that is important in this industry. Drone technology promises the accuracy of information obtained through the use of appropriate sensors in the collection of images and data such as RGB and multispectral sensors to estimate crop densities and biomass. Through appropriate analysis of the method, the accuracy of the yield estimation can be improved.

**3.6. Crop Health Monitoring.** In precision agriculture application, the most common technique to assess vegetation health is remote sensing techniques and image analytics. Meanwhile, one of the most widely used RS approach is



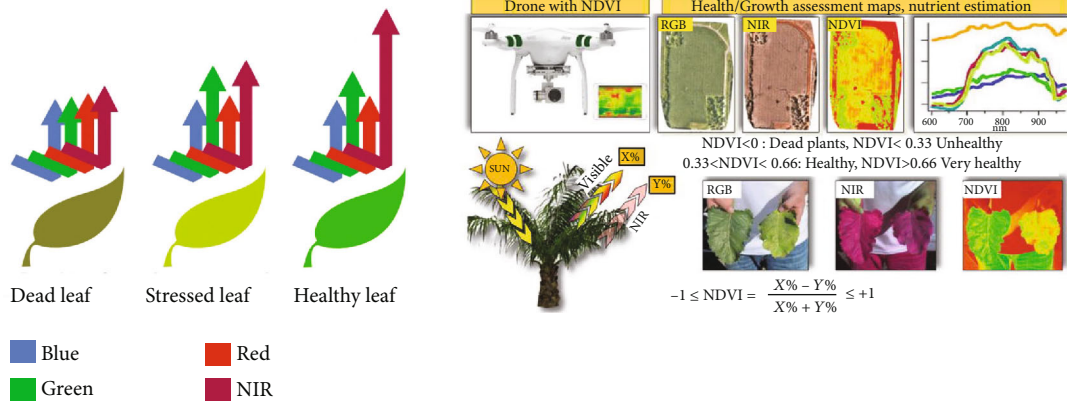


FIGURE 8: Normalized difference vegetation index.

aerial inspection, using satellite acquired imagery and manned aircrafts, as well as drones [102, 103]. In the context of precision agriculture, exploring satellite images is a big investment for a typical farmer, and sometimes, their quality and resolution are not acceptable and technical. However, conversely to previous cases, aerial photos acquired by manned aircrafts reveals a more acceptable quality compared to satellite images. On the other hand, drone is less cost-effective and can provide high-resolution images. Drone, an unmanned aircraft, will be operated remotely by an operator. It can carry several cameras such as multispectral and hyperspectral that acquire aerial photos. More so, these images will be used for the extraction of vegetation indices that allows farmers to inspect crop variability and stress conditions constantly.

Duan et al. [104] used the application of NDVI in monitoring plant growth. This NDVI technique calculated photosynthetic and assessing the canopy status of green plants. He used a multispectral sensor (RedEdge) at low flight altitudes to record images from various bands from various stages of plant growth with a transformation ratio measured between the reflectance measured at the red wavelength range and NIR wavelength range. With all the data obtained from multispectral sensors and field verification using handheld sensors (e.g., Green Seeker), this range of information had assisted in the development process of crop growth mechanisms.

Reinecke and Prinsloo et al. [97] were more focus in studying the capabilities and limitations of drones in maximizing crop yields and crop management. By using two drone camera technologies, namely, UVIRCO and Aerobic, his study concluded that many farmers invested in drone technology to improve their crop management capabilities. It is because his technology has the ability to produce digital maps that can provide crop information such as crop health, crop loss, irrigation system, and crop spraying.

Kerkech et al. [105] used a convolutional neural network (CNN) system and color information to detect plant health status. CNN used diverse color space with various crop indexes with a combination of the information analyzed using six methods: capture the image, divide the image into blocks, create two sliding window schemes, color conversion from RGB to HSV, and separate the intensity information

chrominance by using LAB and YUV. The results were classified according to healthy plant, potentially diseased and diseased plant classes, mapping disease plant generation, postprocessing steps such as mathematical morphology, removal of small areas, contour detection, and overlapping disease maps on RGB images.

**3.7. Pest and Disease Detection.** The detection of pest and disease has become a significant concern in oil palm plantation. This is a result of timely detection of pest and disease that can be of help in prevention of an outbreak. The most common disease in the oil palm industry is caused by *Ganoderma boninensis*. This disease often causes huge losses in oil palm management. A fungal disease internally rots the oil palms trunk, and this makes it to be fundamentally vulnerable and collapse due to strong wind [106]. It is a highly contagious disease. However, in the early stage, the infected palms often show sign till it deteriorates. If the diseases invested oil palms can be identified earlier, it can be quarantine and remove properly to prevent the spread of this disease to other plants [107]. Using remote sensing and UAV imagery system, the status of palms can be assessed on the basis of the signs shown at given spots earlier, and the diseases or pest infestation can be diagnosed as soon as possible [108]. On the basis of research hypothesis, oil palm infected by *Ganoderma* will show noticeable signs at the beginning; therefore, several researches were carried out to remove the oil palms infected with *Ganoderma* from the plantation at the early phase of infection. The use of NIR cameras integrated in the UAV able implies the high reflectance of vegetation in the NIR region that is invisible to the human eye. This can be used to demonstrate the health of a particular plant. The RGB and NIR images coupled with geographic information system (GIS) analysis will be successfully used to monitor *Ganoderma* BSR in oil palm plantation.

Day by day, chemical usage is increasing, which has led to the environmental impact and health risk aspect on the user and has become crucial to be considered. Indeed, chemicals may threaten the important inhabitants that live around the areas. Furthermore, pesticides are also being adopted by crop and natural resources like water and soil and result to some concealed substances in the food chain. This can also increase the risk for both livestock and humans. However,

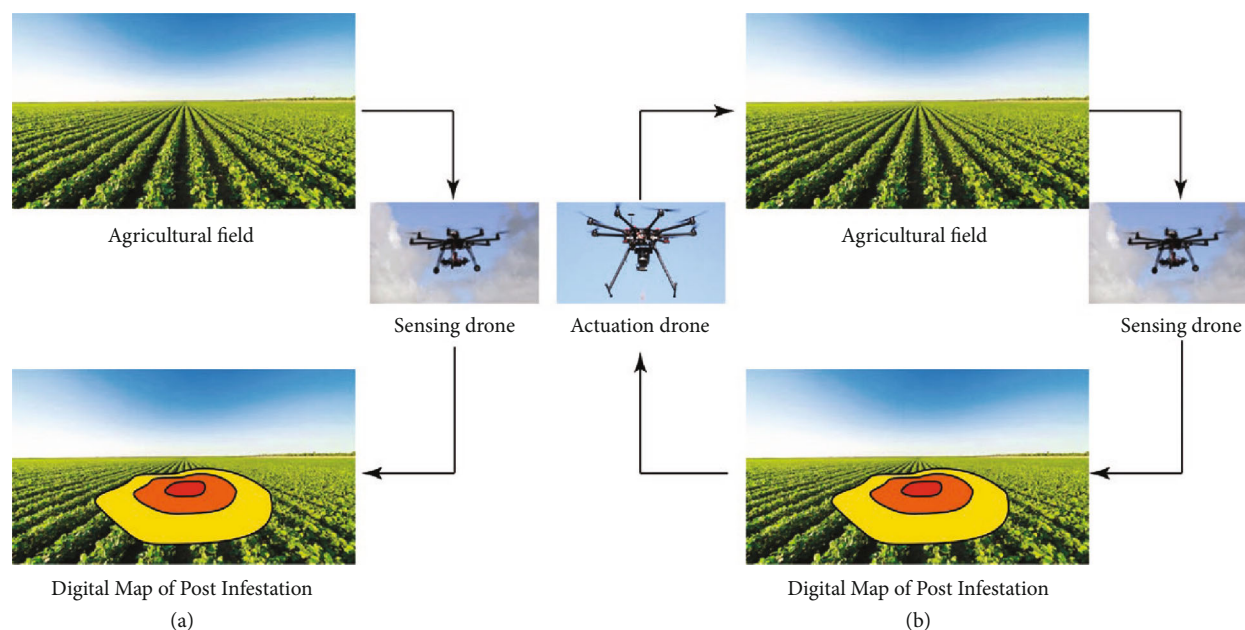


FIGURE 9: Drone used for detection of pest hotspots adapted from [37, 112].

by autonomous precision agriculture, these effects can be controlled. Additives, like fertilizer and pesticides, are sprayed when necessary, rather than being sprayed over a vast or specific area that crucially need will be identified beforehand through drones in agriculture. Many vegetation indexes involving several data characteristics such as the NDVI have been developed. Unique camera systems capable of acquiring data from an invisible part of the electromagnetic spectrum known as NIR and extract adequate information, which includes the presence of algae in the rivers or oil spills near coasts, were developed [109]. Currently, drone usage has recently been introduced for big areas to inspect and target areas that need to be irrigated and fertilized [110]. This approach can be time saving for agronomists, water resources, and minimize chemical application. This type of farming method has the tendency to improve of crop production and quality. Specifically, lack of water, nutrient stress, or diseases can also be recorded and localized.

Furthermore, an object-based image analysis (OBIA) was performed to classified oil palms in a selected area into three categories such as healthy, moderately infected, and severely infected. These results showed that the OBIA can be used to analyzed multispectral images of oil palms to detect moderate and severe infection of Ganoderma disease. Izzudin et al. [111] stated that the Ganoderma disease severity index (GDSI) can be obtained from the aerial images of the infected oil palms. Through this, the detection of early infection of Ganoderma has become more feasible with an advanced algorithms and classifiers which incorporated with multispectral and hyperspectral aerial images application.

Detection of pest hotspots using drones is known as sensing drones, while drones used for precision distribution are known as actuation drones. Both types of drones could be used together to initiate a communication to establish a closed-loop (integrated pest management) IPM solution (Figure 9). Using drones in precision pest management are

very cost-effective and reduce harm to the environment. Meanwhile, sensing drones could reduce the time required to scout for pests, while actuation drones could reduce the costs of dispensing natural enemies [37, 112].

**3.8. Weed Mapping and Management.** Biotic threats such as weeds, insects, bacteria, fungi, and viruses are major factors influencing crop quality and yield. Weed problems are the main threat causing huge losses in crop yields globally [113]. Weeds are the main competitors for crops in obtaining their nutrients [114], light [115], space [116], and water [117]. Besides that, the weeds' formation of toxic molecules and chemical signals will also interfere with crop development [118].

Drone technology is very suitable in weed detection, and the main advantage of drones in comparing to the conventional conditions in shorter time and optimal control of resistance on crops planted in rows [119] is to increase the effectiveness of drone usage for this purposes. In just a few minutes, a drone can be able to collect data covering several acres of area and provide images to detect the weed patches [120]. Later, those images will be processed using deep neural networks [121], convolutional neural networks, and OBIA [29, 60]. The final data will be concluded in three types of sensors such as RGB, multispectral, and hyperspectral sensors.

Weed infections in farm areas are usually uneven, and drone technology systems offer the best methods to map weeds and provide site-specific weed management (SSWM) methods. Two methods of weed detection are used, namely, the detection of spectral band differences between weeds and crops, and the second is the use of remote sensing data that is not from a multitemporal drone [122]. By using a drone application, the data obtained can be processed by supervised classification method only by using RGB sensors if the difference of the spectral signal is successfully identified

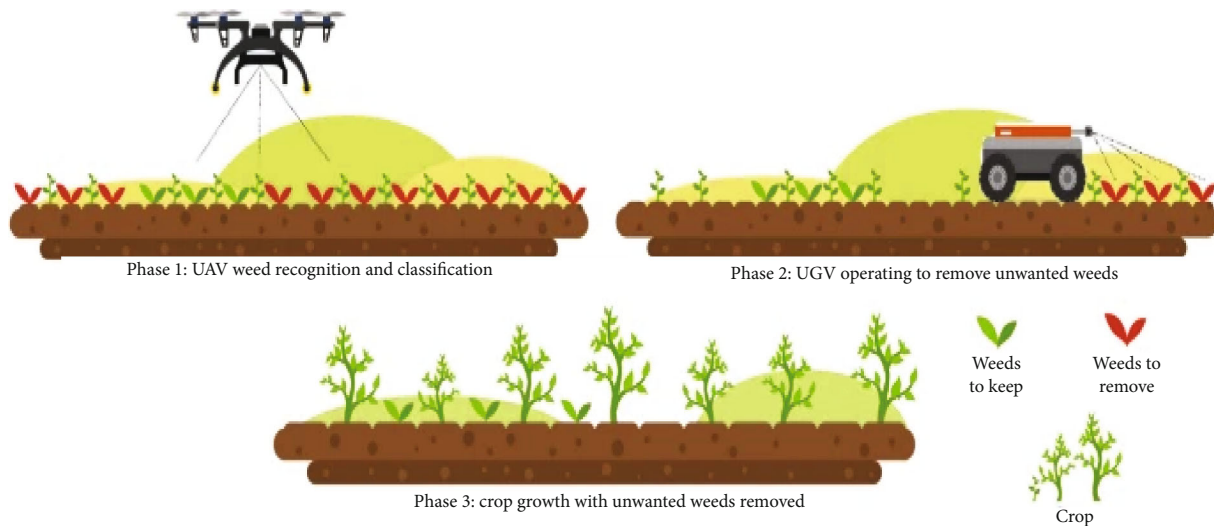


FIGURE 10: Weed management phase in a plantation system using drone technology [131].

between weeds and plants [123, 124] as it can produce a map that can pinpoint the location for herbicide spraying [125]. However, there is no guarantee that it can be fully resolved [126]; drone handling techniques and related tools such as accurate and fast field data support can help in effective solutions in a timely manner [127]. The second approach is for early monitoring at the beginning of the crop development using high-resolution images drones and a unique method called OBIA. This method analyzes nonpixel objects like the traditional method, and the RGB sensors are very suitable to use because their spatial resolution exceeds the spectral resolution [128]. Using the latest technology can save a lot of labor and time identifying weeds and their eradication methods [129, 130]. This drone technology has been shown to significantly reduce the use of poisons without affecting crop yields [122]. In the future, high-resolution hyperspectral with a combination of spectral discrimination and OBIA will be utilized effectively. Figure 10 shows the weed management phase in a plantation system using drone technology.

**3.9. Irrigation Management.** In recent years, crop irrigation information can be obtained through satellite remote sensing images from various platforms as it has an advantage in terms of crop coverage area. However, the problem of public coverage and satellite remote sensing that is not in the orbital position during the plant development stage affects drone technology's use completely [132]. Izzuddin et al. [133] proposed an installation of thermal infrared sensor on a drone to enable the system to obtain the canopy temperature as this sensor is lighter and can produce more stable information; however, it will easily influence by air temperature and human activity [134] compared to multi-spectral sensors.

Besides that, drones equipped with thermal cameras can detect possible pooling or leaks in any irrigation system. A single high-resolution integrated with geolocated map of the field will highlight stressed areas. This map can also be used in the context of variable rate irrigation (VRI) applications. VRI applications can optimize the irrigation system

around the fields and automate the process based on data collected by sensors, maps, and GPS [135]. It can also contribute to identifying the water pollution around courses and bodies and consequent degradation of water-related ecosystems that might raise due to usage of agricultural chemicals that seep into nearby water system. Furthermore, drone application can also observe serious soil degradation, which threatens plant productivity [136].

#### 4. Challenges of Drone Application/Limitations

The use of drone technology for the plantation sector is among the main challenges. The cost of procuring drones, sensors and related materials, flight time, limited payload, and frequently changing regulations by the relevant authorities increases the chances of utilizing the drone effectiveness. More comprehensive information on the opportunities and challenges of drone application for the plantation and environmental sectors were effectively discussed by Hardin and Jensen [137], Zhang and Kovacs [138], and Ken and Hugenholtz [139].

**4.1. Regulations.** Drones equipped with the right sensors can aid a farmer to navigate the location in the fields, observe it, and generate statistics data related to the health and status of the crops. Under the Department of Civil Aviation (DCA) regulations, all measurements and observations done using a drone must fall within the drone operator's visual line of sight (VLOS). The problem in drone application is most larger farms have larger VLOS distance. It is impossible to conduct multiple operations continuously and stitch the multiple images together into a larger map as this will take a lot of time and need technical expertise. Moreover, the use of UAVs for agriculture is more commercial-based, and all relevant legislation and national rules should be followed.

**4.2. Operating Time.** For legal and safety purposes, drones need to have an active pilot. Using a drone in agriculture

does not facilitate multitasking. There must be someone to be present if something goes wrong. Even if a farmer is executing an autopilot flight, the pilot cannot walk away to take care of something else.

A common problem that usually arises is the estimation of the flight durations as it usually affects ideal conditions. A software may predict a time of flight based on a given area of interest, but in real conditions, it may take four or five times longer than the software prediction. Besides that, once the images are acquired, it needs to be processed and analyzed to extract all the useful information. With an average super-computer, few hours will be taken to analyze thousands of photos.

**4.3. Disadvantages of the Use of UAVs.** Though drone applications for precision agriculture are growing, there is a number of barriers to their successful widespread adoption. Various issues must be considered when employing a drone, and these include the path-planning process that does not utilize an expert pilot, the high-speed ultra-low scenario, data downloading task in real-time application, size, and payload to prevent bottlenecks and software for automatic analysis [138]. Another deterrent to invest in drone applications is the high cost of purchasing an unmanned aerial system. On the other side, the lack of a consistent workflow encourages stakeholders to use ad hoc procedures for implementing precision applications. Furthermore, because precision agriculture necessitates data-intensive techniques for utilization of the collected images, qualified personnel and professionals are frequently required as a result, and an average farmer may require training or the assistance of an expert to assist with picture processing, thereby increasing the cost. Therefore, each farmer with a few and tiny agricultural lands may be unable to use drone technologies. Hence, stakeholders with vast cultivated areas who has higher profit rates can use more advanced and expensive drone management systems. The most industrial drones have a shorter flight duration, ranging from 20 min to 1 h, which can only cover restricted area at each flight. On the other hand, longer-flying drones are more costly. Furthermore, the successful utilization of drones is influenced by the weather. The flight should be postponed, for example, on a very bad day. The weight and size of the sensors in the low-cost drone are the drone's other restrictions such as smaller and medium-sized drones are usually less steady and precise, and less powerful engines and low-cost drones have difficulty reaching a specific altitude [140].

## 5. Conclusion and Recommendations

Precision agriculture has incorporated cutting-edge technologies to boost crop output over the last decade. These technologies are important in situations where it is impossible to spray chemicals on crops due to a lack of labor. This method also makes the work of spraying easier and faster. The suggested solution explains how to monitor crops using a multispectral camera mounted on a drone. The camera gathers photographs, and the geographic indicator analyzes them throughout a single trip. It may be easier to pinpoint the

areas that require pesticide or fertilizer application based on the findings. The pesticides will be sprayed by the drone sprinkling system using GPS coordinates exclusively on affected regions where the NDVI has identified no vegetation. This could help cut down on resource waste like water and chemicals. Precision agriculture with drones is still in its early stages, and drone technology for agriculture applications has room for improvement. Enhanced image processing approach, less costly, minimum flight duration, new sensor designs, batteries, low volume sprayers, and nozzle types are all expected to be examined as drone technology advances. Drones based on remote sensing for agricultural applications should be the subject of a large number of experimental research. In the not-too-distant future, these systems will be more prominent in precision agriculture and environmental monitoring.

## Abbreviations

BSR:	Basal stem rot
CCCI:	Canopy-chlorophyll content index
CNN:	Convolutional neural network
CWSI:	Crop-water stress index
DCA:	Department of Civil Aviation
DSM:	Digital surface model
GDSI:	Ganoderma disease severity index
GIS:	Geographic information system
GNSS:	Global navigation satellite system
GPS:	Global positioning system
GSM:	Global system for mobile communications
HSV:	Hue, saturation, value
ICT:	Information and communication technology
IMU:	Inertial measurement unit
IoT:	Internet of Things
IPM:	Integrated pest management
Lab:	A color-opponent space with dimension $L$ for lightness and $a$ and $b$ for color-opponent dimensions
LCD:	Liquid-crystal display
LiDAR:	Light detection and ranging
LiPo:	Lithium-ion polymer
MAVLink:	A very lightweight messaging protocol for communicating with drones
MEMS:	Microelectromechanical system
MS:	Multispectral
NDVI:	Normalized difference vegetation index
NIR:	Near infrared reflectance
OBIA:	Object-based image analysis
PA:	Precision agriculture
RGB:	Red-green-blue
RPAS:	Remotely piloted aerial systems
RS:	Remote sensing
SSWM:	Site-specific weed management
TIR:	Thermal infrared
UAS:	Unmanned aerial systems
UAV:	Unmanned aerial vehicle
VIS-C:	Visible-color
VisualSFM:	Visual structure from motion system
VLOS:	Visual line of sight

VRI: Variable rate irrigation  
 YUV: One luminance and two chrominance.

## Conflicts of Interest

The authors have declared that no conflict of interest exists.

## Acknowledgments

The authors would like to thank Assoc. Prof. Dr. Nazmi Mat Nawi, Head of Laboratory, at Universiti Putra Malaysia, for the assistance, guidelines, and instruction.

## References

- [1] B. Kalantar, M. O. Idrees, S. Mansor, and A. A. Halins, "Smart counting – oil palm tree inventory with UAV," *Coordinates*, pp. 17–22, 2017.
- [2] R. Corley and P. Tinker, *The Oil Palm*, vol. 592 Wiley-Blackwell, 4 edition, 2008.
- [3] W. Darmosarkoro and S. S. Edy, *Winarma Lahan dan Pemupukan Kelapa Sawit*, vol. 1, Pusat Penelitian Kelapa Sawit, 2003.
- [4] D. W. Lamb and R. B. Brown, "PA–precision agriculture: remote-sensing and mapping of weeds in crops," *Journal of Agricultural Engineering Research*, vol. 78, no. 2, pp. 117–125, 2001.
- [5] D. J. Mulla, "Twenty five years of remote sensing in precision agriculture: key advances and remaining knowledge gaps," *Biosystems Engineering*, vol. 114, no. 4, pp. 358–371, 2013.
- [6] S. K. Seelan, S. Laguetta, G. M. Casady, and G. A. Seielstad, "Remote sensing applications for precision agriculture: a learning community approach," *Remote Sensing of Environment*, vol. 88, no. 1-2, pp. 157–169, 2003.
- [7] J. V. Stanford, "Implementing precision agriculture in the 21st century," *Journal of Agricultural Engineering Research*, vol. 76, no. 3, pp. 267–275, 2000.
- [8] B. Kalantar, S. Mansor, M. I. Sameen, B. Pradhan, and H. Z. M. Shafri, "Drone-based land-cover mapping using a fuzzy unordered rule induction algorithm integrated into object-based image analysis," *International Journal of Remote Sensing*, vol. 38, no. 8-10, pp. 2535–2556, 2017.
- [9] H. A. H. Al-najjar, B. Kalantar, B. Pradhan, and V. Saeidi, "Land cover classification from fused DSM and UAV images using convolutional neural networks," *Remote Sensing*, vol. 11, no. 12, p. 1461, 2019.
- [10] B. K. G. Harandi, S. B. Mansor, and H. Z. M. Shafri, "Image mosaic methods for UAV sequence images," in *ACRS 2015 - 36th Asian Conf. Remote Sens. Foster. Resilient Growth Asia, Proc*, 2015.
- [11] D. Krijnen and C. Dekker, "AR drone 2.0 with Subsumption architecture," in *In proceedings of the Artificial intelligence research seminar*, 2014.
- [12] A. Cavoukian, *Privacy and drones: Unmanned Aerial Vehicles*, Information and Privacy Commissioner of Ontario, Canada, 2012.
- [13] S. G. Gupta, D. M. Ghonge, and P. M. Jawandhiya, "Review of unmanned aircraft system (UAS)," *SSRN Electronic Journal*, vol. 2, 2013.
- [14] B. Kalantar, S. B. Mansor, A. Abdul Halin, H. Z. M. Shafri, and M. Zand, "Multiple moving object detection from UAV videos using trajectories of matched regional adjacency graphs," *IEEE Transactions on Geoscience and Remote Sensing*, vol. 55, no. 9, pp. 5198–5213, 2017.
- [15] H. Zhu, H. Nie, L. Zhang, X. Wei, and M. Zhang, "Design and assessment of octocopter drones with improved aerodynamic efficiency and performance," *Aerospace Science and Technology*, vol. 106, article 106206, 2020.
- [16] S. Salazar-Cruz, F. Kendoul, R. Lozano, and I. Fantoni, "Real-time stabilization of a small three-rotor aircraft," *IEEE Transactions on Aerospace and Electronic Systems*, vol. 44, no. 2, pp. 783–794, 2008.
- [17] T. S. Kabra, A. V. Kardile, D. B. Mane, P. R. Bhosale, and A. M. Belekar, "Design, Development & optimization of a quadcopter for agricultural applications," *International Research Journal of Engineering and Technology*, vol. 4, no. 7, 2017.
- [18] J. Verbeke, D. Hulens, H. Ramon, T. Goedeme, and J. De Schutter, "The design and construction of a high endurance hexacopter suited for narrow corridors," in *2014 International Conference on Unmanned Aircraft Systems (ICUAS)*, pp. 543–551, 2014.
- [19] G. W. Wasantha and S. Wang, "Heavy payload tethered hexarotors for agricultural applications: power supply design," *International Research Journal of Engineering and Technology*, vol. 2, pp. 641–645, 2015.
- [20] B. Kalantar, N. Ueda, H. A. H. Al-Najjar, H. Moayedi, A. A. Halin, and S. Mansor, "Uav and lidar image registration: a surf-based approach for ground control points selection," *The International Archives of the Photogrammetry, Remote Sensing and Spatial Information Sciences*, vol. XLII-2/W13, pp. 413–418, 2019.
- [21] B. Kalantar, S. B. Mansor, H. Z. M. Shafri, and A. A. Halin, "Integration of template matching and object-based image analysis for semi-Automatic oil palm tree counting in UAV images," in *Proceedings of the 37th Asian Conference on Remote Sensing, ACRS 2016*, vol. 3, 2016.
- [22] D. B. Kingston, R. Beard, T. McLain, M. Larsen, and W. Ren, "Autonomous vehicle technologies for small fixed-wing UAVs," *Journal of Aerospace Computing, Information, and Communication*, vol. 2, no. 1, pp. 92–108, 2005.
- [23] A. Lindqvist, E. Fresk, and G. Nikolakopoulos, "Optimal design and modeling of a tilt wing aircraft," in *2015 23rd Mediterranean Conference on Control and Automation (MED)*, pp. 701–708, 2015.
- [24] S. Bose, R. Verma, K. Garuda, A. Tripathi, and S. Clement, "Modeling, analysis and fabrication of a thrust vectoring spherical VTOL aerial vehicle," in *2014 IEEE aerospace conference*, 2014.
- [25] C. W. Lum, K. Gauksheim, T. Kosel, and T. McGeer, "Assessing and estimating risk of operating unmanned aerial systems in populated areas," in *11th AIAA Aviation Technology, Integration, and Operations (ATIO) Conference, including the AIAA Balloon Systems Conference and 19th AIAA Lighter-Than*, 2011.
- [26] Z. Mohammad Zain, D. S. Ganraj, and A. K. Hussin, "An ultralight helicopter for rice farmers," in *19th AIAA Applied Aerodynamics Conference*, 2001.
- [27] M. Hejduk, "The use of unmanned aerial vehicles - drones supply courier," *Thesis Inzynierska*, International University of Logistics and Transport, Wroclaw, 2015.
- [28] G. Yang, J. Liu, C. Zhao et al., "Unmanned aerial vehicle remote sensing for field-Based crop phenotyping: current

- status and perspectives,” *Frontiers in Plant Science*, vol. 8, p. 1111, 2017.
- [29] D. C. Tsouros, S. Bibi, and P. G. Sarigiannidis, “A Review on UAV-Based Applications for Precision Agriculture,” *Information*, vol. 10, no. 11, p. 349, 2019.
- [30] J. Xue and B. Su, “Significant remote sensing vegetation indices: a review of developments and applications,” *Journal of sensors*, vol. 2017, Article ID 1353691, 17 pages, 2017.
- [31] M. S. Tehrani, H. Özener, B. Kalantar et al., “Application of an ensemble statistical approach in spatial predictions of bushfire probability and risk mapping,” *Journal of sensors*, vol. 2021, Article ID 6638241, 31 pages, 2021.
- [32] M. Maimaitijiang, A. Ghulam, P. Sidike et al., *Unmanned Aerial System (UAS)-Based Phenotyping of Soybean Using Multi-Sensor Data Fusion and Extreme Learning Machine*, vol. 134, 2017.
- [33] M. Hassanein, Z. Lari, and N. El-Sheimy, “A new vegetation segmentation approach for cropped fields based on threshold detection from hue histograms,” *Sensors*, vol. 18, no. 4, p. 1253, 2018.
- [34] L. Deng, Z. Mao, X. Li, Z. Hu, F. Duan, and Y. Yan, “UAV-based multispectral remote sensing for precision agriculture: a comparison between different cameras,” *ISPRS Journal of Photogrammetry and Remote Sensing*, vol. 146, pp. 124–136, 2018.
- [35] S. Bhandari, A. Raheja, M. R. Chaichi et al., “Effectiveness of uav-based remote sensing techniques in determining lettuce nitrogen and water stresses,” in *Proceedings of 14th International Conference on Precision Agriculture*, pp. 1066403–1066415, 2018.
- [36] M. Hassanalian and A. Abdelkefi, “Classifications, applications, and design challenges of drones: a review,” *Progress in Aerospace Science*, vol. 91, pp. 99–131, 2017.
- [37] A. C. Watts, V. G. Ambrosia, and E. A. Hinkley, “Unmanned aircraft systems in remote sensing and scientific research: classification and considerations of use,” *Remote Sensing*, vol. 4, no. 6, pp. 1671–1692, 2012.
- [38] M. Arjomandi, *Classification of Unmanned Aerial Vehicles Related Papers*, 2007.
- [39] *911 Security Newsletter October 2020 Newsletter*, The University of Adelaide, 2007.
- [40] R. R. Shamshiri, I. A. Hameed, S. K. Balasundram, D. Ahmad, C. Weltzien, and M. Yamin, “Fundamental research on unmanned aerial vehicles to support precision agriculture in oil palm plantations,” *Agricultural Robots-Fundamentals and Application*, J. Zhou and B. Zhang, Eds., pp. 91–116, 2018.
- [41] P. Gennari, A. Heyman, and M. Kainu, *FAO statistical pocketbook*, World food and agriculture. Food Agric. Organ, United Nations, Rome, Italy, 2015.
- [42] R. R. Shamshiri, “A breakthrough in oil palm precision agriculture: smart management of oil palm plantations with autonomous UAV imagery and robust machine vision,” in *Int. Conf. Agric. Food Eng.*, 2016.
- [43] M. B. A. Gibril, H. Z. M. Shafri, A. Shanableh, R. Al-Ruzouq, A. Wayayok, and S. J. Hashim, “Deep convolutional neural network for large-scale date palm tree mapping from uav-based images,” *Remote Sensing*, vol. 13, no. 14, p. 2787, 2021.
- [44] R. R. Shamshiri, *Integration of Smart Sensors and Robotics in Increasing Agricultural Productivity with Higher Yields at Lower Costs*, Asian Sp. Technol. Summit, 2017.
- [45] P. Mylonas, Y. Voutos, and A. Sofou, “A Collaborative Pilot Platform for Data Annotation and Enrichment in Viticulture,” *Information*, vol. 10, no. 4, p. 149, 2019.
- [46] K. Chartzoulakis and M. Bertaki, “Sustainable water management in agriculture under climate change,” *Agriculture and Agricultural Science Procedia*, vol. 4, pp. 88–98, 2015.
- [47] P. Saccon, “Water for agriculture, irrigation management,” *Applied Soil Ecology*, vol. 123, pp. 793–796, 2018.
- [48] P. Garre and A. Harish, “Autonomous agricultural pesticide spraying UAV,” in *IOP Conference Series: Materials Science and Engineering*, vol. 455, Bristol, UK, 2018.
- [49] B. Allreda, L. Martinez, M. K. Fessehazion et al., “Overall results and key findings on the use of UAV visible-color, multispectral, and thermal infrared imagery to map agricultural drainage pipes,” *Agricultural Water Management*, vol. 232, p. 106036, 2020.
- [50] H. Lu, T. Iseley, J. Matthews, W. Liao, and M. Azimi, “An ensemble model based on relevance vector machine and multi-objective salp swarm algorithm for predicting burst pressure of corroded pipelines,” *Journal of Petroleum Science and Engineering*, vol. 203, article 108585, 2021.
- [51] M. P. Christiansen, M. S. Laursen, R. N. Jørgensen, S. Skovsen, and R. Gislum, “Designing and testing a uav mapping system for agricultural field surveying,” *Sensors*, vol. 17, no. 12, p. 2703, 2017.
- [52] J. Primicerio, S. Filippo, D. Gennaro et al., “A flexible unmanned aerial vehicle for precision agriculture,” *Precision Agriculture*, vol. 13, no. 4, pp. 517–523, 2012.
- [53] L. G. Santesteban, S. F. Di Gennaro, A. Herrero-Langreo, C. Miranda, J. B. Royo, and A. Matese, “High-resolution UAV-based thermal imaging to estimate the instantaneous and seasonal variability of plant water status within a vineyard,” *Agricultural Water Management*, vol. 183, pp. 49–59, 2017.
- [54] A. Vasudevan, D. A. Kumar, and N. S. Bhuvaneshwari, “Precision farming using unmanned aerial and ground vehicles,” in *2016 IEEE technological innovations in ICT for agriculture and rural development (TIAR)*, pp. 146–150, 2016.
- [55] X. Li, Y. Zhao, J. Zhang, and Y. Dong, “A hybrid pso algorithm based flight path optimization for multiple agricultural uavs,” in *2016 IEEE 28th international conference on tools with artificial intelligence (ICTAI)*, pp. 691–697, 2016.
- [56] B. Dai, Y. He, F. Gu, L. Yang, J. Han, and W. Xu, “A vision-based autonomous aerial spray system for precision agriculture,” in *2017 IEEE international conference on robotics and biomimetics (ROBIO)*, pp. 507–513, 2017.
- [57] K. Uto, H. Seki, G. Saito, and Y. Kosugi, “Characterization of rice paddies by a UAV-mounted miniature hyperspectral sensor system,” *IEEE Journal of Selected Topics in Applied Earth Observations and Remote Sensing*, vol. 6, no. 2, pp. 851–860, 2013.
- [58] R. O. Bura, S. W. Apriyani, K. Ariwibawa, and E. Adharian, “UAV application for oil palm harvest prediction,” *Journal of Physics Conference Series*, vol. 1130, p. 012001, 2018.
- [59] T. Kattenborn, M. Sperlich, K. Bataua, and B. Koch, “Automatic single tree detection in plantations using UAV-based photogrammetric point clouds,” *The International Archives of Photogrammetry, Remote Sensing and Spatial Information Sciences*, vol. 40, pp. 139–144, 2014.
- [60] W. H. Maes and K. Steppe, “Perspectives for remote sensing with unmanned aerial vehicles in precision agriculture,” *Trends in Plant Science*, vol. 24, no. 2, pp. 152–164, 2019.

- [61] B. P. Hudzietz and S. Saripalli, "An experimental evaluation of 3D terrain mapping with an autonomous helicopter," *International Society for Photogrammetry and Remote Sensing*, vol. 38, 2011.
- [62] H. Freimuth and M. König, "Generation of waypoints for uav-assisted progress monitoring and acceptance of construction work," in *15th International Conference on Construction Applications of Virtual Reality*, 2015.
- [63] S. Siebert and J. Teizer, "Mobile 3D mapping for surveying earthwork projects using an unmanned aerial vehicle (UAV) system," *Automation in Construction*, vol. 41, pp. 1–14, 2014.
- [64] Z. Yang, "Fast template matching based on normalized cross correlation with centroid bounding," in *2010 International Conference on Measuring Technology and Mechatronics Automation* no. 2, pp. 224–227, 2010.
- [65] *SOPB Sarawak Oil Palms Berhad Annual Report 2018*, Sarawak Oil Palms Berhad, 2018.
- [66] A. J. Pinz, "A computer vision system for the recognition of trees in aerial photographs," *Multisource Data Integration in Remote Sensing*, vol. 3099, pp. 111–124, 1991.
- [67] R. Woodham and R. Pollock, "The automatic recognition of individual trees in aerial images of forests based on a synthetic tree crown image model," *Doctoral dissertation*, University of British Columbia, 1996.
- [68] M. A. Mansur, R. B. Mukhtar, and J. Al-Doksi, "The usefulness of unmanned airborne vehicle (UAV) imagery for automated palm oil tree counting," *Research Journal*, vol. 1, 2014.
- [69] L. Wang, P. Gong, and G. S. Biging, "Individual tree-crown delineation and treetop detection in high-spatial-resolution aerial imagery," *Photogrammetric Engineering and Remote Sensing*, vol. 70, no. 3, pp. 351–357, 2004.
- [70] T. Brandtberg and F. Walter, "Automated delineation of individual tree crowns in high spatial resolution aerial images by multiple-scale analysis," *Machine Vision and Applications*, vol. 11, no. 2, pp. 64–73, 1998.
- [71] A. Tellaeche, X. P. BurgosArtizzu, G. Pajares, A. Ribeiro, and C. Fernández-Quintanilla, "A new vision-based approach to differential spraying in precision agriculture," *Computers and Electronics in Agriculture*, vol. 60, no. 2, pp. 144–155, 2008.
- [72] G. Sylvester, *E-Agriculture in action: drones for agriculture*, Food and Agriculture Organization of the United Nations and International Telecommunication Union, Bangkok, 2018.
- [73] D. Zhang, L. Chen, R. Zhang et al., "Evaluating effective swath width and droplet distribution of aerial spraying systems on M-18B and thrush 510G airplanes," *International Journal of Agricultural and Biological Engineering*, vol. 8, pp. 21–30, 2015.
- [74] S. R. Kurkute, B. D. Deore, P. Kasar, M. Bhamare, and M. Sahane, "Drones for smart agriculture: a technical report," *International Journal for Research in Applied Science and Engineering Technology*, vol. 6, no. 4, pp. 341–346, 2018.
- [75] B. Sadhana, G. Naik, R. J. Mythri, P. G. Hedge, and K. S. B. Shyama, "Development of quad copter based pesticide spraying mechanism for agricultural applications," *International Journal of Innovative Research in Electrical, Electronics*, vol. 5, no. 2, pp. 121–123, 2017.
- [76] K. Gayathri Devi, N. Sowmiya, K. Yasoda, K. Muthulakshmi, and B. Kishore, "Review on application of drones for crop health monitoring and spraying pesticides and fertilizer," *Journal of Critical Reviews*, vol. 7, no. 6, pp. 667–672, 2020.
- [77] S. Kedari, P. Lohagaonkar, M. Nimbokar, G. Palve, and P. Yevale, "Quadcopter-a smarter way of pesticide spraying," *Imperial Journal of Interdisciplinary Research*, vol. 2, no. 6, 2016.
- [78] R. Laudien, G. Bareth, and R. Doluschitz, "multitemporal hyperspectral data analysis for regional detection of plant stress by using an airborne- and tractor-based spectrometer – case study: sugar beet disease *Rhizoctonia Solani* –,” in *Proceedings of the Analysis and Applications, International Society for Photogrammetry and Remote Sensing (ISPRS)*, Beijing, China, 2005.
- [79] I. Colomina and P. Molina, "Unmanned aerial systems for photogrammetry and remote sensing: a review," *ISPRS Journal of Photogrammetry and Remote Sensing*, vol. 92, pp. 79–97, 2014.
- [80] F. Nex and F. Remondino, "UAV for 3D mapping applications: a review," *Applied Geomatics*, vol. 6, no. 1, pp. 1–15, 2014.
- [81] J. Bendig, A. Bolten, S. Bennertz, J. Broscheit, S. Eichfuss, and G. Bareth, "Estimating Biomass of Barley Using Crop Surface Models (CSMs) Derived from UAV-Based RGB Imaging," *Remote Sensing*, vol. 6, no. 11, pp. 10395–10412, 2014.
- [82] F. A. Vega, F. C. Ramírez, M. P. Saiz, and F. O. Rosúa, "Multi-temporal imaging using an unmanned aerial vehicle for monitoring a sunflower crop," *Biosystems Engineering*, vol. 132, pp. 19–27, 2015.
- [83] R. A. Díaz-Varela, R. D. Rosala, L. León, and P. J. Zarco-Tejada, "High-resolution airborne uav imagery to assess olive tree crown parameters using 3d photo reconstruction: application in breeding trials," *Remote Sensing*, vol. 7, no. 4, pp. 4213–4232, 2015.
- [84] J. Torres-Sánchez, F. López-Granados, N. Serrano, O. Arquero, and J. M. Peña, "High-throughput 3-D monitoring of agricultural-tree plantations with unmanned aerial vehicle (UAV) technology," *Technology*, vol. 10, no. 6, 2015.
- [85] L. Kumar, K. S. Schmidt, S. Dury, and A. K. Skidmore, "Imaging spectrometry and vegetation science," in *Imaging Spectrometry - Basic Principles and Prospective Application*, F. D. Meer and S. M. Jong, Eds., vol. 4, pp. 111–155, Remote Sensing and Digital Image Processing, 2001.
- [86] W. Koppe, M. L. Gnyp, S. D. Hennig et al., "Multi-temporal hyperspectral and radar remote sensing for estimating winter wheat biomass in the North China Plain," *Photogrammetrie-Fernerkundung-Geoinformation*, vol. 2012, no. 3, pp. 281–298, 2012.
- [87] S. Migdall, H. Bach, J. Bobert, M. Wehrhan, and W. Mauser, "Inversion of a canopy reflectance model using hyperspectral imagery for monitoring wheat growth and estimating yield," *Precision Agriculture*, vol. 10, no. 6, pp. 508–524, 2009.
- [88] C. Yang, J. H. Everitt, and J. M. Bradford, "Yield estimation from hyperspectral imagery using spectral angle mapper (SAM)," *Transactions of the ASABE*, vol. 51, no. 2, pp. 729–737, 2008.
- [89] V. Hoyos-Villegas and F. B. Fritschi, "Relationships among vegetation indices derived from aerial photographs and soybean growth and yield," *Crop Science*, vol. 53, no. 6, pp. 2631–2642, 2013.
- [90] T. Sakamoto, A. A. Gitelson, A. L. Nguay-Robertson et al., "An alternative method using digital cameras for continuous

- monitoring of crop status,” *Agricultural and Forest Meteorology*, vol. 154-155, pp. 113–126, 2012.
- [91] P. J. Zarco-Tejada, J. A. Berni, L. Suárez, and E. Fereres, “A new era in remote sensing of crops with unmanned robots,” *Proceedings of SPIE*, vol. 10, p. 7480, 2008.
- [92] T. Chu, R. Chen, J. A. Landivar, M. M. Maeda, C. Yang, and M. J. Starek, “Cotton growth modeling and assessment using unmanned aircraft system visual-band imagery,” *Journal of Applied Remote Sensing*, vol. 10, no. 3, article 036018, 2016.
- [93] A. Gracia-Romero, S. C. Kefauver, O. Vergara-Díaz et al., “Comparative performance of ground vs. aerially assessed RGB and multispectral indices for early-growth evaluation of maize performance under phosphorus fertilization,” *Frontiers in Plant Science*, vol. 8, p. 2004, 2017.
- [94] A. C. Kyratzis, D. P. Skarlatos, G. C. Menexes, V. F. Vamvakousis, and A. Katsiotis, “Assessment of vegetation indices derived by UAV imagery for durum wheat phenotyping under a water limited and heat stressed Mediterranean environment,” *Frontiers in Plant Science*, vol. 8, p. 1114, 2017.
- [95] X. Zhou, H. B. Zheng, X. Q. Xu et al., “Predicting grain yield in rice using multi-temporal vegetation indices from UAV-based multispectral and digital imagery,” *ISPRS Journal of Photogrammetry and Remote Sensing*, vol. 130, pp. 246–255, 2017.
- [96] J. Bendig, A. Bolten, and G. Bareth, “Introducing a low-COST mini-UAV for thermal- and multispectral-imaging,” *The International Archives of the Photogrammetry, Remote Sensing and Spatial Information Sciences*, vol. 39, pp. 345–349, 2012.
- [97] M. Reinecke and T. Prinsloo, “The influence of drone monitoring on crop health and harvest size,” in *2017 1st International conference on next generation computing applications (NextComp)*, pp. 5–10, 2017.
- [98] A. K. Bhandari, A. Kumar, and G. K. Singh, “Feature extraction using normalized difference vegetation index (NDVI): a case study of Jabalpur City,” *Procedia Technology*, vol. 6, pp. 612–621, 2012.
- [99] J. W. Rouse, R. H. Haas, J. A. Schell, and D. W. Deering, “Monitoring vegetation systems in the great plains with ERTS,” in *3rd ERTS Symp. NASA SP-351*, pp. 309–317, Washingt. DC, 1973.
- [100] DJI DJI - Official Website, <https://www.dji.com>.
- [101] J. Huang, H. Wang, Q. Dai, and D. Han, “Analysis of NDVI data for crop identification and yield estimation,” *IEEE Journal of Selected Topics in Applied Earth Observations and Remote Sensing*, vol. 7, no. 11, pp. 4374–4384, 2014.
- [102] A. Matese, P. Toscano, S. F. GennaroDi et al., “Intercomparison of uav, aircraft and satellite remote sensing platforms for precision viticulture,” *Remote Sensing*, vol. 7, no. 3, pp. 2971–2990, 2015.
- [103] R. Austin, “Unmanned aircraft systems: UAVS design,” in *Development and Deployment*, John Wiley & Sons, 54th edition, 2010.
- [104] T. Duan, S. C. Chapman, Y. Guo, and B. Zheng, “Dynamic monitoring of NDVI in wheat agronomy and breeding trials using an unmanned aerial vehicle,” *Field Crops Research*, vol. 210, pp. 71–80, 2017.
- [105] M. Kerkech, A. Hafiane, and R. Canals, “Deep leaning approach with colorimetric spaces and vegetation indices for vine diseases detection in UAV images,” *Computers and Electronics in Agriculture*, vol. 155, pp. 237–243, 2018.
- [106] S. Liaghat, R. Ehsani, S. Mansor et al., “Early detection of basal stem rot disease (Ganoderma) in oil palms based on hyperspectral reflectance data using pattern recognition algorithms,” *International Journal of Remote Sensing*, vol. 35, no. 10, pp. 3427–3439, 2014.
- [107] G. Singh, “Ganoderma - the scourge of oil palm in the coastal area,” in *Proceedings of Ganoderma workshop, Bangi, Selangor, Malaysia, 11 September 1990*, pp. 7–35, 1991.
- [108] H. Z. M. Shafri and N. Hamdan, “Hyperspectral imagery for mapping disease infection in oil palm plantation using vegetation indices and red edge techniques,” *American Journal of Applied Sciences*, vol. 6, no. 6, pp. 1031–1035, 2009.
- [109] I. Manfredonia, C. Stallo, M. Ruggieri, G. Massari, and S. Barbante, “An early-warning aerospace system for relevant water bodies monitoring,” in *2015 IEEE Metrology for Aerospace (MetroAeroSpace)*, pp. 536–540, 2015.
- [110] J. Gago, C. Douthe, R. E. Coopman et al., “UAVs challenge to assess water stress for sustainable agriculture,” *Agricultural Water Management*, vol. 153, pp. 9–19, 2015.
- [111] M. A. Izzuddin, A. Hamzah, M. N. Nisfariza, and A. S. Idris, “Analysis of multispectral imagery from unmanned aerial vehicle (UAV) using object-based image analysis for detection of ganoderma disease in oil palm,” *Journal of Oil Palm Research*, vol. 32, pp. 497–508, 2020.
- [112] K. Anderson and K. J. Gaston, “Lightweight unmanned aerial vehicles will revolutionize spatial ecology,” *Frontiers in Ecology and the Environment*, vol. 11, no. 3, pp. 138–146, 2013.
- [113] E.-C. Oerke, “Crop losses to pests,” *The Journal of Agricultural Science*, vol. 144, no. 1, pp. 31–43, 2006.
- [114] C. R. Thompson, J. A. Dille, and D. E. Peterson, “Weed competition and management in Sorghum,” *Sorghum: A State of the Art and Future Perspectives*, vol. 58, pp. 347–360, 2019.
- [115] A. C. Guglielmini, A. M. C. Verdú, and E. H. Satorre, “Competitive ability of five common weed species in competition with soybean,” *International journal of pest management*, vol. 63, no. 1, pp. 30–36, 2017.
- [116] S. Korav, V. Ram, L. I. P. Ray, R. Krishnappa, N. J. Singh, and N. Premaradhya, “Weed pressure on growth and yield of groundnut (*Arachis hypogaea* L.) in Meghalaya, India,” *International Journal of Current Microbiology and Applied Sciences*, vol. 7, pp. 2852–2858, 2018.
- [117] H. Kaur, G. Singh Brar, and P. P. A. Shete, “A Review on different Weed Management approaches,” *International Journal of Current Microbiology and Applied Sciences*, vol. 8, no. 8, pp. 2854–2859, 2019.
- [118] A. Zohaib, T. Abbas, and T. Tabassum, “Weeds cause losses in field crops through allelopathy,” *Notulae Scientia Biologicae*, vol. 8, no. 1, pp. 47–56, 2016.
- [119] M. Hassanein and N. El-Sheimy, “An efficient weed detection procedure using low-cost UAV imagery system for precision agriculture applications,” *International Archives of the Photogrammetry, Remote Sensing & Spatial Information Sciences*, vol. XLII-1, pp. 181–187, 2018.
- [120] K. R. Krishna, *Agricultural Drones: A Peaceful Pursuit*, Apple Academic Press, Inc., 2018.
- [121] M. Crimaldi, V. Cristiano, A. VivoDe, M. Isernia, P. Ivanov, and F. Sarghini, “Neural network algorithms for real time plant diseases detection using UAVs,” *Lecture Notes in Civil Engineering*, vol. 67, pp. 827–835, 2020.



- [122] F. López-Granados, “Weed detection for site-specific weed management: mapping and real-time approaches,” *Weed Research*, vol. 51, no. 1, pp. 1–11, 2011.
- [123] T. K. Alexandridis, A. A. Tamouridou, X. E. Pantazi et al., “Novelty detection classifiers in weed mapping: *Silybum marianum* detection on UAV multispectral images,” *Sensors*, vol. 17, no. 9, p. 2007, 2017.
- [124] A. A. Tamouridou, T. K. Alexandridis, X. E. Pantazi et al., “Application of multilayer perceptron with automatic relevance determination on weed mapping using uav multispectral imagery,” *Sensors*, vol. 17, no. 10, p. 2307, 2017.
- [125] F. Castaldi, F. Pelosi, S. Pascucci, and R. Casa, “Assessing the potential of images from unmanned aerial vehicles (UAV) to support herbicide patch spraying in maize,” *Precision Agriculture*, vol. 18, 2017.
- [126] J. P. T. Lambert, H. L. Hicks, D. Z. Childs, and R. P. Freckleton, “Evaluating the potential of unmanned aerial systems for mapping weeds at field scales: a case study with *Alopecurus myosuroides*,” *Weed Research*, vol. 58, no. 1, pp. 35–45, 2018.
- [127] A. Chlingaryan, S. Sukkarieh, and B. Whelan, “Machine learning approaches for crop yield prediction and nitrogen status estimation in precision agriculture: a review,” *Computers and Electronics in Agriculture*, vol. 151, pp. 61–69, 2018.
- [128] A. I. de Castro, J. Torres-Sánchez, J. M. Peña, F. M. Jiménez-Brenes, O. Csillik, and F. López-Granados, “An automatic random forest-OBIA algorithm for early weed mapping between and within crop rows using UAV imagery,” *Remote Sensing*, vol. 10, no. 3, p. 285, 2018.
- [129] M. Pérez-Ortiz, J. M. Peña, P. Antonio Gutiérrez, J. Torres-Sánchez, C. Hervás-Martínez, and F. López-Granados, “Selecting patterns and features for between- and within-crop-row weed mapping using UAV-imagery,” *Expert Systems with Applications*, vol. 47, pp. 85–94, 2016.
- [130] J. Gao, W. Liao, D. Nuytens et al., “Fusion of pixel and object-based features for weed mapping using unmanned aerial vehicle imagery,” *International Journal of Applied Earth Observation and Geoinformation*, vol. 67, pp. 43–53, 2018.
- [131] M. Esposito, M. Crimaldi, V. Cirillo, F. Sarghini, and A. Maggio, “Drone and sensor technology for sustainable weed management: a review,” *Chemical and Biological Technologies in Agriculture*, vol. 8, 2021.
- [132] W. Ren, D. Wu, and L. Qin, “Preliminary study on data collecting and processing of unmanned airship low altitude hyperspectral remote sensing,” *Ecology and Environmental Monitoring of Three Gorges*, vol. 1, pp. 52–57, 2016.
- [133] Z. ZhiTao, B. Jiang, H. WenTing, F. QiuPing, C. ShuoBo, and C. Ting, “Cotton moisture stress diagnosis based on canopy temperature characteristics calculated from UAV thermal infrared image,” *Transactions of the Chinese Society of Agricultural Engineering*, vol. 34, pp. 77–84, 2018.
- [134] K. Ribeiro-Gomes, D. Hernández-López, J. F. Ortega, R. Ballesteros, T. Poblete, and M. A. Moreno, “Uncooled thermal camera calibration and optimization of the photogrammetry process for uav applications in agriculture,” *Sensors*, vol. 17, no. 10, p. 2173, 2017.
- [135] L. Quebrajo, M. Perez-Ruiz, L. Pérez-Urrestarazu, G. Martínez, and G. Egea, “Linking thermal imaging and soil remote sensing to enhance irrigation management of sugar beet,” *Biosystems Engineering*, vol. 165, pp. 77–87, 2018.
- [136] J. Salmelin, I. Pölönen, H.-H. Puupponen et al., “Hyperspectral imaging of macroinvertebrates—a pilot study for detecting metal contamination in aquatic ecosystems,” *Water, Air, & Soil Pollution*, vol. 229, no. 9, 2018.
- [137] P. J. Hardin and R. R. Jensen, “Small-scale unmanned aerial vehicles in environmental remote sensing: challenges and opportunities,” *GIScience & Remote Sensing*, vol. 48, no. 1, pp. 99–111, 2011.
- [138] C. Zhang and J. M. Kovacs, “The application of small unmanned aerial systems for precision agriculture: a review,” *Precision Agriculture*, vol. 13, no. 6, pp. 693–712, 2012.
- [139] W. Ken and H. Hugenholtz Chris, “Remote sensing of the environment with small unmanned aircraft systems (UASs), part 1: a review of progress and challenges1,” vol. 2, pp. 69–85,, 2014.
- [140] J. Romeo, G. Pajares, M. Montalvo, J. M. Guerrero, M. Guijarro, and A. Ribeiro, “Crop row detection in maize fields inspired on the human visual perception,” *Scientific World Journal*, vol. 2012, article 484390, 10 pages, 2012.

## Research Article

# Fire-Net: A Deep Learning Framework for Active Forest Fire Detection

Seyd Teymoor Seydi,<sup>1</sup> Vahideh Saeidi ,<sup>2</sup> Bahareh Kalantar ,<sup>3</sup> Naonori Ueda,<sup>3</sup> and Alfian Abdul Halin <sup>4</sup>

<sup>1</sup>School of Surveying and Geospatial Engineering, College of Engineering, University of Tehran, Tehran 14174-66191, Iran

<sup>2</sup>Department of Mapping and Surveying, Darya Tarsim Consulting Engineers Co. Ltd, Tehran 15119-43943, Iran

<sup>3</sup>RIKEN Center for Advanced Intelligence Project, Goal-Oriented Technology Research Group, Disaster Resilience Science Team, Tokyo 103-0027, Japan

<sup>4</sup>Department of Multimedia, Faculty of Computer Science and Information Technology Universiti Putra Malaysia, Serdang, Seri Kembangan 43400, Malaysia

Correspondence should be addressed to Bahareh Kalantar; bahareh.kalantar@riken.jp

Received 31 August 2021; Revised 6 January 2022; Accepted 26 January 2022; Published 21 February 2022

Academic Editor: Giorgio Pennazza

Copyright © 2022 Seyd Teymoor Seydi et al. This is an open access article distributed under the Creative Commons Attribution License, which permits unrestricted use, distribution, and reproduction in any medium, provided the original work is properly cited.

Forest conservation is crucial for the maintenance of a healthy and thriving ecosystem. The field of remote sensing (RS) has been integral with the wide adoption of computer vision and sensor technologies for forest land observation. One critical area of interest is the detection of active forest fires. A forest fire, which occurs naturally or manually induced, can quickly sweep through vast amounts of land, leaving behind unfathomable damage and loss of lives. Automatic detection of active forest fires (and burning biomass) is hence an important area to pursue to avoid unwanted catastrophes. Early fire detection can also be useful for decision makers to plan mitigation strategies as well as extinguishing efforts. In this paper, we present a deep learning framework called Fire-Net, that is trained on Landsat-8 imagery for the detection of active fires and burning biomass. Specifically, we fuse the optical (Red, Green, and Blue) and thermal modalities from the images for a more effective representation. In addition, our network leverages the residual convolution and separable convolution blocks, enabling deeper features from coarse datasets to be extracted. Experimental results show an overall accuracy of 97.35%, while also being able to robustly detect small active fires. The imagery for this study is taken from Australian and North American forests regions, the Amazon rainforest, Central Africa and Chernobyl (Ukraine), where forest fires are actively reported.

## 1. Introduction

Forests, lands dominated by trees, cover approximately 4 billion hectares of the earth's land area [1]. This is equivalent to around 29% of the earth. Forest management and conservation are therefore essential tasks for sustaining biodiversity at global scale [2]. Forest fires, which can be manmade or naturally occurring, are events that can threaten our planet leaving behind catastrophic circumstances such as damages and losses [3–7]. Forest fires have long-term devastating effects on ecosystems such as destroying vegetation dynam-

ics, emission of greenhouse gases, loss of wildlife habit, and also devastation of land covers [8–11]. Therefore, accurate and timely detection of active forest fires is critical to minimize and/or prevent such hazards.

In recent years, advanced remote sensing (RS) technologies have been adopted to monitor and observe the earth and land covers, which can be on a large scale [12–15]. Availability of high spatio-temporal resolution data and multispectral imagery allow tremendous applications of forest monitoring such as burned area mapping [7], active fire detection [11, 16], burning biomass detection [17, 18], and forest

disturbance monitoring [19, 20]. It is worth noting that one widely and freely available RS data source can be used for all the tasks, which are imagery from Landsat satellites.

Active fire detection is an important application of RS in forest monitoring. The active fire detection and analysis can be used in many applications such as source point pollution in air quality analysis, initial seed point in burned area mapping, and prediction of growth and spread of active fires [21]. Until now, many researchers detect active fires using multispectral satellite imagery, assisted by computer algorithms. For instance, Wooster and Nightingale [4] presented an active fire detection method based on Sentinel-3 imagery using Land Surface Temperature Radiometer (LSTR) near nadir scans and fire characterization (potential fire pixel classification) through middle infrared radiance calculation method. Cruz et al. [22] proposed a fire detection method according to color index. Their method was based on classification of vegetation to detect the smoke and fire flames. They claimed their method could be applied in real-time using unnamed aerial vehicle (UAV) dataset. Schroeder et al. [23] studied active fire detection by exploiting Visible Infrared Imaging Radiometer Suite (VIIRS) sensor data 375 (m). Their method deployed a contextual algorithm built on the heritage MODIS (MODerate Resolution Imaging Spectroradiometer) fire and thermal anomaly product. Jang et al. [24] designed forest fire detection algorithm based on Himawari-8 geostationary satellite data for detection of fire candidate pixels with thresholding based on multi-temporal analysis. Jiao et al. [25] proposed a deep learning based forest detection algorithm based on UAV dataset. They used YOLOV3 (You Only Look Once version 3), RGB (Red, Green, and Blue) imagery. They reported the potential of YOLOV3 in detection of location of active fires. Yuan et al. [26] designed an active fire detection framework based on UAV imagery for forest areas. Their method was deployed in three stages: (1) color detection for forest candidate pixels, (2) motion detection for reducing false alarm pixels, and (3) classification fires pixels based on extracted features (direction and magnitude). Schroeder et al. [21] detected the active fire by using Landsat-8 imagery for both daytime and nighttime fires. They applied thresholding short-wave infrared, optical and near infrared bands. Amraoui et al. [27] presented the active fire detection based on Meteosat-8/SEVIRI (Spinning Enhanced Visible and Infrared Imager) dataset. The fire detection in this framework as following: (1) mask non-target object (water, desert, urban), (2) identification high potential pixels based on thresholding brightness temperature and solar zenith angle, (3) removing contaminated pixels (cloud pixels, sun glint, highly reflective surfaces) by thresholding spectral and thermal bands, and (4) making decision on obtained potential fire pixels by obtained contextual information. Chen et al. [28] proposed a Convolutional Neural Network (CNN) based forest fire detection method using UAV dataset. In their framework after dataset capturing, some pre-processing such as histogram equalization, low-pass filtering was conducted and then, the CNN network with seven convolution layers and some hidden layers were utilized for binary classification. Gargiulo et al. [29] designed a fusion

framework for active fire detection using Sentinel-2 imagery and CNN to improve the spatial resolution Short Wave Infrared (SWIR) bands toward 10m resolution. They enhanced the spatial resolution of SWIR bands and improved the performance of active fire detection. Lin et al. [30] proposed an active fire detection framework using FengYun-2G dataset. The active fire detection procedure in this framework was based on comparing predicted value and observed value. That algorithm deployed image analysis for reducing false alarm pixels and temporal analysis for confirming fire pixels. Zhang et al. [31] investigated the active fire detection based on VIIRS dataset. This method was applied in 5 steps: (1) initial data screening by thresholding spectral and thermal bands, (2) data partitioning, (3) the detection of thermal anomaly pixels, (4) contextual analysis, (5) confirmed thermal anomaly pixels based on thresholding of the view zenith and solar zenith angles.

Similarly, there are many active fire detection frameworks exploiting RS datasets. In general, active fire detection methods based on traditional fire detection methods can be applied based three basic principles [32]: (1) detection of hot-temperature pixels using thresholding methods, (2) context-based methods where hot-temperature pixels are compared with the background, and (3) detection of fire pixels based on generated smoke and moving fire plumes. Generally, these active detection methods using RS imagery face their own respective challenges. Thresholding methods tend to fail due to tremendously varying environmental conditions and air temperature. Air temperature variations originating from various factors such as shadow, clouds, wind, illumination angle, seasonal variation, and climate change, can also be a problem for contextual methods. Then, small fires make smoke and non-fire objects detection problematic, especially when dealing with medium and low-resolution RS dataset (i.e. VIRIIS, and MODIS, Sentinel-3). It is also worth mentioning that most of the aforementioned methods rely on traditional machine learning classification, which requires feature engineering.

As one of the widely used RS data, Landsat-8 satellite data was selected for this research. The dataset has higher spatial resolution compared to other modalities such as MODIS, VIRIIS, and Sentinel-3. Landsat-8 also allows improved affordability in detecting small fires as the high-resolution imagery allows for a potentially more improved discrimination capabilities. To minimize the challenges mentioned above (pertaining to datasets), it is necessary to design an advance method for active fire detection. Therefore, this research presents a novel active fire detection method based on deep learning. This method combines the RGB and Thermal images from Landsat-8 satellite imagery. The proposed deep learning framework has two-stream channels and can detect deep features by exploiting the prowess of its convolutional neural network architecture. The key contributions of this research are presented as follows:

- (a) Presenting a framework for active fire detection based on deep learning called active-fire-net (Fire-Net).
- (b) High efficiency against detection of small fires using freely available data

- (c) Taking advantages of deep features that combined spatial and spectral features instead of single spectral features
- (d) Accurate and automatic detection of active fires with the potential of being applied as real time
- (e) Taking advantages of residual and depth-wise and separable convolution block
- (f) Introducing novel loss function for imbalancing problems
- (g) Testing the transferability of training datasets

## 2. Study area

Table 1 describes the five study areas selected for active fire detection. Generally, the areas cover North America, Australia, the Amazon rainforest, Central Africa and Chernobyl (Ukraine). Different areas were selected due to the varying climate conditions, temperature affecting the thermal bands and also forest density. This allows for a variety of data to be analyzed with the hope of producing a more generalized model. The Fire-Net model utilizes training data from the active fires in North America and Australia. Model testing is done on the Central Africa, Brazil, Chernobyl and also data from Australia (the parts were not involved in training). [33]. The North American's forest includes 4 regions (Figure 1(a)) where the active fires were reported in 2013-2014. The Australian forests, which had average temperature of 19°C and humidity of 62%, were obtained in June 2019 where the southern and eastern parts of Australia exhibited intense wildfire. The area includes 6 sub-regions with active fires in 2019-2020 (Figure 1(b)). The third study area is part of the Amazon rainforest, whose average humidity and temperature are 76% and 18.5°C, respectively. The fourth study area is that of north-central Africa wildfires (occurred in December 2018), which was caused by human activity. The average of humidity and temperature of this study area are 72% and 25°C, respectively. The fifth study area belongs to Chernobyl, Ukraine. The wildfires began in April 2020, which was spread quickly by wind. At the time of wildfire, the scene was mostly cloudy. Due to variations temperature and presence of cloud, this case study was chosen to evaluate the performance of proposed methodology against mentioned factors. The average of humidity and temperature are 46% and 9°C, respectively.

**2.1. Landsat-8 Dataset.** The Landsat-8 satellite sensor was designed by NASA (National Aeronautics and Space Administration) and was launched on into orbit in February 2013. This sensor is able to capture data in 11 spectral bands with spatial resolutions of 15 meters (panchromatic), 30 meters (visible, NIR, and SWIR), and 100 meters (thermal). Furthermore, this sensor collects dataset form Earth with a temporal resolution of 16-days. Since this study requires 4 spectral bands (R, G, B, and thermal), we chose the standard terrain corrected Level 1 T datasets.

**2.2. Inventory data.** The inventory (sample) data is meant as training images (maps and images) for the proposed supervised Fire-net network. The quality and quantity of sample data are the most important factors to obtain promising result. Therefore, we carefully identified the location of active fires from related resources such as [34, 35]. This was mainly done through visual inspection guided by expert knowledge to generate the reference data. The corresponding active fire locations were then extracted from Landsat-8 datasets for training (65% of the samples), validating (15% of the samples), and testing (20% of the samples). In this research 722 patches were generated with the size of  $256 \times 256$  pixels representing the training, validation, and testing datasets by 469, 109, and 144 patches, respectively.

## 3. Methodology

Out of five study areas, two regions were selected as the training and validation samples for the Fire-Net deep learning algorithm and multi-scale residual learning networks (MSR-U-Net). This two-streamed pixel classification deep learning-based (Fire-Net) method was proposed to detect active fires from Landsat-8 imagery. This network uses the encoder-decoder architecture for active fire detection. Due to the unique structure of active fires and spatial resolution of the Landsat-8 dataset, a two-stream deep feature extractor architecture is proposed. This means that the Fire-Net framework consists of two deep feature extractor channels. The first channel is meant to detect the active fires whereas the second channel for background and non-fire objects detection. The general overview of Fire-Net is presented in Figure 2.

For dataset preparation, the Landsat-8 images are pre-processed and converted into image patches. Image patches can suppress speckle noise and optimize segmentation. Basically, we divide each image into a grid of patches, specifically,  $256 \times 256$  in size. Since we are considering 4-bands, the total number of  $256 \times 256$  images are 4. As with any other machine learning algorithm, we divide the dataset into three parts: (1) training dataset, (2) validation dataset, and (3) testing dataset. The training and validation datasets (which form what is called the development set) were used to discover the optimal weights for the entire network. For this work, we defined the stopping condition as 250-epochs. The testing dataset was used to evaluate the trained-and-validated network where seven metrics were calculated. Finally, the trained network is deployed to detect the active fires through the second (Australian Wildfire, the parts were not involved in training), third (Amazon rainforest), forth (Central Africa), and fifth study areas (Chernobyl). The next subsection presents the details of Fire-Net deep learning architectures.

**3.1. Image Pre-processing.** For the landsat-8 L1-T product some pre-processing as radiometric correction and orthorectification were conducted. The atmospheric correction was also done by Fast Line-of-sight Atmospheric Analysis of Hypercubes (FLAASH) modules. Besides, the thermal bands need to convert into radiance and then to brightness

TABLE 1: The descriptions of datasets for five study areas.

Case study	Date	Description
North American	2013-08-31,2014-09-19	Training, and validation
Australian wildfire	2019-09-03,2019-10-19, 2019-10-21,2019-10-28, 2019-11-06, 2019-11-13,2019-12-08, 2019-12-15,2019-12-31,2020-02-01	Training, validation, and testing
Amazon rainforest	2019-08-25	Testing the transferability
Central Africa	2019-01-04,2018-12-19, and 2018-12-19 (different area)	Testing the transferability
Chernobyl	2020-04-10	Testing the transferability

temperature. The final step was splitting data to small patches with size of  $256 \times 256$  pixels to be fed into Fire-Net.

**3.2. Proposed Deep Learning Architecture (Fire-Net).** A two-stream feature deep learning method was proposed for forest fire detection. This architecture is based on multiscale-residual convolution layers where it takes the advantage of the point/depth-wise convolution, residual, and multiscale convolution blocks. The multiscale block increases the robustness of Fire-Net against size variations [36]. This allows Fire-Net to improve detection performance of small fires. The residual blocks also has been shown to prevent the vanishing gradient problem and also affords efficiency equal to that of a deeper network [37]. The depth/point-wise convolutions furthermore are cheaper operators that effectively reduce the number of model parameters and computational cost [38]. The Fire-Net architecture is presented by Figure 3 in two-streams for deep feature extraction. Firstly, the shallow features are extracted by the multiscale 2D convolutional layers. Next, the extracted deep features are fed to each deep feature extractor channels. Since small fires can cover small areas, we used up-sampling with a rate of two for the first channel before extracting the deep features. This stream combined residual block and multiscale residual block for extracting deep features. Simultaneously, the second channel was discovered by the deep features from the original resolution dataset by combing the residual block and multiscale residual block that are presented by Figure 4. Then, the extracted deep features from two layers were fused by the summation operator. Finally, the extracted features were fed to 2D-convolution layer as a single feature map to decide on the final class label (active fire or not). The details of Fire-Net architecture are explained in next subsections.

**3.2.1. Convolution Layers.** In CNN, the main task of the convolution layers is to extract high level deep features from the input dataset [39, 40]. For a convolutional layer in the  $l$ -th layer, the computation is expressed according to equation (1) [41].

$$y^l = g(w^l x^{l-1}) + b^l \quad (1)$$

where  $x$  is the input data from layer  $l-1$ ;  $g$  is the activation function;  $w$  is the weighted template; and  $b$  is the bias vector.

In 2D convolution layer, the output of the  $j^{\text{th}}$  feature map ( $f$ ) in  $i^{\text{th}}$  layer at the spatial location  $(x, y)$  can be com-

puted using equation (2) [41].

$$f_{i,j}^{xy} = g \left( b_{i,j} + \sum_m \sum_{r=0}^{R_i-1} \sum_{s=0}^{S_j-1} W_{i,j}^{r,s} v_{i-1,m}^{(x+r)(y+s)} \right) \quad (2)$$

where  $m$  is the feature cube connected to the current feature cube in the  $(i-1)^{\text{th}}$  layer;  $W$  is the  $(r, s)^{\text{th}}$  value of the kernel connected to the  $m^{\text{th}}$  feature cube in the preceding layer; and  $R$ , and  $S$  are the length and width of the convolution kernel size, respectively.

The Fire-Net architecture employs three strategies: (1) consistent with [36], we make use of multiscale kernel convolution (i.e. different kernel size convolutions) to ensure robustness against variations in scale [42], (2) we prevent the problem of vanishing or exploding gradient by utilizing residual blocks (or skip connection) layers, which allows the gradient to be directly back-propagated to earlier layers [43], and (3) Depth/Point-wise convolution block: this kind of convolution layer considers only a single filter for each input feature [44, 45]. Figure 5 represents the main differences of standard and depth/point-wise convolution layers.

The loss function used for measuring the training error is based on predicted value of true value [46]. This research is used a hybrid loss function (Equation (3)) is known weight-binary-cross-entropy-dice (WBCED) loss function that it is more efficient for small targets [47]. The WBCED loss function is combined dice loss (Equation (4)) and weighted cross entropy loss (Equation (5)) that can be defined between predicted value ( $p$ ) of true value ( $y$ ) as following:

$$Loss_{WBCED} = Loss_{weighted\ binary\ cross\ entropy} + Loss_{Dice} \quad (3)$$

$$Loss_{Dice} = 1 - \frac{2 \sum y \times p}{\sum y + \sum p} \quad (4)$$

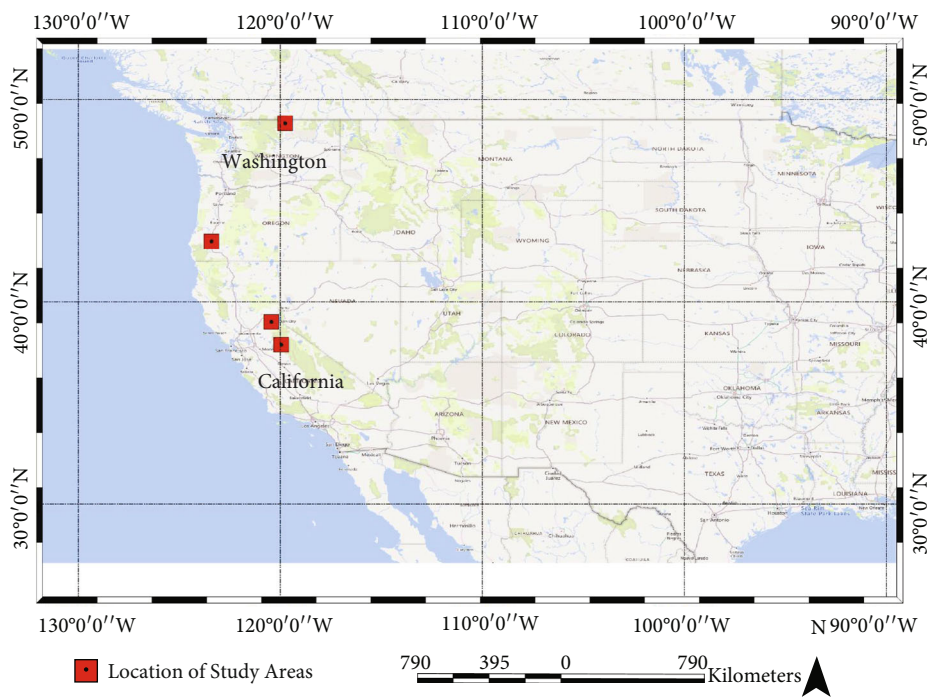
$$Loss_{weighted\ binary\ cross\ entropy} = -w(y \log(p) + (1-y) \log(1-p)) \quad (5)$$

$$Loss_{binary\ cross\ entropy} = -(y \log(p) + (1-y) \log(1-p)) \quad (6)$$

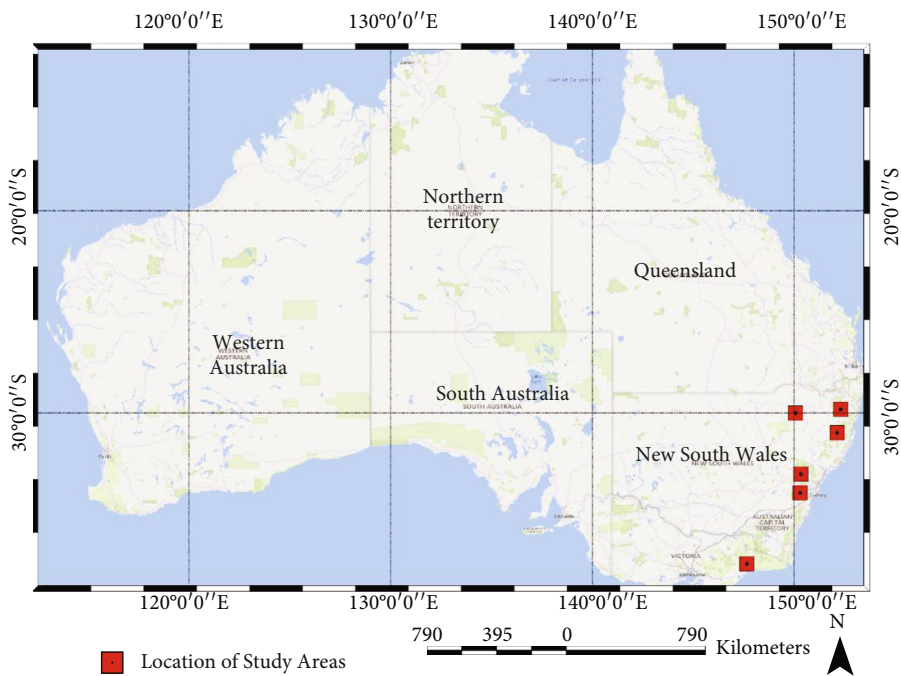
$$w = \frac{\sum_{i=1}^s \sum_{j=1}^t x_{i,j}}{e^{-5 \times |Mask-0.5|} / \sum e^{-5 \times |Mask-0.5|}} \quad (7)$$

where  $Mask$  is obtained by overage pooling of reference map furthermore,  $s$ ,  $t$  are width and length of  $Mask$ .

The Fire-Net architecture is trained by an Adaptive Moment Estimation (Adam) optimizer [48] through



(a)



(b)

FIGURE 1: Location of active fire in (a) the USA, (b) Australia.

backpropagation where weights were initialized using the Golorot initializer [49]. The hyperparameters for training Fire-Net is as follows:

- (i) Batch-size = 7-patches
- (ii) Learning rate =  $10^{-3}$
- (iii) Number of Epochs = 250

The shuffle technique was used during training process. Fire-Net was implemented on Tensorflow v2.4.1 and Keras v2.4.3.

*3.2.2. Evaluation Indices/methods or accuracy assessment.* We performed two types of evaluation for Fire-Net. Firstly, visual analysis was performed where the results were compared with reference data. Next, we calculated seven quality

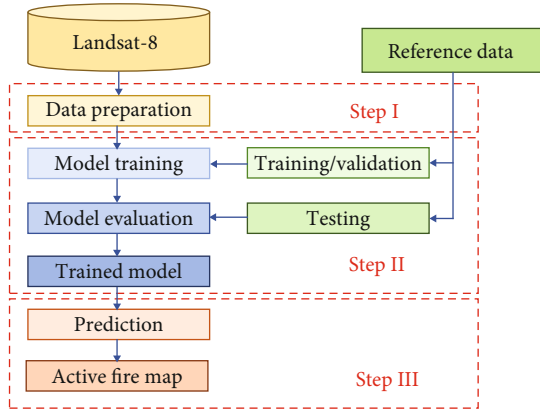


FIGURE 2: Overview of general framework of active fire detection.

indices namely overall accuracy (OA), recall, precision false positive rate (FPR), miss-detection (MD), F1-score, and kappa coefficient (KC). More details of these indices can be found in [41]. We also performed a comparison between Fire-Net with an established CNN, namely the MSR-U-Net. The main reason is due to MSR-U-Net's similarity to Fire-Net in combining multi-scale kernel convolution filters with residual blocks deep features extraction [50, 51]. MSR-U-Net also uses an encoder-decoder structure for exploring deep features. For a detailed evaluation of Fire-Net's efficiency, 5 machine learning methods (K-Nearest-Neighbor (KNN), Support Vector Machine (SVM), Multi-Layer Perceptron (MLP), Random Forest (RF), and Extreme Gradient Boosting (XGBoost)) were used for comparing fire detection results. Brief explanations of each algorithm are provided in the following:

- (1) KNN: This is a simple non-parametric classifier. Without any assumption about the dataset, KNN classifies the data based on each data point's neighbors. This research used the Euclidian metric and the numbers of neighbors were set to 4
- (2) SVM: The SVM is a supervised machine learning classifier that is widely used in RS. The main idea behind SVM is to find a hyperplane that best separates a dataset into two-classes. Although in its original form, the SVM is meant for binary classification, it can still be used for multi-class classification tasks. In general, a kernel function is used to generate a nonlinear decision boundary in the feature space. In this work, we empirically tuned two of the SVM parameters, which are the penalty coefficient and the (Radial Basis) kernel parameter. They were set to  $10^1$  and  $10^3$ , respectively
- (3) MLP: This classifier is a supplement of a feed forward neural network. The MLP has several hidden layers where each has several neurons. The neurons are trained using the back propagation learning algorithm. We constructed a two hidden-layer MLP with 40 and 30 neurons in the first and second layers, respectively

- (4) RF: RF is a supervised learning classifier consisting of an ensemble of decision trees where the final decision is obtained by majority voting. RF is trained by a bagging method where the gist of bagging is the combination of learning models that improves overall classification results. This algorithm has two main parameters i.e. number of trees and number of features to split. Each were set to 93 and 3, respectively
- (5) XGBoost: XGBoost is a decision-tree-based ensemble supervised learning method, based on the gradient boosting framework. Several parameters need to be tuned for this classifier, namely number of estimators (set to 105), max-depth (set to 4), eta (set to 0.03), min-child-weight (set to 1), subsample (set to 0.8) and colsample-bytree (set to 0.8).

## 4. Results

This section explains the experimental setup and results of the proposed active fire detection algorithm (Fire-Net). The dataset we used contains 22 tiles of Landsat-8 images covering the first and second study areas (i.e. North USA and Australia). From the 22 tiles, 14 tiles were used for training, 3 tiles for validation, and 5 tiles for testing. For the ease of processing, the 22 tiles were split into small patches in size of  $256 \times 256$ . At the end, to check the transferability of the Fire-Net method it was tested on other study areas (i.e. the Amazon rainforest, Central Africa and Chernobyl).

*4.1. Australian Forest.* The results of the Australian's forest fire detection, by methods, are presented by Figures 6(b) and 6(c). Visually, both deep learning methods managed to detect fire areas. However, misclassification occurred in the patch boundaries for MSR-U-Net (Figure 6(b)). Based on the evaluation metrics, the main difference between the two networks were in detection of active fires with low MD and FPR rates. Many false positive pixels were detected using MSR-U-Net, while Fire-Net had lower false positives.

The numerical results of active fire detection for the first test are presented in Table 2(a). Fire-Net outperformed MSR-U-Net with a higher overall accuracy of 99.95%, precision of 97.94%, F1-Score of 97.57%, and KC of 0.975 indices. MSR-U-Net exhibited a lower rate of MD (near 0%), while considerably showing a higher FPR compared to Fire-Net. There is however a trade-off between detecting fire pixels and non-fire pixels. The Fire-Net model has lower error rates for active fire detection whereas MSR-U-Net has lower MD rates but higher FPR rates. The ideal situation is when a method can effectively detect both fire and non-fire pixels with lowest error. The numerical results for active fire detection by the other machine learning algorithms are presented in Table 3(a). Although the SVM had the most accurate OA (99.03%), its performances against the other indices of Precision, Recall and F1-Score were low. The MD index (99.98%) for SVM revealed that it could not effectively detect active fires. RF and XGBOOST on the other hand showed good performance compared to the other algorithms. In all

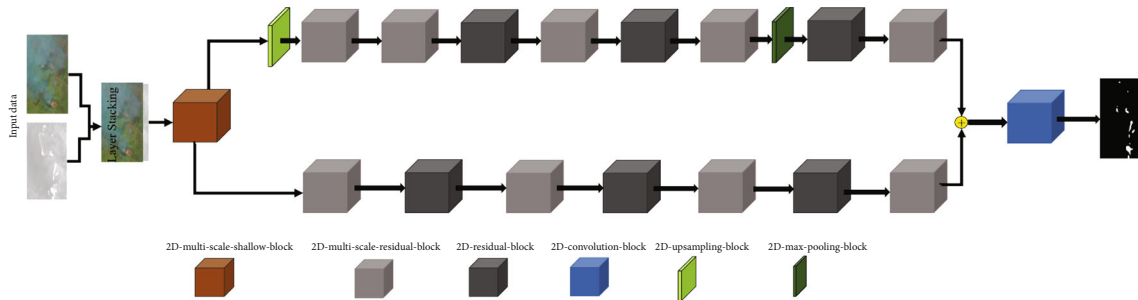


FIGURE 3: The training process for active fire detection.

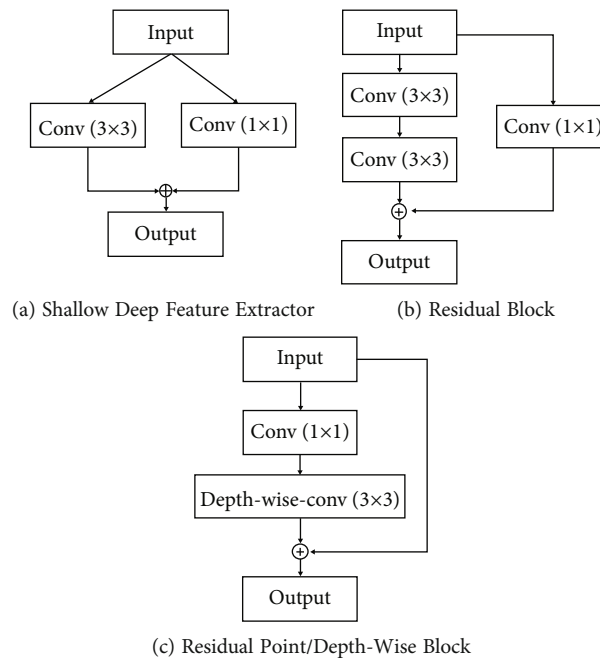


FIGURE 4: Three convolution blocks in the Fire-Net architecture.

however, Fire-Net outperformed all these algorithms where they lacked the robustness, correctness, and certainty against the 7 evaluation metrics.

**4.2. Central Africa Forest Fire.** The result of active fire detection for Central Africa is presented in Figures 6(f) and 6(g). It shows background from foreground segmentation for each scene. For this case study, the active fire areas were small compared to the north of USA and Australia. Both methods were able to detect active fires with cases of misclassifications.

Fire pixels can be seen when zooming into Figures 7(b) and 7(c). Compared to MSR-U-Net, Fire-Net provides more fitting segmentations, covering more relevant areas of fire areas. This indicates that Fire-Net detects almost all relevant fire pixels that were not detected by MSR-U-Net.

Table 2(b) shows the accuracy assessments for both networks. The results indicate that both methods performed well in detecting non-fire pixels, while their accuracies decreased when detecting fire pixels. For this dataset, the MD rate is high and both networks focused on non-fire pixels. The low values of KC indicate the decrease of perfor-

mance reliability of both networks. Table 3(b) shows the quantitative evaluations for 5 machine learning methods to detect active fires. Accordingly, most of them were successful in detection of non-active fires as indicated by FPR values lower than 1%. Moreover, the lower Precision and F1-Scores values show that consistency and balance among all 7 evaluation metrics were not seen amongst those 5 methods compared with Fire-Net.

**4.3. Brazilian's Forest Fire.** The active fire maps for Brazil's forest produced by the different methods are illustrated in Figures 6(j) and 6(k). The southern part of the region was mainly classified as having active fires. Seemingly, both methods generated active fires map with lowest error.

Figures 7(g) to 7(i) presents a closer look of the active fire areas. Figure 7(i) is the active fire map generated by Fire-Net. It is comparable and as complete as the one produced by MSR-U-NET. The Accuracy assessment for the generated fires maps are presented in Table 2(c). It can be seen that both methods successfully detected the fires, with Fire-Net outperforming MSR-U-Net. Fire-Net's precision is 95.98%, recall 98.04%, near zero-FPR, and an F1-Score of



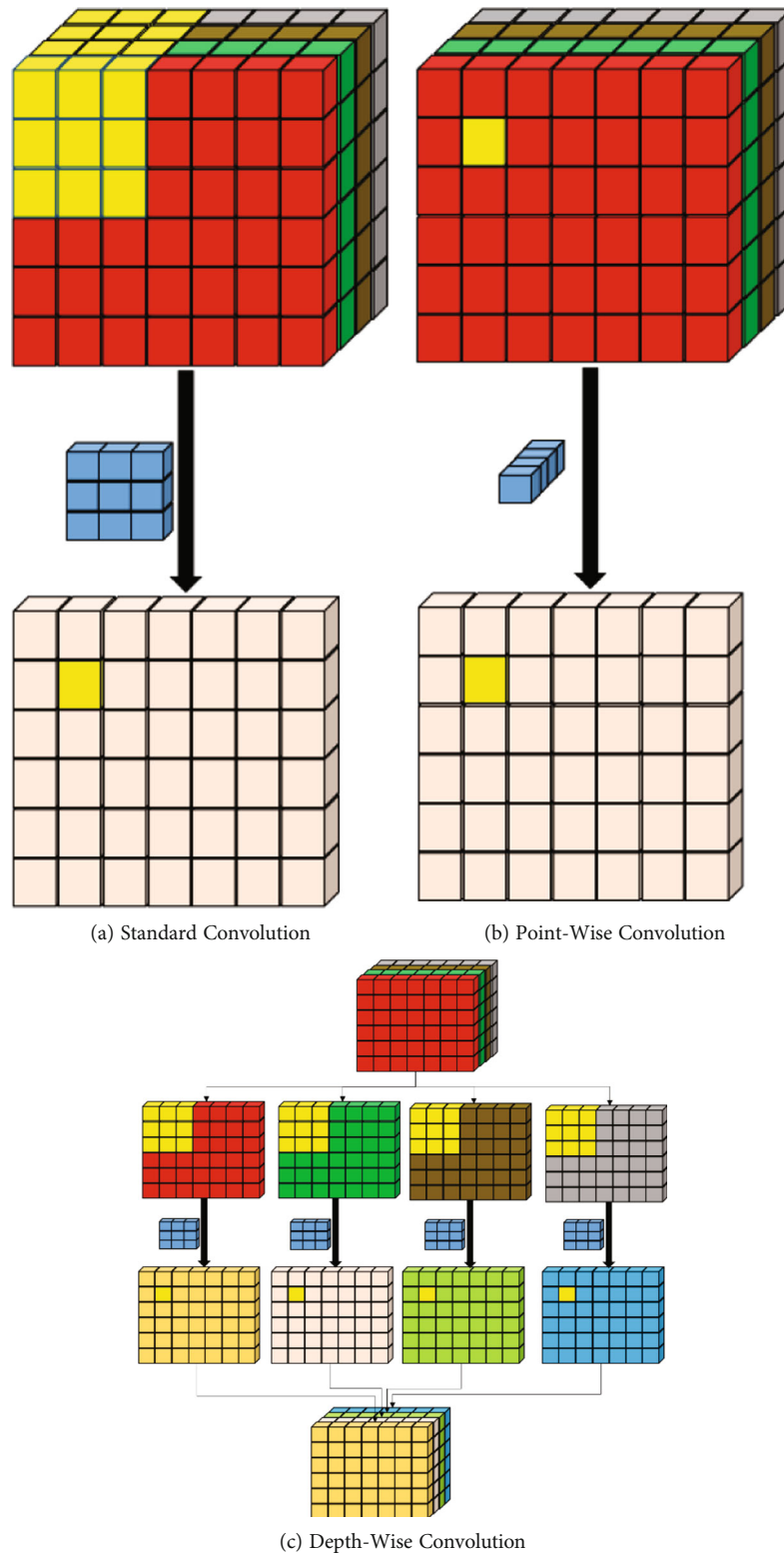


FIGURE 5: Comparison of three convolution layers in the Fire-Net architecture.

97.0%. The numerical assessments for the 5 machine learning algorithms are shown in Table 3(c). OA was mostly equal for all at approximately 99%. Precision on the other hand were lower than 60% with low FPR rates (below 1%) and higher MD rates. These indicate weak active fire detec-

tion. Therefore, the 5 machine learning methods were not comparable with Fire-Net in this region.

4.4. *Chernobyl's Forest Fire*. Figures 6(n) and 6(o) shows both network's fire detection performance in the Chernobyl

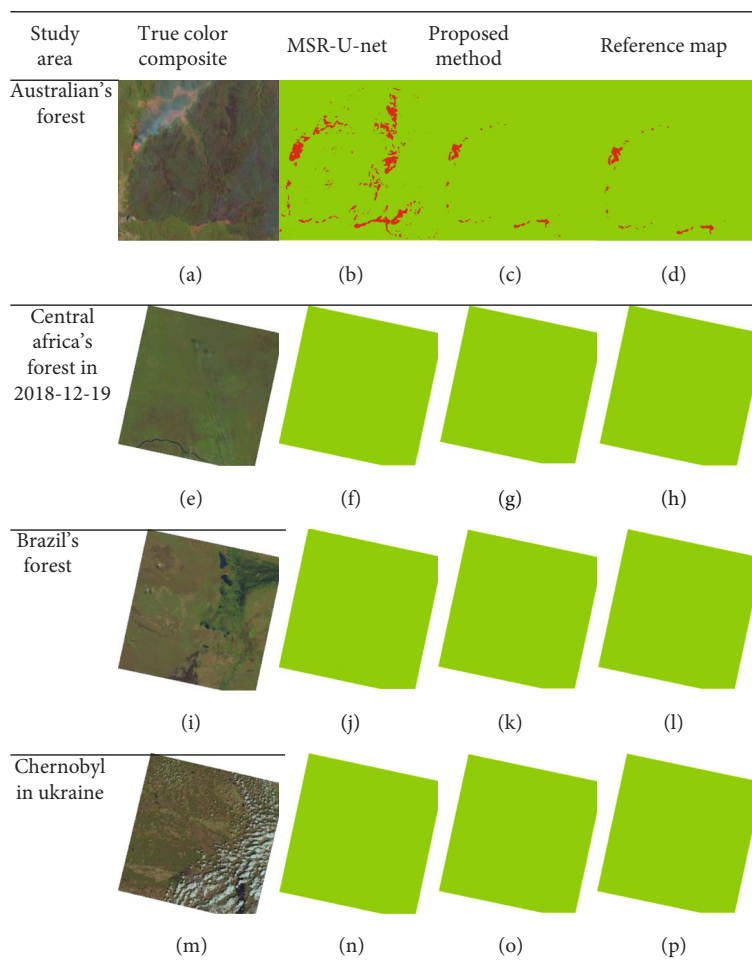


FIGURE 6: The result of active fire detection and red and green are fire and non-fire, respectively.

forest. Note that fire detection in this region is challenging due to the presence of high clouds and fires of small sizes. Nonetheless, both networks performed well with MSR-U-Net failing to detect a small number of active fires (Figures 7(j)–7(m)). As with the other regions, Fire-Net showed higher precision, recall, and f1-Score. However, we posit that the diversity of the terrain might be the cause for higher MD rates compared to FPR. The results of active fire detection using the 5 machine learning methods are presented in Table 3(d). OAs exceeding 99% for KNN, RF, and XGBOOST, with an added low FPR (below 1%) indicates accurate active fire detection. However, SVM and MLP were successful in the mapping of non-active fires. Again, based on the 7 evaluation metrics, the Fire-Net method showed its superiority.

## 5. Discussion

**5.1. Accuracy.** Timely detection of active fires is critical for disaster management. This research proposes a deep network called Fire-Net for active forest fire detection based on optical RGB and thermal dataset. The accuracy of the network was evaluated based on 4 different case study areas. Furthermore, Fire-Net's results were also compared against

the established MSR-U-Net deep neural network. The evaluation metrics and visual inspection of active fire detection results showed that the proposed method outperformed the MSR-U-Net and exhibited higher accuracy in detection of fire and non-fire pixels. For a more detailed analysis, Fire-Net was compared against 5 other popular machine learning algorithms. It was discovered that MLP, RF, SVM, KNN, and XGBOOST required a relatively small number of samples, with the exception that several parameters must be tuned for optimal classification. Despite good performance, all these methods require manual handcrafted features which is laborious and time-consuming.

As for the evaluation metrics, Recall is an evaluation metric that finds true positive (TP) pixels. The mean of recall of the Fire-Net algorithm was 92.64% while MSR-U-Net was 86.25%. This indicates Fire-Net's superiority in detecting more TP pixels. On the other hand, precision is a metric that describes a model's ability to identify positive pixels. In our study, Fire-Net had a precision of 93%, indicating high-confidence in detection of active fire pixels. MSR-U-Net on the other hand only had a precision of under 67%. Although Fire-Net clearly has higher precision and recall scores, the F1-Score is important to measure as well since it provides a harmonic mean of precision and recall. With regards to

TABLE 2: Accuracy assessment of active fire detection (Comparison of Fire-Net and MSR-U-Net).

Method	OA (%)	Precision (%)	Recall (%)	FPR (%)	MD (%)	F1-score (%)	KC
<i>(a) Australian's Forest</i>							
MSR-U-net	94.73	16.55	<b>100</b>	4.91	<b>0.00</b>	28.40	0.272
Fire-net	<b>99.95</b>	<b>97.94</b>	97.20	<b>0.02</b>	2.79	<b>97.57</b>	<b>0.975</b>
<i>(b) Central Africa's Forest in 2018-12-19</i>							
MSR-U-net	99.99	72.91	70.70	0.0001	29.29	71.79	0.429
Fire-net	<b>99.99</b>	<b>84.06</b>	<b>77.27</b>	<b>0.00007</b>	<b>22.72</b>	<b>80.52</b>	<b>0.429</b>
<i>(c) Brazil's forest</i>							
MSR-U-net	99.99	86.14	87.15	0.001	12.85	86.64	0.429
Fire-net	<b>99.99</b>	<b>95.98</b>	<b>98.04</b>	<b>0.0004</b>	<b>1.95</b>	<b>97.00</b>	0.429
<i>(d) Chernobyl</i>							
MSR-U-net	99.99	86.14	87.15	0.004	15.45	81.96	0.429
Fire-net	<b>99.99</b>	<b>95.98</b>	<b>98.04</b>	<b>0.0006</b>	<b>4.58</b>	<b>97.24</b>	0.429

TABLE 3: Accuracy assessment of active fire detection (Comparison of five common Classification methods).

Method	OA (%)	Precision (%)	Recall (%)	FPR (%)	MD (%)	F1-score (%)	KC
<i>(a) Australian's Forest</i>							
MLP	99.02	0.00	0.00	0.009	100	0.00	0.00
KNN	97.13	25.13	99.63	2.88	0.37	40.14	0.391
RF	96.29	20.66	100	3.73	0.00	34.24	0.331
SVM	99.03	14.28	0.01	0.001	99.98	0.03	0.03
XGBOOST	96.29	20.66	100	3.73	0	34.24	0.331
<i>(b) Central Africa's Forest in 2018-12-19</i>							
MLP	99.48	0.00	0.00	0.51	100	0.00	0.1964
KNN	99.99	79.95	70.20	0.01	29.79	72.96	0.4293
RF	99.99	57.47	75.75	0.02	24.24	65.35	0.4293
SVM	99.99	0	0	0	100	0	0.4293
XGBOOST	99.99	57.47	75.75	0.02	24.24	65.35	0.4293
<i>(c) Brazil's Forest</i>							
MLP	99.64	0.002	0.08	0.34	99.91	0.34	0.1426
KNN	99.99	60.16	91.77	0.006	8.22	0.006	0.4294
RF	99.98	49.93	98.19	0.011	1.80	66.20	0.4294
SVM	99.98	50.00	0.02	0.00	99.97	0.04	0.4292
XGBOOST	99.98	49.93	98.19	0.011	1.80	66.20	0.4294
<i>(d) Chernobyl</i>							
MLP	99.99	0	0	1.27	100	0	0.2705
KNN	99.99	83.84	75.60	0.00	24.39	79.51	0.4293
RF	99.99	70.35	91.17	0.00	8.83	79.42	0.4293
SVM	99.99	0	0	0	100	0	0.4293
MLP	99.99	70.35	91.17	0.00	8.83	79.42	0.4293

this metric, Fire-Net had a score of more than 93% compared to MSR-U-Net at 67%. The high rate of F1-Scores expresses the model has either the high believable and high ability in prediction of TP pixels. The OA index is one of the most common factors in quantity assessment. This index associates the relation among TN and TP pixels with all pixels. The OA proposed Fire-Net algorithm is more than 99% in all datasets. This subject shows the proposed method has high performance in prediction TP and true negative

(TN) pixels. The KC measures the reliability of model in classification that mainly, the proposed method was provided the moderated level.

MD and FPR are two metrics that should be low for effective active fire detection. This is especially true for MD because undetected fire pixels are more costly than labeling false detections. Our results show that Fire-Net's average MD is at 8% with an FPR of 0.0001%. MSR-U-Net on the other hand had an average of MD rate more than 14% with

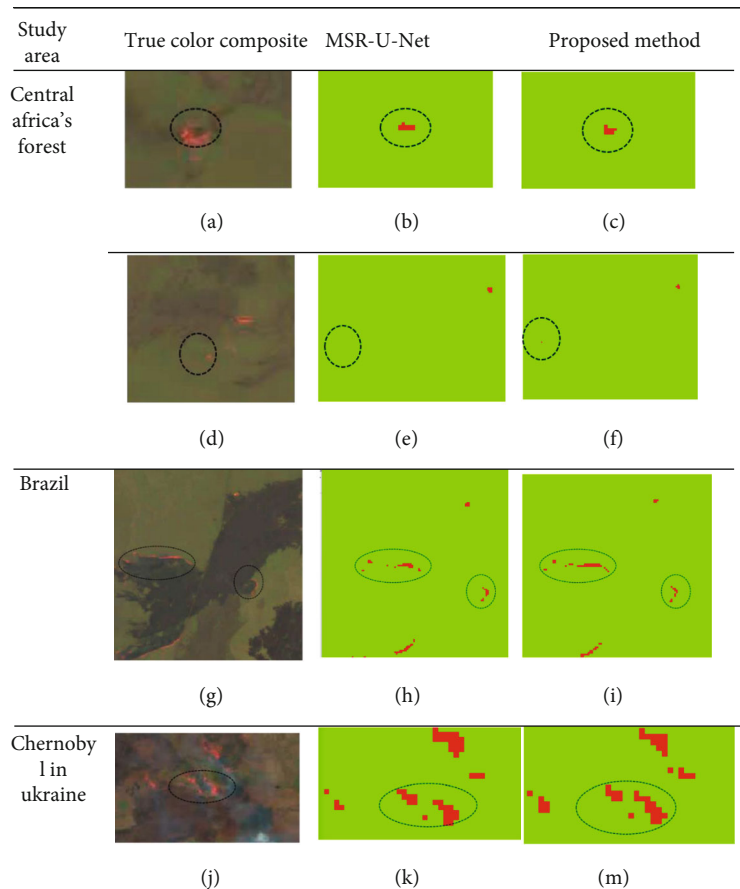


FIGURE 7: The zoom active fire area and red and green are fire and non-fire, respectively.

TABLE 4: Comparison of performance proposed Fire-Net algorithm with other fire detection methods.

	Index	Method	Dataset
Saeed, et al. [40]	OA: 99(%)	Deep learning based	Close rage dataset
Jang, Kang, Im, Lee, Yoon and Kim [17]	Precision: 93.08	RF and threshold based	Himawari-8 geostationary satellite data
Jiao, Zhang, Xin, Mu, Yi, Liu and Liu [18]	Precision: 83 FPR: 3.2	Deep learning (YOLOv3)	UAV dataset
Schroeder, Oliva, Giglio, Quayle, Lorenz and Morelli [14]	FPR: 0.2	Thresholding based	Landsat 8
Lin, Chen, Li, Yu, Jia, Zhang and Liang [23]	OA: 54 MD: 78	Contextual based	FengYun-2G S-VISSR data
Proposed fire-net	Precision: 93.49 FPR: 0.0001 OA: 99.98	Deep learning based	Landsat 8

a mean FPR of 1%. Essentially, precision, recall, and the F1-Scores significantly improved by the Fire-Net algorithm within all study areas. From the valuations, the 5 machine learning algorithms showed high performance, mainly in mapping non-fire areas. They however failed to map active fires. In comparison to the deep networks (especially to Fire-Net), all 5 machine learning methods had lower success rates. Fire-Net showed the highest precision for the active

fire detection task. Recently, more research has been done for active fire detection based on RS imagery. Table 4 presents the obtained results by other active fire detection methods.

There are some products for active fire detection as globally that they mainly are generated by MODIS, VIIRIS (Visible Infrared Imaging Radiometer Suite), and NOAA (National Oceanic and Atmospheric Administration)

sensors. Oliva and Schroeder [52] investigated the active fire product based on VIIRS dataset by comparing the Landsat-8 dataset. The result of mentioned study shows the accuracy of this product depend on size fires as the accuracy of product covers ranges 7% through 100%. Furthermore, Giglio et al. [53] had investigated the performance of collection six MODIS active fire products. The numerical results had shown the FPR rate of this product is nearby 2.4%.

One of most important issue of deep learning method is balancing dataset. The fire areas cover very small areas while the non-fire areas are dominant in the scene. Therefore, for solving this issue we introduced novel loss function. This loss function combines dice-loss and weighted-binary cross-entropy.

**5.2. Feature Extraction.** More active fire detection methods focus on spectral features and contextual information [30]. The ability of deep learning methods for feature extraction have been proven by many researches [12, 40, 42, 43, 54]. The deep learning methods are able to detect deep features containing various spectral/spatial features. The quality and quantity of active fire methods based on manual hand crafted features is the main challenge in traditional active fire detection methods. The deep learning methods can extract deep informative features in an automatic manner. It is worth noting that the proposed method used only four coarse bands (Red, Green, Blue, and thermal). These bands are the most common bands and widely available data in most RS satellite imagery. Therefore, this methodology can be deployed by other satellites with higher temporal resolution in active fire detection and forest management for real time and continuous fire monitoring.

**5.3. Transferability.** Most of the proposed active fire detection methods are based on thresholding [21, 24, 55]. Due to different environmental conditions and diversity in forest layouts, it is impractical to fix constant threshold values for decision making. From deep learning point of view, both the methods are based on deep learning, which does not require hardcoding threshold values. Instead, during the training step, each network discovers the best weights connecting each node through an optimization process. The transferability is clearly shown with high accuracy for all regions.

## 6. Conclusion

Early detection of active forest fires is critical to determine the starting point of the fire for effective emergency responses. In this study, active fire detection was performed on a medium spatial resolution dataset (Landsat-8 imagery) where the extent of active fires was very low. A deep CNN (Fire-Net) was proposed in this work to detect active forest fires in various regions. Specifically, the USA and Australia regions were used to train the network whereas testing was done for Africa, Brazil, Ukraine, Australia (the parts was not involved in training) regions. The results depicted a high transferability of the proposed method. Then, the Fire-Net was compared with another state-of-the-art deep network,

i.e., MSR-U-Net and other common machine learning algorithms. The results for active fire detection were qualitatively and quantitatively assessed. The performance evaluations showed there was a trade-off between active fire and non-active fires detection. Due to the extent of active fires in small areas, most of the machine learning algorithms could not detect active fires. The high accuracies measured by OA index for these algorithms, were mostly for non-fire zones. The other indices namely precision, KC, and F1-score for these models were low for the detection of active fires. In contrast, the proposed Fire-Net method showed high efficacy for both active and non-active fire detection. Here, small active fires were detected with high accuracy and low miss detection rates. The efficiency of Fire-Net originated in its architecture and convolution layers structure enabling high level and informative features extraction. Experimental results indicate that Fire-Net: (1) has higher accuracy, (2) obtains higher sensitivity to small active fires, (3) the proposed method can be applied as real time processing due to high transferability. Future work will be based on using geostationary satellite imagery for rapid monitoring of active fires to provides high temporal resolution for fast monitoring in a larger scale.

## Data Availability

The data used to support the findings of this study are available from the corresponding author upon request.

## Conflicts of Interest

The author(s) declare(s) that they have no conflicts of interest.

## References

- [1] D. Oom and J. M. C. Pereira, "Exploratory spatial data analysis of global MODIS active fire data," *International Journal of Applied Earth Observation and Geoinformation*, vol. 21, pp. 326–340, 2013.
- [2] K. Ahmadi, B. Kalantar, V. Saeidi, E. K. G. Harandi, S. Janizadeh, and N. Ueda, "Comparison of machine learning methods for mapping the stand characteristics of temperate forests using multi-spectral sentinel-2 data," *Remote Sensing*, vol. 12, no. 18, p. 3019, 2020.
- [3] B. Kalantar, N. Ueda, V. Saeidi et al., "Deep neural network utilizing remote sensing datasets for flood Hazard susceptibility mapping in Brisbane, Australia," *Remote Sensing*, vol. 13, no. 13, p. 2638, 2021.
- [4] M. J. Wooster, W. Xu, and T. Nightingale, "Sentinel-3 SLSTR active fire detection and FRP product: pre-launch algorithm development and performance evaluation using MODIS and ASTER datasets," *Remote Sensing of Environment*, vol. 120, pp. 236–254, 2012.
- [5] H. A. H. Al-Najjar and B. Pradhan, "Spatial landslide susceptibility assessment using machine learning techniques assisted by additional data created with generative adversarial networks," *Geoscience Frontiers*, vol. 12, no. 2, pp. 625–637, 2021.
- [6] B. Kalantar, N. Ueda, M. O. Idrees, S. Janizadeh, K. Ahmadi, and F. Shabani, "Forest fire susceptibility prediction based on

- machine learning models with resampling algorithms on remote sensing data,” *Remote Sensing*, vol. 12, no. 22, 2020.
- [7] S. T. Seydi, M. Akhoondzadeh, M. Amani, and S. Mahdavi, “Wildfire Damage Assessment over Australia Using Sentinel-2 Imagery and MODIS Land Cover Product within the Google Earth Engine Cloud Platform,” *Remote Sensing*, vol. 13, no. 2, p. 220, 2021.
- [8] M. S. Tehrani, H. Özener, B. Kalantar et al., “Application of an ensemble statistical approach in spatial predictions of bushfire probability and risk mapping,” *Journal of Sensors*, vol. 2021, Article ID 6638241, 31 pages, 2021.
- [9] C. Vancutsem, F. Achard, J. F. Pekel et al., “Long-term (1990–2019) monitoring of forest cover changes in the humid tropics,” *Science Advances*, vol. 7, no. 10, pp. 1–22, 2021.
- [10] I. G. Hendel and G. M. Ross, “Efficacy of remote sensing in early Forest fire detection: a thermal sensor comparison,” *Canadian Journal of Remote Sensing*, vol. 46, no. 4, pp. 414–428, 2020.
- [11] C. A. Varotsos, V. F. Krapivin, and F. A. Mkrtychyan, “A new passive microwave tool for operational forest fires detection: a case study of siberia in 2019,” *Remote Sensing*, vol. 12, no. 5, p. 835, 2020.
- [12] B. Pradhan, H. A. H. Al-Najjar, M. I. Sameen, I. Tsang, and A. M. Alamri, “Unseen land cover classification from High-Resolution orthophotos using integration of zero-shot learning and convolutional neural networks,” *Remote Sensing*, vol. 12, no. 10, 2020.
- [13] M. B. A. Gibril, B. Kalantar, R. Al-Ruzouq et al., “Mapping heterogeneous urban landscapes from the fusion of digital surface model and unmanned aerial vehicle-based images using adaptive multiscale image segmentation and classification,” *Remote Sensing*, vol. 12, no. 7, p. 1081, 2020.
- [14] M. Hasanlou, R. Shah-Hosseini, S. T. Seydi, S. Karimzadeh, and M. Matsuoka, “Earthquake damage region detection by multitemporal coherence map analysis of radar and multispectral imagery,” *Remote Sensing*, vol. 13, no. 6, p. 1195, 2021.
- [15] M. Hasanlou and S. T. Seydi, “use of multispectral and hyperspectral satellite imagery for monitoring Waterbodies and Wetlands,” *Southern Iraq’s Marshes*, vol. 36, pp. 155–181, 2021.
- [16] J. E. Pereira-Pires, V. Aubard, R. A. Ribeiro, J. M. Fonseca, J. M. N. Silva, and A. Mora, “Semi-automatic methodology for fire break maintenance operations detection with sentinel-2 imagery and artificial neural network,” *Remote Sensing*, vol. 12, no. 6, p. 909, 2020.
- [17] S. Mukai, I. Sano, and M. Nakata, “Improved algorithms for remote sensing-based aerosol retrieval during extreme biomass burning events,” *Atmosphere*, vol. 12, no. 3, p. 403, 2021.
- [18] A. A. Floutsi, H. Baars, M. Radenz et al., “Advection of biomass burning aerosols towards the southern hemispheric mid-latitude station of Punta Arenas as observed with multiwavelength polarization raman lidar,” *Remote Sensing*, vol. 13, no. 1, 2021.
- [19] S. Ye, J. Rogan, Z. Zhu, and J. R. Eastman, “A near-real-time approach for monitoring forest disturbance using Landsat time series: stochastic continuous change detection,” *Remote Sensing of Environment*, vol. 252, p. 112167, 2021.
- [20] J. Reiche, A. Mullissa, B. Slagter et al., “Forest disturbance alerts for the Congo Basin using Sentinel-1,” *Environmental Research Letters*, vol. 16, no. 2, p. doi:10.1088/1748-9326/abd0a8, 2021.
- [21] W. Schroeder, P. Oliva, L. Giglio, B. Quayle, E. Lorenz, and F. Morelli, “Active fire detection using Landsat-8/OLI data,” *Remote Sensing of Environment*, vol. 185, pp. 210–220, 2016.
- [22] H. Cruz, M. Eckert, J. Meneses, and J. F. Martínez, “Efficient forest fire detection index for application in unmanned aerial systems (UASs),” *Sensors*, vol. 16, no. 6, 2016.
- [23] W. Schroeder, P. Oliva, L. Giglio, and I. A. Csizsar, “The New VIIRS 375 m active fire detection data product: Algorithm description and initial assessment,” *Remote Sensing of Environment*, vol. 143, pp. 85–96, 2014.
- [24] E. Jang, Y. Kang, J. Im, D. W. Lee, J. Yoon, and S. K. Kim, “Detection and monitoring of forest fires using Himawari-8 geostationary satellite data in South Korea,” *Remote Sensing*, vol. 11, no. 3, p. 271, 2019.
- [25] Z. Jiao, Y. Zhang, J. Xin et al., “A deep learning based forest fire detection approach using uav and yolov3,” in *2019 1st International Conference on Industrial Artificial Intelligence (IAI)*, pp. 1–5, Shenyang, China, 2019.
- [26] C. Yuan, Z. Liu, and Y. Zhang, “Aerial images-based Forest fire detection for firefighting using optical remote sensing techniques and unmanned aerial vehicles,” *Journal of Intelligent & Robotic Systems*, vol. 88, no. 2-4, pp. 635–654, 2017.
- [27] M. Amraoui, C. C. DaCamara, and J. M. C. Pereira, “Detection and monitoring of African vegetation fires using MSG-SEVIRI imagery,” *Remote Sensing of Environment*, vol. 114, no. 5, pp. 1038–1052, 2010.
- [28] Y. Chen, Y. Zhang, J. Xin et al., “UAV image-based forest fire detection approach using convolutional neural network,” in *2019 14th IEEE Conference on Industrial Electronics and Applications (ICIEA)*, pp. 2118–2123, Xi’an, China, 2019.
- [29] M. Gargiulo, D. A. G. Dell’ Aglio, A. Iodice, D. Riccio, and G. Ruello, “A CNN-based super-resolution technique for active fire detection on Sentinel-2 data,” in *2019 Photonics & Electromagnetics Research Symposium - Spring (PIERS-Spring)*, pp. 418–426, Rome, Italy, 2019.
- [30] Z. Lin, F. Chen, B. Li et al., “A contextual and multitemporal active-fire detection algorithm based on FengYun-2G S-VISSR data,” *IEEE Transactions on Geoscience and Remote Sensing*, vol. 57, no. 11, pp. 8840–8852, 2019.
- [31] T. Zhang, M. J. Wooster, and W. Xu, “Approaches for synergistically exploiting VIIRS I- and M-band data in regional active fire detection and FRP assessment: a demonstration with respect to agricultural residue burning in eastern China,” *Remote Sensing of Environment*, vol. 198, pp. 407–424, 2017.
- [32] J. San-Miguel-Ayanz, N. Ravail, V. Kelha, and A. Ollero, “Active fire detection for fire emergency management: potential and limitations for the operational use of remote sensing,” *Natural Hazards*, vol. 35, no. 3, pp. 361–376, 2005.
- [33] H. A. Al-Najjar, B. Kalantar, B. Pradhan et al., “Land cover classification from fused DSM and UAV images using convolutional neural networks,” *Remote Sensing*, vol. 11, no. 12, p. 1461, 2019.
- [34] “National Aeronautics and Space Administration NASA Official: Brian Dunbar Available online,” September 2021, <https://www.nasa.gov/image-feature/goddard>.
- [35] “National Aeronautics and Space Administration NASA Official Available online,” September 2021, <https://www.nasa.gov/>.
- [36] F. H. Maskouni and S. T. Seydi, “Forest burned area mapping using bi-temporal Sentinel-2 imagery based on a convolutional neural Network: Case Study in Golestan Forest,” *Engineering Proceedings*, vol. 10, no. 1, pp. 6–11, 2021.

- [37] A. Veit, M. J. Wilber, and S. Belongie, "Residual networks behave like ensembles of relatively shallow networks," *Advances in Neural Information Processing Systems*, vol. 29, 2016.
- [38] F. Chollet, "Xception: Deep learning with depthwise separable convolutions," in *Proceedings of the IEEE Conference on Computer Vision and Pattern Recognition (CVPR)*, pp. 1251–1258, Honolulu, Hawaii, USA, 2017.
- [39] S. T. Seydi and M. Hasanlou, "Binary hyperspectral change detection based on 3D convolution deep learning," *International Archives of the Photogrammetry, Remote Sensing & Spatial Information Sciences*, vol. XLIII-B3-2020, pp. 1629–1633, 2020.
- [40] S. T. Seydi and H. Rastiveis, "A deep learning framework for roads network damage assessment using post-earthquake lidar data," *International Archives of the Photogrammetry, Remote Sensing & Spatial Information Sciences*, vol. XLII-4/W18, pp. 955–961, 2019.
- [41] S. T. Seydi, M. Hasanlou, and M. Amani, "A new end-to-end multi-dimensional CNN framework for land cover/land use change detection in multi-source remote sensing datasets," *Remote Sensing*, vol. 12, no. 12, p. 2010, 2020.
- [42] S. Nah, T. H. Kim, and K. M. Lee, "Deep multi-scale convolutional neural network for dynamic scene deblurring," in *Proceedings of the IEEE Conference on Computer Vision and Pattern Recognition (CVPR)*, pp. 257–265, Honolulu, Hawaii, USA, 2017.
- [43] K. He, X. Zhang, S. Ren, and J. Sun, "Deep residual learning for image recognition," in *Proceedings of the IEEE conference on computer vision and pattern recognition*, pp. 770–778, Las Vegas, NV, USA, 2016.
- [44] A. G. Howard, M. Zhu, B. Chen et al., "MobileNets: Efficient Convolutional Neural Networks for Mobile Vision Applications," <http://arxiv.org/abs/1704.04861>.
- [45] M. Sandler, A. Howard, M. Zhu, A. Zhmoginov, and L. C. Chen, "MobileNetV2: inverted residuals and linear bottlenecks," in *Proceedings IEEE Conference on Computer Vision and Pattern Recognition*, pp. 4510–4520, 2018.
- [46] J. Wang, S. Feng, Y. Cheng, and N. Al-Nabhan, "Survey on the loss function of deep learning in face recognition," *Journal of Information Hiding and Privacy Protection*, vol. 3, no. 1, pp. 29–45, 2021.
- [47] K. C. L. Wong, M. Moradi, H. Tang, and T. Syeda-Mahmood, "3D segmentation with exponential logarithmic loss for highly unbalanced object sizes," in *International Conference on Medical Image Computing and Computer-Assisted Intervention*, pp. 612–619, Springer, 2018.
- [48] D. P. Kingma and J. L. Ba, "Adam: A method for stochastic optimization," <http://arxiv.org/abs/1412.6980>.
- [49] Z. Liu, H. Wang, L. Weng, and Y. Yang, "Ship rotated bounding box space for ship extraction from high-resolution optical satellite images with complex backgrounds," *IEEE Geoscience and Remote Sensing Letters*, vol. 13, no. 8, pp. 1074–1078, 2016.
- [50] L. Bao, Z. Yang, S. Wang, D. Bai, and J. Lee, "Real image denoising based on multi-scale residual dense block and cascaded U-net with block-connection," in *Proceedings of the IEEE/CVF Conference on Computer Vision and Pattern Recognition (CVPR) Workshops*, pp. 1823–1831, 2020.
- [51] H. Nian, P. Cheng, and Z. Q. Zhu, "Independent operation of DFIG-based WECS using resonant feedback compensators under unbalanced grid voltage conditions," *IEEE Transactions on Power Electronics*, vol. 30, no. 7, pp. 3650–3661, 2015.
- [52] P. Oliva and W. Schroeder, "Assessment of VIIRS 375 m active fire detection product for direct burned area mapping," *Remote Sensing of Environment*, vol. 160, pp. 144–155, 2015.
- [53] L. Giglio, W. Schroeder, and C. O. Justice, "The collection 6 MODIS active fire detection algorithm and fire products," *Remote Sensing of Environment*, vol. 178, pp. 31–41, 2016.
- [54] B. Kalantar, N. Ueda, H. A. H. Al-Najjar, and A. A. Halin, "Assessment of convolutional neural network architectures for earthquake-induced building damage detection based on Pre- and post-event orthophoto images," *Remote Sensing*, vol. 12, no. 21, p. 3529, 2020.
- [55] A. A. A. Alkhatib, "A review on forest fire detection techniques," *International Journal of Distributed Sensor Networks*, vol. 10, no. 3, 2014.

## Research Article

# Evaluating the Street Greening with the Multiview Data Fusion

Lishuang Sun , Jianing Wang , Zhiwei Xie , Ruren Li , Xinyu Wu , and Yifan Wu 

*School of Transportation Engineering, Shenyang Jianzhu University, Shenyang 110168, China*

Correspondence should be addressed to Ruren Li; [renenli@163.com](mailto:renenli@163.com)

Received 24 May 2021; Revised 12 October 2021; Accepted 5 November 2021; Published 6 December 2021

Academic Editor: Bahareh Kalantar

Copyright © 2021 Lishuang Sun et al. This is an open access article distributed under the Creative Commons Attribution License, which permits unrestricted use, distribution, and reproduction in any medium, provided the original work is properly cited.

Street greening, an indispensable element of urban green spaces, has played an important role in beautifying the environment, alleviating the urban heat island effect, and improving residents' comfort. Vegetation coverage is a common index used for measuring street greening. However, there are some shortcomings in the traditional evaluation methods of vegetation coverage. Part of the vegetation coverage cannot be determined from a two-dimensional perspective, such as shrubs and green walls. In this paper, the Sentinel-2 image was used to extract the street fractional vegetation cover (SFVC) and the Baidu street view panoramas were used to extract the green view index (GVI). To overcome the lack of a single perspective from the street vegetation coverage evaluation, the above two indices were merged to construct a comprehensive street greening evaluation index (CSGEI). The research area is the Longhua District of Shenzhen city in Southern China. All three indices were divided into five classes using natural breakpoint methods based on previous research experience. The results showed that Baidu street view panoramas could effectively identify shrubs and green walls that were deficient in the Sentinel-2 image. The GVI is a supplement to the street vegetation coverage. The SFVC and GVI were divided into five classes, from L1 to L5 implying a gradual increase in the percentage of the vegetated area. The result has shown that the SFVC was in the L1, accounting for 53.68%. After index merging, the process of accounting for the L1 decreased to 31.29%. The multiperspective integrated CSGEI could comprehensively measure the distribution information of street greening and guide the planning and management of urban green landscapes.

## 1. Introduction

A forest is an ecosystem of trees and countless forms of biodiversity [1]; rapid urbanization and land-use changes near cities have led to changes in the forest structure and composition [2]. Therefore, the urban forest has an influence on the forest near cities. As an essential element of the urban forest, street greening has the functions of purifying the air, dividing traffic routes, preventing fire, and beautifying cities [3]. Street greening is very important to improve citizens' satisfaction with their living environment and promote sustainable urban development [4]. Urban street green spaces are divided into four functions—beautification function, ecological environment function, leisure activity function, and landscape culture function. With these functions, urban street green spaces directly or indirectly provide all city-related services [5]. Urban street green spaces have important relationships with mental health, air pollution, and travel behavior [6–8]. From multiple perspectives, therefore,

the qualitative and quantitative analyses of city street greening are of great significance.

With the development of high-resolution remote sensing technology, images, which contain rich information on ground objects and complex spatial relationships, are characterized by high dimensionality, high resolution, and large amounts of data. Thus, remote sensing technology has become a method for extracting urban street green spaces [9]. The vegetation index is calculated by the linear and non-linear combination of multispectral data obtained by remote sensors. Different vegetation indices, such as the ratio vegetation index (RVI), difference vegetation index (DVI), and normalized differential vegetation index (NDVI), are obtained by different combinations of measured values in different bands. The vegetation index is a simple and effective algorithm for quantitative and qualitative evaluations of vegetation cover, vitality, and growth dynamics, among other applications [10]. The vegetation index plays an important role in vegetation extraction and monitoring



[11]. Compared with traditional urban green space measurement methods such as field surveys, questionnaire surveys, and statistical analysis, the vegetation index has the characteristic of high efficiency. Additionally, the problem of the high cost of LIDAR data and 3D laser point cloud data [12, 13] will be avoided. The NDVI is a better index of vegetation growth status and vegetation coverage factors, but it is easily saturated and has low vegetation coverage area noise problems such as incompleteness. Fractional vegetation cover (FVC) is generally defined as the percentage of the vegetation vertical projection area to ground cover in the observation area. It is one of the essential indices describing the surface vegetation cover [14]. It is a quantitative description with the combination of the NDVI and pixel dichotomy model. FVC plays a vital role in vegetation monitoring and ecosystem change [15]. The high-resolution remote sensing images and other ground observation data have been applied to the extraction of large-scale urban green spaces, such as urban forests and green space parks. Although the resolution of the images is constantly improving, there is still a problem of low accuracy in the extraction of single-plant vegetation on both sides of the street. It is impossible to observe green walls, shrubs, and lawns under vegetation coverage.

The concept of the green view index (GVI) originated in Japan, and it is a physical quantity used to measure the level of urban greening. It became one of the conventional greening evaluation indices identified by the Japanese government in 2004 [16]. Unlike vegetation cover, GVI as a pedestrian perspective measure of greenery has been widely used in various fields, such as urban traffic, socioeconomics, and residents' health [17–20]. With the development of the Internet, street view images appear in public view. Street view images from Google, Baidu, and Tencent [21–26] have been used to study the spatial changes in urban streets. Street view images have the characteristics of wide coverage and directly reflect urban facade information. Thus, it is an important data source for extracting the GVI [27]. The efficiency and accuracy of GVI extracted from street view images in measuring street greenery has led more and more scholars to study GVI [28]. Traditional extraction of GVI has been divided into manual overlay, HSL color space, and interband calculations. Semantic segmentation refers to a process of assigning a semantic label (e.g., car and people) to each pixel of an image [29]. With semantic segmentation achieving good segmentation results in all fields, the extraction of the GVI has changed from traditional extraction [30, 31] to semantic segmentation [32]. Chen et al. [33] carried out research on the GVI and vegetation coverage extracted from remote sensing images, which realized the multidimensional observation of urban street greening; the NDVI, leaf area index (LAI), and GVI are used to evaluate street greening from districts and blocks. Kumakoshi et al. [34] put forward the standardization green view index (sGVI), combined with NDVI, which was used to analyze the greening distribution. Based on spatial domain interpolation, Cao et al. [35] combined street view images with aerial images to realize urban land use classification. Yu et al. [36] carried out a study on urban street greening; it had found that the correlation between the GVI and NDVI

was reduced with the increase in buffer radius. However, the method to measure greening from a vertical view, such as the vegetation index, could only describe the greening from one description. Using GVI to measure greening in a horizontal view, it is possible to describe the greening around the sample points. The LIDAR data and 3D laser point cloud data are more suitable to measure the three-dimensional greening; this is only used in a small study area because of the high cost. Nevertheless, previous studies have considered only the correlation between the GVI and other vegetation indices; it has shown that the correlation was decreased with the distance. But it has not yet built an urban street vegetation three-dimensional observation model to quantitatively describe the street greening from multiview.

Accordingly, street view image and remote sensing data complement and verify each other in the scope, scale, precision, and dimension of greening quantification. This research innovatively proposed a comprehensive street greening evaluation index (CSGEI) to measure street greening from a multiview. Therefore, the impact on forest management of the near city's urban street green space could be explored.

## 2. Study Area and Materials

*2.1. Study Area.* Shenzhen, as an important economic and political center in the Guangdong-Hong Kong-Macao Greater Bay Area, is one of the fastest-growing urbanized areas in South China. Figure 1 shows the location of the Shenzhen Longhua District. Shenzhen is located in a low-latitude area with a typical subtropical marine climate, abundant rainfall, mild climate, and long hours of sunshine, so the impact on the green vegetation with the change of seasons is less. It has an average altitude of 70 to 120 meters above sea level. The annual mean temperature is 22.3°C, the maximum temperature is 36.6°C, and the minimum temperature is 1.4°C. The rainy season is from May to September every year, and the average annual rainfall is 1,924.7 mm. Therefore, it is a suitable location to analyze urban street greening by using street view images. Longhua District is located in the geographical center of Shenzhen and is the central axis of Shenzhen's development. As a large industrial district, its total area is 175.6 km<sup>2</sup>. Moreover, it is located south of the Tropic of Cancer. In recent years, Longhua District, with the goal of "a modern, international and innovative new city with the central axis," has continued to improve the quality of its ecological environment and built the first "Talent Greenway" demonstration section in China. The Longhua District of Shenzhen city is typical of Chinese cities due to its high-density urban construction space and green space.

### 2.2. Materials

*2.2.1. Baidu Street View Panoramas.* As a kind of data storing spatial information, street view images emphasize human perception while expressing the local characteristics of the streetscape. In contrast to the top-down observation of remote sensing images, street view images quantitatively

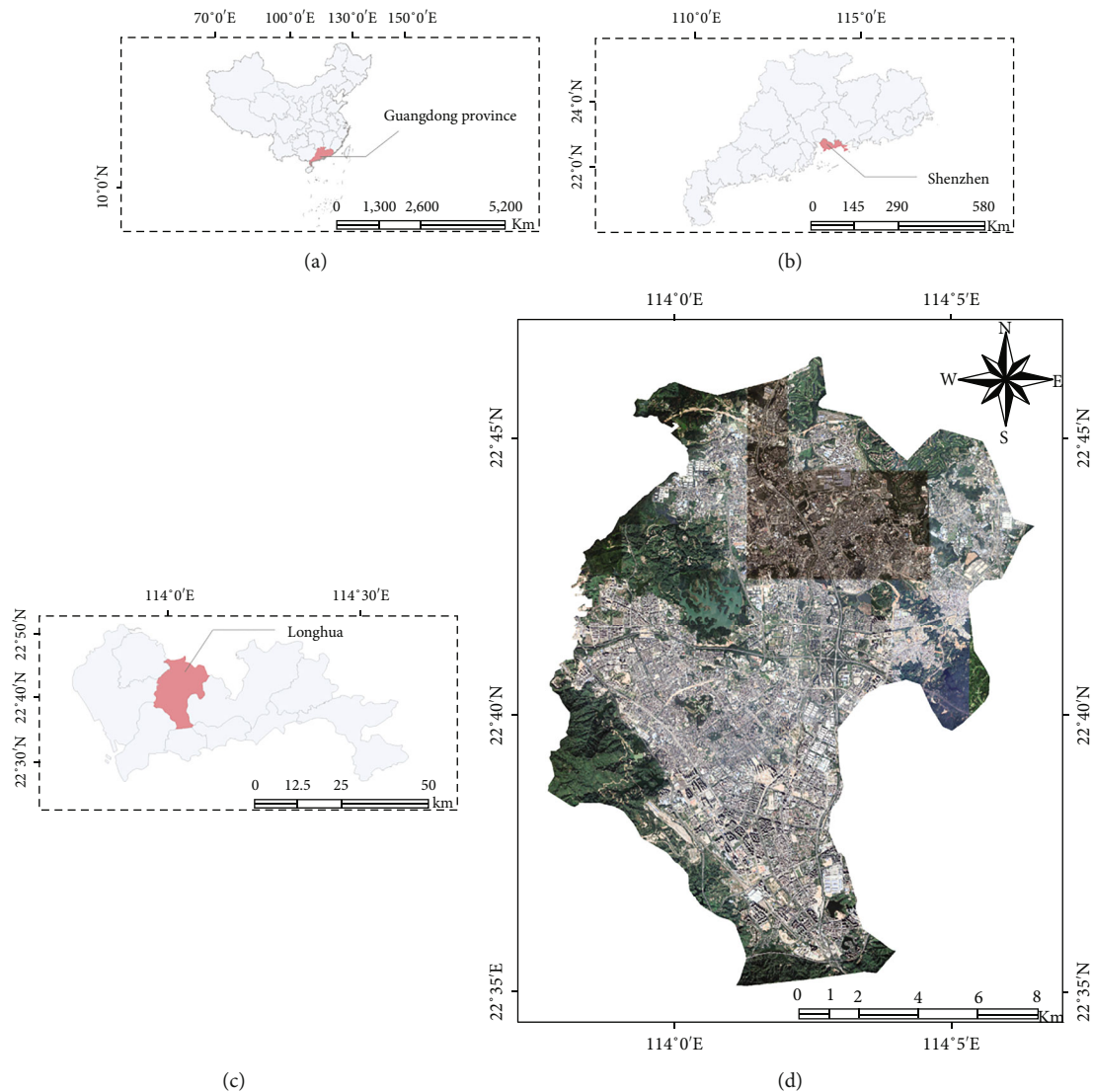


FIGURE 1: Location of the study area. (a–c) Is the geographical location of Guangdong, Shenzhen, and Longhua District of China. (d) Is an enlarged image of Longhua District.

measure the effect of street facades [37]. The street view images are electronic maps based on the actual landscape. These maps provide rich and extensive street view images containing a wealth of information about city streets. As a result, street view images have become important data for assessing the visual perception of city streets. In most cities in China, the streets have already been covered by the street view and the Baidu street view panoramas with high coverage were selected for the data in this study. The Baidu Map Street View metadata application programming interface (API) stores panoramic images covering street sites at 360° horizontally and 180° vertically, and it is freely accessible online to everyone. To depict the street greenery in the study area, the road network data of Longhua District were downloaded through OpenStreetMap (OSM) and the centerlines of the road network were extracted in ArcGIS. This study used the Baidu Map Street View API to download Baidu street view panoramas, and sampling was carried out with

an interval of 50 m in the centerlines of the road network. The Baidu street view panorama is a 360° surround image generated by stitching together. The pictures are taken by horizontal and vertical cameras, as shown in Figure 2. The direction indicated by the arrow is the forward direction, and the 360° surrounding image around the simulated person has been formed at the observation point. A total of 7,466 Baidu street view panoramas were downloaded in this study, and Figure 3 shows the distribution of sampling points of Baidu street view panoramas.

However, due to the distortion characteristics of the panoramic images, a python program has been used to extract the part of the panoramic images which is equivalent to the pedestrian's viewpoint with low distortion. By this method, the cropping of 7466 images was completed in just one day. The Baidu street view panoramas provide the longitude, latitude, and date of images. Because the image is updated every 2–3 years, the Baidu street view panoramas

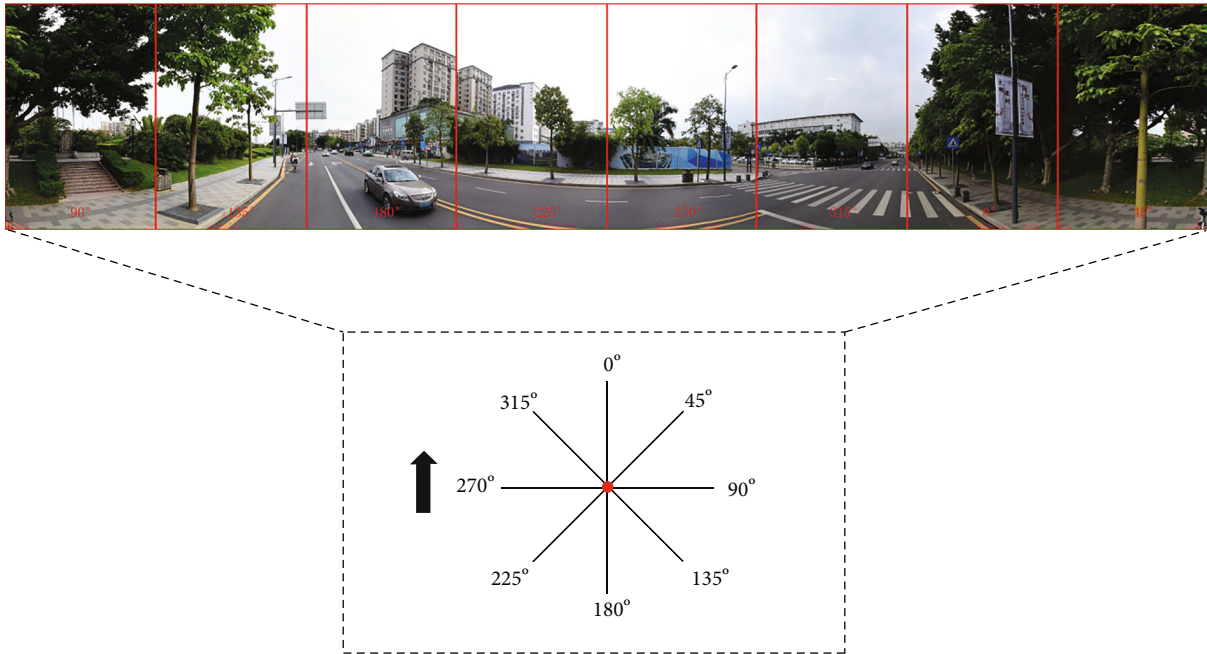


FIGURE 2: The Baidu street view panorama and its observation view, where the red point represents the observation point and the arrow represents the forward direction.

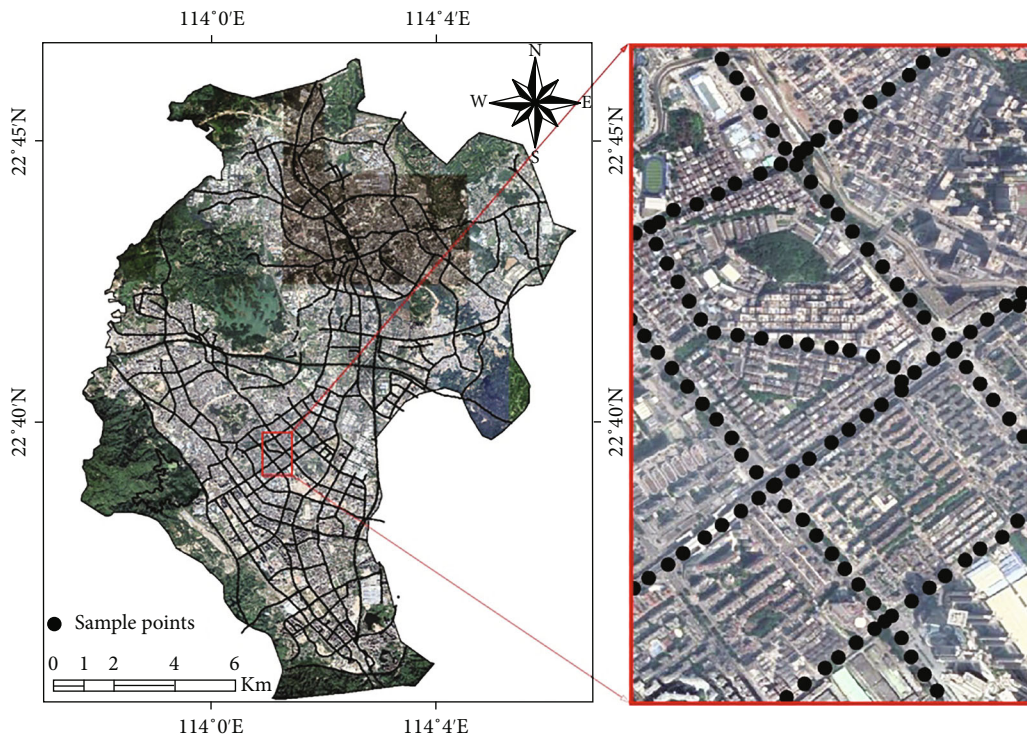


FIGURE 3: Distribution of sampling points in Longhua District, with 50 m intervals between adjacent points. (a) An enlarged view of the white boxed area on (b).

used in this study were taken from 2013 to 2019. The images collected in 2017–2019 were used as the primary data, and other years were used as supplementary data.

**2.2.2. Sentinel Data.** Sentinel-2 is the 2<sup>nd</sup> satellite launched in the Copernicus program, with high resolution, wide mowing width, and a short revisit period. It has a good advantage in

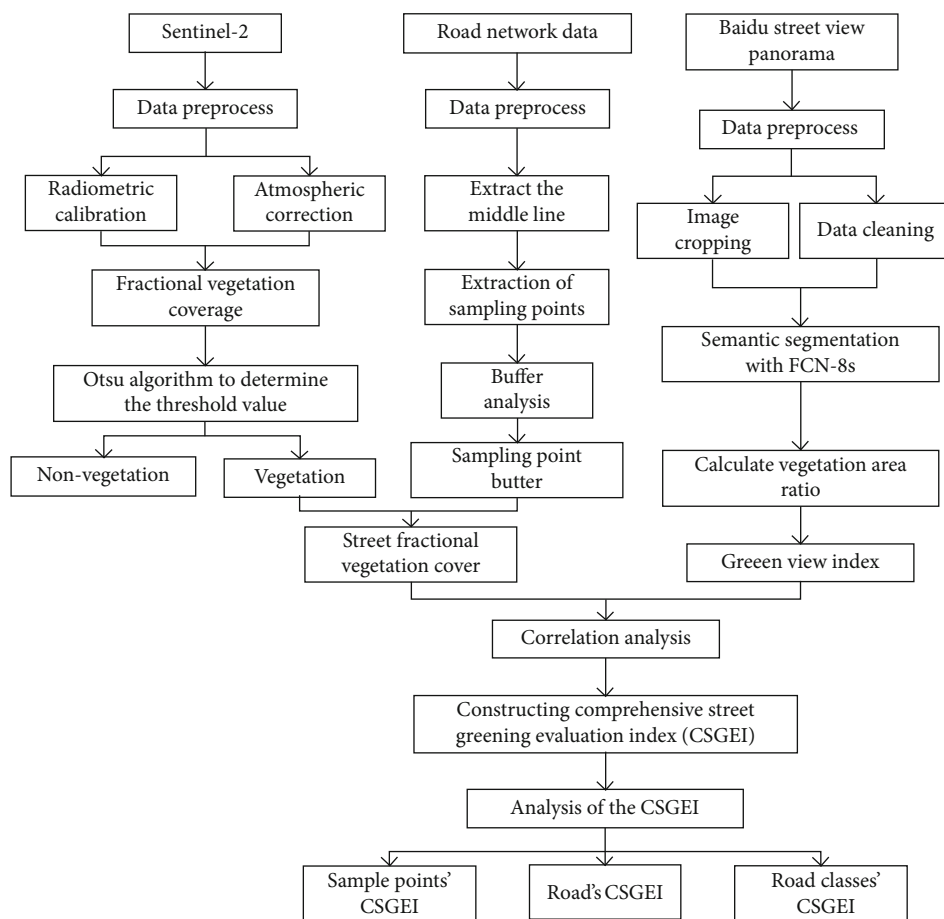


FIGURE 4: Study route.

global change monitoring and the analysis of emergent events [38]. Sentinel-2 carries a multispectral imager (MSI) covering 13 spectral bands with ground resolutions of 10 m, 20 m, and 60 m. The range is from visible to near infrared to shortwave infrared, with different spatial resolutions. Among the optical data, Sentinel-2 is the only satellite with three wavelengths in the red range for effective monitoring vegetation information. Level-2A data of Sentinel-2 were downloaded on the Google Earth Engine (GEE) platform. Statistically, the Baidu street view panoramas were from 2013–2019. To reduce the error when fusing the two types of data, the image was selected when it contained less than 5% clouds between 2013 and 2019. The data in October 2018 were used for measuring urban street greening from the vertical perspective.

### 3. Methodology

The image of Sentinel-2 was used as the horizontal data. The street fractional vegetation cover was extracted by the combination of the NDVI and image dichotomy. The threshold of vegetation and nonvegetation was automatically determined using the Otsu method. By this method, the oversaturation problem of the NDVI is eliminated. The proportion of vegetation pixels in the buffer was calculated. The width

of the buffer was determined by the road classes. The street fractional vegetation cover (SFVC) could be calculated. The Baidu street view panoramas were used as the vertical data. The semantic segmentation of the FCN-8s network was used to extract the GVI. The two indices were graded into five categories. The comprehensive street greening evaluation index (CSGEI) was constructed by fusing the indices. The research route of this paper is shown in Figure 4.

*3.1. Extraction of Fractional Vegetation Coverage Based on the Otsu Method.* The near-infrared wavelengths contained in the remote sensing images have higher reflectivity and absorptivity to vegetation. NDVI was calculated from the NIR band and the R band of the Sentinel-2 to quantify the urban green space in this research. Before NDVI calculation, the Sentinel-2 should be preprocessed such as atmospheric correction and radiometric calibration. The NDVI is the spectral information of ground objects received by remote sensing sensors to reflect the condition of surface vegetation. In this paper, the FVC was estimated quantitatively based on the NDVI. The NDVI value of a pixel is expressed as the information contributed by the green vegetation part and the uncovered (bare soil) part. Therefore, the formula for calculating the FVC using NDVI is shown in equation (1) as follows:

TABLE 1: Shenzhen road class table and sampling point buffer radius.

OSM	Road classes	Number of motor vehicles	Lane width (max. width)	Buffer radius (m)
Motorway	Elevated and expressway	4 bars–8 bars	3.5 (3.75)	60
Secondary	Urban main roads	6 bars	3.25 (3.5)	42
Primary				
Tertiary	Urban secondary roads	4 bars	3.25	26
Residential	Urban feeder roads	2 bars	3.25	25
Unclassified				
Cycleway	Cycle path			25

$$\begin{aligned} \text{NDVI} &= \frac{\text{NIR} - R}{\text{NIR} + R}, \\ \text{FVC} &= \frac{\text{NDVI} - \text{NDVI}_{\text{soil}}}{\text{NDVI}_{\text{veg}} - \text{NDVI}_{\text{soil}}}, \end{aligned} \quad (1)$$

where NIR is the near-infrared band and  $R$  is the red band, NDVI is the normalized differential vegetation index, with a value between  $-1$  and  $1$ ,  $\text{NDVI}_{\text{soil}}$  is the NDVI value of the area completely covered by bare soil or no vegetation,  $\text{NDVI}_{\text{veg}}$  is the NDVI value of the area completely covered by vegetation, and FVC is the fractional vegetation cover.

For most types of land,  $\text{NDVI}_{\text{soil}}$  represents the theoretical value of the bare soil surface and  $\text{NDVI}_{\text{veg}}$  is the maximum value of the entire vegetation image. However, the value of  $\text{NDVI}_{\text{veg}}$  changes with time and space, so  $\text{NDVI}_{\text{veg}}$  and  $\text{NDVI}_{\text{soil}}$  cannot be chosen as fixed values.  $\text{NDVI}_{\text{veg}}$  and  $\text{NDVI}_{\text{soil}}$  are determined by the maximum and minimum values of a given confidence interval. By analyzing the Sentinel-NDVI data and considering the actual condition of vegetation cover in the study area, the NDVI value corresponding to a frequency of 5% was taken as  $\text{NDVI}_{\text{soil}}$ ; it is in the annual maximum synthetic NDVI frequency accumulation table, and the NDVI value with a cumulative frequency of 95% was taken as  $\text{NDVI}_{\text{veg}}$ .

The Otsu algorithm [39] is an adaptive threshold segmentation algorithm based on the principles of probabilistic statistics and was proposed by the Japanese scholar Zhenyuki Otsu in 1979. The basic idea is to divide the image gray value into two parts: background and target. The gray value that maximizes the variance between classes is selected as the optimal threshold. If the variance between classes is more significant, the probability of misclassification of the two classes is more negligible. Due to the excellent segmentation effect, it is widely used in image thresholding. The optimal FVC threshold was selected based on the Otsu algorithm to achieve street vegetation information extraction in the Longhua District.

In this paper, the sampling points were taken as the center of the circle to create the buffer zones and it was affected by the road width of different road classes. The maximum width of a single lane and the number of two-way vehicle lanes were taken as the reference to establish a buffer zone of sampling points. The maximum width of the vehicle lanes and the radius of the buffer area are shown in Table 1. Since

TABLE 2: SFVC evaluation level classification.

SFVC	Grade of SFVC
[0, 9.02]	L1
(9.02, 25.79]	L2
(25.79, 46.33]	L3
(46.33, 75.97]	L4
(75.97, 100]	L5

the buffers were created according to the width of the vehicle lanes, for lanes less than 25 m wide, 25 m was used as the minimum buffer radius. (Because there is partial scenery overlap between two adjacent Baidu street view panoramas, 1/2 of the sampling interval was selected as the minimum buffer radius. The reason is to ensure that the vertical vegetation between the two adjacent sampling points in the Sentinel-2 image was the same as that in the Baidu street view panoramas.) Based on the percentage of vegetation in the buffer area, the street fractional vegetation coverage (SFVC) was constructed. The SFVC calculation formula is shown in equation (2).

$$\text{SFVC} = \frac{\text{area}_{b-g}}{\text{area}_b} \times 100\%, \quad (2)$$

where SFVC is the street fractional vegetation coverage at the sampling points.  $\text{Area}_{b-g}$  is the number of green vegetation image pixels in the buffer zone.  $\text{Area}_b$  is the total number of image pixels in the buffer.

The SFVC was classified into five levels according to the natural breakpoint grading method, from L1 to L5 which means that the area of vegetation in the buffer zone is gradually increasing. The classification criteria are shown in Table 2.

*3.2. Extraction of the GVI Based on FCN-8s.* A good GVI attracts pedestrians, and the primary factors affecting urban street greening are the canopy size, the type of trees, the arrangement of street trees, and the arrangement of plants in the pedestrian path. This research used the Baidu street view panoramas to extract vegetation for GVI calculation. Because the street view images only have three bands: red, yellow, and blue, it is impossible to accurately separate vegetation from artificial green. It is still difficult to extract green vegetation from street view images quickly and accurately.

Semantic segmentation is an advanced image pixel classification method that divided the image into several parts (e.g., buildings, sky, and greenery) by pixels and needs. It extracts numerous elements from the Baidu street view panoramas. The combination of the Baidu street view panoramas and semantic segmentation has also been described as the street green landscapes from a pedestrian perspective. A fully convolutional network (FCN) is based on a convolutional neural network (CNN) that removes the fully connected layer and adds the deconvolution layer while proposing the idea of a jump structure to solve the image semantic segmentation problem. The FCN-8s was used for semantic segmentation of the Baidu street view panoramas. It is more efficient and avoids the problem of double calculation and wasted space caused by using the neighborhood. Previous studies have shown that FCN performs well in street view image segmentation [40, 41]. FCN-8s has 5 convolutional layers. Unlike traditional convolutional layers that use only large convolutional kernels for one convolution, each convolutional layer of FCN-8s uses  $3 \times 3$  small convolutional kernels for multiple convolutions. The FCN-8s network used in this paper was trained on the ADE\_20K dataset, which performed well in the Pascal visual object class. The setting of FCN-8s is shown in Table 3 [42]. In combination with the Baidu street view panoramas, it could predict the semantic properties of each pixel in the image.

The Japanese scholar Yoji Aoki proposed that when the GVI is higher than 25%, pedestrians have a good feeling about the greenery of the street. When the GVI is higher than 50%, pedestrians have the psychology of very splendid greenery. Thus, Natsuhi Origahara divided the GVI evaluation into five classes, as shown in Table 4 [43]. From L1 to L5 means that the green vegetation is becoming more and more intense for pedestrians. In recent years, the GVI has been widely used in various aspects of street greening calculation and evaluation. Due to the limitation of the sampling angle and sampling amount, the Baidu street view panoramas were used directly to extract and measure the GVI. Therefore, the calculation of the GVI was slightly different. The calculation of the GVI in this paper is shown in equation (3) as follows:

$$\text{GVI} = \frac{\text{area}_g}{\text{area}_t} \times 100\%, \quad (3)$$

where GVI is the green view index of the sampling points,  $\text{area}_g$  is the total number of green vegetation pixels in Baidu street view panoramas, and  $\text{area}_t$  is the total number of image pixels in the Baidu street view panoramas.

**3.3. Constructing the Comprehensive Street Greening Evaluation Index.** This paper obtains the distribution map of street vegetation coverage in the buffer zone based on Sentinel-2 data. However, the green vegetation on the walls and the lawn under the tree canopy cannot be reflected by remote sensing images. Using the Baidu street view panoramas as the data extracts the GVI, the vegetation distribution of the sampling points could be described from the pedestrian's perspective. The combination of the vegetation

TABLE 3: The setting of FCN-8s.

Name	Parameter
Scanning window	500 × 500
Learning rate	0.1
The early stopping minimum learning rate	0.001
Batch size	32

TABLE 4: GVI evaluation level classification.

GVI	Grade of GVI
[0, 5]	L1
(5, 15]	L2
(15, 25]	L3
(25, 35]	L4
(35, 100]	L5

coverage extracted from the Sentinel-2 data essentially compensates for the disadvantage of the lack of vegetation from a single viewpoint. The SFVC at the Baidu street view panorama sampling points was analyzed with the GVI by Pearson's correlation coefficient; the calculation formula of the Pearson's correlation is shown in equation (4) as follows:

$$\rho_{XY} = \frac{\sum_{i=1}^n (X_i - E(X))(Y_i - E(Y))}{\sqrt{\sum_{i=1}^n (X_i - E(X))^2} \sqrt{\sum_{i=1}^n (Y_i - E(Y))^2}}, \quad (4)$$

where  $n$  is the number of sampling points (7466),  $X_i$  is the GVI value at the  $i^{\text{th}}$  sampling point,  $Y_i$  is the SFVC value at the  $i^{\text{th}}$  sampling point,  $X$  and  $Y$  are the values of two variables (GVI and SFVC), and  $\rho_{XY}$  is Pearson's correlation coefficient between the GVI and the SFVC.

When  $\rho_{XY} > 0$ , the two indices are positively correlated. In contrast, the two indices are negatively correlated and the larger the absolute value of  $\rho_{XY}$  is, the stronger the correlation between the two indices is. The correlation was calculated to be 0.52, which indicates a weak correlation. Based on the above knowledge, the GVI was fused with the SFVC for rank classification and the original data were converted to between [0,1] based on the maximum-minimum normalization formula to construct the CSGEI. The expressions are shown in equation (5) as follows:

$$\begin{aligned} \text{CSGEI} &= \text{GVI}_{\text{level}} + \text{SFVC}_{\text{level}}, \\ \text{CSGEI} &= \frac{\text{CSGEI} - \text{CSGEI}_{\text{min}}}{\text{CSGEI}_{\text{max}} - \text{CSGEI}_{\text{min}}}, \end{aligned} \quad (5)$$

where  $\text{GVI}_{\text{level}}$  is the level of GVI at the sampling points,  $\text{SFVC}_{\text{level}}$  is the level of SFVC at the sampling point, and CSGEI is the comprehensive street greening evaluation index.

Therefore, the SFVC and GVI were divided into five levels, from L1 to L5, and the value of the level was an integer ranging from 1 to 5. The higher the level is, the better the

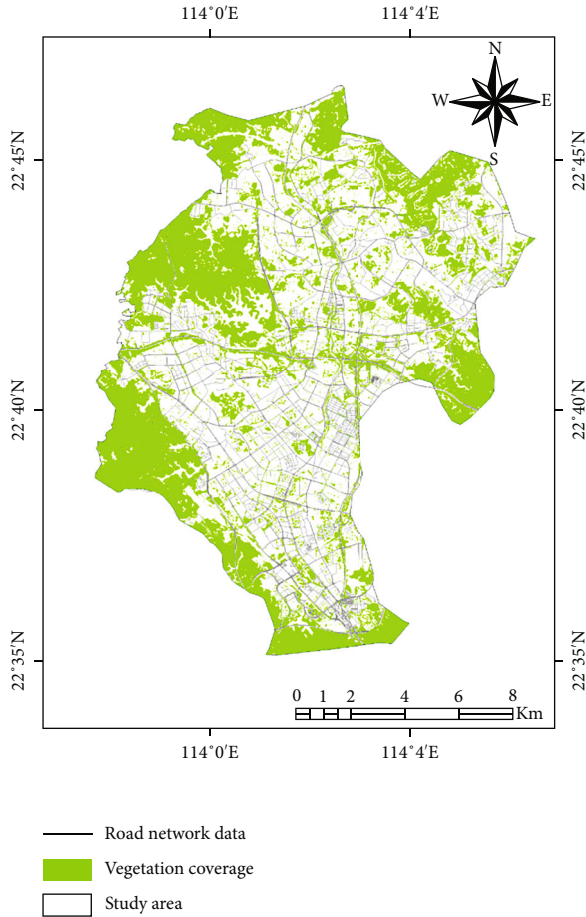


FIGURE 5: Distribution of FVC in Longhua District.

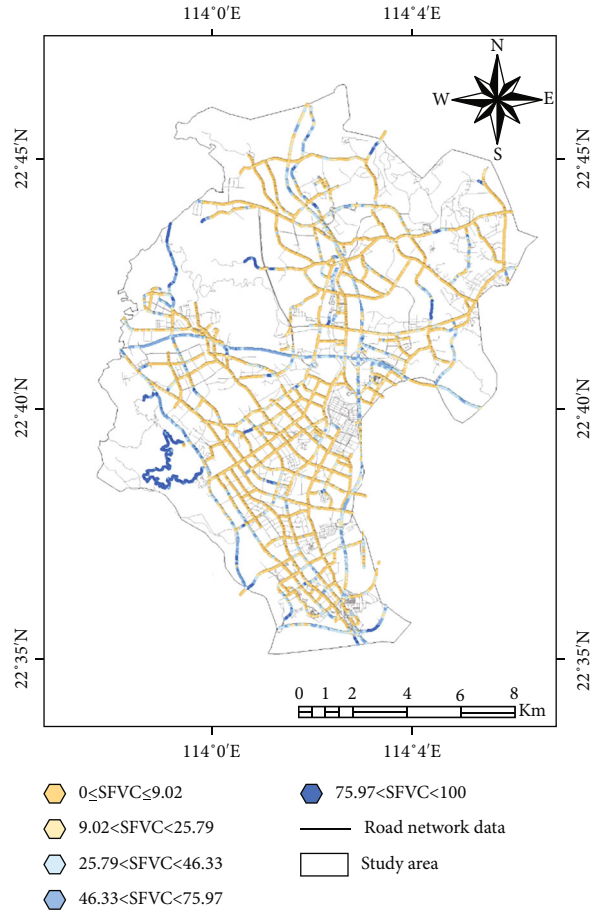


FIGURE 6: Distribution of the GVI, from yellow to blue is the SFVC grade from low to high change

vegetation greening effect is. The final CSGEI value ranges were from 0 to 100.

## 4. Results

**4.1. Analysis of the Distribution and Characteristics of SFVC.** The combination of the NDVI and pixel dichotomy was used to extract the fractional vegetation coverage of the Longhua District. The threshold value of FVC was determined by the Otsu method as 0.48. The result of the fractional vegetation coverage of the Longhua District is shown in Figure 5. Constructing the buffer range of sampling points of different road levels, the SFVC of sampling points was obtained. The result of the SFVC index was spatialized and displayed in Figure 6. The street fractional vegetation coverage in Longhua District was inadequate, and the SFVC index in L1 accounts for 53.68%. The lowest street SFVC index was found for Tao Yuan road, whose average SFVC was 0%, but the GVI for Tao Yuan Road was 10.91%. Huan Guan Nan road, with the lowest street SFVC, had a mean SFVC of 4.40%, and the SFVC index was as high as 93.24% for Yang Tai Shan Greenway with a high street GVI. Thus, the SFVC of this vertical angle is not able to identify the features under the large vegetation cover, such as roads and houses.

TABLE 5: Semantic segmentation evaluation index results and accuracy comparison.

Splitting method	MPA (%)	MIoU (%)	Time (s)
Reference data	84.45	76.38	60
FCN-8s semantic segmentation	88.08	76.88	5
K-means algorithm	65.01	44.87	30

**4.2. Analysis of the Distribution and Characteristics of GVI.** The FCN-8s network was used for the semantic segmentation of 7466 Baidu street view panoramas. The network model of FCN-8s obtained 81.44% accuracy on the training dataset and 66.83% accuracy on the test dataset. To further verify the accuracy of the semantic segmentation extraction results, 100 images were randomly selected in this paper and green vegetation was extracted by three methods: manual recognition, K-means algorithm, and FCN-8s semantic segmentation. The manual recognition used Photoshop's magic to extract the green vegetation. Two evaluation metrics were used to compare green vegetation extraction: the mean pixel accuracy (MPA) was used to measure the proportion of pixels correctly labeled as vegetation to the total pixels, and the formula is shown in equation (6). The mean intersection over union (MIoU) was used to measure the

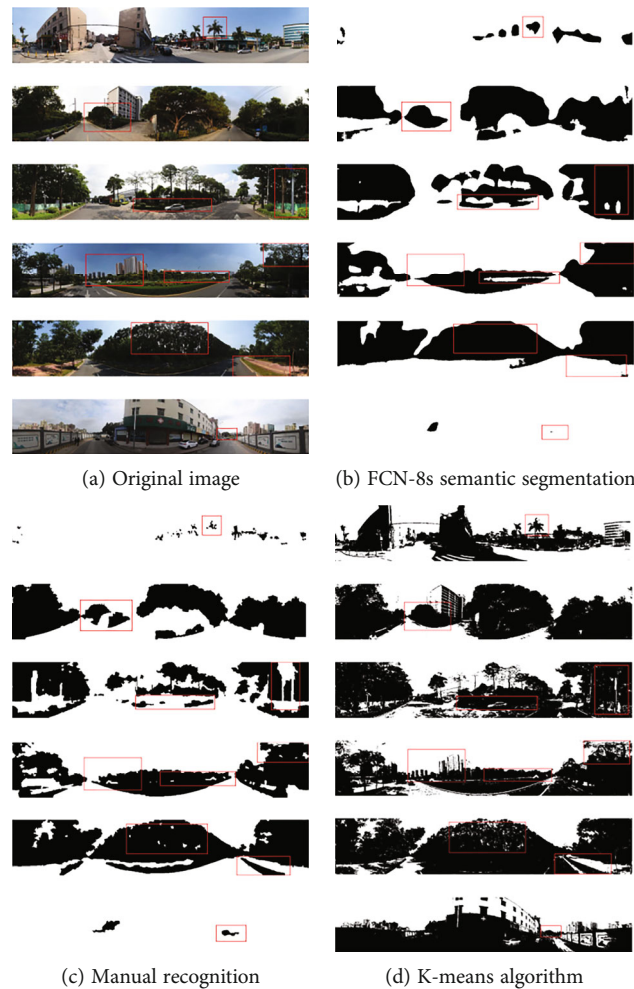


FIGURE 7: Comparison of the results of semantic segmentation of vegetation and nonvegetation.

accuracy of vegetation pixels being correctly labeled, and the formula is shown in equation (7). These measures are usually used to evaluate the accuracy of classification results. Table 5 shows the accuracy of the semantic segmentation results compared with the reference data. Figure 7 shows the comparison between the results of semantic segmentation and the other methods' results. For the scattered branches and leaves of trees, there was a misclassification at the edge of the segmentation results. The K-means algorithm has lots of misclassification in buildings and vegetation. The red boxes in the figures represent the locations where the two segmentation results were different. In general, the segmentation method used in this study meets the needs of this experiment and saves time for manual recognition.

$$\text{MPA} = \frac{1}{k} \times \frac{\sum_{i=1}^k \text{TP}_i + \text{TN}_i}{\sum_{i=1}^k \text{TP}_i + \text{TN}_i + \text{FP}_i + \text{FN}_i}, \quad (6)$$

$$\text{MIoU} = \frac{1}{k} \times \sum_{i=1}^k \frac{\text{TP}_i}{\text{TP}_i + \text{FP}_i + \text{FN}_i} + \frac{\text{TN}_i}{\text{TN}_i + \text{FN}_i + \text{FP}_i}, \quad (7)$$

where  $k$  is the number of images,  $\text{TP}_i$  is true positive identified vegetation pixels of image  $i$ ,  $\text{TN}_i$  is true negative rejected vegetation pixels of image  $i$ ,  $\text{FP}_i$  is false positive identified vegetation pixels of image  $i$ , and  $\text{FN}_i$  is false negative rejected vegetation pixels of image  $i$ .

The analysis of the GVI among the streets in Longhua District showed that the minimum value of the street GVI was 0, while the maximum value was as high as 82.66%. The difference in the value of the GVI among the streets was noticeable. (Streets with fewer than 10 sampling points were not analyzed in this paper.) The GVI results of Longhua District are displayed spatially, and the result is shown in Figure 8. The street with the highest GVI value was Cui'an road, whose average GVI value was as high as 50.83%, followed by those of Yangtaishan Greenway, South Sili road, Lanjing road, and Kesheng road. However, the overall green distribution of the Yangtaishan Greenway was higher than that of the Cui'an road. It provides a good visual experience for cyclists as a cycle path. The lowest GVI value was found for Shiqing avenue, with an average street GVI of 5.42%. The street GVI distribution in Longhua District showed a low middle and high periphery. It was influenced by the greenways covering



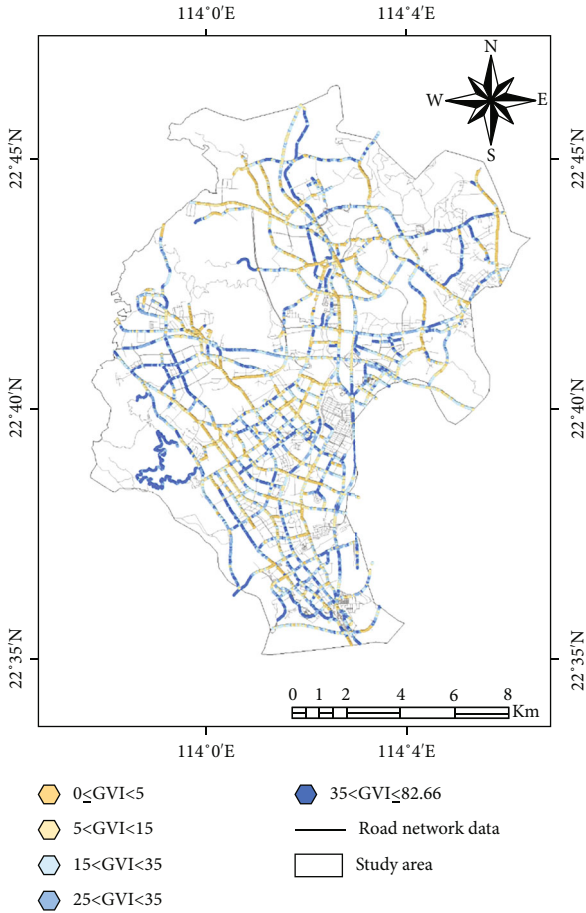


FIGURE 8: Distribution of the GVI from yellow to blue is the GVI class from low to high change.

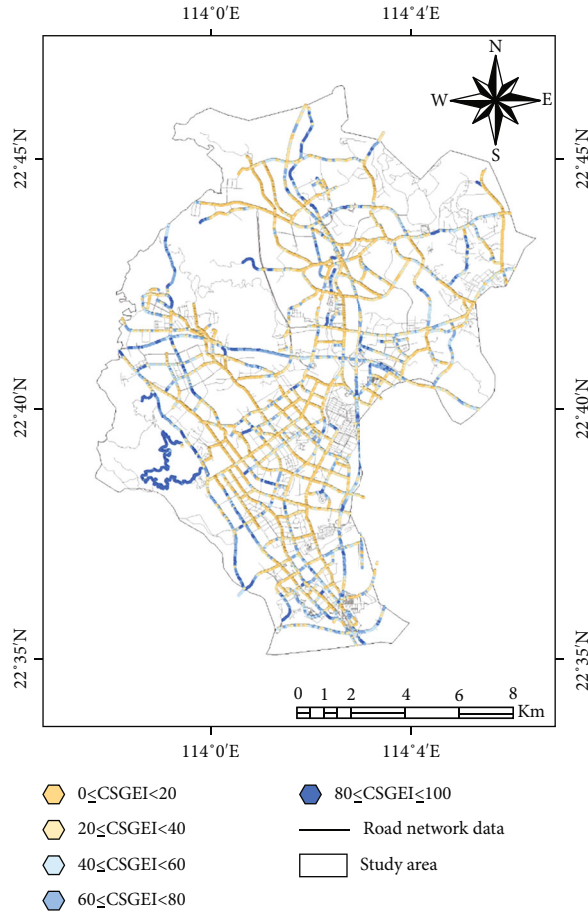


FIGURE 9: Distribution of the CSGEI from yellow to blue is the CSGEI class from low to high change.

the southwestern part of the study area, where the GVI was higher than that in the city center.

4.3. Analysis of the Distribution and Characteristics of the CSGEI. The normalized CSGEI in this paper achieved the observation and analysis of street greening in Longhua District from multiple perspectives. In this paper, the normalized CSGEI was divided into five classes; the result is shown in Figure 9. From L1 to L5 means that the distribution of street vegetation becomes better and better. The statistical analysis of the three indices of each street showed that the GVI was higher than SFVC on the following roads: Guanle road, Si Li south road, Lanqing first road, Longhua Square second road, Jinlong road, and Feng Guan road. The SFVC is higher than the GVI in the Minglang road, Yangtaishan Greenway, Nanping Express, Crushed Stone road separate interchange, and Fulong road. The CSGEI integrated the two indices and avoided the disadvantage of generalization in the description of street greening.

The index after integration showed that the comprehensive greening of Yangtaishan Greenway, Cui'an road, Lanjing road, Kesheng road, and Minglang road was higher and the difference between the two indices was smaller on

the roads of Cui'an road, Lanjing road, and Kesheng road. The greening distribution of Longhua District showed the phenomenon in which low greening was located at the center and high greening was located in the periphery. Figure 10(a) shows the distribution of the SFVC index for each class of roads. It has been seen from the figure that for urban secondary roads, urban main roads, and urban feeder roads, which are widely distributed in the inner city, the SFVC index at the lower level accounted for a higher proportion. The reasons for the above phenomenon are attributed to two points: one is due to scattered vegetation planting in the inner city, and the other is that the resolution of Sentinel-2 is low resulting in a single piece of vegetation failing to be identified by Sentinel-2. As shown in Figure 10(b), the different levels of the GVI for urban trunk roads, urban secondary roads, and urban feeder roads were evenly distributed, while L5 of the GVI cycle path accounted for more than 80%, which was in line with the characteristics of the cycle path design. According to the road network data of OSM to study the streets in Longhua District, the sampling points were divided into five categories. As shown in Figure 10(c), the CSGEI for service and entertainment of the cycle path was higher. It could provide a good visual sensation to pedestrians, and it was also conducive to

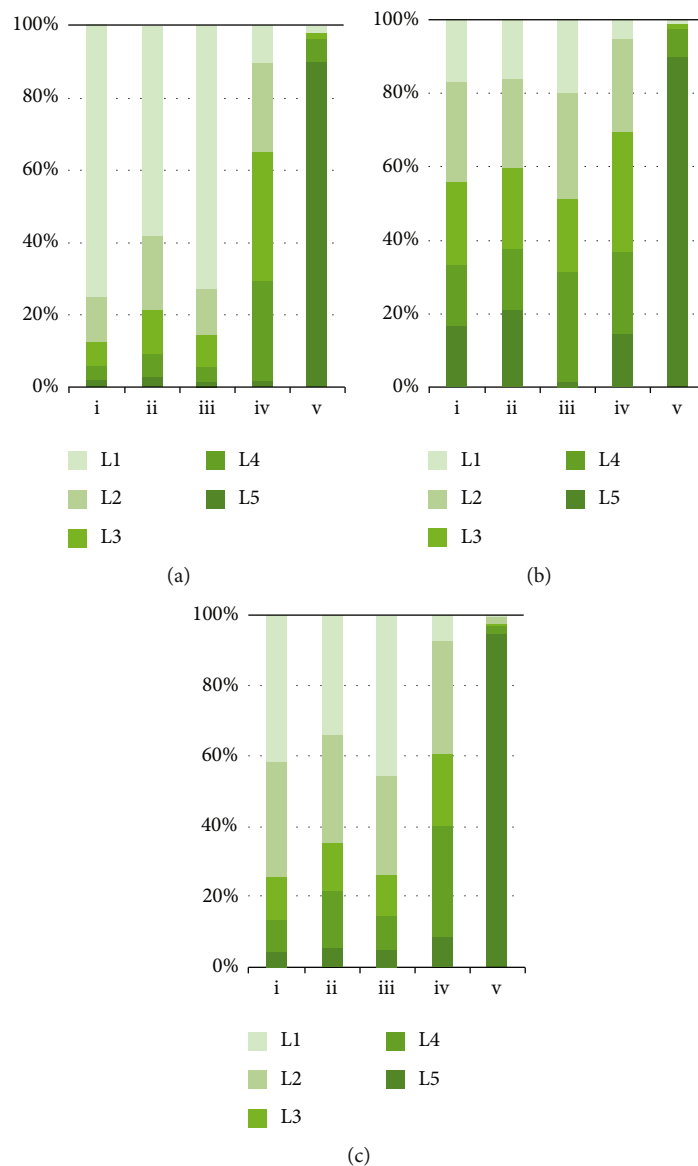


FIGURE 10: Analysis of three indices for different classes of roads, where (a) is SFVC, (b) is GVI, (c) is CSGEI, i is urban secondary roads, ii is urban main roads, iii is urban feeder roads, iv is the elevated and expressway, and v is the cycle path.

maintaining the ecological environment. According to the correlation analysis of the GVI and SFVC index among different classes of roads, the lowest correlation coefficient was 0.38 for the cycle path, followed by 0.39 for elevated and expressways and 0.64 for urban feeder roads, and the overall correlation coefficient was low. This paper used a random sampling method to evaluate the CSGEI. The result is shown in Figure 11.

## 5. Discussion

The multiview data from the horizontal and vertical view has provided a new direction for extracting urban street greening. Different visual effects in green perception could be obtained from two azimuth data; it is helpful to realize the quantitative analysis of urban street greening. Considering

that the grade of the road was divided into five classes, three pictures of five kinds of classes were randomly selected to verify the CSGEI. Combining the pictures and data analysis, it was seen that the GVI was higher than the SFVC index in the greening of urban secondary roads, urban main roads, and urban feeder roads. Figure 11 shows that the vegetation distribution of urban secondary roads was dominated by rows or a single vegetation distribution on both sides of the street. This distribution resulted in the vegetation coverage extraction from Sentinel-2 data having the phenomenon of missing fractions affected by the resolution. The SFVC index in the elevated and expressway was significantly higher than that in the GVI. The same phenomenon was observed for the cycle path, where the SFVC index of the cycle path was higher than the GVI by as much as 95.83%. The street vegetation coverage extracted from Sentinel-2

Road classes	Baidu street view panorama	SFVC
Urban secondary roads		
Urban feeder roads		
Urban main roads		
Elevated and express-way		
Cycle path		

FIGURE 11: Combining Baidu street view panorama and street vegetation coverage to analyze street greening.

data covered the ground objects under the trees due to the shading of trees. As a result, the description of two-dimensional greening was more than the actual description. The 53.68% SFVC was at the L1 level which was less than 9.02% and almost all urban main roads and urban secondary roads. The GVI extracted from the Baidu street view panoramas could effectively identify shrubs and green walls and complement street vegetation coverage. An SFVC in L1 showed a significant increase of approximately 76.67%. After the indices merged, the process of accounting for L1 decreased to 31.29% and the distribution of street greening was in line with the actual situation.

The result has been compared with similar studies [26, 36, 44]. Similarly, a correlation has been found between the GVI and the NDVI in this paper. Different from the previous study, the sample buffer determined by road width was used as the unit to extract the NDVI. The Sentinel-2 is much easier to obtain than LIDAR. Another dimension, the vertical view, has been added to the measurement of urban street green space. The CSEGI could achieve the quantitative evaluation in the urban street space. In addition, it has been confirmed that semantic segmentation is well used in extracting street view images.

However, there are still shortcomings in this paper. For horizontal street greening extracting, the resolution of Sentinel-2 is 10 m and it is not able to recognize the young trees. For vertical street greening extracting, there is no guarantee that street view data was acquired on the same day. In addition, the time span of the Baidu street view panoramas cannot guarantee the same acquisition time as Sentinel-2. The evaluation of street greening at multiple scales from the point, line, and polygon will be realized in future studies.

## 6. Conclusions

This study used a combination of Baidu street view panoramas and Sentinel-2 to extract and analyze the three-dimensional greening information of streets. The results showed that the Baidu street view panoramas and Sentinel-2 could provide two perspectives of street greening distribution. The combination of the two kinds of data was an effective method for evaluating and analyzing street greening. The higher polarization of SFVC compared to GVI is mainly due to the low resolution of Sentinel-2 images and the poor uniformity of vegetation distribution on both sides of the street. The spatial distribution of the GVI showed the characteristics of being low in the middle and high in the periphery due to the buildings and sidewalks in the central city, which occupy part of the greenery space. The CSGEI evaluated street greening from two perspectives, reducing the workload of a large-scale questionnaire survey. Combined with the Sentinel-2 image, this approach compensated for the deficiency of single-angle observations of vegetation in the Baidu street view panoramas and the inconsistency of the Baidu street view panorama acquisition time. The results showed that street view images could identify lawns, shrubs, and roads under the tree canopy in remote sensing images. Remote sensing images could be used to describe the lateral growth of trees in the Baidu street view pano-

ramas to objectively evaluate the greening level of the street at the observation point. The CSGEI proposed in this paper could merge the two perspectives of street greening evaluation levels. As the street view images are updated, the latest data will be used to measure the urban green space, enabling monitoring of the three-dimensional changes in street greening. The index helps to identify the streets lacking greening and to formulate corrective measures in a targeted manner. It would provide important references for street greening planners.

## Data Availability

The data used to support the findings of this study are available from the corresponding author upon request.

## Conflicts of Interest

The authors declare that there is no conflict of interest regarding the publication of this paper.

## Acknowledgments

This work was supported by the Education Department of Liaoning Province Fund (no. Infw202013), National Natural Science Foundation of China (4210010785), and Humanities and Social Science Foundation of the Ministry of Education (CN) (21YJC790129).

## References

- [1] R. L. Chazdon, P. Brancalion, L. Laestadius et al., "When is a forest a forest? Forest concepts and definitions in the era of forest and landscape restoration," *Ambio*, vol. 45, no. 5, pp. 538–550, 2016.
- [2] A. Blood, G. Starr, F. Escobedo, A. Chappelka, and C. Staudhammer, "How do urban forests compare? Tree diversity in urban and periurban forests of the Southeastern US," *Forests*, vol. 7, no. 12, pp. 120–120, 2016.
- [3] E. G. McPherson, N. van Doorn, and J. de Goede, "Structure, function and value of street trees in California, USA," *Urban Forestry & Urban Greening*, vol. 17, pp. 104–115, 2016.
- [4] E. Y. Choe, A. Jorgensen, and D. Sheffield, "Does a natural environment enhance the effectiveness of mindfulness-based stress reduction (MBSR)? Examining the mental health and wellbeing, and nature connectedness benefits," *Landscape and Urban Planning*, vol. 202, article 103886, 2020.
- [5] A. Belmeziti, F. Cherqui, and B. Kaufmann, "Improving the multi-functionality of urban green spaces: relations between components of green spaces and urban services," *Sustainable Cities and Society*, vol. 43, pp. 1–10, 2018.
- [6] Y. Liu, R. Wang, G. Grekousis, Y. Liu, Y. Yuan, and Z. Li, "Neighbourhood greenness and mental wellbeing in Guangzhou, China: what are the pathways?," *Landscape and Urban Planning*, vol. 190, article 103602, 2019.
- [7] S. Jin, J. Guo, S. Wheeler, L. Kan, and S. Che, "Evaluation of impacts of trees on PM<sub>2.5</sub> dispersion in urban streets," *Atmospheric Environment*, vol. 99, pp. 277–287, 2014.
- [8] P. Zang, X. Liu, Y. Zhao, H. Guo, Y. Lu, and C. Q. L. Xue, "Eye-level street greenery and walking behaviors of older adults,"

- International Journal of Environmental Research and Public Health*, vol. 17, no. 17, p. 6130, 2020.
- [9] S. Chen, L. Zhang, R. Feng, and C. Zhang, "High-resolution remote sensing image classification with RmRMR-enhanced bag of visual words," *Computational Intelligence and Neuroscience*, vol. 2021, Article ID 7589481, 10 pages, 2021.
  - [10] J. Xue and B. Su, "Significant remote sensing vegetation indices: a review of developments and applications," *Journal of Sensors*, vol. 2017, Article ID 1353691, 17 pages, 2017.
  - [11] L. Zhou, C. J. Tucker, R. K. Kaufmann, D. Slayback, N. V. Shabanov, and R. B. Myneni, "Variations in northern vegetation activity inferred from satellite data of vegetation index during 1981 to 1999," *Journal of Geophysical Research: Atmospheres*, vol. 106, no. D17, pp. 20069–20083, 2001.
  - [12] K. Anderson, S. Hancock, S. Casalegno et al., "Visualising the urban green volume: exploring LiDAR voxels with tangible technologies and virtual models," *Landscape and Urban Planning*, vol. 178, pp. 248–260, 2018.
  - [13] D. Seidel, P. Annighöfer, A. Thielman et al., "Predicting tree species from 3D laser scanning point clouds using deep learning," *Frontiers in Plant Science*, vol. 12, p. 141, 2021.
  - [14] H. Lu, M. R. Raupach, T. R. McVicar, and D. J. Barrett, "Decomposition of vegetation cover into woody and herbaceous components using AVHRR NDVI time series," *Remote Sensing of Environment*, vol. 86, no. 1, pp. 1–18, 2003.
  - [15] X. Mu, W. Song, Z. Gao, T. R. McVicar, R. J. Donohue, and G. Yan, "Fractional vegetation cover estimation by using multi-angle vegetation index," *Remote Sensing of Environment*, vol. 216, pp. 44–56, 2018.
  - [16] Y. Aoki, "Relationship between perceived greenery and width of visual fields," *Journal of The Japanese Institute of Landscape Architecture*, vol. 51, no. 1, pp. 1–10, 1987.
  - [17] J. Wu, L. Cheng, S. Chu, N. Xia, and M. Li, "A green view index for urban transportation: how much greenery do we view while moving around in cities?," *International Journal of Sustainable Transportation*, vol. 14, no. 12, pp. 972–989, 2020.
  - [18] R. Wang, Y. Lu, X. Wu, Y. Liu, and Y. Yao, "Relationship between eye-level greenness and cycling frequency around metro stations in Shenzhen, China: a big data approach," *Sustainable Cities and Society*, vol. 59, article 102201, 2020.
  - [19] J. Chen, C. Zhou, and F. Li, "Quantifying the green view indicator for assessing urban greening quality: an analysis based on Internet-crawling street view data," *Ecological Indicators*, vol. 113, article 106192, 2020.
  - [20] Y. Xiao, Y. Zhang, Y. Sun, P. Tao, and X. Kuang, "Does green space really matter for residents' obesity? A new perspective from Baidu street view," *Frontiers in Public Health*, vol. 8, 2020.
  - [21] F. Zhang, B. Zhou, L. Liu et al., "Measuring human perceptions of a large-scale urban region using machine learning," *Landscape and Urban Planning*, vol. 180, pp. 148–160, 2018.
  - [22] L. Yin and Z. Wang, "Measuring visual enclosure for street walkability: using machine learning algorithms and Google Street View imagery," *Applied Geography*, vol. 76, pp. 147–153, 2016.
  - [23] H. Zhou, S. He, Y. Cai, M. Wang, and S. Su, "Social inequalities in neighborhood visual walkability: using street view imagery and deep learning technologies to facilitate healthy city planning," *Sustainable Cities and Society*, vol. 50, article 101605, 2019.
  - [24] Y. Ye, W. Zeng, Q. Shen, X. Zhang, and Y. Lu, "The visual quality of streets: a human-centred continuous measurement based on machine learning algorithms and street view images," *Environment and Planning B: Urban Analytics and City Science*, vol. 46, no. 8, pp. 1439–1457, 2019.
  - [25] L. Cheng, S. Chu, W. Zong, S. Li, J. Wu, and M. Li, "Use of Tencent street view imagery for visual perception of streets," *ISPRS International Journal of Geo-Information*, vol. 6, no. 9, p. 265, 2017.
  - [26] M. Tong, J. She, J. Tan, M. Li, R. Ge, and Y. Gao, "Evaluating street greenery by multiple indicators using street-level imagery and satellite images: a case study in Nanjing, China," *Forests*, vol. 11, no. 12, p. 1347, 2020.
  - [27] A. Dubey, N. Naik, D. Parikh, R. Raskar, and C. A. Hidalgo, "Deep learning the city: quantifying urban perception at a global scale," *European Conference on Computer Vision*, vol. 9905, pp. 196–212, 2016.
  - [28] D. Ki and S. Lee, "Analyzing the effects of green view index of neighborhood streets on walking time using Google Street View and deep learning," *Landscape and Urban Planning*, vol. 205, article 103920, 2021.
  - [29] H. Yu, Z. Yang, L. Tan et al., "Methods and datasets on semantic segmentation: a review," *Neurocomputing*, vol. 304, pp. 82–103, 2018.
  - [30] X. Li, C. Zhang, W. Li, R. Ricard, Q. Meng, and W. Zhang, "Assessing street-level urban greenery using Google Street View and a modified green view index," *Urban Forestry & Urban Greening*, vol. 14, no. 3, pp. 675–685, 2015.
  - [31] X. Chen, Q. Meng, D. Hu, L. Zhang, and J. Yang, "Evaluating greenery around streets using baidu panoramic street view images and the panoramic green view index," *Forests*, vol. 10, no. 12, p. 1109, 2019.
  - [32] M. Helbich, Y. Yao, Y. Liu, J. Zhang, P. Liu, and R. Wang, "Using deep learning to examine street view green and blue spaces and their associations with geriatric depression in Beijing, China," *Environment International*, vol. 126, pp. 107–117, 2019.
  - [33] Y. P. Chen, B. H. Zheng, and X. P. Zeng, "Multidimensional quantization of urban green space based on street view and remote sensing image: a case study of Chenzhou," *Economic Geography*, vol. 39, no. 12, pp. 80–87, 2019.
  - [34] Y. Kumakoshi, S. Y. Chan, H. Koizumi, X. Li, and Y. Yoshimura, "Standardized green view index and quantification of different metrics of urban green vegetation," *Sustainability*, vol. 12, no. 18, p. 7434, 2020.
  - [35] R. Cao, J. Zhu, W. Tu et al., "Integrating aerial and street view images for urban land use classification," *Remote Sensing*, vol. 10, no. 10, p. 1553, 2018.
  - [36] X. Yu, G. Zhao, C. Chang, X. Yuan, and F. Heng, "Bgvi: a new index to estimate street-side greenery using baidu street view image," *Forests*, vol. 10, no. 1, p. 3, 2019.
  - [37] C. Wu, N. Peng, X. Ma, S. Li, and J. Rao, "Assessing multiscale visual appearance characteristics of neighbourhoods using geographically weighted principal component analysis in Shenzhen, China," *Computers, Environment and Urban Systems*, vol. 84, article 101547, 2020.
  - [38] M. Drusch, U. del Bello, S. Carlier et al., "Sentinel-2: ESA's optical high-resolution mission for GMES operational services," *Remote Sensing of Environment*, vol. 120, pp. 25–36, 2012.
  - [39] N. Otsu, "A threshold selection method from gray-level histograms," *IEEE Transactions on Systems, Man, and Cybernetics*, vol. 9, no. 1, pp. 62–66, 1979.

- [40] L. Meng, K.-H. Wen, Z. Zeng, R. Brewin, X. Fan, and Q. Wu, "The impact of street space perception factors on elderly health in high-density cities in Macau—analysis based on street view images and deep learning technology," *Sustainability*, vol. 12, no. 5, p. 1799, 2020.
- [41] L. Dai, C. Zheng, Z. Dong et al., "Analyzing the correlation between visual space and residents' psychology in Wuhan, China using street-view images and deep-learning technique," *City and Environment Interactions*, vol. 11, article 100069, 2021.
- [42] Y. Yao, Z. Liang, Z. Yuan et al., "A human-machine adversarial scoring framework for urban perception assessment using street-view images," *International Journal of Geographical Information Science*, vol. 33, no. 12, pp. 2363–2384, 2019.
- [43] X. Xi, W. Yikai, and L. Min, "The method of measurement and applications of visible green index in Japan," *Urban Planning International*, vol. 2, 2018.
- [44] E. Barbierato, I. Bernetti, I. Capecchi, and C. Saragosa, "Integrating remote sensing and street view images to quantify urban forest ecosystem services," *Remote Sensing*, vol. 12, no. 2, p. 329, 2020.

## Research Article

# A Method to Locate Tree Positions Using Ultrawideband Technology

Fangxing Yuan,<sup>1,2</sup> Sheng Chen,<sup>3</sup> Luming Fang <sup>1,2</sup> Siqing Zheng,<sup>1,2</sup> Yuzhen Liu,<sup>1,2</sup> and Junjun Ren<sup>1,2</sup>

<sup>1</sup>Key Laboratory of Forestry Intelligent Monitoring and Information Technology Research of Zhejiang Province, Zhejiang A & F University, Lin'an, 311300 Zhejiang, China

<sup>2</sup>College of Information Engineering, Zhejiang A & F University, Lin'an, 311300 Zhejiang, China

<sup>3</sup>Zhejiang Forest Resources Monitoring Center, Hangzhou, 310004 Zhejiang, China

Correspondence should be addressed to Luming Fang; [flming@zafu.edu.cn](mailto:flming@zafu.edu.cn)

Received 24 January 2021; Revised 30 April 2021; Accepted 21 May 2021; Published 6 July 2021

Academic Editor: Bahareh Kalantar

Copyright © 2021 Fangxing Yuan et al. This is an open access article distributed under the Creative Commons Attribution License, which permits unrestricted use, distribution, and reproduction in any medium, provided the original work is properly cited.

Tree position plays an important role in research on forest resources and ecological functions, and quickly and accurately obtaining tree position data has long been the focus of investigators. However, the classical method is time-consuming and laborious; thus, a convenient method of measuring tree position is needed. The primary achievements of this study include the following: (1) a device was designed for precise location of trees; (2) a new location algorithm was proposed for pentagonal localization based on the received signal strength indication and ultrawideband technology; and (3) a PC software application was developed for automatically storing and uploading tree position data. The device was applied to 10 circular plots with a diameter of 24 m to test the positioning speed and accuracy. The results showed that the tree positions could be accurately estimated. On the  $x$ - and  $y$ -axes, the biases were -3.94 and 3.36 cm, respectively, and the root mean square errors (RMSEs) were 28.39 and 28.53 cm, respectively. The mean error (Ed) between the estimated and reference distances was 36.13 cm, and the standard deviation was 16.67 cm. The device is inexpensive and easy to use and carry in the field; thus, it is suitable for locating trees in environments with complex terrain.

## 1. Introduction

Tree position measurements are of great significance in forest resource investigations. The rapid and accurate acquisition of tree position in sample plots is helpful for predicting the growth of tree DBH and population development trends and has important ecological significance for revealing the relationship between trees and tree species [1, 2]. Traditional measurements use a box compass combined with tapes or a laser distance meter. The measurement process is time-consuming and laborious, and the data are read and recorded manually, which is inefficient and easily confounded, thus seriously restricting the quality and efficiency of acquiring tree positions in sample field surveys [3–7]. Developing a method of improving the quality and efficiency of tree position information acquisition has long been an issue for forestry researchers [8–10].

In recent years, many devices and methods have been developed for locating trees in sample plots. The Haglöf Postex<sup>®</sup> Laser uses ultrasonic solution for tree position measurement; however, due to the short distance of ultrasonic measurement, the size of the sample plot will be limited [11]. The global navigation satellite system (GNSS) [12–15] can provide positioning coordinate information in most environments. However, signal attenuation or even signal disappearance occurs in stands with high canopy density, which is also greatly affected by the density of trees in the sample plot [16–18]. Total stations are a type of precise electronic survey system with a mapping instrument that integrates rangefinders, electronic theodolites, and microprocessors [19]. Such systems provide an effective method for locating trees on the sample plot but have some disadvantages, such as inconvenience, complicated operation, and expensive price. Terrestrial laser scanning

(TLS), also known as ground-based light detection and ranging (LiDAR) [20–24], has been applied for the extraction of various forestry attributes [25–28]; however, due to some operational and performance limitations, laborious carrying and installation, and complex data processing, TLS cannot be widely used [29, 30]. Close-range photogrammetry (CRP) [31–33] and smartphones with time of flight (TOF) [34–36] cameras have also been applied to obtain tree locations; however, they are highly susceptible to stand density, surface vegetation, and light intensity and require specialized knowledge to handle complex point cloud computing [37]. Therefore, there are some limitations to applying these devices and methods for determining the position of trees.

Advances in sensing technology have led to the development of devices for precisely locating trees in the field. Ultrawideband (UWB) technology [38–42] is a kind of communication technology that uses discontinuous less-than-nanosecond pulses without carriers and has the advantages of a high transmission rate, strong multipath resolution, strong anti-interference ability, and strong penetration ability. It has been widely used in the determination of distance and position. Compared with other wireless communication technologies (Wi-Fi, ZigBee, etc.), it has higher precision [43–45].

In this paper, a measurement device using UWB sensors was developed for accurate positioning, rapid measurement recording, automatic transmission, and processing of trees, and it has the advantages of low cost and ease of carrying.

## 2. System Design

**2.1. Design of the Main Device.** The device is mainly composed of a base station and a mobile station, as shown in Figure 1. The base station consists of a supporting tripod and five 1m long poles with a UWB module on top. The poles and supporting tripod can be folded and shrunk, which facilitates the carrying of the device by survey crews in the field. Mobile station is the location tag. Table 1 describes the components used by the device and their main properties. The circuit of the base station is mainly composed of a microprocessor, power module, gyroscope module, compass module, UWB module, and display screen. The circuit of the mobile station is mainly composed of a microprocessor, power module, UWB module, secure digital memory card (SD card), Bluetooth module, button, and display screen. The device uses an 8-bit microprocessor, which is high speed and low cost and has strong anti-interference. The power module is composed of a lithium battery, a power management chip, and a switch. The lithium battery is used as the supply power to the system components, and the power management chip can protect the lithium battery and other circuits from overcurrent. The gyroscope module is used to collect the location information of the base station. The compass module is used to collect the azimuth information. The base station is equipped with five UWB modules, and the mobile station is equipped with one UWB module

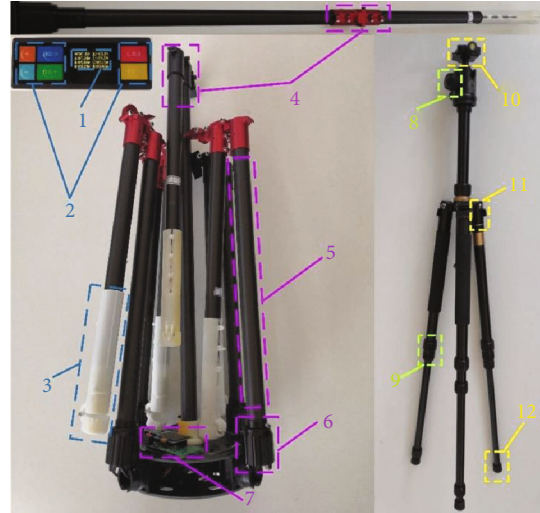


FIGURE 1: Main device and its components: 1: display panel; 2: keys; 3: UWB casings; 4: metal folding pieces; 5: carbon fibers; 6: fixing knobs; 7: printed circuit board (PCB); 8: level adjusting knob; 9: rotary locks; 10: fixing card buckle; 11: limit card buckles; 12: rubber pads.

to measure the distance between the mobile station and the base station. The display screen displays the measurement information, the SD card stores the distance and location coordinate data collected by the mobile station, and the Bluetooth module transmits the data between the mobile station and host computer.

**2.2. Principle of UWB Ranging.** To accurately measure the distances, the UWB sensor based on the double-sided two-way ranging (DS-TWR) principle [46, 47] was selected. Due to the error introduced by clock deviation in single-sided two-way ranging (SS-TWR) [48, 49] measurement, DS-TWR adds another round of communication on the basis of SS-TWR to compensate for the error introduced through two communication times and increase the accuracy of ranging. The principle is shown in Figure 2, and the formula is shown in

$$D = c \times T_{\text{prop}} = c \times \frac{T_{\text{round1}} \times T_{\text{round2}} - T_{\text{reply1}} \times T_{\text{reply2}}}{T_{\text{round1}} + T_{\text{round2}} + T_{\text{reply1}} + T_{\text{reply2}}}, \quad (1)$$

where Node A and Node B are communication nodes,  $D$  is the distance between Node A and Node B,  $T_{\text{prop}}$  is the time for the wireless pulse signal to travel in the air,  $c$  is the speed of light,  $T_{\text{round1}}$  is the total time of Node A receiving and sending pulses in the first round of communication,  $T_{\text{reply1}}$  is the waiting time of Node B in the first round of communication,  $T_{\text{round2}}$  is the total time required for Node B to receive and send pulses in the second round of communication, and  $T_{\text{reply2}}$  is the waiting time of Node A in the second round of communication.

**2.3. Design of Software Process.** The software was designed to acquire the distances between the base station and the mobile



TABLE 1: Descriptive statistics of the device’s components<sup>1</sup>.

Component	Chip model/type	Interface type	Parameter	Function
Microprocessor	STC15W4K56S4	Digital, serial port, SPI, etc.	SRAM: 4 KB; flash: 56 KB data processing	Microprocessor
Power management circuit	TP4056, AMS1117, etc.	Digital, power	Input: 3.7 V-4.2 V, 5 V; output: 5 V, 3.3 V	Power management
Battery	Lithium battery	Power	4000 mAh	Power supply
Gyroscope module	JY901B	Serial port	Resolution: 0.01°	Attitude measurement
Compass module	GY-26	Serial port	Resolution: 0.1°	Azimuth measurement
UWB module	D-DWM-PG1.7	Serial port	Resolution: 1 cm; range: 0-50 m	Distance measurement
Display	OLED	SPI	128 × 64 pixels	Data display
Keyboard	PVC	Digital	6 keys	Data recording
SD card	Micro SD	SPI	2 GB	Data storage
Bluetooth	HC-06	Serial port	Range: 0-15 m	COMM with upper computer

<sup>1</sup>SPI: serial peripheral interface; SRAM: static random-access memory; KB: kilobyte; V: voltage; mAh: milliampere-hour; GB: gigabyte; COMM: communication.

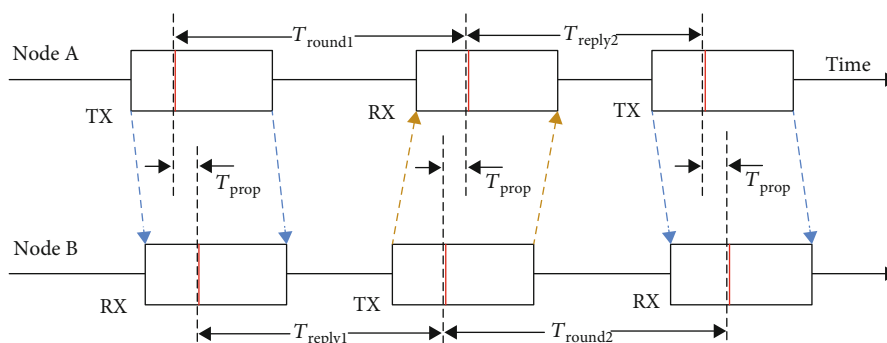


FIGURE 2: Scheme of double-sided, two-way ranging (DS-TWR).

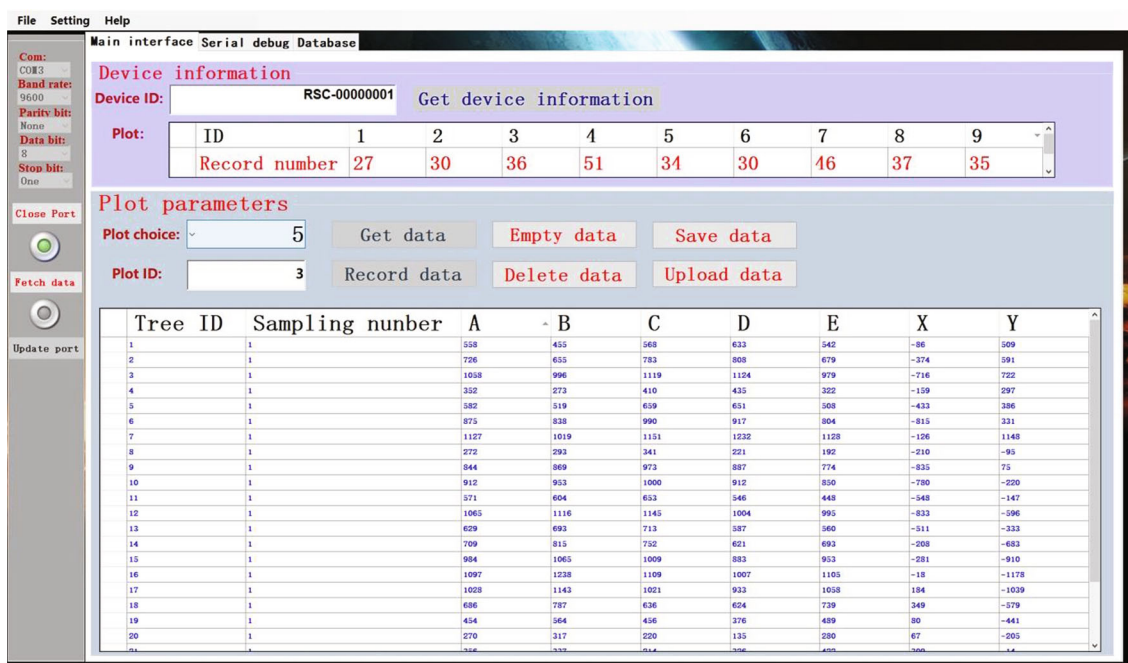


FIGURE 3: Host computer interface.

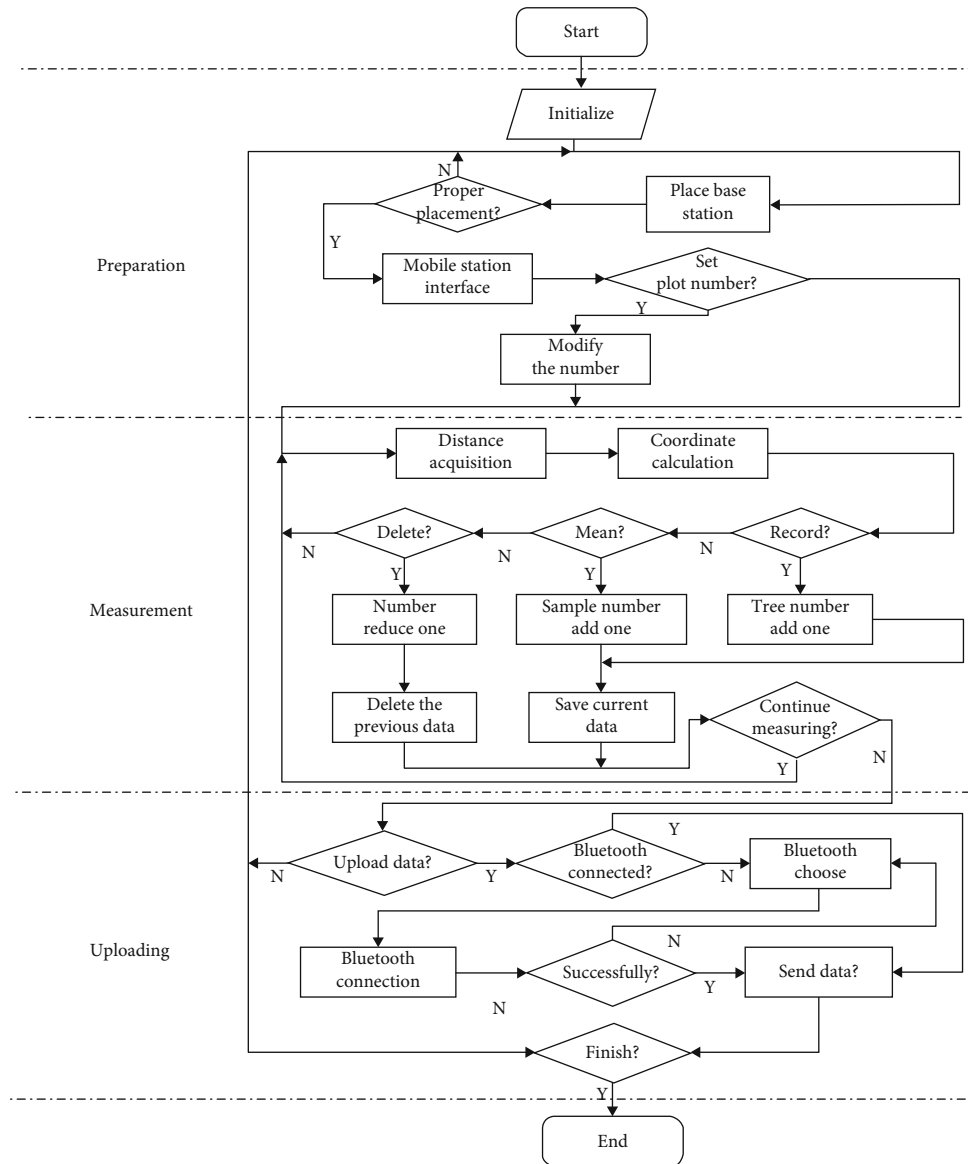


FIGURE 4: Flowchart of the system.

station and to calculate the positioning coordinates, key control, and data management, as shown in Figure 3. The GUI enables investigators to read device information, calculate data statistics, and export data to facilitate data processing and analysis. The general flow of the software is shown in Figure 4, which is divided into three stages: preparation, measurement, and upload. During the measurement, the tree number and the corresponding position information can be automatically completed.

### 3. Materials and Methods

**3.1. Study Area.** The test site chosen here was Zhejiang A and F University, Hangzhou, China ( $30^{\circ}15'N$ ,  $119^{\circ}43'E$ ). A total of 10 circular plots with a diameter of 24 m (371 trees in total)

were measured (a circular plot with a radius of 11.28 m is usually used in forest surveys in South China; therefore, we set the radius as 12 m). The surfaces were mainly covered by leaf litter in plots 1 to 6 and denser weeds in plots 7 to 10 (Table 2).

#### 3.2. Methods

**3.2.1. Measurement Process Design.** To test the positioning accuracy, the reference data measured using theodolite with a laser rangefinder were compared with the data measured by the device. All measurements used the local east, north, up (ENU) coordinate system. The measurement operation for theodolite with a laser rangefinder and the device are shown in Figures 5 and 6, respectively. Poles B and C of the device pointing to the north and east were the positive  $y$ -

TABLE 2: Descriptive statistics of the sample plot<sup>2</sup>.

Plot	Number of trees	Dominant species	Slope (°)
1	27	S1	0.9
2	30	S1, S2, S3	1.9
3	36	S1, S3, S4, S5, S6	4.8
4	51	S3, S4, S11, S12	5.8
5	34	S3, S5, S6	2.5
6	30	S1, S3, S6	4.9
7	45	S1, S3, S4, S7	12.6
8	37	S5, S8, S9	14.1
9	35	S3, S4, S5, S10, S13	13.8
10	46	S5, S10, S13	12.1

<sup>2</sup>S1: soapberry; S2: southern magnolia; S3: camphor tree; S4: tulip tree; S5: *Michelia alba*; S6: pine tree; S7: *Dalbergia hupeana*; S8: *Ormosia hosiei*; S9: *Ginkgo biloba*; S10: *Chinese parasol*; S11: *Michelia maudiae*; S12: *Celtis sinensis*; S13: *Zelkova schneideriana*.



FIGURE 5: The theodolite with a laser rangefinder measurement.

and  $x$ -axes, respectively. Pole A was the positive  $z$ -axis. The device measurement process was as follows.

- (1) The base station was placed in the center of the circle plot. According to the gyroscope data, the station was adjusted to the horizontal position and then pole B was moved to the north according to the compass data
- (2) The plot ID was set on the mobile station
- (3) We placed the mobile station at the measuring position of the trees (1.3 m above the ground), pressed the record button, and recorded the position data. To ensure that the measured value is close to the reference value, the survey crew can press the average key for multiple samplings. Finally, the average value is automatically calculated. The actual operation is shown in Figure 7



FIGURE 6: Placement of the device.



FIGURE 7: Position of the tree. On the display screen, 1 is the tree code and sampling number, 2 is the coordinates, 3 is the distances between the base stations and the mobile station, 4 is the delete key, 5 is the page key, 6 is the record key, and 7 is the average key.

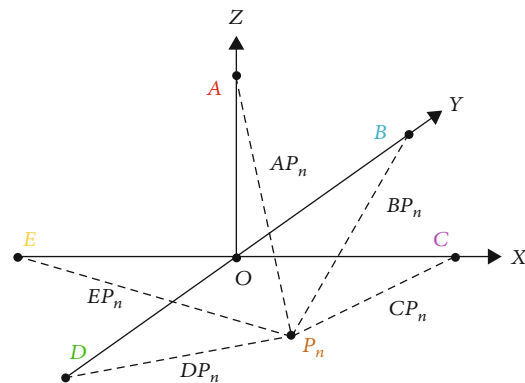


FIGURE 8: A diagram of pentagonal localization.  $|OA| = |OB| = |OC| = |OD| = |OE| = 1$  m.

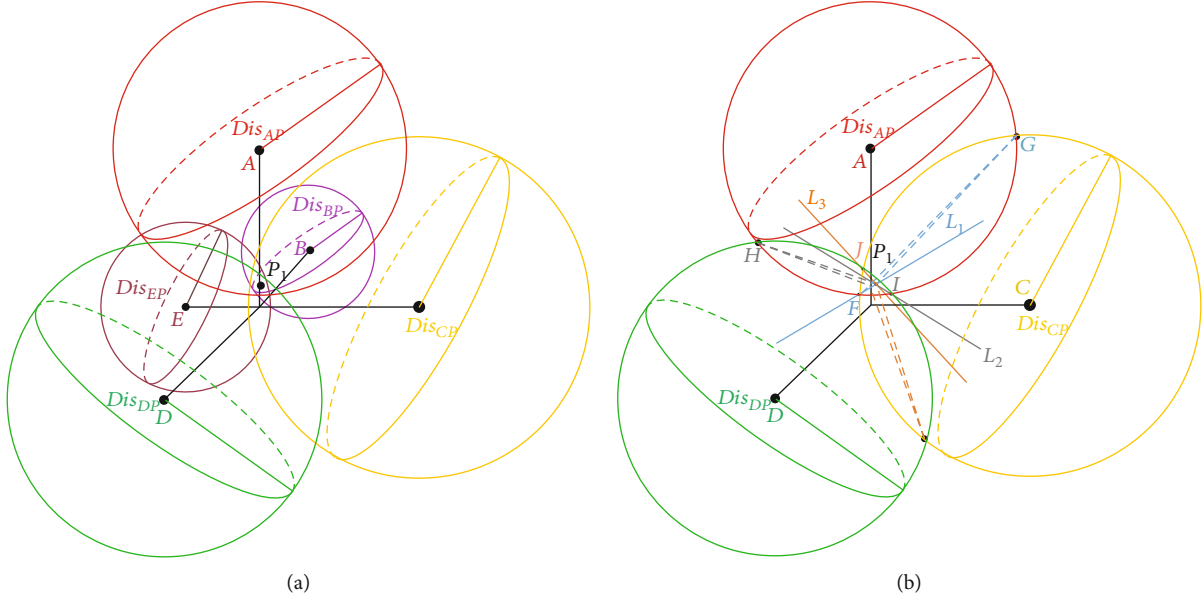


FIGURE 9: Position estimation using (a) pentagonal localization and (b) trilateration localization.

- (4) After measuring the position of trees in the plot, the data were uploaded to the host computer for statistical analysis

3.2.2. *Estimation Method of Tree Position.* The distances between  $P_n$  and each antenna anchor point are shown in Figure 8.

Taking  $OC$  as the positive  $x$ -axis,  $OB$  as the positive  $y$ -axis, and  $OA$  as the positive  $z$ -axis, the coordinates of points A–E can be obtained:

$$\begin{aligned}
 (X_A, Y_A, Z_A) &= (0, 0, 1), \\
 (X_B, Y_B, Z_B) &= (0, 1, 0), \\
 (X_C, Y_C, Z_C) &= (1, 0, 0), \\
 (X_D, Y_D, Z_D) &= (0, -1, 0), \\
 (X_E, Y_E, Z_E) &= (-1, 0, 0).
 \end{aligned} \tag{2}$$

Assuming that the  $P_n$  coordinates are  $(X_n, Y_n, Z_n)$ , the distance between  $P_n$  and each anchor point is as follows:

$$\begin{aligned}
 AP_n &= \sqrt{(X_n - X_A)^2 + (Y_n - Y_A)^2 + (Z_n - Z_A)^2} \\
 &= \sqrt{X_n^2 + Y_n^2 + (Z_n - 1)^2},
 \end{aligned} \tag{3}$$

$$\begin{aligned}
 BP_n &= \sqrt{(X_n - X_B)^2 + (Y_n - Y_B)^2 + (Z_n - Z_B)^2} \\
 &= \sqrt{X_n^2 + (Y_n - 1)^2 + Z_n^2},
 \end{aligned} \tag{4}$$

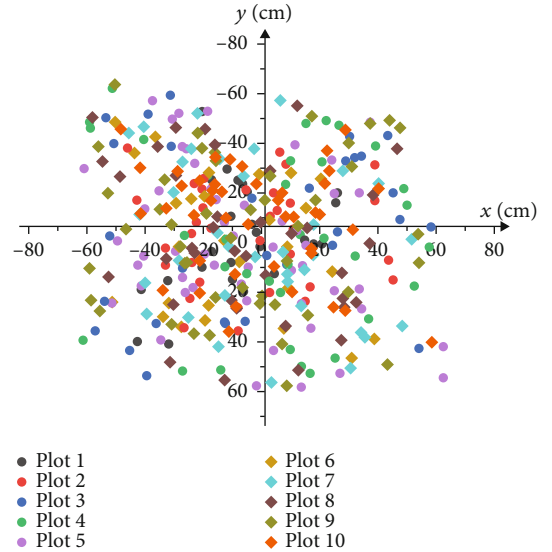


FIGURE 10: Errors measured by the device.

$$\begin{aligned}
 CP_n &= \sqrt{(X_n - X_C)^2 + (Y_n - Y_C)^2 + (Z_n - Z_C)^2} \\
 &= \sqrt{(X_n - 1)^2 + Y_n^2 + Z_n^2},
 \end{aligned} \tag{5}$$

$$\begin{aligned}
 DP_n &= \sqrt{(X_n - X_D)^2 + (Y_n - Y_D)^2 + (Z_n - Z_D)^2} \\
 &= \sqrt{X_n^2 + (Y_n + 1)^2 + Z_n^2},
 \end{aligned} \tag{6}$$

$$\begin{aligned}
EP_n &= \sqrt{(X_n - X_E)^2 + (Y_n - Y_E)^2 + (Z_n - Z_E)^2} \\
&= \sqrt{(X_n + 1)^2 + Y_n^2 + Z_n^2}.
\end{aligned} \tag{7}$$

In Equations (3)–(7), any four equations can be used to determine the  $P_n$  coordinates.

As shown in Figure 9(a), in practical applications, the UWB wireless signal will be obstructed and experience interference by the surrounding environment, such as the trunks, branches, and leaves, resulting in signal attenuation [50, 51] and slightly longer communication time; therefore, the  $AP_n$ ,  $BP_n$ ,  $CP_n$ ,  $DP_n$ , and  $EP_n$  values are slightly greater than the actual values and do not intersect at a common point. To achieve accurate positioning and mitigate the influence of signal attenuation on ranging, some scholars have proposed using trilateration and quadrilateral localization for corresponding positioning depending on the received signal strength indication (RSSI) [52, 53].

According to the principles of trilateration [54, 55] and quadrilateral localization [56], 10 sets of pairwise intersecting spheres can be developed from Figure 9(a) for triangular localization. Take Figure 9(b) as an example, where three spheres A, C, and D intersect in pairs and the intersection is three planes (FGP<sub>1</sub>, HIP<sub>1</sub>, and JKP<sub>1</sub>). The plane equation

can be obtained by subtracting Equations (3), (5), and (6) in pairs:

$$\begin{aligned}
&2(X_C - X_A)X_n + 2(Y_C - Y_A)Y_n + 2(Z_C - Z_A)Z_n \\
&= AP_n^2 + X_C^2 + Y_C^2 + Z_C^2 - CP_n^2 - X_A^2 - Y_A^2 - Z_A^2, \\
&2(X_D - X_A)X_n + 2(Y_D - Y_A)Y_n + 2(Z_D - Z_A)Z_n \\
&= AP_n^2 + X_D^2 + Y_D^2 + Z_D^2 - DP_n^2 - X_A^2 - Y_A^2 - Z_A^2, \\
&2(X_D - X_C)X_n + 2(Y_D - Y_C)Y_n + 2(Z_D - Z_C)Z_n \\
&= CP_n^2 + X_D^2 + Y_D^2 + Z_D^2 - DP_n^2 - X_C^2 - Y_C^2 - Z_C^2.
\end{aligned} \tag{8}$$

In addition, because the three planes intersect in pairs, three lines  $L_1$ ,  $L_2$ , and  $L_3$  can be obtained by pairwise combination in Equation (8). The three lines intersect at point  $P_1$ , and the coordinates of  $P_1$  ( $X_1, Y_1, Z_1$ ) can be obtained according to Equation (8). In the same way, the coordinates of the other nine combinations can be obtained:  $P_2$  ( $X_2, Y_2, Z_2$ ),  $P_3$  ( $X_3, Y_3, Z_3$ ),  $P_4$  ( $X_4, Y_4, Z_4$ ),  $P_5$  ( $X_5, Y_5, Z_5$ ),  $P_6$  ( $X_6, Y_6, Z_6$ ),  $P_7$  ( $X_7, Y_7, Z_7$ ),  $P_8$  ( $X_8, Y_8, Z_8$ ),  $P_9$  ( $X_9, Y_9, Z_9$ ), and  $P_{10}$  ( $X_{10}, Y_{10}, Z_{10}$ ). As trees are located according to two-dimensional coordinates [33, 57], the coordinates of  $P_n$  ( $X_n, Y_n$ ) only need to be obtained to locate trees in the sample plot:

$$\begin{aligned}
X_n &= \frac{(X_1/(AP_n^2 + BP_n^2 + CP_n^2)) + (X_2/(AP_n^2 + BP_n^2 + DP_n^2)) + (X_3/(AP_n^2 + BP_n^2 + EP_n^2)) + (X_4/(AP_n^2 + CP_n^2 + DP_n^2)) + (X_5/(AP_n^2 + CP_n^2 + EP_n^2)) \\
&+ (X_6/(AP_n^2 + DP_n^2 + EP_n^2)) + (X_7/(BP_n^2 + CP_n^2 + DP_n^2)) + (X_8/(BP_n^2 + CP_n^2 + EP_n^2)) + (X_9/(BP_n^2 + DP_n^2 + EP_n^2)) + (X_{10}/(CP_n^2 + DP_n^2 + EP_n^2))}{(1/(AP_n^2 + BP_n^2 + CP_n^2)) + (1/(AP_n^2 + BP_n^2 + DP_n^2)) + (1/(AP_n^2 + BP_n^2 + EP_n^2)) + (1/(AP_n^2 + CP_n^2 + DP_n^2)) + (1/(AP_n^2 + CP_n^2 + EP_n^2)) \\
&+ (1/(AP_n^2 + DP_n^2 + EP_n^2)) + (1/(BP_n^2 + CP_n^2 + DP_n^2)) + (1/(BP_n^2 + CP_n^2 + EP_n^2)) + (1/(BP_n^2 + DP_n^2 + EP_n^2)) + (1/(CP_n^2 + DP_n^2 + EP_n^2))} \\
Y_n &= \frac{(Y_1/(AP_n^2 + BP_n^2 + CP_n^2)) + (Y_2/(AP_n^2 + BP_n^2 + DP_n^2)) + (Y_3/(AP_n^2 + BP_n^2 + EP_n^2)) + (Y_4/(AP_n^2 + CP_n^2 + DP_n^2)) + (Y_5/(AP_n^2 + CP_n^2 + EP_n^2)) \\
&+ (Y_6/(AP_n^2 + DP_n^2 + EP_n^2)) + (Y_7/(BP_n^2 + CP_n^2 + DP_n^2)) + (Y_8/(BP_n^2 + CP_n^2 + EP_n^2)) + (Y_9/(BP_n^2 + DP_n^2 + EP_n^2)) + (Y_{10}/(CP_n^2 + DP_n^2 + EP_n^2))}{(1/(AP_n^2 + BP_n^2 + CP_n^2)) + (1/(AP_n^2 + BP_n^2 + DP_n^2)) + (1/(AP_n^2 + BP_n^2 + EP_n^2)) + (1/(AP_n^2 + CP_n^2 + DP_n^2)) + (1/(AP_n^2 + CP_n^2 + EP_n^2)) \\
&+ (1/(AP_n^2 + DP_n^2 + EP_n^2)) + (1/(BP_n^2 + CP_n^2 + DP_n^2)) + (1/(BP_n^2 + CP_n^2 + EP_n^2)) + (1/(BP_n^2 + DP_n^2 + EP_n^2)) + (1/(CP_n^2 + DP_n^2 + EP_n^2))}
\end{aligned} \tag{9}$$

where

$$\begin{aligned}
&\frac{1/(AP_n^2 + BP_n^2 + CP_n^2)}{(1/(AP_n^2 + BP_n^2 + CP_n^2)) + (1/(AP_n^2 + BP_n^2 + DP_n^2)) + (1/(AP_n^2 + BP_n^2 + EP_n^2)) + (1/(AP_n^2 + CP_n^2 + DP_n^2)) + (1/(AP_n^2 + CP_n^2 + EP_n^2))} \\
&+ \frac{1}{(AP_n^2 + DP_n^2 + EP_n^2)} + \frac{1}{(BP_n^2 + CP_n^2 + DP_n^2)} + \frac{1}{(BP_n^2 + CP_n^2 + EP_n^2)} + \frac{1}{(BP_n^2 + DP_n^2 + EP_n^2)} + \frac{1}{(CP_n^2 + DP_n^2 + EP_n^2)}
\end{aligned} \tag{10}$$

etc. are the weighting coefficients.

**3.2.3. Accuracy Evaluation.** The reference value of the tree position was also measured and converted into the  $xoy$  plane

coordinate system. First, the DBH was measured at 1.3 m using tape. Then, half of the tree DBH values were added to the reference and estimated position values of the plane coordinates in the  $y$ -axis and  $x$ -axis directions, respectively.

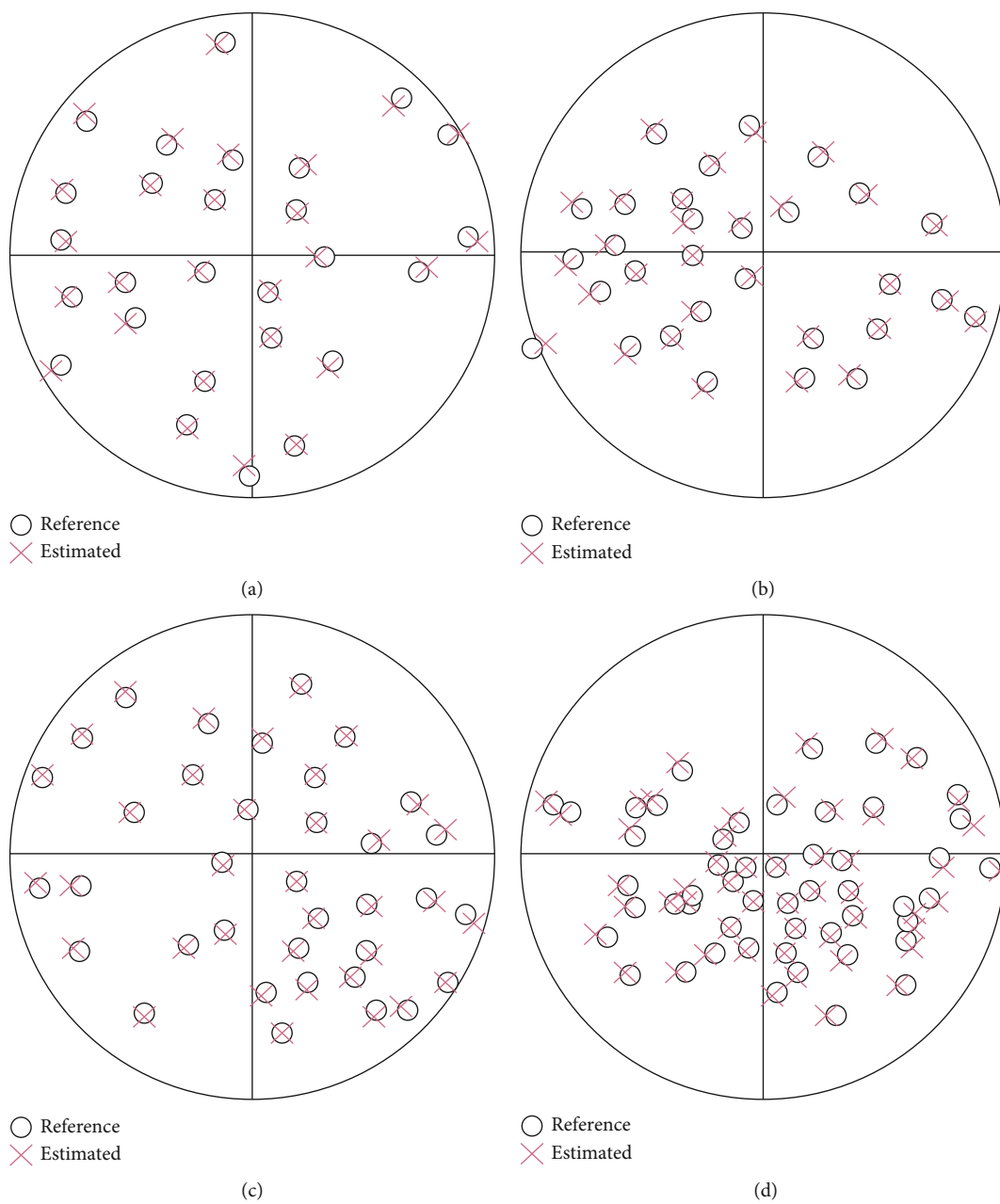


FIGURE 11: Continued.

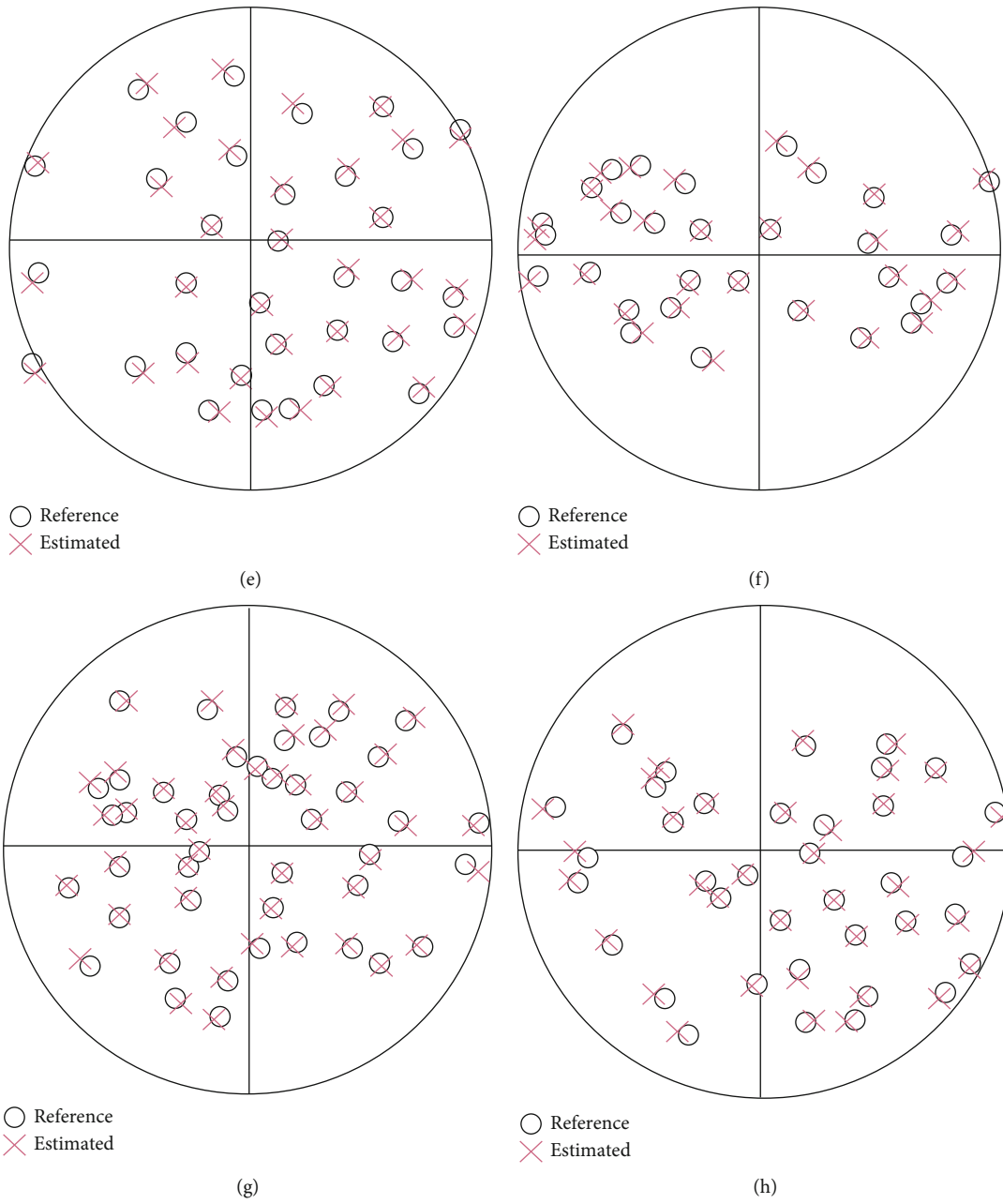


FIGURE 11: Continued.

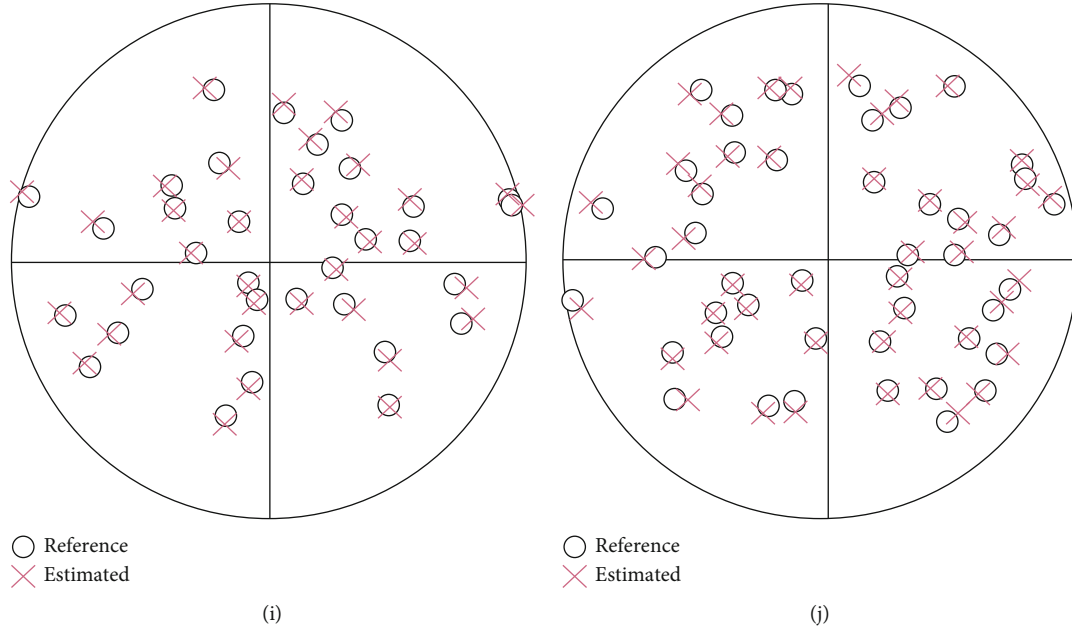


FIGURE 11: Comparisons of estimated and reference points: (a) plot 1; (b) plot 2; (c) plot 3; (d) plot 4; (e) plot 5; (f) plot 6; (g) plot 7; (h) plot 8; (i) plot 9; (j) plot 10.

TABLE 3: Accuracy in the  $x$ -axis and  $y$ -axis directions estimated by the device.

Plot	X (cm)		Y (cm)	
	BIAS	RMSE	BIAS	RMSE
1	-4.85	20.79	4.11	22.41
2	-3.97	24.10	2.23	21.09
3	-3.37	37.33	5.28	33.27
4	4.46	32.58	2.61	34.80
5	-6.99	29.19	-1.22	30.48
6	-8.05	27.85	2.74	27.90
7	-2.22	27.19	0.77	30.76
8	-6.39	28.50	1.35	30.02
9	-6.41	32.07	3.98	30.60
10	-1.65	24.34	9.34	23.93
Total	-3.94	28.39	3.36	28.53

TABLE 4: Summary statistics of the error of the distance between estimated and reference points.

Plot	Ed (cm)			
	Mean	Max	Min	Std
1	26.63	58.53	1.39	15.01
2	29.28	59.79	1.03	12.97
3	46.63	73.55	5.27	18.05
4	43.36	80.65	12.16	19.81
5	37.86	82.73	4.33	18.66
6	35.57	77.81	8.92	17.01
7	37.54	63.60	6.03	16.63
8	37.49	77.11	7.64	17.55
9	40.72	81.30	10.75	17.52
10	31.38	71.01	8.79	13.44
Total	36.13	82.73	1.03	16.67

According to Equations (11), (12), and (13), the bias, root mean square error (RMSE), and straight-line distance error between the estimation point and the reference point on the  $x$ - and  $y$ -axes were calculated separately to evaluate the accuracy of the method:

$$\text{BIAS} = \frac{\sum_{i=1}^n (d_i - D_{ir})}{n}, \quad (11)$$

$$\text{RMSE} = \sqrt{\frac{\sum_{i=1}^n (d_i - D_{ir})^2}{n}}, \quad (12)$$

$$\text{Ed} = \sqrt{(X_i - X_{ir})^2 + (Y_i - Y_{ir})^2}, \quad (13)$$

where  $d_i$  is the  $i$ th measured value,  $D_{ir}$  is the  $i$ th reference value,  $X_i$  and  $Y_i$  are the  $i$ th estimates on the  $x$ -axis and  $y$ -axis, respectively,  $X_{ir}$  and  $Y_{ir}$  are the  $i$ th reference values on the  $x$ -axis and  $y$ -axis, respectively, and  $n$  is the total number of measurements.

**3.2.4. Efficiency Evaluation.** To evaluate the efficiency of measurement, the times required for traditional and device measurement were recorded. To ensure that the two methods worked in the same order, the trees were numbered prior to measurement. Using the theodolite with a laser rangefinder measurement requires two people in a group: one stands in the middle of the circle to operate the theodolite with laser rangefinder correctly and then records the distances and angles from the center of the



TABLE 5: Comparison of work efficiency.

Method	Number of surveyors	Times of measurement	Total time (s)	Mean time (s)
Theodolite with a laser rangefinder	2	1	25880.96	69.76
UWB device	1	1	8299.27	22.37

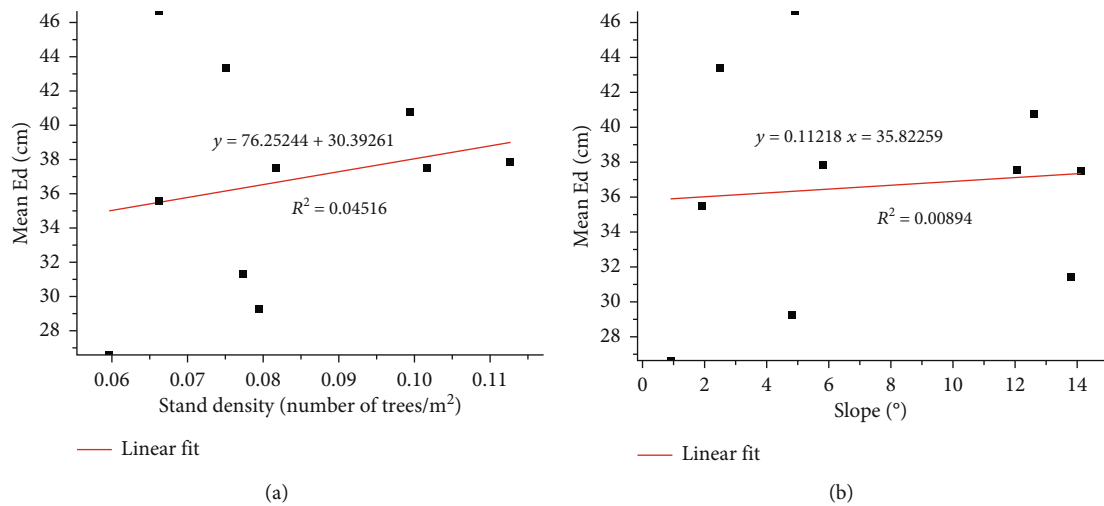


FIGURE 12: Scatter plot between mean Ed and (a) stand density and (b) slope.

circle plot (the angles to due north) and the other holds a surveyor's pole at the tree position. After the measurement is completed, the data recorded on a paper form is entered into the computer. When using the device for measurements, one person performs ranging and recording integration.

## 4. Results

**4.1. Accuracy of Position Measurement.** The error distribution and comparison results between the estimated points and the reference points are shown in Figures 10 and 11, respectively. The statistical results of the coordinate accuracy on the  $x$ -axis and  $y$ -axis and the statistical results of the linear distance errors between the estimated point and the reference point are shown in Tables 3 and 4, respectively. The results showed that the bias, RMSE, and total bias on the  $x$ - and  $y$ -axes were  $-8.05$  to  $4.46$  cm and  $-1.22$  cm to  $9.34$  cm,  $20.79$  to  $37.33$  cm and  $21.09$  to  $34.80$  cm, and  $-3.94$  and  $3.36$  cm, respectively (Table 3). The mean Ed was  $36.13$  cm, the maximum Ed was  $82.73$  cm, the minimum Ed was  $1.03$  cm, and the standard deviation was  $16.67$  cm (Table 4). The Ed range of the estimated points and the reference points in the  $xy$  plane was  $0$  cm to  $83$  cm (Figure 10). Systematic error was observed between the estimated values and the reference values of each sample plot, although the total error was small (Figure 11). The mean Ed values in the sample plots from 1 to 6 and 7 to 10 were  $36.55$  cm and  $36.78$  cm, respectively, indicating that the slope of the measured sample plot had no significant influence on the location.

**4.2. Efficiency of Position Measurement.** The measurement times of the two methods are shown in Table 5. The results

showed that the mean measurement times were  $22.37$  and  $69.76$  s using the device and traditional methods, respectively. The measurement efficiency can be increased more than threefold using the proposed method.

## 5. Discussion

Tree position measurement is an important task in forest resource surveys. In recent years, a large number of tree location devices and methods have been reported. The Haglöf Postex<sup>®</sup> Laser, which was similar to the developed device, used an ultrasonic solution for position measurements, but ultrasound had a short measurement range and was not suitable for measurements of large sample plots. In addition, the device was not cheap [11]. Oveland et al. [18] proposed a positioning scheme under relatively rough conditions using a moving terrestrial laser scanner and GNSS. However, due to the serious attenuation of GNSS signals under the crown, this scheme was not suitable for accurate tree positioning; moreover, the devices were also expensive. Gollob et al. [30] located tree trunk positions using a terrestrial laser scanner; however, the data processing was complex and the device was hard to carry and thus was unsuitable for widespread application in forestry. Fan et al. [33] estimated tree position using an RGB-D smartphone combined with the simultaneous localization and mapping (SLAM) algorithm, and the results showed that the biases on the  $x$ - and  $y$ -axes were the same ( $-0.12$  to  $0.13$  m) while the RMSEs were  $0.09$  m to  $0.17$  m and  $0.07$  m to  $0.17$  m, respectively. Although this method had high positioning accuracy, it was highly susceptible to the influence of the surrounding environment and requires professional training to handle the complex point

cloud processing. Our device only used the RSSI algorithm and pentagonal localization algorithm, which could be run on STC15 (8-bit) microprocessors (price under \$1) and had much lower complexity in both time and space.

In this study, we designed a tree positioning device (cost of approximately \$250) using UWB sensors. To test the estimation accuracy, we chose 10 circular plots with a diameter of 24 m to carry out our experiment. The results showed that the  $x$ - and  $y$ -axes had biases of -8.05 to 4.46 cm and -1.22 cm to 9.34 cm, respectively. The RMSEs of the  $x$ - and  $y$ -axes were 20.79 to 37.33 cm and 21.09 to 34.80 cm, respectively (Table 3). The mean error (Ed) and standard deviation of the distance between the estimated points and the reference points were 36.13 and 16.67 cm, respectively (Table 4). In terms of measurement efficiency, the traditional method required two people to complete the work and the data need to be recorded manually. However, the proposed device could be operated by one person and equipped with corresponding host computer software that integrated data measurement, recording, and uploading. The mean times required by the traditional method and the proposed device were 69.76 s and 22.37 s, respectively (Table 5). The device could locate trees accurately, and the measuring efficiency could be improved by more than three times.

Although the proposed device accurately located trees, considerable improvements remain to be made. For example, the maximum distance between the two anchor points was 2 m, which precludes the device's deployment in sample plots with high stand density. Note that using the device to measure the tree position may be affected by the plot environment. Compared with the slope, the stand density was more influential (Figure 12 and Table 2). In future research, we will ensure the positioning precision to reduce the size of the base station and conduct deeper research in a variety of complex sample environments to identify methods that can improve the positioning accuracy and reduce the impact of the plot environment on ranging.

## 6. Conclusions

This paper reports a novel device that uses UWB sensor technology to locate trees. It has a delicate mechanical structure and is based on trilateration and quadrilateral localization. A pentagonal localization algorithm was constructed to precisely locate trees. Through the host computer software, it performs data measurement, recording, and uploading integration, which increases the measurement efficiency more than three times compared to the traditional method.

## Data Availability

The data used to support the findings of this study are available from the corresponding author upon request.

## Conflicts of Interest

The authors declare no conflict of interest.

## Acknowledgments

This work was financially supported by Science and Technology Program of Zhejiang Province (2018C02013) and New Seedling Talent Project of Zhejiang Province (2020R412045).

## References

- [1] M. Mokoř, J. Výbořtok, J. Tomařtik et al., "High precision individual tree diameter and perimeter estimation from close-range photogrammetry," *Forests*, vol. 9, p. 696, 2018.
- [2] M. Mokoř, X. Liang, P. Surovy et al., "Evaluation of close-range photogrammetry image collection methods for estimating tree diameters," *ISPRS International Journal of Geo-Information*, vol. 7, no. 3, p. 93, 2018.
- [3] J. A. Kershaw, M. J. Ducey, T. W. Beers, and B. Husch, *Forest mensuration*, John Wiley & Sons, Ltd., Chichester, UK, 2016.
- [4] H. Kramer and A. Akça, *Leitfaden zur Waldmesslehre*, J. D. Sauerlanderverslag, Bad Orb, Germany, 2008.
- [5] J. B. Kuffman, V. B. Arifanti, I. Basuki et al., *Protocols for the Measurement, Monitoring, and Reporting of Structure, Biomass, Carbon Stocks and Greenhouse Gas Emissions in Tropical Peat Swamp Forests*, Center for International Forestry Research (CIFOR), Bogor, Indonesia, 2017.
- [6] M. Kohl, S. Magnussen, and M. Marchetti, *Sampling Methods, Remote Sensing and GIS Multiresource Forest Inventory; Tropical Forestry*, Springer Berlin Heidelberg, Berlin, Heidelberg, 2006.
- [7] X. Liang, A. Kukko, J. Hyypa et al., "In-situ measurements from mobile platforms: an emerging approach to address the old challenges associated with forest inventories," *ISPRS Journal of Photogrammetry and Remote Sensing*, vol. 143, pp. 97–107, 2018.
- [8] X. Liang, V. Kankare, J. Hyypa et al., "Terrestrial laser scanning in forest inventories," *ISPRS Journal of Photogrammetry and Remote Sensing*, vol. 115, pp. 63–77, 2016.
- [9] X. Liang, J. Hyypa, H. Kaartinen et al., "International benchmarking of terrestrial laser scanning approaches for forest inventories," *ISPRS Journal of Photogrammetry and Remote Sensing*, vol. 144, pp. 137–179, 2018.
- [10] T. Ritter, M. Schwarz, A. Tockner, F. Leisch, and A. Nothdurft, "Automatic mapping of forest stands based on three-dimensional point clouds derived from terrestrial laser-scanning," *Forests*, vol. 8, no. 8, p. 265, 2017.
- [11] HaglofSweden, *Haglof Postex® Laser*, 2021, <https://haglofsweden.com/project/postex-laser/>.
- [12] J. Ryding, E. Williams, M. Smith, and M. Eichhorn, "Assessing handheld mobile laser scanners for forest surveys," *Remote Sensing*, vol. 7, no. 1, pp. 1095–1111, 2015.
- [13] S. Bauwens, H. Bartholomeus, K. Calders, and P. Lejeune, "Forest inventory with terrestrial LiDAR: a comparison of static and hand-held mobile laser scanning," *Forests*, vol. 7, no. 12, p. 127, 2016.
- [14] C. Cabo, S. Del Pozo, P. Rodriguez-Gonzalvez, C. Ordonez, and D. Gonzalez-Aguilera, "Comparing terrestrial laser scanning (TLS) and wearable laser scanning (WLS) for individual tree modeling at plot level," *Remote Sensing*, vol. 10, no. 4, p. 540, 2018.
- [15] B. Del Perugia, F. Giannetti, G. Chirici, and D. Travaglini, "Influence of scan density on the estimation of single-tree attributes by

- hand-held mobile laser scanning,” *Forests*, vol. 10, no. 3, p. 277, 2019.
- [16] S. Chen, H. Liu, Z. Feng, C. Shen, and P. Chen, “Applicability of personal laser scanning in forestry inventory,” *PLoS One*, vol. 14, no. 2, article e0211392, 2019.
- [17] A. Kukko, R. Kaijaluoto, H. Kaartinen, V. V. Lehtola, A. Jaakkola, and J. Hyypä, “Graph SLAM correction for single scanner MLS forest data under boreal forest canopy,” *ISPRS Journal of Photogrammetry and Remote Sensing*, vol. 132, pp. 199–209, 2017.
- [18] I. Oveland, M. Hauglin, T. Gobakken, E. Næsset, and I. Maalen-Johansen, “Automatic estimation of tree position and stem diameter using a moving terrestrial laser scanner,” *Remote Sensing*, vol. 9, no. 4, p. 350, 2017.
- [19] X. Liang and J. Hyypä, “Automatic stem mapping by merging several terrestrial laser scans at the feature and decision levels,” *Sensors*, vol. 13, no. 2, pp. 1614–1634, 2013.
- [20] P. J. Watt and D. N. M. Donoghue, “Measuring forest structure with terrestrial laser scanning,” *International Journal of Remote Sensing*, vol. 26, no. 7, pp. 1437–1446, 2005.
- [21] C. Vonderach, T. Vögtle, P. Adler, and S. Norra, “Terrestrial laser scanning for estimating urban tree volume and carbon content,” *International Journal of Remote Sensing*, vol. 33, no. 21, pp. 6652–6667, 2012.
- [22] J. Liu, X. Liang, J. Hyypä et al., “Automated matching of multiple terrestrial laser scans for stem mapping without the use of artificial references,” *International Journal of Applied Earth Observation and Geoinformation*, vol. 56, pp. 13–23, 2017.
- [23] T. Ritter and A. Nothdurft, “Automatic assessment of crown projection area on single trees and stand-level, based on three-dimensional point clouds derived from terrestrial laser-scanning,” *Forests*, vol. 9, no. 5, p. 237, 2018.
- [24] L. M. Moskal and G. Zheng, “Retrieving forest inventory variables with terrestrial laser scanning (TLS) in urban heterogeneous forest,” *Remote Sensing*, vol. 4, no. 1, pp. 1–20, 2012.
- [25] X. Liang, P. Litkey, J. Hyypä, H. Kaartinen, M. Vastaranta, and M. Holopainen, “Automatic stem mapping using single-scan terrestrial laser scanning,” *IEEE Transactions on Geoscience and Remote Sensing*, vol. 50, no. 2, pp. 661–670, 2012.
- [26] M. Béland, J.-L. Widlowski, R. A. Fournier, J.-F. Côté, and M. M. Verstraete, “Estimating leaf area distribution in savanna trees from terrestrial LiDAR measurements,” *Agricultural and Forest Meteorology*, vol. 151, no. 9, pp. 1252–1266, 2011.
- [27] H. M. Rizzei, H. Z. M. Shafri, M. A. Mohamoud, B. Pradhan, and B. Kalantar, “Oil palm counting and age estimation from worldview-3 imagery and LiDAR data using an integrated OBIA height model and regression analysis,” *Journal of Sensors*, pp. 1–13, 2018.
- [28] S. Srinivasan, S. Popescu, M. Eriksson, R. Sheridan, and N.-W. Ku, “Terrestrial laser scanning as an effective tool to retrieve tree level height, crown width, and stem diameter,” *Remote Sensing*, vol. 7, no. 2, pp. 1877–1896, 2015.
- [29] P. Pueschel, G. Newnham, G. Rock, T. Udelhoven, W. Werner, and J. Hill, “The influence of scan mode and circle fitting on tree stem detection, stem diameter and volume extraction from terrestrial laser scans,” *ISPRS Journal of Photogrammetry and Remote Sensing*, vol. 77, pp. 44–56, 2013.
- [30] C. Gollob, T. Ritter, C. Wassermann, and A. Nothdurft, “Influence of scanner position and plot size on the accuracy of tree detection and diameter estimation using terrestrial laser scanning on forest inventory plots,” *Remote Sensing*, vol. 11, no. 13, article 1602, 2019.
- [31] J. Hyypä, J.-P. Virtanen, A. Jaakkola, X. Yu, H. Hyypä, and X. Liang, “Feasibility of Google Tango and Kinect for crowdsourcing forestry information,” *Forests*, vol. 9, p. 6, 2018.
- [32] J. Tomašík, Š. Saloň, D. Tunák, F. Chudý, and M. Kardoš, “Tango in forests - an initial experience of the use of the new Google technology in connection with forest inventory tasks,” *Computers and Electronics in Agriculture*, vol. 141, pp. 109–117, 2017.
- [33] Y. Fan, Z. Feng, A. Mannan, T. Ullah Khan, C. Shen, and S. Saeed, “Estimating tree position, diameter at breast height, and tree height in real-time using a mobile phone with RGB-D SLAM,” *Remote Sensing*, vol. 10, no. 11, article 1845, 2018.
- [34] T. Mikita, P. Janata, and P. Surový, “Forest stand inventory based on combined aerial and terrestrial close-range photogrammetry,” *Forests*, vol. 7, no. 12, p. 165, 2016.
- [35] L. Sun, L. Fang, L. Tang, and J. Liu, “Developing portable system for measuring diameter at breast height,” *Journal of Beijing Forestry University*, vol. 40, pp. 82–89, 2018.
- [36] P. Surový, A. Yoshimoto, and D. Panagiotidis, “Accuracy of reconstruction of the tree stem surface using terrestrial close-range photogrammetry,” *Remote Sensing*, vol. 8, no. 2, p. 123, 2016.
- [37] M. Forsman, N. Börlin, and J. Holmgren, “Estimation of tree stem attributes using terrestrial photogrammetry with a camera rig,” *Forests*, vol. 7, no. 12, p. 61, 2016.
- [38] S. Sun, J. Hu, J. Li, R. Liu, M. Shu, and Y. Yang, “An INS-UWB based collision avoidance system for AGV,” *Algorithms*, vol. 12, no. 2, p. 40, 2019.
- [39] C. Baard, Y. Liu, and N. Nikolova, “Ultra-wideband low-cost high-efficiency cavity-backed compound spiral antenna,” *Electronics*, vol. 9, no. 9, article 1399, 2020.
- [40] J. Jung, Y. Choi, and Y. Kwon, “Location-aware point-to-point RPL in indoor IR-UWB networks,” *Electronics*, vol. 9, no. 5, p. 861, 2020.
- [41] X. Hu, Z. Luo, and W. Jiang, “AGV localization system based on ultra-wideband and vision guidance,” *Electronics*, vol. 9, no. 3, p. 448, 2020.
- [42] M.-H. Weng, F.-Z. Zheng, H.-Z. Lai, and S.-K. Liu, “Compact ultra-wideband bandpass filters achieved by using a stub-loaded stepped impedance resonator,” *Electronics*, vol. 9, no. 2, p. 209, 2020.
- [43] S. Monica and G. Ferrari, “Impact of the number of beacons in PSO-based auto-localization in UWB networks,” in *Applications of Evolutionary Computation; Lecture Notes in Computer Science, Volume 7835*, pp. 42–51, Springer, Berlin/Heidelberg, Germany, 2013.
- [44] S. Krishnan, P. Sharma, Z. Guoping, and O. H. Woon, “A UWB based localization system for indoor robot navigation,” in *2007 IEEE International Conference on Ultra-Wideband*, pp. 77–82, Singapore, September 2007.
- [45] S. Monica and F. Bergenti, “A comparison of accurate indoor localization of static targets via WiFi and UWB ranging,” in *Trends in Practical Applications of Scalable Multi-Agent Systems; Lecture Notes in Computer Science, Volume 9662*, pp. 111–123, Springer, Cham, Switzerland, 2016.
- [46] R. Matteo, V. D. V. Samuel, S. Heidi, and E. De Poorter, “Analysis of the scalability of UWB indoor localization solutions for high user densities,” *Sensors*, vol. 18, article 1875, 2018.

- [47] H. Xiaoping, W. Fei, Z. Jian, Z. Hu, and J. Jin, "A posture recognition method based on indoor positioning technology," *Sensors*, vol. 19, article 1464, 2019.
- [48] J. He, Y. Wu, S. Duan et al., "Model of human body influence on UWB ranging error," *The Journal of Communication*, vol. 38, pp. 58–66, 2017.
- [49] S. Juri, S. Volker, S. Norbert, M. Arensa, and U. Hugentobler, "Decawave UWB clock drift correction and power-self-calibration," *Sensors*, vol. 19, article 2942, 2019.
- [50] S. Hamdoun, A. Rachedi, and A. Benslimane, "Comparative analysis of RSSI-based indoor localization when using multiple antennas in wireless sensor networks," in *2013 International Conference on Selected Topics in Mobile and Wireless Networking (MoWNeT)*, pp. 146–151, Montreal, QC, Canada, August 2013.
- [51] X. Zhu and Y. Feng, "RSSI-based algorithm for indoor localization," *Communications and Network*, vol. 5, no. 2, pp. 37–42, 2013.
- [52] V. Barral, C. J. Escudero, J. A. García-Naya, and R. Maneiro-Catoira, "NLOS identification and mitigation using low-cost UWB devices," *Sensors*, vol. 19, no. 16, article 3464, 2019.
- [53] A. Harter, A. Hopper, P. Steggles, A. Ward, and P. Webster, "The anatomy of a context-aware application," *Wireless Networks*, vol. 8, no. 2/3, pp. 187–197, 2002.
- [54] M. Stefania and B. Federico, "Hybrid indoor localization using WiFi and UWB technologies," *Electronics*, vol. 8, p. 334, 2019.
- [55] J. Wen, J. Jin, and H. Yuan, "Quadrilateral localization algorithm for wireless sensor networks," *Transducer and Microsystem Technologies*, vol. 27, pp. 108–110, 2008.
- [56] H. Gao and L. Xu, "Tightly-coupled vehicle positioning method at intersections aided by UWB," *Sensors*, vol. 19, no. 13, article 2867, 2019.
- [57] L. Sun, L. Fang, Y. Weng, and S. Zheng, "An integrated method for coding trees, measuring tree diameter, and estimating tree positions," *Sensors*, vol. 20, p. 144, 2020.

## Research Article

# Canopy Extraction and Height Estimation of Trees in a Shelter Forest Based on Fusion of an Airborne Multispectral Image and Photogrammetric Point Cloud

Xuewen Wang <sup>1,2,3</sup>, Qingzhan Zhao <sup>1,2,3</sup>, Feng Han,<sup>1,2</sup> Jianxin Zhang,<sup>4</sup> and Ping Jiang<sup>3,5</sup>

<sup>1</sup>College of Information Science & Technology, Shihezi University, Shihezi, China

<sup>2</sup>Geospatial Information Engineering Research Center, Xinjiang Production and Construction Corps, Shihezi, China

<sup>3</sup>Industrial Technology Research Institute, Xinjiang Production and Construction Corps, Shihezi, China

<sup>4</sup>Agricultural Development Service Center of 150 Regiments, Shihezi, China

<sup>5</sup>College of Mechanical and Electrical Engineering, Shihezi University, Shihezi, China

Correspondence should be addressed to Qingzhan Zhao; [zqz\\_inf@shzu.edu.cn](mailto:zqz_inf@shzu.edu.cn)

Received 27 January 2021; Revised 25 April 2021; Accepted 19 May 2021; Published 28 June 2021

Academic Editor: Bahareh Kalantar

Copyright © 2021 Xuewen Wang et al. This is an open access article distributed under the Creative Commons Attribution License, which permits unrestricted use, distribution, and reproduction in any medium, provided the original work is properly cited.

To reduce data acquisition cost, this study proposed a novel method of individual tree height estimation and canopy extraction based on fusion of an airborne multispectral image and photogrammetric point cloud. A fixed-wing drone was deployed to acquire the true color and multispectral images of a shelter forest. The Structure-from-Motion (SfM) algorithm was used to reconstruct the 3D point cloud of the canopy. The 3D point cloud was filtered to acquire the ground point cloud and then interpolated to a Digital Elevation Model (DEM) using the Radial Basis Function Neural Network (RBFNN). The DEM was subtracted from the Digital Surface Model (DSM) generated from the original point cloud to get the canopy height model (CHM). The CHM was processed for the crown extraction using local maximum filters and watershed segmentation. Then, object-oriented methods were employed in the combination of 12 bands and CHM for image segmentation. To extract the tree crown, the Support Vector Machine (SVM) algorithm was used. The result of the object-oriented method was vectorized and superimposed on the CHM to estimate the tree height. Experimental results demonstrated that it is efficient to employ point cloud and the proposed approach has great potential in the tree height estimation. The proposed object-oriented method based on fusion of a multispectral image and CHM effectively reduced the oversegmentation and undersegmentation, with an increase in the *F*-score by 0.12–0.17. Our findings provided a reference for the health and change monitoring of shelter forests as well.

## 1. Introduction

Shelter forests are considered the green barriers at the edge of deserts, which are able to prevent land desertification and provide wind proofing and sand fixation. Thus, they play an indispensable role in enhancing the self-regulation ability of the ecosystem and slowing down the expansion of land desertification. With the degradation of shelter forests due to man-made destruction and climate change, the prevention of land desertification has become more urgent [1]. To improve the ecological environment and reduce natural disasters, the Chinese government has also successively implemented ecological restoration projects aimed at pre-

venting land desertification, such as the Three-North Shelterbelt Project (TNSP) and the Grain to Green Program (GGP) [2, 3]. Therefore, monitoring the growth parameters of shelter forests has become crucial. Among these parameters, tree height is an important indicator of shelter forest structural characteristics and is essential in the estimation of canopy density and aboveground biomass [4, 5]. The rapid and accurate extraction of tree heights of shelter forests is of great significance to maintain desert ecosystems.

For the estimation of tree height, manual measurement and satellite remote sensing methods cannot cater to the needs of forestry management departments for monitoring products, such as thematic maps of tree height. Traditionally,

heights of individual trees are obtained using the ground measurement method, in which the tree height is measured with a laser range finder and other measuring equipment, allowing higher accuracy of tree height measurement results to be obtained, but consuming significant manpower and material resources [6]. The rapid development of high-resolution remote sensing technology not only improves the efficiency of the tree height estimation but also provides a wider range of data sources, including WorldView-2 [7] and GF-2 [8], which have been used to prove the potential of spaceborne satellite imagery in the estimation of tree height. For satellite data, researchers use a high-precision Digital Elevation Model (DEM) to assist in generating a canopy height model (CHM) [8–10]. But the drawbacks of DEM are obvious: low data accuracy, the highest of which is only 30 m [11], low resolution, and limited ability to display the subtle changes in the topography and generate the CHM in the forest area of the complex terrain. Xu et al. [12] built a high-precision DEM from the point cloud generated by Light Detection and Ranging (LiDAR) and then subtracted the DEM from the DSM generated from the photogrammetric point cloud to obtain CHM. LiDAR can penetrate the shelter forest canopy to the interior and the ground through laser echoes, thereby obtaining vertical forest structure information, which is beneficial to generate a high-precision DEM. However, the approach is neither economically optimal, which is because the LiDAR data is more expensive and not applicable in large-scale shelter forest monitoring. Furthermore, when there exist several influential factors, such as clouds covering, the satellite data is difficult to deliver forestry monitoring products necessary for forestry management at a specific time.

Unmanned aerial vehicle (UAV) images with a high overlap rate can generate photogrammetric point clouds with lower cost and higher economic benefits. The image data of the shelter forest is updated in real time to guarantee large-scale flight operations as planned. The CHM generated by a UAV photogrammetric point cloud shows good performance in the tree height estimation [13–15]. However, the photogrammetric point cloud is generated by image matching, and the forest structure is allowed to be reconstructed only when the distance between trees is far enough to identify the ground between and below the canopy. Moreover, the CHM generated from a UAV photogrammetric point cloud usually underestimates tree height [16, 17]. To meet economic benefits and data requirements, obtaining high-precision DEM through photogrammetric point clouds has become a key issue. In the meantime, Radial Basis Function Neural Network (RBFNN) with excellent spatial interpolation ability provides the possibility for this. RBFNN has been applied in hydrological data spatial interpolation prediction [18], soil element interpolation [19], point cloud interpolation [20], etc. Zhao et al. [20] used RBFNN to interpolate the point cloud of LiDAR, and obtained the results that the point cloud elevation prediction coefficient ( $R^2$ ) was 0.887, and the root mean square error (RMSE) was 0.168 m. The RBFNN has a high prediction accuracy for spatial data, but few studies applied it into the prediction of the elevation in the photogrammetric point cloud. Therefore, this study

focuses on the applicability of generating DEM only based on photogrammetric point clouds.

To date, many scholars have conducted researches on individual tree height estimation methods under different woodland scenarios based on the CHM generated by point cloud data. Brieger et al. [21] used UAV photogrammetric point cloud data to generate a CHM, selecting three types of stand data about sparse deciduous forest, dense deciduous forest, and dense mixed forest, and used local maximum filters (LMF) in variable window size for the tree height estimation. Huang et al. [22] used photogrammetric point clouds to generate the DEM and Digital Surface Model (DSM) through Triangulated Irregular Network (TIN) interpolation to obtain the CHM and estimated tree height with LMF. In leafless and sparse forest areas, it is found to be difficult to reconstruct the three-dimensional (3D) structure of the forest areas, resulting in low accuracy of the tree height estimation. In contrast, in forest areas with sufficient leaves, the accuracy of tree height estimation is greatly improved, confirming the significant potential of photogrammetric point clouds in the estimation of individual tree heights of shelter forests. These studies are based on the CHM generated by the point cloud for individual tree height estimation, for which, irrespective of the algorithm used, individual trees will be subject to oversegmentation and undersegmentation [21, 23]. This is more obvious in broad-leaved forests, in which the canopy of an individual tree has multiple vertices and multiple maximum values, which will cause oversegmentation.

Therefore, high accuracy of tree crown extraction is a prerequisite for the high-precision tree height estimation. The Object-Based Image Analysis (OBIA) uses the segmented object as the basic classification unit, and makes full use of the object's spectrum and texture. Compared with the traditional pixel-based classification method, it can effectively improve the classification accuracy. Franklin [24] achieved the result that overall classification accuracy of approximately 50%, 60%, and 80%, respectively, for nine commercial coniferous trees by employing pixel-based unsupervised clustering, supervised maximum likelihood classifications, and OBIA of UAV-based multispectral imagery. No matter which classification method is used, the accuracy of near-infrared spectroscopy is better than using RGB band alone, which confirms that multispectral data has a unique advantage over RGB in describing the canopy. Thus, it is theoretically possible to combine point clouds with multi/hyperspectral remote sensing images to extract tree canopy to reduce the oversegmentation and undersegmentation of individual trees.

In view of the above problems, our research objectives are to solve the problem of low DEM accuracy due to tree canopy occlusion by using RBFNN interpolation prediction, and to combine point cloud with multispectral data by using OBIA to reduce oversegmentation and undersegmentation of the canopy. Three areas are selected for experimental verification, and the main contributions of this work are listed as follows:

- (1) We have solved the problem of low DEM accuracy of the current point cloud data of the photographic point cloud in the forest with high canopy coverage

- (2) Compared with the tree crown extraction method based on CHM alone, extracting the tree crown from the multispectral images fusing DEM has obvious advantages

## 2. Study Area and Materials

**2.1. Study Area.** We selected the Three North Shelter forest area (45°10'N, 85°56'E) of 150 regiments in the north of the Mosuowan reclamation area as the study area, which is approximately 150 km north of Shihezi City, Xinjiang Uygur Autonomous Region, China (Figure 1). The regiments are located at the northern foot of the Tianshan Mountain and the south edge of Gurbantunggut Desert in the Junggar Basin and are surrounded by sand to the east, west, and north. The shelter forest is planted in a wedge shape around the edge of the desert, dominated mainly by deciduous broad-leaved forests such as *Ulmus pumila*, *Populus bolleana*, *Populus euphratica*, *Elaeagnus angustifolia*, and *Haloxylon ammodendron*, all of which are known for their drought tolerance. In addition, their strong windproof and sand fixation ability make these tree species provide excellent sand fixation and afforestation effects in arid desert areas. Furthermore, characteristics of *Ulmus pumila* and *Elaeagnus angustifolia*, such as large and dense canopy, diverse growth conditions, uneven spatial distribution, and presence of additional green plants (such as weeds) at the tree base, provide an opportunity to test the accuracy of tree height estimation against a complex background.

We selected three areas as the research area, and the characteristics of the three areas of the shelterbelt are as follows: (1) study area 1—mixed artificial forest consisting of *Ulmus pumila*, *Populus bolleana*, *Populus euphratica*, and *Elaeagnus angustifolia*, where the smaller spacing between the canopies is dense forest, as shown in Figure 1(b); (2) study area 2—sparse pure forest consisting of *Populus bolleana* which is mostly in good health, where the gap between the canopy is large, as shown in Figure 1(c); and (3) study area 3—sparse pure forest consisting of *Populus bolleana* which is mostly not in good condition, where the gap between the canopy is large, as shown in Figure 1(d).

**2.2. Remote Sensing Data Acquisition.** The UAV platform used in this study was a fixed-wing UAV CW-20 produced by JOUAV Company. It was equipped with a SONY-A7RII visible light camera and a Micro MCA12 Snap multispectral camera, which acquire visible light images and multispectral images taken as the data sources of our study. The UAV has the advantages of fully autonomous takeoff and rapid installation. It was a professional-level aerial survey UAV at a cruising speed of 26–40 m/s and with a battery life of 3 h. It was operated by a GCS-202 ground station and CWCom commander software and used Real-Time Kinematic/Post Processed Kinematic (RTK/PPK) positioning technology. The location information of the remote sensing images obtained could reach centimeter-level accuracy, and such devices have been widely used in the acquisition of remote sensing data for large-scale agriculture and forestry in China. We selected October 9, 2019 as the data acquisition date, and set a relative

flight height of 400 m and the flight coverage area of the study area as 8.48 square kilometers, which was to meet the requirements of the high-precision photogrammetry point cloud, according to the suggestion of a previous study in [25]. The lateral direction and route overlap rate was set to be 80% for the SONY-A7RII visible light camera, and the spatial resolution was 0.05 m. 1716 images were acquired to create a point cloud. To meet stitching requirements, the Micro MCA12 Snap multispectral cameras (Micro MCA12 Snap sensor band parameters are shown in Table 1) were at the settings: line overlap rate of 60%, side overlap rate of 70%, relative flight height of 400 m, and spatial resolution of 0.2 m. In addition, we set four radiation targets on the ground, with reflectivity of 3%, 22%, 48%, and 64% for future radiation correction.

**2.3. Field Measurements.** The field measurements were made on October 7, 2019. The location (including latitude and longitude coordinates) of individual trees was recorded using the geolocation function of the Aowei software which is based on Google Maps. The health (good or bad condition) of each tree was recorded, and multifunction laser distance measurement instrument (BAOSHIAN-CS600VH) was used to measure the height of individual tree whose sampling situation is shown in Figures 1(b)–1(d) and sampling number is shown in Table 2. Besides, canopy sampling numbers (number of manually delineated tree crowns in the study area) are shown in Table 2.

The recorded geographic location was imported into ArcGIS 10.6 software and any deviations were corrected. According to the similarity of species and the overall similarity between the forest stand structure of field data, including tree cover, density, and planting type, three areas were selected, so that the data would not be affected by the growth of the shelter forest. All the field measurements of the shelter forest for the three areas were collected within one week with UAV data acquisition.

## 3. Methods

The technical workflow of this research is shown in Figure 2, which includes the following steps.

**3.1. Data Preprocessing.** After the flight mission was completed, the Position and Orientation System (POS) data in the base station was sorted and imported into Pix4Dmapper 4.4.10 software for processing. After feature extraction, image matching, bundle adjustment, automatic triangulation, camera self-checking, and optimize external parameters, the image was preliminarily processed. A dense point cloud based on Structure-from-Motion (SfM) was generated by selecting the following parameters: the image scale was half (the default value) with the multiscale option selected, point density was set to be optimal, and the minimum number of matches was 3. This operation resulted in a photogrammetric point cloud data in LAS format and generated orthophotos with a spatial resolution of 0.05 m. Photogrammetric point cloud was imported into Terrasolid software to go through such processes: first, noise was removed from the point cloud



FIGURE 1: Schematic diagram of the study area: (a) the area acquired by the unmanned aerial vehicle (UAV) visible light camera; (b) study area 1 and its sampling locations; (c) study area 2 and its sampling locations; (d) study area 3 and its sampling locations.

TABLE 1: The band feature parameters of the Micro MCA12 Snap sensor [26].

Band	Wavelength (nm)	Wavewidth (nm)	Band characteristics
1	470	10	Distinguish vegetation and soil rock surface
2	515	10	Green wave peaks in the visible light spectrum
3	550	10	Sensitive to changes in water quality
4	610	10	Initial band of red light in the vegetation spectral reflection curve
5	656	10	Renormalized vegetation index
6	710	10	Red edge band of the vegetation spectral reflection curve
7	760	10	Red edge band of the vegetation spectral reflection curve
8	800	10	Normalized vegetation index
9	830	10	Different types of vegetation
10	860	10	Significantly correlated with plant total chlorophyll content
11	900	20	Calculation of the specific crop water sensitivity index
12	950	40	Calculate the water band index

data, and then the point cloud filtering was performed using the TIN densification filtering method built into the Terrasolid software to derive the ground point cloud. Using the generated original photogrammetric point cloud, through Inverse Distance Weighted (IDW) interpolation operation of ArcGIS 10.6 software, a DSM of 0.2 m resolution was generated.

The acquired original multispectral images were exported in RAW format, and Tetracam PixelWrench2 software was used to convert them into standard TIFF format raster image data. The one-to-one correspondence between the POS and the image was performed in the Pix4Dmapper 4.4.10 software to obtain multispectral image data with 0.2 m spatial



TABLE 2: Sampling statistics in the study area.

Study area	Tree height sampling number	Average tree height (m)	Maximum tree height (m)	Minimum tree height (m)	Number of manually delineated tree crowns
1	19	8.02	12.40	4.00	457
2	20	4.01	6.40	2.70	694
3	21	5.77	9.50	2.60	315

resolution. Radiometric correction was performed on ortho-photos that had been stitched together, and the relationship between the actual digital quantization value (DN) of the UAV multispectral image and the ground reflectance (Ref) is

$$\text{Ref} = \text{DN} \times a + b, \quad (1)$$

where  $a$  is the scaling gain coefficient and  $b$  is the offset value.

According to the calibration equation, the DN values of the four target images on the ground were calculated by drawing the area of interest, corresponding to the standard reflectance values of the four targets. The least square method was used to fit the empirical linear model. This operation provided the coefficients  $a$  and  $b$  of the UAV Micro MCA12 Snap multispectrometer radiation calibration. Based on the visible light image, 30–40 control points were selected, and the corrected multispectral image data was geographically registered in ArcGIS 10.6 software for subsequent canopy segmentation.

**3.2. RBFNN Predictive Interpolation Generates DEM.** RBFNN [27, 28] can usually be used for classification or spatial data interpolation. Due to its advantages of simple structure, fast learning speed, and not easily falling into a local minimum, it was often used in spatial data interpolation prediction [29]. RBFNN has been applied to generate DEM through the interpolation of airborne LiDAR point cloud, which is also trying to generate DEM in the photogrammetric point cloud [30]. Therefore, we used the network to take the ground point cloud obtained by filtering as an input and interpolated each point to generate the height value. RBFNN is usually composed of an input layer, a hidden layer, and an output layer (Figure 3).

The output formula is

$$f(I) = \sum_{i=1}^m W_i D_i(I). \quad (2)$$

We usually describe  $D_i(I)$  as

$$D_i(I) = \exp\left(-\frac{\|I - C_i\|^2}{2r_i^2}\right), \quad (3)$$

where  $f(I)$  is the output layer function of RBFNN,  $W_i$  is the weight of the sample  $i$  hidden neuron to the neuron of the output layer,  $D_i(I)$  uses the Gaussian function,  $C_i$  is the center of the basis function in the sample  $i$  hidden layer neuron, and  $r_i$  is the width of the cell of the sample  $i$  hidden layer neuron.

The DEM with a resolution of 0.2 m was generated from the ground point cloud which was produced by RBFNN interpolation, and the CHM was obtained by subtracting it from the DSM (Figure 4).

**3.3. Multispectral Image Combined with CHM Canopy Extraction.** The selected three areas had a variety of features such as bare soil, shadows, and weeds around the canopy, which made it difficult to extract the canopy. In order to describe the canopies of individual shelter forests, this study proposed an OBIA method based on fusion of multisource data (FMSD-OBIA) to identify the canopy. The traditional pixel-based supervised classification method is based on statistical spectral features, in which the selected sample feature values were clustered to obtain pixel-level classification results. The improvement of image resolution resulted in the spectral feature of a single pixel and the reduced texture information. The OBIA method was based on the characteristics of spectral, texture, shape, etc., divided into regions or sets, which was more applicable to high-resolution image data. In this paper, we used the multispectral sensor Micro MCA12 Snap equipped with two bands of red edges. The red edges had a high sensitivity to vegetation, which could reflect the spectral characteristics of vegetation better, and had certain advantages in the classification of vegetation. Twelve original bands and the CHM were selected for combination, and the tree crown was extracted based on the FMSD-OBIA method.

Segmentation and classification operations of FMSD-OBIA were carried out in ENVI 5.3, including three main steps: segmentation, merging, and supervised classification. Reasonable segmentation and merging scales are very important in FMSD-OBIA methods. If the scales of segmentation are too large, results of the method will be subject to merge and recognize smaller tree crowns, otherwise, results of the methods will be subject to divide larger tree crowns into considerable multiple parts and broken patches. In ENVI 5.3, the edge algorithm was selected for segmentation, the full lambda schedule algorithm was selected for merging, and through repeated experiments, FMSD-OBIA parameters were selected (Table 3).  $K$ -Nearest Neighbor (KNN) and Support Vector Machine (SVM), the supervised versions of the algorithms, were typically used in the following FMSD-OBIA segmentation. SVM is an excellent small sample learning algorithm, which has shown good robustness in remote sensing image classification. In this study, tree canopy and other object (considered as background) were classified into two categories, and the training samples (70% of all manually delineated canopies) were selected by using the sigmoid kernel function. The SVM algorithm performed the supervised classification and obtained the crown vector image.

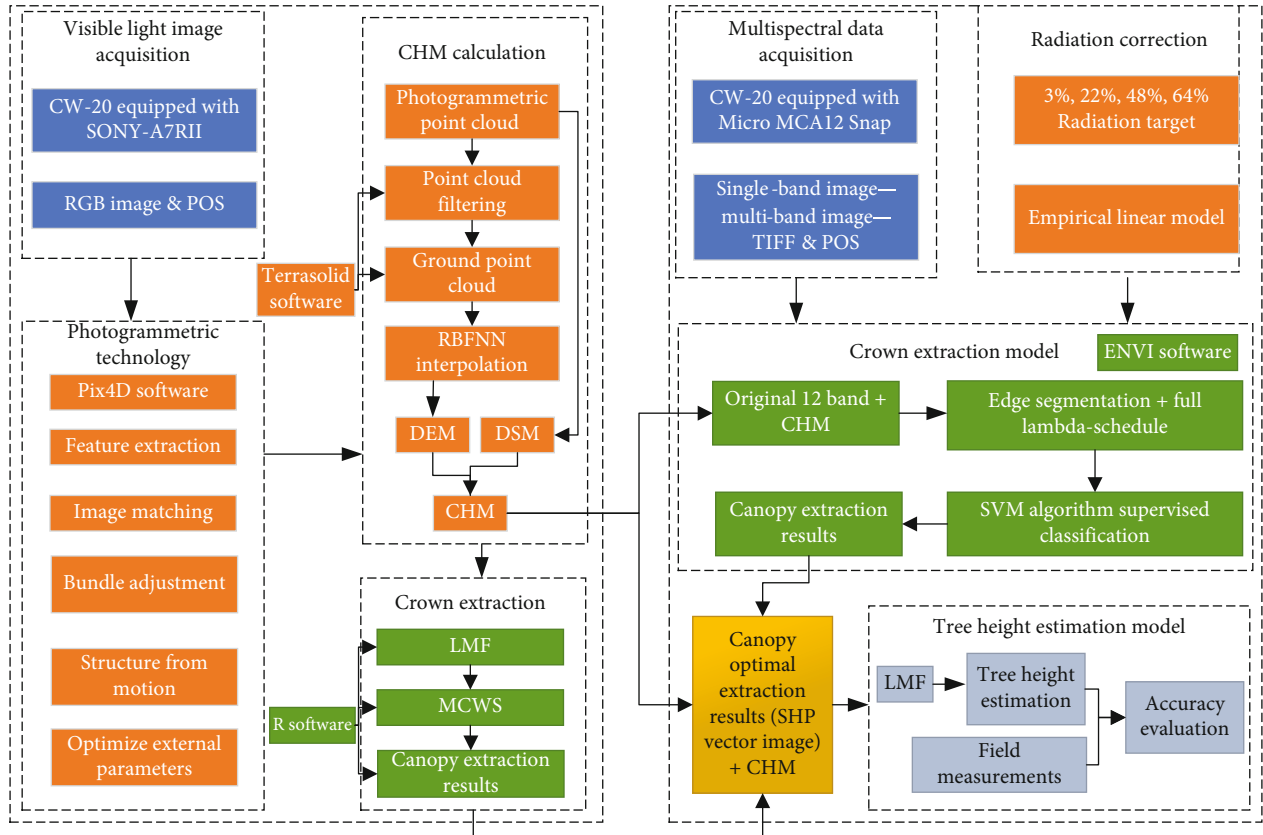


FIGURE 2: Workflow of the height estimation of the shelter forest based on the UAV photogrammetry fusion multispectral image.

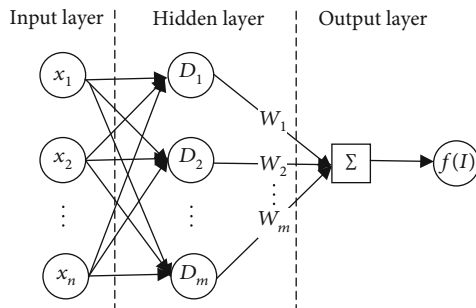


FIGURE 3: Architecture of the RBFNN.

**3.4. Canopy Extraction Based on CHM and Tree Height Estimation.** Based on the CHM, R-package ForestTools (<https://github.com/AndyPL22/ForestTools>, Plowright, 2020) [31] was used to complete the position detection and canopy area division of individual shelter forests. We used Variable Window Filter (VWF), a single-tree detection function that is an LMF based on a dynamic circular moving window [32]. Since the crown size of different trees was different, various linear functions were needed to be used. The height value of pixels was used to estimate the radius of the search window. According to the suggestion of a previous study in [21], when the crown of trees was narrow, a smaller search radius was suggested to be used, while when the crown of trees was larger, a larger search radius was suggested. Through repeated experiments, the

search radius of the study area was selected, as shown in Table 4.

Then, the marker-controlled Inverse Watershed Segmentation (MCWS) method was used to explore the tree crown size based on the detected tree crown vertices. The watershed algorithm [33] was proposed by Vincent, whose basic idea was to treat the image as a topographic map, in which each gray value in the image represented the altitude of the point, each local minimum value and its affected area represented the water catchment basin, and the boundary formed a watershed. However, images with irregular noise and gradients were prone to oversegmentation, so that a watershed algorithm that incorporates prior labels was devised to address this problem. The algorithm reversed the CHM, used the crown vertex as the seed point, calculated the gradient of each grid cell to the neighborhood, determined the contour of the crown area, and set the minimum height of the single tree minHeight parameter to 2 m. Through the above operations, the tree crown extraction results were received.

The results obtained by the FMSD-OBIA method were vectorized, and the vector image was superimposed on CHM to get the acquired data (CHM + tree crown extraction results). The LMF algorithm was applied to the numerical statistics of each polygon (tree crown), whose maximum value was the tree height.

**3.5. Accuracy Evaluation of Tree Crown and Tree Height.** In order to further evaluate the generated crown maps, the

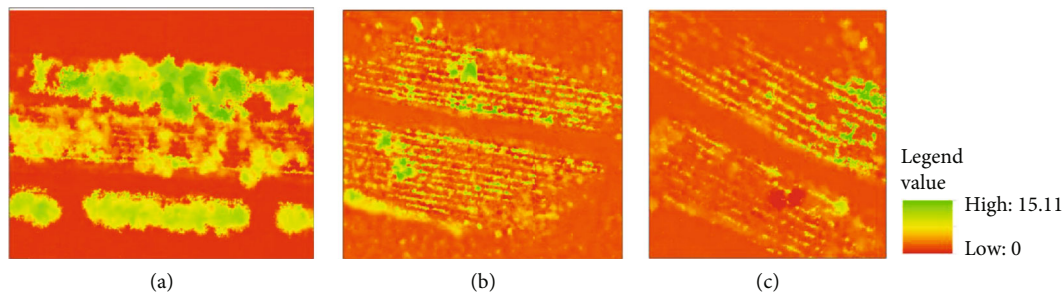


FIGURE 4: Canopy height models of three study areas: (a) canopy height model of study area 1; (b) canopy height model of study area 2; (c) canopy height model of study area 3.

TABLE 3: Parameter selection of object-oriented classification.

Study area	Segmentation scale (pixel)	Merging scale (pixel)
1	10	60
2	20	40
3	20	40

multispectral images of the three areas were manually delineated by an experienced researcher and then the resulting manually delineated crown maps were used for space comparison with the model-generated crown maps. For the sake of simplicity, the map automatically drawn by the extraction model and the map drawn manually were called the target map and the reference map, respectively. The reference crowns near the image boundary had been removed and only the remained crowns were used in the following evaluation. According to the spatial relationship between all remaining reference crowns and target segments, they were divided into the following five categories [34, 35]:

- Crown matched: the target canopy map (canopy extraction results of the model) and the reference canopy map exceed 50% of each other, which was regarded as a crown matched
- Crown nearly matched: the target canopy map and the reference canopy map only exceed 50% of one of them, which was regarded as a crown nearly matched
- Crown missed: Both the target canopy map and the reference canopy map were not within 50% of each other, which was regarded to be a crown missed
- Crown merged: if there were multiple reference crowns with more than half the area covered by a target canopy, the multiple reference crown maps were taken as crowns merged in the automatic delineation
- Crown split: if there were multiple target segments with more than half the area covered by a reference crown, the reference crown map was considered a crown split in the automatic delineation

Crown matched and crown nearly matched are considered to be the correct crown width extraction results and recorded as True Positive (TP); crown missed and crown

merged are considered to be omission errors and recorded as False Negative (FN); and crown split corresponds to commission errors and is recorded as False Positive (FP). Then, the crown extraction recall rate (recall), accuracy rate (precision), and  $F$ -score are defined as follows [36]:

$$\text{recall} = \frac{\text{TP}}{\text{TP} + \text{FN}} \times 100\%, \quad (4)$$

$$\text{precision} = \frac{\text{TP}}{\text{TP} + \text{FP}} \times 100\%, \quad (5)$$

$$F\text{-score} = 2 \times \frac{\text{recall} \times \text{precision}}{\text{recall} + \text{precision}} \times 100\%. \quad (6)$$

To estimate the tree height, the linear regression was applied to analyze the estimation results of models and the collected field measurements, and the coefficients of determination ( $R^2$ ) and Root Mean Square Error (RMSE) were employed to quantitatively evaluate the accuracy of the estimation. The value of  $R^2$  ranges between 0 and 1, a larger value of which indicates that a good fitting effect is obtained. The RMSE was used to measure the deviation between the predicted value and the measured value, a smaller value of which indicates that the error is small and the prediction effect is good. The calculation formulae of  $R^2$  and RMSE are as follows:

$$R^2 = 1 - \frac{\sum_{i=1}^n (y_i - \hat{y}_i)^2}{\sum_{i=1}^n (y_i - \bar{y})^2}, \quad (7)$$

$$\text{RMSE} = \sqrt{\frac{\sum_{i=1}^n (\hat{y}_i - y_i)^2}{n}}, \quad (8)$$

where  $\hat{y}_i$  is the predicted value of the sample  $i$  of the tree height estimation model,  $y_i$  is the measured value of the sample  $i$  of the shelter forest,  $\bar{y}$  is the mean value of the measured sample, and  $n$  is the total number of samples.

## 4. Results

4.1. Analysis of the Results of Extracting the Crown of the Individual Shelterbelt. The results of different methods for extracting the canopy of three selected areas are shown in Figure 5, which can be seen through the combination of field sampling, photos, and visual observation. From the method

TABLE 4: Search radius  $r$  of linear function for single tree detection.

Study area	$r(x)$ (m)	Canopy characteristics
1	$0.08x + 1.5$	Mixed forests with inconsistent crown sizes
2	$0.04x + 0.6$	Sparse forest with small crown, tall trees, and good growth
3	$0.04x + 0.6$	Sparse forest with small crown and mostly dead trees

of combination of LMF and MCWS in study area 1, a splitting of one tree crown into two (oversegmentation phenomenon) appeared and two tree crowns were merged into one (undersegmentation phenomenon). Oversegmentation phenomena also appeared in study areas 2 and 3, and there were also many crowns missed. The canopy extracted by the FMSD-OBIA method effectively solved the problems of oversegmentation and undersegmentation phenomena in study area 1, although undersegmentation phenomena in study areas 2 and 3 still appeared, which had been reduced. Furthermore, incidences of the crown omission phenomenon also decreased. Overall, the FMSD-OBIA method was better than the traditional method of the combination of LMF and MCWS, and the crown extraction performance is also improved.

In order to qualitatively evaluate the results of different canopy extraction methods on the extraction accuracy of individual canopies of the shelter forests in study area, we calculated relevant evaluation indexes, as shown in Table 5. The FMSD-OBIA method achieved good results in the three study areas: the average  $F$ -score was above 0.89, while the average  $F$ -score of the combination method of LMF and MCWS did not exceed 0.8, with values between 0.75 and 0.79, indicating that the crown result of the FMSD-OBIA method was more consistent with the actual shelter forest crown result.

For study area 1, the sizes of the individual tree crowns in the dense forest area were inconsistent, which posed a significant challenge to the method of combining LMF and MCWS, and resulted in some individual trees with small crowns missed or merged, with the healthy tree recall value of 0.74 and the dead tree recall value of 0.70. Furthermore, there were multiple local maxima in broad-leaved forests (such as *Ulmus pumila* and *Elaeagnus angustifolia*), causing individual trees to be divided into multiple trees. A total of 40 healthy trees and 19 dead trees were subject to oversegmentation, with precision values of 0.83 and 0.84, respectively. The FMSD-OBIA method effectively reduced the occurrence of these two phenomena: the recall values increased by 0.12 and 0.16, and the oversegmentation phenomenon decreased by 16 and 13 trees, respectively, hence resulting in increases in the precision values by 0.08 and 0.11.

The healthy trees in study area 2 were compact but sparse, comprised mostly of *Populus bolleana*. In addition, the canopy area was small: the multispectral images with 0.2 m spatial resolution were mostly 20–50 pixels, and the canopy area was 0.8–2 m<sup>2</sup>. The oversegmentation of all methods was obviously reduced, and the precision value of healthy trees was above 0.93. The recall values of the healthy tree and the dead tree increased by 0.13 and 0.20 relative to

the method of combining LMF and MCWS, and the  $F$ -score were increased by 0.09 and 0.16, respectively, which demonstrated that the FMSD-OBIA method effectively avoided the missing and merging of the trees.

There were more dead trees than healthy trees in study area 3, which also had numerous shrubs under the trees. It was difficult to distinguish trees using height information alone. Multispectral images combined with height information were used to extract crowns based on objects, effectively removing shrubs from the crown images. The adhesion and merging improved the recall and precision values, which increased by 0.23 and 0.07, respectively, indicating that the spectral information played a key role in extracting the canopy.

**4.2. The Accuracy Evaluation of the Tree Height Estimation Model.** Individual tree height was extracted using the method proposed in this paper and compared to the field-based tree height measurements with linear fitting in study areas 1 to 3 (Table 6). The RMSE values of the three types of the shelter forest study area were different as shown in Table 6. It can be noticed that the value of study area 3 was the highest, in which there were the dead trees, with an RMSE of 1.03 m. The value of the mixed forest in study area 1 was the second highest, which contained multiple tree species and a denser shelter forest, with an RMSE of 0.68 m. And the RMSE of study area 2 was the lowest with a value of 0.30 m, indicating that the dead tree area without leaves resulted in a larger error. We also analyzed the average value of the samples in each study area and the estimated tree height. The results are described as follows. The measured average tree height in study area 1 was 8.02 m and the estimated average tree height was 7.6 m. The average measured tree height in study area 2 was 4.01 m and the estimated average tree height was 3.7 m. And the average measured tree height in research area 3 was 5.77 m and the estimated average tree height was 5.1 m. The results can explain the overall underestimation of the estimated tree height using the CHM. The underestimation situation presented above had a difference in various types of shelter forests, and the best estimation was acquired in a vigorous and sparse forest ( $R^2 = 0.93$ ), with a high correlation, nearly as great as the one acquired in mixed forest ( $R^2 = 0.91$ ). The weakest correlation was obtained in a sparse forest with many dead trees ( $R^2 = 0.88$ ), which showed the difference in the ability of photogrammetric point clouds to rebuild the canopies of different shelter forests.

Because we did not collect ground points, this study used the original point cloud without the RBFNN interpolation. And the DEM was directly generated from Pix4D software to estimate the tree height for comparison, verifying the

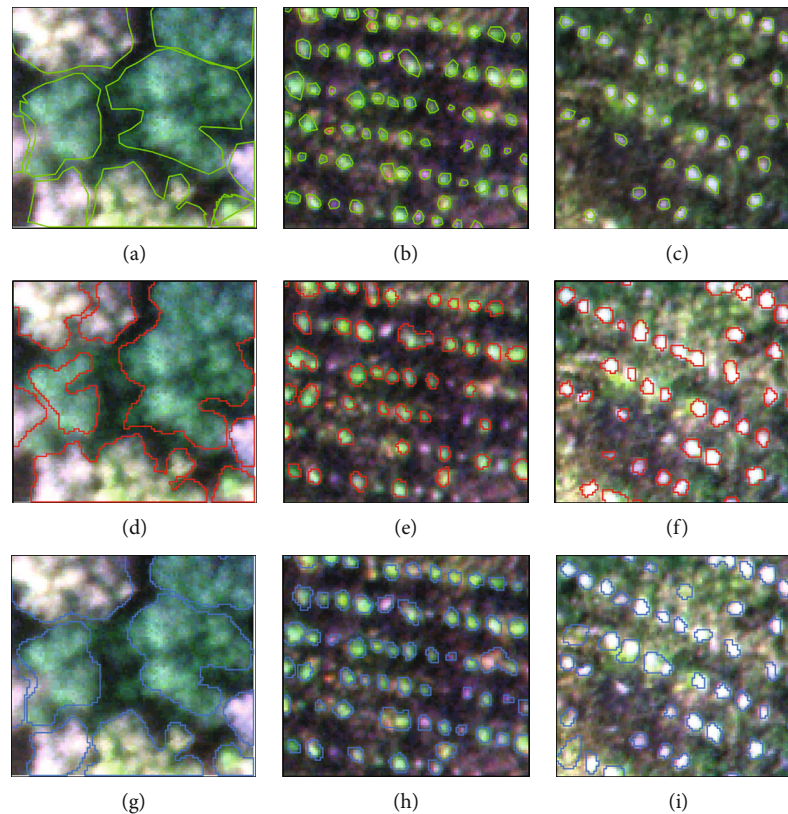


FIGURE 5: The performance of different extraction methods on the crown of individual trees in the study area: (a–c) multispectral raw image data for study areas 1–3 (the green polygonal area represents a reference drawing of the tree canopy drawn by experienced researchers); (d–f) the red polygonal area is the crown extracted results using the method of combining LMF with MCWS in study areas 1–3; (g–i) the blue polygonal area is the crown extracted results using the FMSD-OBIA method in study areas 1–3.

feasibility and scientificity of RBFNN interpolation. It can be seen from Table 6 that the accuracy of the tree height estimation results after RBFNN interpolation was overall higher than those of the other two methods. The error of the results without RBFNN interpolation increased, and the correlation of those decreased, which demonstrated the effectiveness of RBFNN interpolation prediction. RBFNN interpolation can be used to address the problem of low DEM accuracy of the photogrammetric point cloud caused by the large canopy. The canopy coverages of study areas 2 and 3 were small. After RBFNN interpolation,  $R^2$  and RMSE were higher than the other two methods (DEM generated without RBFNN interpolation and DEM directly generated by Pix4D software), which proved that RBFNN was effective and feasible in photogrammetric point cloud. On the whole, the tree height estimation results of RBFNN interpolation were more accurate and efficient.

## 5. Discussion

**5.1. Analysis of the Results of Extracting the Crown of the Individual Shelterbelt.** Due to the discontinuous change of the gray level of the pixels in the CHM, the segmentation process will generate smaller segmentation units, and oversegmentation and undersegmentation often occur. The method based on combining spectral information with the CHM and using an FMSD-OBIA method to extract the

crown, which considered the object the basic unit, is a better approach than the traditional methods for the extraction of the crown of a shelter forest. It effectively reduces the misclassification of the pixels of shelter forest crowns as other feature categories. Thus, with more corrected information (such as spectrum and height) related to the canopy extraction, the accuracy of the proposed model is improved, which is consistent with the research results in [37].

The method based on combining LMF and MCWS had a large difference in the crown extraction results in the three study areas. The accuracy of the canopy extraction of the sparse forest (in study area 2) was better than that of the mixed dense forest (in study area 1), but the sparse forest in study area 3 resulted in the worst extraction effect. The main reason for the difference is the large difference in the characteristics of the three types of shelter forest. In study area 3, there were many withered (dead) trees, and the coverage area was small; thus, the canopy vegetation features were not obvious. In addition, the protection forest had large row spacing and small density, which also made it difficult to extract the canopy. If the canopy is too small to extract, the phenomenon of omission error is more serious. Relatively, the sparse forest in study area 2 had large line spacing and low density, but the area of the crown width was appropriate, which could be more easy to well distinguish the crown from the background and thus result in a better extraction accuracy.

TABLE 5: Evaluation of the accuracy of different extraction methods in the study areas.

Study area number	Crown extraction method	Shelter forest health situation	Crown matched	Crown nearly matched	Crown missed	Crown merged	Crown split	Recall	Precision	F-score
1	a	Healthy	158	31	20	45	40	0.74	0.83	0.78
		Dead	60	41	22	21	19	0.70	0.84	0.77
	b	Healthy	194	39	8	29	24	0.86	0.91	0.88
		Dead	83	51	13	9	7	0.86	0.95	0.90
2	a	Healthy	323	25	60	46	27	0.77	0.93	0.84
		Dead	97	28	36	29	23	0.66	0.84	0.74
	b	Healthy	389	31	27	19	15	0.90	0.97	0.93
		Dead	144	32	17	11	9	0.86	0.95	0.90
3	a	Healthy	19	4	7	5	4	0.66	0.85	0.74
		Dead	139	25	54	31	27	0.66	0.86	0.75
	b	Healthy	27	6	1	2	3	0.92	0.92	0.92
		Dead	189	38	15	18	16	0.87	0.93	0.90

a: the method of combination of LMF and MCWS; b: the method of FMSD-OBIA.

TABLE 6: Comparison of linear fitting accuracy evaluation of different methods for estimating tree height.

Study area	Method	$R^2$	RMSE (m)
1	DEM (after RBFNN interpolation)	0.91	0.68
	DEM (without RBFNN interpolation)	0.47	1.48
	DEM (Pix4D software)	0.50	1.93
2	DEM (after RBFNN interpolation)	0.93	0.30
	DEM (without RBFNN interpolation)	0.84	0.41
	DEM (Pix4D software)	0.64	1.52
3	DEM (after RBFNN interpolation)	0.88	1.03
	DEM (without RBFNN interpolation)	0.60	1.68
	DEM (Pix4D software)	0.45	2.01

In the mixed forest in study area 1, the large differences of the crown size made it difficult to determine the search radius of the VWF function into the procedure of individual tree detection, causing the oversegmentation and omission error of the extreme trees that were too large or too small. The accuracy of the sample-based object-oriented method in all three research areas was higher than that of the method of the combination of LMF and MCWS. The canopy extraction results were ideal, meaning that the canopy edges were better identified and the tree crown information was completely described. Regardless of whether it was a sparse forest or a mixed forest, the emergence of the oversegmentation and undersegmentation was reduced, and the overall accuracy of the sparse forest with the FMSD-OBIA method was higher than that of the mixed dense forest. Dead trees with smaller crown areas had higher accuracy than the mixed dense forest because, after adding spectral information, there was a cer-

tain difference between the dead tree and the surrounding environment spectrum, which could be effectively distinguished. However, the best results cannot be obtained using spectral information alone, which is 11%–14% lower than the canopy extraction results of the study in [38].

In general, the FMSD-OBIA method for crown extraction can effectively solve the problems of oversegmentation and undersegmentation. However, the study still has some limitations. Although the object-oriented method had high precision, the degree of automation was not ideal, as the threshold needed to be set manually which were usually obtained requiring a number of attempts. Different parameters also needed to be set as for different types of shelter forest and especially in mixed forests, it was almost impossible to define different canopy areas to get accurate boundary information, contributing to the difference between the results of the extraction of different canopy areas and the actual edges. Therefore, a single optimal segmentation scale was not suitable for extracting tree crowns with large differences in crown areas in the same image.

*5.2. Analysis of Differences in the Tree Height Estimation of Different Shelter Forest Types.* In the study of using the UAV photogrammetric point cloud to estimate the height of individual trees for different types of shelter forest, the availability of the DEM generated based on RBFNN interpolation was confirmed. This approach has high estimation accuracy and can be implemented economically. The method would be replaced the point cloud data with the one obtained by LiDAR or laser scanner. Existing studies have shown that DEM accuracy will be affected by vegetation coverage, slope, and interpolation algorithms [39]. The shelterbelt was located on the edge of a desert, where the terrain was relatively flat and the vegetation coverage was not large. The data acquisition time was during the transition between autumn and winter seasons. Studies in [40, 41] have shown that the DEM is the most accurate in winter with low vegetation

coverage. The CHM obtained by interpolation through the RBFNN can theoretically get a more accurate tree height estimation. Analyzing the actual tree height and estimating the average tree height showed that the overall estimated tree height was underestimated (between 0.3 and 0.7 m). Nuijten et al. [42] indicated that the tree height may be underestimated when leaves have fallen. After the frost in October in the northern Xinjiang region, the leaves of the shelterbelt began to become yellow and gradually fell, while the vegetation coverage of the canopy also diminished, which led to the overall underestimation phenomenon of tree heights.

The difference in tree height estimation of different shelterbelt types was mainly due to the acquisition and reconstruction of photogrammetric point clouds. The image data obtained from the UAV platform was affected by many factors in the reconstruction of the 3D canopy point cloud [13, 39, 43], including the UAV platform, sensors, image acquisition parameters, and protection forest type. This study focused on the differences in the ability to reconstruct photogrammetric point clouds in different types of shelter forest, selecting image data acquired on the same day, of the same sort, and using the same flight platform, overlap rate, and lighting conditions, to prevent these parameters from having an impact on the reconstruction of the point cloud. Through this research, it was found that the tree species and health status of the shelter forest had different effects on the tree height estimation. For dead trees without leaves (*Populus bolleana*, sparse forest), the RMSE was 1.03 m, and the correlation with the measured data was lower than that of other types. The dense mixed forest had a lower RMSE than the sparse forest with more dead trees. The crown area of dead trees was significantly smaller than that of healthy trees, and the vegetation information was not obvious, which made the reconstruction of point clouds difficult. Generally speaking, the higher the point cloud density, the more canopy information was obtained; this was more conducive to the reconstruction of canopy point cloud information, and higher point cloud density can provide higher estimation accuracy of tree height [44]. Dead trees had a small canopy and a limited number of point clouds. The lower canopy coverage results in fewer features that can be extracted, which reduces the ability to reconstruct the point cloud. This resulted in a higher tree height estimation error, which is consistent with the research results in [22].

## 6. Conclusions

This study proposed a novel method of individual tree height estimation based on fusion of an airborne multispectral image and photogrammetric point cloud and selected 3 areas in the shelter forest for verification. The DEM generated after RBFNN interpolation could meet the requirement of estimating tree height, which confirmed that the photogrammetric point cloud obtained by a CW-20 fixed-wing UAV, equipped with SONY-A7RII camera, had the significant potential for the estimation of tree height. The coverage and health condition of protective forest canopies had a certain influence on the reconstruction of photogrammetric point clouds. Dead trees had a small canopy area and no

physiological characteristics of healthy vegetation, so that the SfM algorithm extracted fewer features from the images. The FMSD-OBIA methods were employed in the combination of 12-bands and CHM increased the spectral information of the shelterbelt forest canopy, effectively reduced the phenomena of oversegmentation and undersegmentation, increased the *F*-score by 0.12–0.17, and improved the accuracy of canopy extraction. The proposed method is effective for estimating the tree height of individual trees of shelter forests in a desert area but nonetheless requires further improvement. The degree of automation of object-oriented methods is not ideal, and there is definitely room for further improvement of the accuracy and the speed of the canopy, which can be replaced with deep learning methods. Moreover, the two types of forest stand data, from dense and sparse forest areas, can be used to build a tree height growth model based on multiperiod image data, which will be helpful to conduct health assessments to protect the desert forest and provide an important reference for maintenance and replacement.

## Data Availability

The data used to support the findings of this study are available from the corresponding author upon request.

## Conflicts of Interest

The authors declare that they have no conflicts of interest.

## Acknowledgments

The authors would like to acknowledge the support from colleagues of the Geospatial Information Engineering Research Center, Xinjiang Production and Construction Corps, especially Yongjian Ma, Wenzhong Tian, and Xiang Long. This study was financially supported by the Xinjiang Production and Construction Corps Science and Technology Project (2017DB005); the Geospatial Information Engineering Research Center to Create, Xinjiang Production and Construction Corps (2016BA001); and the Central Government Directs Local Science and Technology Development Special Funds (201610011).

## References

- [1] J. Huang, H. Yu, X. Guan, G. Wang, and R. Guo, "Accelerated dryland expansion under climate change," *Nature Climate Change*, vol. 6, no. 2, pp. 166–171, 2016.
- [2] F. Wang, X. Pan, C. Gerlein-Safdi et al., "Vegetation restoration in northern China: a contrasted picture," *Land Degradation & Development*, vol. 31, no. 6, pp. 669–676, 2020.
- [3] C. Deng, B. Zhang, L. Cheng, L. Hu, and F. Chen, "Vegetation dynamics and their effects on surface water-energy balance over the Three-North Region of China," *Agricultural and Forest Meteorology*, vol. 275, pp. 79–90, 2019.
- [4] G. B. West, B. J. Enquist, and J. H. Brown, "A general quantitative theory of forest structure and dynamics," *Proceedings of the National Academy of Sciences*, vol. 106, no. 17, pp. 7040–7045, 2009.



- [5] B. J. Enquist, G. B. West, and J. H. Brown, "Extensions and evaluations of a general quantitative theory of forest structure and dynamics," *Proceedings of the National Academy of Sciences*, vol. 106, no. 17, pp. 7046–7051, 2009.
- [6] K. T. Moe, T. Owari, N. Furuya, and T. Hiroshima, "Comparing individual tree height information derived from field surveys, LiDAR and UAV-DAP for high-value timber species in northern Japan," *Forests*, vol. 11, no. 2, p. 223, 2020.
- [7] M. L. Hobi and C. Ginzler, "Accuracy assessment of digital surface models based on WorldView-2 and ADS80 stereo remote sensing data," *Sensors*, vol. 12, no. 5, pp. 6347–6368, 2012.
- [8] W. J. Ni, D. F. Zhang, Y. Wang et al., "Extraction of forest height by using GF-2 cross-track stereo images," *Journal of Remote Sensing*, vol. 22, no. 3, pp. 392–399, 2018.
- [9] M. Karpina, M. Jarzabek-Rychard, P. Tymków, and A. Borkowski, "UAV-based automatic tree growth measurement for biomass estimation," *ISPRS - International Archives of the Photogrammetry, Remote Sensing and Spatial Information Sciences*, vol. XLI-B8, pp. 685–688, 2016.
- [10] Y.-C. Hsieh, Y.-C. Chan, and J.-C. Hu, "Digital elevation model differencing and error estimation from multiple sources: a case study from the Meiyuan Shan landslide in Taiwan," *Remote Sensing*, vol. 8, no. 3, p. 199, 2016.
- [11] H. Li and J. Y. Zhao, "Evaluation of the newly released worldwide AW3D30 DEM over typical landforms of China using two global DEMs and ICESat/GLAS data," *IEEE Journal of Selected Topics in Applied Earth Observations and Remote Sensing*, vol. 11, no. 11, pp. 4430–4440, 2018.
- [12] Z. Xu, X. Shen, L. Cao, N. C. Coops, and X. Wu, "Tree species classification using UAS-based digital aerial photogrammetry point clouds and multispectral imageries in subtropical natural forests," *International Journal of Applied Earth Observation and Geoinformation*, vol. 92, p. 102173, 2020.
- [13] S. Krause, T. G. M. Sanders, J. P. Mund, and K. Greve, "UAV-based photogrammetric tree height measurement for intensive forest monitoring," *Remote Sensing*, vol. 11, no. 7, p. 758, 2019.
- [14] M. Imangholiloo, N. Saarinen, L. Markelin et al., "Characterizing seedling stands using leaf-off and leaf-on photogrammetric point clouds and hyperspectral imagery acquired from unmanned aerial vehicle," *Forests*, vol. 10, no. 5, p. 415, 2019.
- [15] Z. Qiu, Z.-K. Feng, M. Wang, Z. Li, and C. Lu, "Application of UAV photogrammetric system for monitoring ancient tree communities in Beijing," *Forests*, vol. 9, no. 12, p. 735, 2018.
- [16] Y. H. Tu, K. Johansen, S. Phinn, and A. Robson, "Measuring canopy structure and condition using multi-spectral UAS imagery in a horticultural environment," *Remote Sensing*, vol. 11, no. 3, p. 269, 2019.
- [17] J. Lin, M. Wang, M. Ma, and Y. Lin, "Aboveground tree biomass estimation of sparse subalpine coniferous forest with UAV oblique photography," *Remote Sensing*, vol. 10, no. 11, p. 1849, 2018.
- [18] C.-Y. Wu, J. Mossa, L. Mao, and M. Almulla, "Comparison of different spatial interpolation methods for historical hydrographic data of the lowermost Mississippi river," *Annals of GIS*, vol. 25, no. 2, pp. 133–151, 2019.
- [19] S. Liu, Y. Zhang, P. Ma, B. Lu, and H. Su, "A novel spatial interpolation method based on the integrated RBF neural network," *Procedia Environmental Sciences*, vol. 10, no. part-PA, pp. 568–575, 2011.
- [20] Q. Z. Zhao, L. I. Peiting, M. A. Yongjian, and T. Wenzhong, "Construction method of point clouds' DEM based on k-means clustering and RBF neural network," *Transactions of the Chinese Society for Agricultural Machinery*, 2019.
- [21] F. Brieger, U. Herzsuh, L. A. Pestryakova, B. Bookhagen, and S. Kruse, "Advances in the derivation of northeast Siberian forest metrics using high-resolution UAV-based photogrammetric point clouds," *Remote Sensing*, vol. 11, no. 12, p. 1447, 2019.
- [22] H. Huang, S. He, and C. Chen, "Leaf abundance affects tree height estimation derived from UAV images," *Forests*, vol. 10, no. 10, p. 931, 2019.
- [23] H. Hamraz, M. A. Contreras, and J. Zhang, "Vertical stratification of forest canopy for segmentation of understory trees within small-footprint airborne LiDAR point clouds," *ISPRS Journal of Photogrammetry and Remote Sensing*, vol. 130, pp. 385–392, 2017.
- [24] S. E. Franklin, "Pixel- and object-based multispectral classification of forest tree species from small unmanned aerial vehicles," *Journal of Unmanned Vehicle Systems*, vol. 6, no. 4, pp. 195–211, 2018.
- [25] V. González-Jaramillo, A. Fries, and J. Bendix, "AGB estimation in a tropical mountain forest (TMF) by means of RGB and multispectral images using an unmanned aerial vehicle (UAV)," *Remote Sensing*, vol. 11, no. 12, p. 1413, 2019.
- [26] Q. Z. Zhao, W. Liu, X. J. Yin, and T. Y. Zhang, "Selection of optimum bands combination based on multispectral images of UAV," *Transactions of the Chinese Society for Agricultural Machinery*, vol. 47, no. 3, pp. 242–248+291, 2016.
- [27] J. A. Bullnaria, "Radial basis function networks: introduction," *Neural Comput. Lect*, vol. 13, pp. L13-2–L13-16, 2004.
- [28] M. Gomroki, M. Jafari, S. Sadeghian, and Z. Azizi, "Application of intelligent interpolation methods for DTM generation of forest areas based on LiDAR data," *PFG – Journal of Photogrammetry, Remote Sensing and Geoinformation Science*, vol. 85, no. 4, pp. 227–241, 2017.
- [29] H. He, Y. Yan, T. Chen, and P. Cheng, "Tree height estimation of forest plantation in mountainous terrain from bare-earth points using a dog-coupled radial basis function neural network," *Remote Sensing*, vol. 11, no. 11, p. 1271, 2019.
- [30] C. Chen, Y. Li, N. Zhao, B. Guo, and N. Mou, "Least squares compactly supported radial basis function for digital terrain model interpolation from airborne LiDAR point clouds," *Remote Sensing*, vol. 10, no. 4, p. 587, 2018.
- [31] A. Plowright, "ForestTools: analyzing remotely sensed forest data. R Package version 0.2.0," 2018, 2009, <https://github.com/AndyPL22/ForestTools>.
- [32] S. C. Popescu and R. H. Wynne, "Seeing the trees in the forest," *Photogrammetric Engineering and Remote Sensing*, vol. 70, no. 5, pp. 589–604, 2004.
- [33] L. Vincent and P. Soille, "Watersheds in digital spaces: an efficient algorithm based on immersion simulations," *IEEE Transactions on Pattern Analysis and Machine Intelligence*, vol. 13, no. 6, pp. 583–598, 1991.
- [34] F. A. Gougeon, "A crown-following approach to the automatic delineation of individual tree crowns in high spatial resolution aerial images," *Canadian Journal of Remote Sensing*, vol. 21, no. 3, pp. 274–284, 1995.
- [35] L. Jing, B. Hu, T. Noland, and J. Li, "An individual tree crown delineation method based on multi-scale segmentation of imagery," *Isprs Journal of Photogrammetry & Remote Sensing*, vol. 70, pp. 88–98, 2012.
- [36] W. Li, Q. Guo, M. K. Jakubowski, and M. Kelly, "A new method for segmenting individual trees from the LiDAR point



- cloud,” *Photogrammetric Engineering and Remote Sensing*, vol. 78, no. 1, pp. 75–84, 2012.
- [37] F. Naveed, B. Hu, J. Wang, and G. B. Hall, “Individual tree crown delineation using multispectral LiDAR data,” *Sensors*, vol. 19, no. 24, article 5421, 2019.
- [38] L. Qiu, L. Jing, B. Hu, H. Li, and Y. Tang, “A new individual tree crown delineation method for high resolution multispectral imagery,” *Remote Sensing*, vol. 12, no. 3, p. 585, 2020.
- [39] J. P. Dandois and E. C. Ellis, “High spatial resolution three-dimensional mapping of vegetation spectral dynamics using computer vision,” *Remote Sensing of Environment*, vol. 136, pp. 259–276, 2013.
- [40] W. Van Iersel, M. Straatsma, E. Addink, and H. Middelkoop, “Monitoring height and greenness of non-woody floodplain vegetation with UAV time series,” *ISPRS Journal of Photogrammetry and Remote Sensing*, vol. 141, pp. 112–123, 2018.
- [41] T. R. Goodbody, N. C. Coops, T. Hermosilla, P. Tompalski, and G. Pelletier, “Vegetation phenology driving error variation in digital aerial photogrammetrically derived terrain models,” *Remote Sensing*, vol. 10, no. 10, p. 1554, 2018.
- [42] R. J. Nuijten, N. C. Coops, T. R. Goodbody, and G. Pelletier, “Examining the multi-seasonal consistency of individual tree segmentation on deciduous stands using digital aerial photogrammetry (DAP) and unmanned aerial systems (UAS),” *Remote Sensing*, vol. 11, no. 7, p. 739, 2019.
- [43] J. Dandois, M. Olano, and E. Ellis, “Optimal altitude, overlap, and weather conditions for computer vision UAV estimates of forest structure,” *Remote Sensing*, vol. 7, no. 10, pp. 13895–13920, 2015.
- [44] S. Ganz, Y. Käber, and P. Adler, “Measuring tree height with remote sensing—a comparison of photogrammetric and LiDAR data with different field measurements,” *Forests*, vol. 10, no. 8, p. 694, 2019.

## Research Article

# Application of an Ensemble Statistical Approach in Spatial Predictions of Bushfire Probability and Risk Mapping

Mahyat Shafapour Tehrany,<sup>1</sup> Haluk Özener,<sup>1</sup> Bahareh Kalantar ,<sup>2</sup> Naonori Ueda,<sup>2</sup> Mohammad Reza Habibi,<sup>3</sup> Fariborz Shabani,<sup>3</sup> Vahideh Saeidi,<sup>4</sup> and Farzin Shabani <sup>5,6</sup>

<sup>1</sup>Kandilli Observatory and Earthquake Research Institute, Department of Geodesy, Bogazici University, 34680 Cengelkoy, Istanbul, Turkey

<sup>2</sup>RIKEN Center for Advanced Intelligence Project, Goal-Oriented Technology Research Group, Disaster Resilience Science Team, Tokyo 103-0027, Japan

<sup>3</sup>Department of Civil Engineering, Kermanshah Azad University, Iran

<sup>4</sup>Department of Mapping and Surveying, Darya Tarsim Consulting Engineers Co. Ltd., Tehran 15119-43943, Iran

<sup>5</sup>ARC Centre of Excellence for Australian Biodiversity and Heritage, Global Ecology, College of Science and Engineering, Flinders University, GPO Box 2100, Adelaide, South Australia, Australia

<sup>6</sup>Department of Biological Sciences, Macquarie University, Sydney, New South Wales, Australia

Correspondence should be addressed to Bahareh Kalantar; bahareh.kalantar@riken.jp and Farzin Shabani; farzin.shabani@flinders.edu.au

Received 12 January 2021; Revised 26 February 2021; Accepted 23 March 2021; Published 23 April 2021

Academic Editor: Abdellah Touhafi

Copyright © 2021 Mahyat Shafapour Tehrany et al. This is an open access article distributed under the Creative Commons Attribution License, which permits unrestricted use, distribution, and reproduction in any medium, provided the original work is properly cited.

The survival of humanity is dependent on the survival of forests and the ecosystems they support, yet annually wildfires destroy millions of hectares of global forestry. Wildfires take place under specific conditions and in certain regions, which can be studied through appropriate techniques. A variety of statistical modeling methods have been assessed by researchers; however, ensemble modeling of wildfire susceptibility has not been undertaken. We hypothesize that ensemble modeling of wildfire susceptibility is better than a single modeling technique. This study models the occurrence of wildfire in the Brisbane Catchment of Australia, which is an annual event, using the index of entropy (IoE), evidential belief function (EBF), and logistic regression (LR) ensemble techniques. As a secondary goal of this research, the spatial distribution of the wildfire risk from different aspects such as urbanization and ecosystem was evaluated. The highest accuracy (88.51%) was achieved using the ensemble EBF and LR model. The outcomes of this study may be helpful to particular groups such as planners to avoid susceptible and risky regions in their planning; model builders to replace the traditional individual methods with ensemble algorithms; and geospatial users to enhance their knowledge of geographic information system (GIS) applications.

## 1. Introduction

Wildfires, alternatively termed forest fires, bushfires, woodland fires, and vegetation fires, boosted by wind and high summer temperatures, are able to destroy entire forests faster than they can be brought under control [1], causing irreversible, incalculable environmental, economic, and social damage [2]. Wildfires cause direct forest degradation [3]. Like the Australian wildfires 2020 [4] which a wide variety of forest

flora [5] and forest species [6] were destroyed within a very short period of time. Soil nutrients loss is a long-lasting effect [7, 8], which wildfires can bring into a region. Ecosystems and biodiversity [9] such as bird nesting and habitats [10, 11] are also so vulnerable to wildfire phenomena. Destroying watersheds [12] and reducing water quality [13, 14] are destructive impacts of this disaster. Last but not least, impacts on human settlements and health [15, 16] can be considered as nonreturnable negative influence of wildfire disaster.

A fundamental requirement in natural hazard management is to accurately locate wildfire endangered regions [17], meaning that to find the areas that have the highest potential for future wildfire occurrence. Throughout proper natural hazard management, wildfire can be controlled and damages are minimized [18]. In fact, assessing the susceptibility of a locality to wildfire occurrence is based on a specific correlation among the historical wildfire events and its related causing factors such as topographical, hydrological, and geological [19].

Numerous approaches and algorithms have been used for wildfire hazard mapping [20]. Recent studies have utilized remote sensing (e.g., aerial photos, LiDAR data, and signals) and thematic maps either directly or indirectly in conjunction with geospatial information systems (GIS), and they have the potential to support assessments of wildfire risk from a variety of aspects such as fuel load [21, 22], burn severity [23], and intensity measurements [24, 25]. Probability and susceptibility are foundational in the field of wildfire research [26], being essential for risk, vulnerability, response, and safety studies [27]. As a practical example, wildfire spatiotemporal distributions can be derived from the susceptibility over a period [28], in order to establish trends, which can be monitored and projected into the future. The existing methods used in wildfire probability mapping cover a variety of algorithms. For instance, qualitative analytical hierarchy process (AHP) and Mamdani fuzzy logic (MFL) methods were used by Pourtaghi et al. [18]. Their outputs denoted that the qualitative analysis might not be accurate as it was a knowledge-based approach and differed from a person to person. Linear and quadratic discriminant analysis, frequency ratio (FR), and weights-of-evidence (WOE) were used together with thirteen causative factors in a research by Hong et al. [27], and the area under the curve (AUC) for the forest fire susceptibility mapping did not exceed 82.2%. Jaafari et al. [29] used five decision tree-based classifiers in the wildfire mapping and reported a high level of performance (AUC = 90%). However, decision tree-based models are often computationally expensive in modeling and sensitive to training the big data [30]. FR which is known as a simple and popular statistical algorithm was also utilized in mapping the wildfire hazard [31]. In this study, however, FR performance (AUC = 79.85%) was less effective compare to Shannon's entropy model (AUC = 83.16%). Support vector machine (SVM) as another popular algorithm was used by Tien Bui et al. [32] to detect the most wildfire susceptible areas in the Cat Ba National Park area (Vietnam) resulting to an AUC of 87.5%. Pourghasemi et al. [33] produced the wildfire susceptibility maps based on evidential belief function (EBF) and binary logistic regression (BLR) models. The validation of the result illustrated the outperformance of EBF (AUC = 81.9%) over BLR (AUC = 74.3%). Wildfire susceptibility mapping using sixteen conditioning factors, Gholamnia et al. [34] exploited machine learning (ML) methods (e.g., artificial neural network (ANN), dmine regression (DR), data mining (DM) neural, least angle regression (LARS), multilayer perceptron (MLP), random forest (RF), radial basis function (RBF), self-organizing maps (SOM), SVM, and decision tree (DT)) and reported the highest

(88%) and lowest accuracy (65%) for RF and logistic regression (LR), respectively. Kalantar et al. [35] mapped the forest fire susceptibility using three ML algorithms, namely, multivariate adaptive regression splines (MARS), SVM, and boosted regression tree (BRT) with resampling techniques in the training phase. They reported the resampling process enhanced the modeling and BRT with an AUC of 91% outperformed others. In this context, several ML methods, for example, DT, have an inherent computational complexity, requiring a number of preanalysis stages and significant processing time [36]. Although the aforementioned studies acquired satisfactory AUC, all the AUC values were less than 91% (majority between 74%-83%), and it motivated us to investigate other algorithms and pursue the higher accuracy for wildfire prediction.

It has been proven by some other researches such as Brun et al. [37] and Podschwit et al. [38] that ensemble and multi-model approaches might lead to much more accurate results. Zhou [39] stated that ensemble modeling offers a state-of-the-art learning approach, which has become a focus of modeling research since the 1990s and has been shown to produce results that are considerably more precise than using a single method [40–43]. A study by Jaafari et al. [44] was undertaken to examine and compare four hybrid (artificial intelligence) methods against a single model in mapping the wildfire probability in the Hyrcanian ecoregion, Iran. Their finding proved up to 18% increase of modeling accuracy using hybrid models rather than a single model. It is apparent that any individual method, whatever its advantages, has limitations. In ensemble modeling by appropriate selection of two methods, it trains multiple algorithms and subsequently combines them for analysis [45], then one can reduce or eliminate the other one's limitations, and vice versa [46]. Hence, in the present study, the ensemble model was proposed to improve the modeling and performance for higher accuracy.

Alternatively, EBF is capable of fast data processing without preassumptions [47]. Applied to wildfire susceptibility mapping, a bivariate statistical analysis (BSA) approach would be based on the comparison of a wildfire inventory map as a dependent variable and a single input influencing map (geology/wildfire, aspect/wildfire, altitude/wildfire, etc.) [48]. In execution, the spatial correlation between wildfire inventory locations and each class of each wildfire influencing factor would be measured. For instance, the weights derived for the geology factor represent the impact of each geology type on wildfire occurrence in the region. In addition, multivariate statistical analysis (MSA) only assesses the impact of factors on wildfire occurrences, rather than the influence of each class. Using an ensemble modeling approach, both the impact of classes and separate factors can be assessed in a single integrated analysis. EBF and IoE are classified as BSA approaches and extract the impact of each class of every conditioning factor. Among various ways to perform LR analysis, it is able to evaluate the impact of the factor itself on the wildfire event irrespective of class impacts. Thus, here, the ensemble analysis has the potential capability of producing more reliable and accurate outcomes compare to an individual algorithm. Although ensemble modeling

has been utilized in the wildfire domain, there is a range of other techniques that have not been tested in ensemble analysis yet. The research literature indicates applications of individual EBF, index of entropy (IoE), and LR modeling, yet their comparability and application in ensemble modeling remain untested, in refining the derived wildfire susceptibility maps, as far as we can ascertain.

For this purpose, an ensemble approach to wildfire modeling using IOE, EBF, and LR algorithm was introduced and examined. The three algorithms were selected on the basis of their relatively quick execution and comprehensibility, as well as the fact that they do not require specific dedicated software [49]. To address the important factors in bushfire occurrence in the Brisbane Catchment, Australia, we evaluated and ranked the initial fourteen causative factors (i.e., altitude, slope, aspect, curvature, topographic wetness index (TWI), topographic position index (TPI), rainfall, geology, soil, land use land cover (LULC), distance from rivers, distance from roads, wind, and normalized difference vegetation index (NDVI)). Especially, the study area faces midsummer heatwave triggering fire conditions, and this study could enlighten the sources of hazard for decision makers to protect the species threatened with extinction [50]. By producing more reliable susceptibility and risk maps, this study would assist in wildfire management, forestry, and strategies to local residents. We believed that combined into an ensemble method, the accuracy can exceed the individual outputs.

## 2. Study Area

The study area (the Brisbane catchment, Australia) is located between  $153^{\circ}12'9.212''\text{E}$   $27^{\circ}17'40.095''\text{S}$  and  $152^{\circ}22'31.144''\text{E}$   $27^{\circ}56'7.549''\text{S}$  (Figure 1), and its LULC is mainly cropping, plantation forestry, and urban and rural areas. Its climate is warm with two seasons, a dry winter and a hot humid summer. Average temperature ranges from 9 to  $12^{\circ}\text{C}$  and 21 to  $29.8^{\circ}\text{C}$ , respectively. The ecoregion of the study area is temperate broadleaf and mixed forest. However, temperate forests experience a wide range of variability in temperature and precipitation. In regions where rainfall is broadly distributed throughout the year, deciduous trees mix with species of evergreens. Species such as *Eucalyptus* and *Acacia* typify the composition of the temperate broadleaf and mixed forests in Australia. In Australia, the temperate forests stretching from southeast Queensland to South Australia enjoy a moderate climate and high rainfall that give rise to unique eucalyptus forests and open woodlands. This biome in Australia has served as a refuge for numerous plant and animal species when drier conditions prevailed over most of the continent. That has resulted in a remarkably diverse spectrum of organisms with high levels of regional and local endemism. Recently, record-breaking temperatures and extreme events such as drought caused devastating wildfire across Australia, destroying million acres of species and threatening human life (<https://www.bloomberg.com/graphics/2020-australia-fires/>), which globally ranks Australia as the most prone country to wildfires [51]. Since there is a very high possibility of wildfire danger in the dry season,

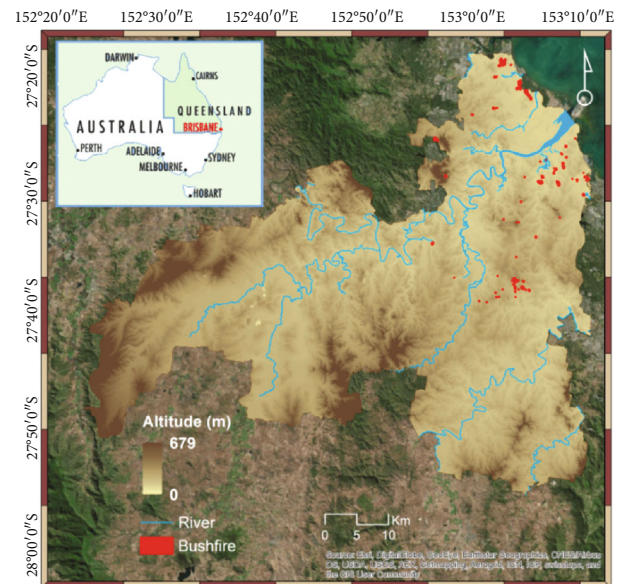


FIGURE 1: Study area and wildfire extent.

we used geographic data on the extent of the wildfires that occurred from 2011 to 2019. Figure 1 shows the study area along with the inventory of the extent of wildfires. Brisbane, the capital of Queensland, is in the southeastern corner of this state and is one of the predominant wildfire regions in Australia.

## 3. Methodology

The mapping algorithms for wildfire susceptibility were applied both individually and as an ensemble in this study. The stepwise methodology flowchart in Figure 2 illustrates different stages of this research. To achieve the primary aim of the study (ensemble modeling), the first four steps were implemented. Subsequently, the outcomes of these steps were entered into the last stage to perform the secondary goal of wildfire risk mapping. The analysis started with a random selection of forest fire inventory points and will be explained in Section 3.1.1. The training dataset, as the initial input, was utilized in both methods of IoE and EBF, in order to evaluate its correlation with influencing factors using the two methods. For the second input to the BSA analysis, a set of conditioning factors was used (Section 3.1.2). Section 3.2 describes the use of multicollinearity and Pearson's correlation analysis to eliminate some of the factors from the dataset to avoid redundancy. In the third step, the BSA was undertaken using both the IoE and EBF methods, and their final susceptibility map was produced using MSA. Area under curve (AUC) technique was used to evaluate the reliability of the outcomes using the testing dataset (30%) (Section 3.6). Subsequently, as illustrated by the dashed arrow in the flowchart, the derived BSA weights were used in ensemble with the LR algorithm. The ensemble analysis was used to produce the final wildfire susceptibility map. Thereafter, the secondary goal of the study was initiated. The most susceptible wildfire class was overlaid on several vulnerability maps derived from different sources. The aim is to show that the

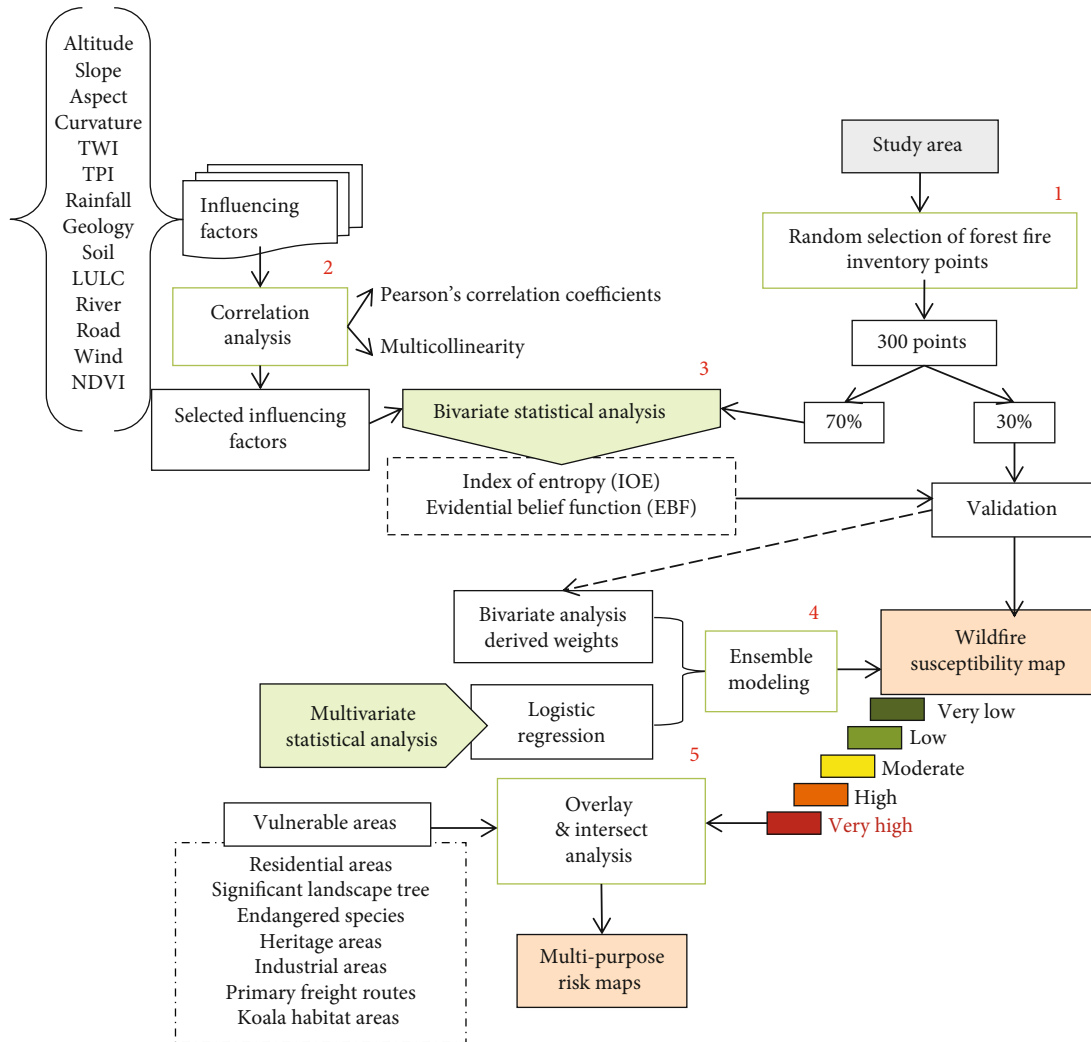


FIGURE 2: Methodology flowchart. (1) Random selection of forest fire inventory points, (2) correlation analysis, (3) bivariate statistical analysis, (4) ensemble modeling, and (5) overlay & intersect analysis.

risk map can be varied based on the application and aim of the analysis.

**3.1. Data Used.** An accurate wildfire-influencing factors dataset together with precise detection of the wildfire-ravaged locations are critical for probabilistic wildfire susceptibility analysis. Both dataset's precision has direct impact on the final outcomes [52]. The characteristics, sources, and descriptions of each dataset will be described in the following subsections.

**3.1.1. Wildfire Inventory Dataset.** Susceptibility analysis can be undertaken through the assessment of similar past events and their causative factors. A range of sources, such as in situ mapping, historical records, reports, remote sensing, and aerial photos can be used to prepare the inventory dataset [53]. In this research, the wildfire inventory dataset was compiled by the Australian Bureau of Agricultural and Resource Economics and Sciences (ABARES) for the National Forest Inventory (NFI). The raw data was delivered in vector format. Each polygon contained details of the location, date,

and size of the burnt areas (Table 1). The inventory dataset covers the wildfire records from 2011 to 2019. According to Table 1, the year 2016 had the highest incidence of wildfire covering 674,072 sqm. In this region, most of the wildfire occurrences were located in the far north and the northeast (Figure 1). Since the inventory data was in polygon format, a random point selection technique was applied, however, with few innovations as described below.

Unlike most of the previous studies [54–56], inventory points were not selected in terms of the whole basin as this would have overlooked the size of the burnt areas. As a preparatory step, four areas of interest were defined (Figure 3) around the inventory regions.

In the next step, the total area of the wildfire polygons (the centroid of the fire) in each zone was measured. Finally, wildfire random points, with respect to their areas, were selected as listed in Table 2. We aimed to choose a total of 300 inventory points. So according to the total area of each zone, the specific numbers of points were derived from them. For instance, in zone 1, the percentage of the forest fire areas with respect to the whole wildfire areas was 12%. Twelve

TABLE 1: Record of the temporal wildfire occurrence in this study.

Date	Suburb	Area (sq m)	Date	Suburb	Area (sq m)	Date	Suburb	Area (sq m)
23/01/2019	Tingalpa	471	16/05/2017	Brighton	854	26/09/2016	Stretton	1044
23/01/2019	Tingalpa	4924	15/05/2017	Brighton	327	13/09/2016	Karawatha	188
5/11/2018	Calamvale	313	1/04/2017	Parkinson	256	8/09/2016	Karawatha	1258
5/11/2018	Calamvale	41	27/03/2017	Carina	6	8/09/2016	Karawatha	2051
18/09/2018	Mt Gravatt	462	27/03/2017	Carina	95	8/09/2016	Karawatha	919
15/09/2018	Mt Gravatt	8	27/03/2017	Carina	394	29/08/2016	Forest Lake	129
31/08/2018	Chermside	42762	27/03/2017	Parkinson	2078	15/08/2016	Bracken Ridge	309109
23/08/2018	Wynnum West	12027	8/03/2017	Hemmant	1035	15/08/2016	Bracken Ridge	48472
13/08/2018	Burbank	1236	25/02/2017	Drewvale	752	7/08/2016	Deagon	98079
26/07/2018	Chermside West	16365	12/02/2017	Hemmant	59	1/07/2016	Tarragindi	2924
22/06/2018	Murarrie	2892	11/02/2017	Tingalpa	1437	28/05/2016	Darra	45758
21/02/2018	Wakerley	3617	7/02/2017	Boondall	262056	15/05/2016	Karawatha	10947
20/02/2018	Wakerley	2942	6/02/2017	Hemmant	186	18/04/2016	Carina	281
20/02/2018	Ransome	368	6/02/2017	Hemmant	275	17/04/2016	Carina	2004
18/02/2018	Wynnum	1385	6/02/2017	Hemmant	266	4/04/2016	Drewvale	1426
10/02/2018	Wynnum West	3568	6/02/2017	Hemmant	271	25/03/2016	Wynnum West	158
29/01/2018	Karawatha	23121	3/02/2017	Hemmant	3460	26/01/2016	Karawatha	13089
9/01/2018	Hemmant	20542	3/02/2017	Hemmant	383	11/01/2016	Wynnum West	31494
30/12/2017	Karawatha	656	3/02/2017	Boondall	50254	24/11/2015	Wynnum West	47616
17/12/2017	Karawatha	98481	1/02/2017	Ransome	15722	1/11/2015	Wynnum West	2578
17/12/2017	Karawatha	4947	1/02/2017	Ransome	33	15/10/2015	Wynnum West	2479
17/12/2017	Karawatha	553	1/02/2017	Ransome	887	24/09/2015	Wynnum West	4722
5/12/2017	Stretton	8023	26/01/2017	Karawatha	5514	10/05/2015	Hemmant	107825
28/09/2017	Wakerley	552	19/01/2017	Karawatha	17353	15/11/2014	Karawatha	794
14/09/2017	Bracken Ridge	49892	19/01/2017	Karawatha	2880	2/11/2014	Ransome	181477
7/09/2017	Chermside	2415	24/12/2016	Ransome	3705	6/10/2014	Wynnum West	217331
7/09/2017	Chermside	1665	24/12/2016	Lota	71	3/09/2014	Hemmant	48449
5/09/2017	Sandgate	3818	23/12/2016	Ransome	447	12/01/2014	Wynnum West	47532
1/09/2017	Runcorn	653	22/12/2016	Stretton	1220	31/12/2013	Nudgee	244318
18/08/2017	Parkinson	3057	22/12/2016	Ransome	31815	29/12/2013	Karawatha	173032
18/08/2017	Rochedale	21753	21/12/2016	Stretton	1692	9/08/2013	Hemmant	194041
17/08/2017	Parkinson	1089	23/10/2016	Brighton	24533	25/09/2012	Hemmant	40043
16/08/2017	Parkinson	816	16/10/2016	Wynnum West	4845	15/09/2012	Wynnum West	17062
10/08/2017	Fitzgibbon	41071	14/10/2016	Hemmant	30668	15/09/2011	Wynnum West	72330
23/06/2017	Drewvale	47	13/10/2016	Hemmant	2200			
16/05/2017	Brighton	951	29/09/2016	Karawatha	3546			

percent of 300 points would be 36 points, which have been randomly derived from this zone. For each fire event (polygon), a buffer zone was generated to avoid marginal fire region. Consequently, 300 nonfire samples were randomly extracted from the remaining areas for modeling purpose.

Our training and testing datasets were created using the space robustness technique, which divides the data into two categories without considering the dates of the events [42].

Once 300 inventory points were acquired, 300 nonfire points were compiled and the data was divided by random selection from the total inventory points according to the standard 70% training, 30% testing proportion [57–59].

*3.1.2. Influencing Factors.* Pourtaghi et al. [18] offers a good review of these factors. Since there is no accepted framework for dataset creation, many studies rely solely on data availability, expert knowledge, and literature [33, 60]. In this study, the primary influencing factors were selected by the traditional literature-based approach. Prior to the main analysis, a statistical multicollinearity analysis was performed on the selected factors (Section 3.2). Our initial selected influencing factors dataset consisted of altitude, slope, aspect, curvature, TWI, TPI, rainfall, geology, soil, LULC, distance from rivers, distance from roads, wind, and NDVI. These factors are the most cited and relevant according to the

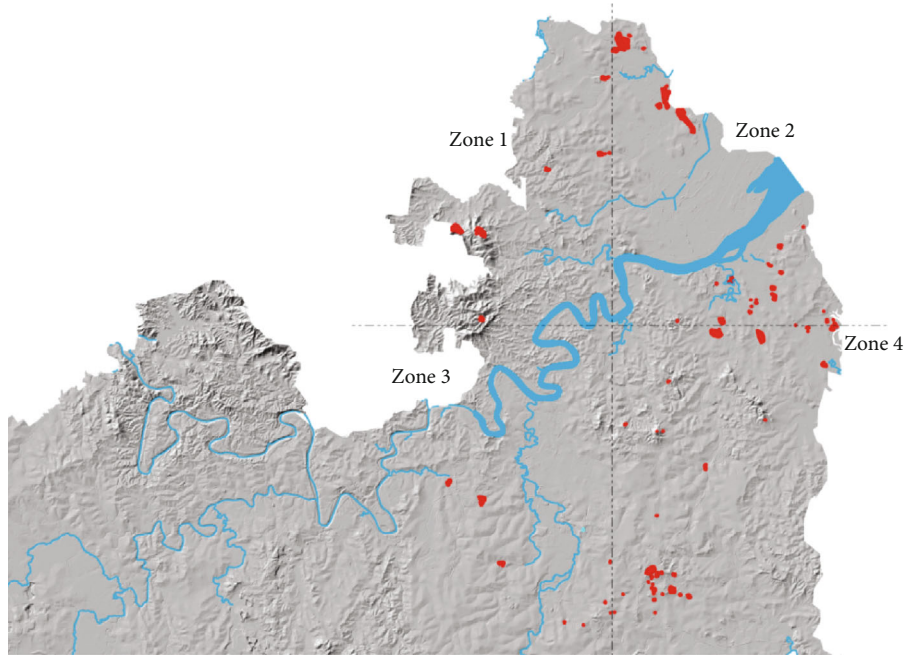


FIGURE 3: Inventory points selection zones. The division lines are arbitrarily located.

TABLE 2: Selection of forest fire random points with respect to their areas.

Map zones	Forest fire areas	Percentage of the forest fire areas	Number of random points
Zone 1	338360	12	36.00
Zone 2	1541738	54	162.00
Zone 3	54754	2	6.00
Zone 4	897361	32	96.00
Total	2832214	100	300.00

literature [18, 61, 62]. The factors were drawn from a variety of sources, which will be mentioned accordingly. A raw dataset was used to derive the primary influencing factors. This comprised (a) a digital elevation model (DEM) with 5-meter spatial resolution (produced from LiDAR data) was used to compute altitude, slope, aspect, curvature, TWI, and TPI; (b) soil map (1:250,000 scale) and geology map (1:100,000 scale) were obtained from the CSIRO and Australian government websites; (c) Landsat imagery which was used to provide NDVI map; (d) roads and rivers networks; and (e) rainfall and wind information from the meteorological stations. Through proper methods and conversions, each factor was prepared and imported to the GIS environment.

Topography is one of the most influential factors in wildfire occurrence. Precipitation, temperature, sun exposure, and wind are all related to the topography of the locality [63]. Topography can affect wildfire in different ways. Slope, aspect, and altitude influence solar radiation levels [64] and impact on the fuel moisture content [65]. The wildfire spread direction is often determined by topographical factors and wind [66]. Topography, fuels, and climate are recognized as

the three main elements in wildfire creation, spread, and intensity [67], with topography the most stable factor.

Altitude influences the wildfire behavior by affecting the extent and timing of precipitation, seasonal drying of fuel, and wind [68]. Higher temperature and lower rainfall in lower lands cause fuels to dry faster. Slope affects fuel preheating and, thus, the rate and direction of spread [69]. Fuel preheating can be affected by the slope. Sharp slopes preheat and dry upslope fuels, causing faster combustion [70]. Therefore, during the wildfire event, slope defines the direction of the spread [71]. Slope position and degree are both important factors in the extent of wildfire spread. Usually, the largest wildfires are initiated at the base of the slope. Additionally, fires tend to spread faster up a slope than down one [72]. Fire tends to move, and based on the landform types of the region, it transfers in various ways [73]. For instance, narrow canyons are one of the most dangerous forms of the land in the event of wildfires [74]. In such a condition, a greater degree of slope increases the destructive power of the wildfires. The reason is this landform creates strong updrafts of air, preheating the upslope fuels, thus, increasing the likelihood of heat transfer. In some cases, if the valley is narrow enough, it might initiate an outbreak of fire on the opposite side.

Aspect defines the direction of the slope. The impact of aspect on fuel temperature and moisture is apparent [75]. Aspect controls the solar radiation received, which indirectly influences the vegetation types and cover [76]. In the southern hemisphere, north-facing slopes tend to have less vegetation and lighter fuel loads, particularly in lower-elevation forests [77]. North slopes receive higher levels of solar radiation and are consequently warmer, so fuels tend to dry out sooner. On the other hand, south slopes contain more vegetation and, therefore, greater fuel quantities. The drying process for these slopes is slower due to shadows. In the case of

wildfire occurrence, they cause more severe wildfire. Curvature, which shows the morphology of topography, is another influential factor in wildfire occurrence [78]. Positive, negative, and zero curvature values specify that the surface is convex, concave, or flat, respectively [79]. One of the ways to evaluate the impact of topography on the hydrological characteristics of the region [80] is TWI. TWI shows the amount of flow accumulation at any point in a drainage basin and the downslope trend of the water by the power of gravity, and it measures the slope and direction of hydrologic flow [81]. The TWI thematic map was generated using the system for automated geo-scientific analyses (ArcGIS).

$$TWI = \ln \frac{\alpha}{\tan \beta}, \quad (1)$$

where  $\alpha$  is the cumulative up slope area draining through a point, and  $\tan \beta$  is the slope angle at the point [46]. Table 3 provides both detailed and general descriptions of soil types in the study area. This information is useful for land management and planning.

TPI defines or characterizes shapes such as canyons and ridges [82]. This factor reflects the difference in elevation between a focal cell and all cells in the neighborhood [83], which can make a simple and useful means to classify the landscape into morphological classes.

One of the characteristics of the study area that has a direct and indirect influence on wildfire incidents is weather condition [63]. Factors such as fire ignition potential, severity, heat transfer, and intensity are all associated with weather condition [84]. Fuel moisture and humidity are directly associated with the precipitation amount [85], while wind speed affects heat transfer and direction [86].

LULC is considered a significant influencing factor for wildfire, as well as for other natural hazards, such as flooding and landslide [87]. In this research, the LULC factor, consisting of 56 classes, was used to investigate the most influential land cover type on wildfire.

In terms of wildfire, vegetation can be grouped into ground fuels (e.g., roots) [88], surface fuels (e.g., grass) [89], ladder fuels (e.g., small-size trees) [90], and crown fuels (e.g., forest canopies) [91]. The wildfire combustion and behavior are highly affected by the size, moisture, and chemical content of the fuels [92]. Regarding the chemical content of fuels, some vegetation-like shrubs contain volatile oils, which make them to burn with higher intensity [93]. Shrubs have small branches as well which can create long flame lengths. Combustible biomass can be measured from a variety of sources. One of the main sources is NDVI. This factor is determined by the density of vegetation in the area using remote sensing [94]. As shown below, to calculate the NDVI the near-infrared (NIR) and red channels of Landsat, imagery was used.

$$NDVI = \frac{(NIR - RED)}{(NIR + RED)}. \quad (2)$$

**3.2. Multicollinearity Analysis.** As was mentioned, not all causative factors were selected for the final modeling.

Although there is no framework available to define the most influential factors, there are a number of statistical models that can assist researchers in their data selection [95]. These methods are able to statistically evaluate a group of factors and highlight the least significant and/or the factors that have duplicate impact. Through these assessments, redundant and less-effective factors can be eliminated from the dataset to decrease the computational time and complexity and increase the functionality. The correlations between factors were evaluated prior to the main analysis using Pearson's correlation coefficients [96] and variance inflation factors (VIF) [97] to exclude multicollinearity [98], which causes errors in analysis [99].

The degree of a factor's interrelatedness with other influencing factors can be calculated using VIF [100] and represents the influencing factor's estimated regression coefficient accordingly. The square root of VIF shows the standard error for that factor. A VIF of 5 or 10 and greater represents a multicollinearity problem in the dataset [95].

The Pearson's correlation coefficients method evaluates the correlation coefficient of two influencing factors, for example, aspect (Sl) and geology (As) in wildfire occurrence [101]. The correlation value is calculated by their covariance divided by the product of their standard deviations (Eq. (3)). A measured value greater than 0.7 indicates a high level of collinearity in the dataset [95].

$$r_{Sl,As} = \sum_{i=1}^n \frac{Sl_i - \bar{Sl}}{\sqrt{\sum_{k=1}^n (Sl_k - \bar{Sl})^2}} \cdot \frac{As_i - \bar{As}}{\sqrt{\sum_{k=1}^n (As_k - \bar{As})^2}}, \quad (3)$$

where  $\bar{Sl}$  is the mean of Sl.

When either of these methods reaches their threshold values, the collinearity should be reduced by eliminating one or more factors from the analysis [97].

**3.3. Bivariate Statistical Analysis (BSA).** The two selected BSA methods were IoE and EBF. The application of IoE is based on the methodology proposed by Vlcko et al. [102], in which the weight value for each factor is expressed as an entropy index. The approach to EBF is based on the Dempster-Shafer theory of evidence [103].

**3.3.1. Index of Entropy Model (IoE).** Entropy is an assessment of the disorder, instability, imbalance, and uncertainty of a system [104], and, according to Boltzmann's principle, the measurement of entropy of a system describes its thermodynamic state in terms of its degree of disorder. Shannon's entropy model for information theory is regarded as superseding Boltzmann's principle [105]. Applying the Shannon model of information, a weighted index of wildfire hazard based on the environmental influencing factors can be extracted.

$$P_{ij} = \frac{b}{a}, \quad (4)$$



TABLE 3: Description of soil units of the study area (based on Queensland soils and land systems) (source: <http://researchbank.rmit.edu.au/>).

Soil ID	Detailed	General
Fu3	Steep hilly to mountainous terrain on metasediments and phyllites rising to 2800 ft above sea level: dominant soils on the slopes are shallow and stony leached loams (Um2.1), as well as (Um5.2) loams.	Shallow and stony leached loams
Tb64	Rolling to hilly terrain with gentle to moderate slopes: dominant soils are hard, acidic, and yellow (Dy3.41) and red (Dr3.41) mottled soils. Associated are hard alkaline yellow (Dy3.43) and red (Dr3.43) mottled soils; sandy acidic yellow mottled soils (Dy5.41), (Dy5.31), and (Dy5.81) and leached sands (Uc2.2), all containing large amounts of nodular ironstone material, also with mottled clays, at depth below the (Uc2) soils.	Sandy and silty clay
Mp6	Low coastal basaltic plateaux and islands of Moreton Bay (about 50 ft above sea level): dominant soils are red friable earths (Gn3. 11) on the gently undulating to flat ridge tops with (Gn3. 14) soils on the beveled slopes of the ridges	Mixed grouping consisting of sand and clay
NY3	Coastal plains, lower and middle reaches of river flood-plains, swamps, estuarine areas, and tidal marshes, generally low-lying poorly drained areas subject to flooding: dominant soils seem to be sandy-surfaced soils, friable acidic grey soils (Dg4.11), (Dg4.41), and (Dg4.81); friable acidic yellow mottled soils (Dy5.11); and acidic grey friable earths (Gn3.91). Associated soils are (Dg2.41), (Dd3.11), and (Db4.11).	Sandy soil
Tb65	Gently rolling areas of the subcoastal lowlands (less than 400 ft above sea level) with a maximum relief of 50 ft between crests and valleys. The soil pattern is complex and controlled by the lithology of the parent rock material. Dominant soils are deep-surfaced loamy duplex (Dy3.41), (Dy3.42), (Dr3.41), and (Dr2.12) on sandstones.	Deep-surfaced loamy duplex
Mm2	Undulating landscape with linear gilgais on some slopes: crests and upper ridge slopes of cracking red-brown clays (Ug5.37) or loamy soils with red clay subsoils (Dr2.33), passing down the slope to cracking brown clays (Ug5.32) on gilgai puffs and cracking grey clays (Ug5.23) in gilgai depressions.	Clay and loamy soil
MM9	Terraced valley plains: dominant soils are brown and grey cracking clays (Ug5.34), (Ug5.39), and (Ug5.2) which occur on the third terrace with (Gn3.21), (Dy3.41), and (Dy3.13) soils.	Sandstones and shales
Fu2	Hilly to steep hilly areas of metasediments and phyllites, traversed by narrow valley plains along the streams: dominant soils are shallow and stony leached loams (Um2.12) and also (Um5.2) loams.	Shallow stony loams
Cd3	Steep hilly to mountainous land: dominant soils seem to be leached sands (Uc2.12) and siliceous sands (Uc1.21 and Uc1.22) on sandstones; grey cracking clays (Ug5.23) on shales; and shallow red clays (Uf6.12) on basalt.	Sandy and clay soils
Sj12	Lower to middle reaches of stream flood-plains: dominant soils are hard, acidic yellow and yellow mottled soils (Dy2.41) and (Dy3.41) with (Dd1.41) on the flat areas, together with leached sands (Uc2.33 and Uc2.32) on low broad sandy banks. Other soils include (Gn3.01) and (Uf6).	Leached sands
Mw30	Gently undulating area of tertiary sediments and igneous rocks: dominant soils are clay loam to light clay texture.	Clay loam to light clay texture
Kb28	Low hilly terrain on basalts and sedimentary rocks: dominant soils are moderate and shallow forms of dark cracking clays (Ug5.14, Ug5.12, and Ug5.13) on the slopes.	Dark cracking clays
P11	Hilly country of sandstones and intruded intermediate and basic rocks, rising to 800 ft above sea level: dominant soils on the moderate to steep slopes are hard acidic red and yellow soils (Dr3.41), (Dr2.41), and (Dy3.41) with some areas of (Dy3.43) and (Dr3.43) soils.	Light sandy loam
Tb62	Undulating to hilly valley slopes flanking creek and river flood-plains: dominant soils on the gentle to moderately steep slopes are hard acidic yellow mottled soils (Dy3.41), (Dy3.21), and (Dy3.61).	Hard-setting loamy soils with mottled yellow clayey subsoils
Kb12	Gently rolling areas of the subcoastal lowland (less than 400 ft above sea level) on altered basic rocks; maximum relief is 50 ft between crests and valleys: dominant soils are shallow dark cracking clays (Ug5.12) with hard neutral red and yellow soils (Dr2.12) and (Dy2.12).	Shallow dark cracking clays

TABLE 3: Continued.

Soil ID	Detailed	General
LL6	Mountainous: steep slopes of loamy soils with an A2 horizon (Um4.2), yellow-brown earths, (Gn2.44), and rock outcrops.	Loamy soils
Rh9	Steep hilly to mountainous: dominant soils seem to be dark-brown friable loam surface soil underlain by light-red to brownish-red heavy but friable clay	Dark-brown friable loam surface
Me8	Low hilly area of tertiary sediments and igneous rocks: dominant soils are brown (Gn3.22) and dark (Gn3.42) friable earths and shallow dark cracking clays (Ug5.12) on the deeply altered igneous rocks.	Sediments and clay
Kd6	Valley plains: dominant soils are dark, cracking clays (Ug5.15 and Ug5.16). Associated are areas of other soils, including (Dd1 .41) and (Dy2.41) on broad terraces.	Dark, cracking clays
Mg26	Plateaux and plateau remnants in mountainous country at moderate to high elevation (>1000 ft): loamy soils, rolling hills of red friable porous earths (Gn4.11), and/or brown friable porous earths (Gn4.31).	Crusty loamy soils

$$(P_{ij}) = \frac{P_{ij}}{\sum_{i=1}^{S_j} P_{ij}}, \quad (5)$$

$$H_j = - \sum_{i=1}^{S_j} (P_{ij}) \log_2(P_{ij}), j = 1, \dots, n, \quad (6)$$

$$H_{j\max} = \log_2 S_j, S_j - \text{number of classes}, \quad (7)$$

$$I_j = \frac{H_{j\max} - H_j}{H_{j\max}}, \quad (8)$$

$$W_j = I_j P_{ij}, \quad (9)$$

where  $a$  and  $b$  are the domain and wildfire percentages, respectively,  $P_{ij}$  denotes the density of the occurrence of wildfire for every class of every influencing factor (e.g., each type of geology),  $H_j$  and  $H_{j\max}$  denote the entropy values,  $I_j$  is the information coefficient, and  $W_j$  represents the calculated weight value for the specific influencing factor, without consideration of the classes.

The final wildfire susceptibility map was generated by summing the weighted products of the secondary parametric maps. The following equation was used to develop the final wildfire susceptibility map from the IoE model.

$$\begin{aligned}
Y = & \left( (\text{Altitude} * W_j) + (\text{Slope} * W_j) + (\text{Aspect} * W_j) \right. \\
& + (\text{Curvature} * W_j) + (\text{TPI} * W_j) + (\text{Rain} * W_j) \\
& + (\text{Geology} * W_j) + (\text{Soil} * W_j) + (\text{LULC} * W_j) \\
& + (\text{Distance from Rivers} * W_j) \\
& + (\text{Distance from Roads} * W_j) \\
& \left. + (\text{Wind Speed} * W_j) \right), \quad (10)
\end{aligned}$$

where  $Y$  is the value of the wildfire susceptibility index.

**3.3.2. Evidential Belief Function (EBF).** The Dempster–Shafer theory of evidence has been introduced by Dempster [106],

and the EBF method has been applied to other natural hazards such as flooding [107] and landslide [108]. Its relevance in natural hazard modeling is that it can accept uncertainty and can integrate information from multiple sources of evidence [109]. It is used for assessing the degree of probability of the truth of a hypothesis, as well as for evaluating the nearness with which the evidence comes to proving the truth [110]. Its functional parameters are the degrees of belief (Bel), disbelief (Dis), uncertainty (Unc), and plausibility (Pls) [111]. The proposition's lower and upper limits of the probability are denoted by Bel and Pls, respectively; the difference between belief and plausibility by Unc, which describes ignorance [112]; and the belief that the proposition is false based according to the evidence by Dis, where  $\text{Dis} = 1 - \text{Pls}$  or  $1 - \text{Unc} - \text{Bel}$ , provided that  $\text{Bel} + \text{Unc} + \text{Dis} = 1$ . In the situation where a class of an influencing factor does not contain any wildfire event, Bel is equal to zero, and Dis is reset to zero. Applied to wildfire occurrence, the EBF estimates the spatial correlations among the classes of each conditioning factor. An overlay of the inventory map on each influencing factor layer displays the pixels that could contain wildfire or nonwildfire influencing factors. A set of factors,  $C = (C_i, i = 1, 2, 3, \dots, n)$ , which contains mutually exclusive and exhaustive factors of  $C_i$ , was used in this study. The calculation is performed using the equation:

$$\text{Bel}(C_{ij}) = \frac{W_{C_{ij}(\text{wildfire})}}{\sum_{j=1}^n W_{C_{ij}(\text{non-wildfire})}}, \quad (11)$$

where the weight of  $C_{ij}$  (e.g., weight of the first class of altitude) is represented by  $W_{C_{ij}(\text{wildfire})}$  and supports the belief that the existence of wildfire exceeds its absence.  $W_{C_{ij}(\text{non-wildfire})}$  denotes the weight of  $C_{ij}$  that supports the belief that wildfire absence exceeds its presence. EBF calculation requires several stages which are not explained in this paper. A more detailed description can be found in Bui et al. [113].

**3.4. Multivariate Statistical Analysis (MSA).** As stated, a BSA method evaluates the impact of each class of each influencing

factor on wildfire occurrence (e.g., the impact of different types of geology on wildfire). In terms of our research objective, the most accurate BSA method will be selected to perform the ensemble modeling with LR. LR is one of the most popular MSA methods to examine the multivariate regression relationship among a dependent factor (e.g., flooding) and several independent influencing factors (e.g., altitude and slope) [114].

For our research purposes, LR is used to measure the wildfire probability in an area, based on a specific formula created by the influencing factors and a dependent factor. The method necessitates a dependent factor established by values of 0 and 1, indicating the nonexistence or existence of wildfire, respectively. The factor was created in ArcGIS using the inventory dataset. To create this dataset, the original influencing factors were reclassified using the BSA weights derived from the most accurate method (either IoE or EBF) in order to implement the ensemble modeling. Subsequently, the dependent and reclassified influencing factors were converted from raster to ASCII format as a requirement of SPSS. LR was executed in the SPSS V.19 software environment. The logistic coefficients were derived and used as inputs in the equation below to measure the final wildfire susceptibility map.

$$P = \frac{1}{(1 + e^{-z})}, \quad (12)$$

where  $P$  is the wildfire probability in the range 0 to 1 on an S-shaped curve.  $Z$  is the linear combination and it follows that LR involves fitting an equation of the following form to the data:

$$z = b_0 + b_1x_1 + b_2x_2 + b_3x_3 + \dots + b_nx_n, \quad (13)$$

where  $b_0$  is the constant intercept of the model,  $b_i (i = 0, 1, 2, \dots, n)$  represents the weight coefficients of the LR model for each factor, and  $x_i (i = 0, 1, 2, \dots, n)$  represents the influencing factors [47].

**3.5. Ensemble Modeling.** For the purpose of the ensemble, the weights derived from the more accurate BSA method (either IoE or EBF) will be used to reclassify each wildfire influencing factor. Subsequently, the reclassified factors will be entered into LR as input variables in order to perform the MSA. The derived final wildfire susceptibility map will be based on this ensemble modeling. Through this integration, the weak points of BSA and MSA will be resolved, and the outcome will be an integration of the two analyses.

**3.6. Accuracy Assessment.** Model validation is a fundamental step in any natural hazards study [115]. The well-known area under curve (AUC) technique has been used in many natural hazard susceptibility mapping studies [116–118], producing the prediction and success rates by means of a comprehensive quantitative method [119]. The validation was achieved by comparing the wildfire inventory data and derived probability maps. The wildfire probability map was initially partitioned into classes of equal area, and these were then

TABLE 4: Multicollinearity diagnosis indices for variables.

No.	Influencing factors	VIF
1	Altitude	3.42
2	Slope	4.37
3	Aspect	2.61
4	Curvature	1.71
5	TWI	6.32
6	TPI	3.99
7	Rainfall	1.09
8	Geology	4.98
9	Soil	4.11
10	LULC	1.38
11	River	1.82
12	Road	0.69
13	Wind	0.03
14	NDVI	9.22

ranked hierarchy from minimum to maximum value [95]. Prediction accuracy was evaluated qualitatively, using AUC by sorting all cells in the study area into a hierarchy of calculated values, arranged in descending order, thus, ranking each prediction. Hence, the values of cells were divided into 100 classes with 1% accumulation intervals. In the subsequent step, the presence of wildfire in each interval was measured using the ArcGIS “Tabulate area” tool. The success and prediction curves denote the percentage of wildfire in each probability class. The curve creation was implemented by plotting the cumulative percentage of areas susceptible to wildfire (from highest to lowest probability) on the  $x$ -axis and the cumulative percentage of wildfire events on the  $y$ -axis. The success and prediction curves determine the percentage of wildfire occurrence for each probability category; the more wildfire events in categories of greater susceptibility, the steeper the AUC curve [95]. A perfect classification occurs where  $AUC = 1$ , rather than one by chance where  $AUC = 0.5$ . The 70% training and 30% testing points will be used to generate the success and prediction rates, respectively, as mentioned in Section 3.1.1. 210 wildfire inventory points were used for training and the remaining 90 points for testing.

## 4. Results and Discussion

**4.1. Correlation Analysis.** Multicollinearity among the wildfire influencing factors has been implemented. Tables 4 and 5 listed the VIF and Pearson’s correlation coefficient values, respectively. As mentioned in the methodology section, a VIF can be computed for each predictor in a predictive model. A VIF value of 1 means that the wildfire influencing factor is not correlated with other factors. The greater the VIF value, the greater the association of the factors with other factors is. A VIF above 5 indicates multicollinearity in the dataset. Table 3 shows that the highest VIF values are 9.22 for NDVI and 6.32 for TWI factors which are above the threshold. In the case of Pearson’s correlation, values greater

TABLE 5: Pearson correlations between pairs of forest fire influencing factors.

Influencing factors	Altitude	Slope	Aspect	Curvature	TWI	TPI	Rainfall	Geology	Soil	LULC	River	Road	Wind	NDVI
Altitude	<b>1</b>													
Slope	0.3	<b>1</b>												
Aspect	0.04	0.5	<b>1</b>											
Curvature	0.02	0.003	-0.03	<b>1</b>										
TWI	0.0001	0.007	0.08	0.6	<b>1</b>									
TPI	0.0004	0.5	0.001	-0.009	-0.01	<b>1</b>								
Rainfall	0.00006	0.004	-0.002	0.003	0.9	0.2	<b>1</b>							
Geology	0.007	0.05	-0.2	0.0002	0.1	0.09	0.006	<b>1</b>						
Soil	0.0008	0.006	0.03	0.01	0.0005	0.003	0.003	0.4	<b>1</b>					
LULC	0.001	0.6	0.009	-0.2	-0.006	0.5	0.009	0.1	0.2	<b>1</b>				
River	0.3	0.02	0.008	0.0001	0.6	0.0001	0.003	0.0002	-0.01	0.006	<b>1</b>			
Road	-0.001	0.001	0.3	0.0003	-0.009	0.4	0.5	0.0007	0.009	0.002	0.01	<b>1</b>		
Wind	-0.6	0.3	0.5	0.1	0.0001	0.00001	0.03	0.01	0.002	0.0008	0.0001	0.006	<b>1</b>	
NDVI	0.004	0.05	0.003	0.2	0.004	0.4	0.0005	0.1	0.06	0.8	0.0005	0.02	0.0007	<b>1</b>

than 0.7 denote high collinearity. The diagonal elements (bold text) are the correlations between each variable and itself. Therefore, their value is always equal to 1. In Table 5, the highest value of 0.9 derived between TWI and rainfall represents a considerable collinearity. The second highest collinearity of 0.8 was detected between LULC and NDVI. Both outcomes of VIF and Pearson's correlation analysis suggest that by including TWI and NDVI in the analysis, the problem of collinearity may arise. These outcomes show that other factors of LULC and rainfall in the dataset already provided adequate information, which would merely be duplicated if we include the TWI and NDVI.

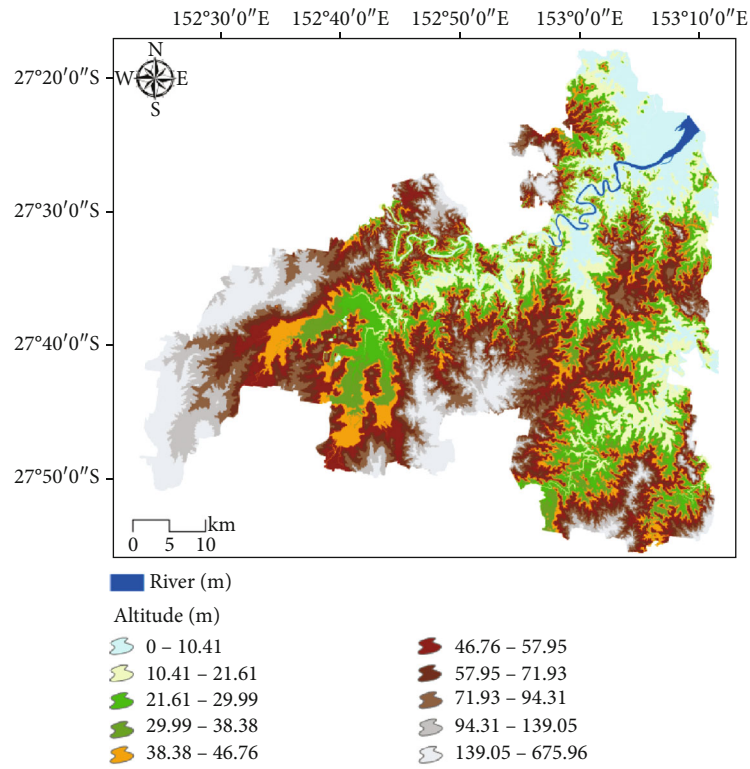
The final selected wildfire influencing factors dataset includes altitude (Figure 4(a)), slope (Figure 4(b)), aspect (Figure 4(c)), curvature (Figure 4(d)), TPI (Figure 4(e)), rain (Figure 4(f)), geology (Figure 4(g)), soil (Figure 4(h)), LULC (Figure 4(i)), distance from river (Figure 4(j)), distance from road (Figure 4(k)), and wind speed (Figure 4(l)). As it can be seen in Figure 4, all the scaled influencing factors have been classified due to the requirement of the BSA techniques. The quantile method was used for the classification [120]. The advantage of quantile is that features are grouped equally in each category (equal-sized subdivisions), with the least external influence. Table 6 represents the statistics related to the scaled wildfire influencing factors, such as minimum, maximum, mean, and standard deviation. For instance, the highest location in the study area has an altitude of 217 m. All the factors were transferred to IoE and EBF in order to extract the correlations among their classes and wildfire occurrence.

*4.2. Weights Derived from Correlation Analyses.* Both IoE and EBF were individually implemented, and the derived weights are listed in Table 7. IoE was computed by considering the frequency of different classes of influencing factors, which significantly reduces the unevenness among the factors and, therefore, provides a realistic and accurate metric of their

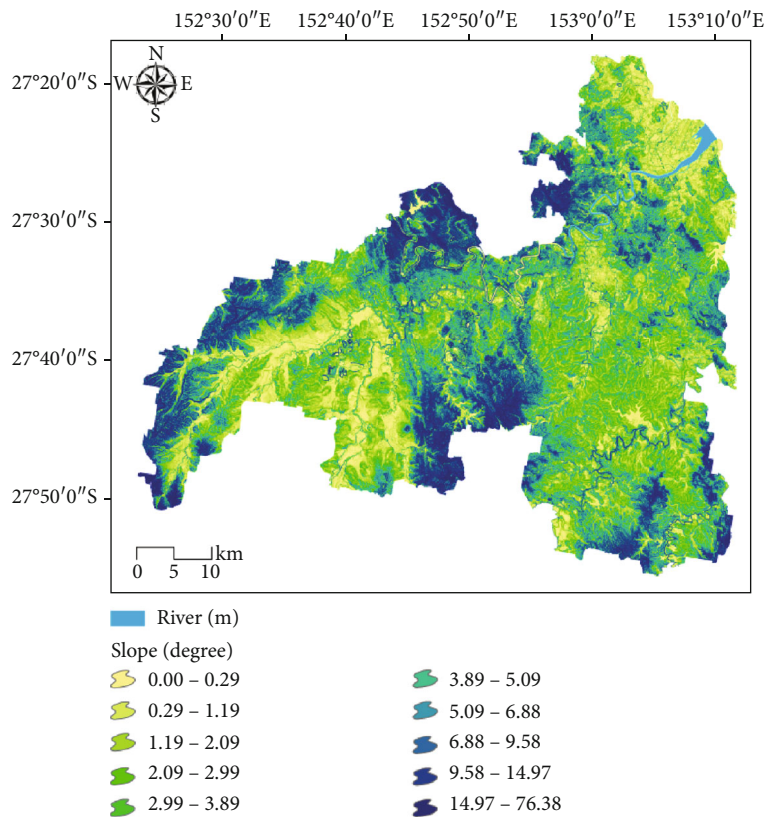
influence on wildfire occurrence. The result of the bivariate analysis of IoE is shown by  $P_{ij}$  values in Table 6.

In the case of EBF, the weights of the bivariate analysis derived for each class were represented by the Bel value. There were some similarities in the calculation of IoE and EBF up to this point, implying that the values of  $P_{ij}$  and Bel were very close. However, this was not the case for the remainder of the processing and the final probability map creation. From this stage forward, there are specific equations related to each method. Using these equations, the correlation assessments were applied to the derived BSA weights from IoE and EBF, and two wildfire probability maps were produced. In order to avoid repeating the BSA values from IoE and EBF, only IoE values will be discussed below.

The outcomes based on BSA values (IoE and EBF) denote that the slope, in the last two ranges of 9.58-14.97 and 14.97-76.38 degree, had the highest values of 0.296 and 0.164, respectively. It is already known that fire on the steep slopes tends to move faster and causes more severe burning. Therefore, these classes of slope received higher weights. The highest derived value (0.248) of rainfall is for the smallest class of rainfall ranging between 536.00-671.32 mm. It is clear that wildfire susceptibility increase by the decrease in rainfall [121]. High rainfall and relative humidity contribute to fuel moisture, which in turn reduces the probability of ignition. With regard to altitude, the middle classes seem to have the highest influence on wildfire occurrence. The class of 46.76-57.95 m with a BSA of 0.338 was detected as the most influential category. The spatial correlation between wildfire incidence and altitude reveals that when the altitude increases, the probability of wildfire decreases. This result is supported by previous findings that low-elevation areas are more vulnerable to fire occurrence [122]. The relation between curvature and wildfire probability revealed that the convex class has the highest BSA value of 0.548. In the case of aspect, the BSA value is highest for northeast-facing slopes with a value of 0.229. As noted in Section 3.1.2, north-facing slopes

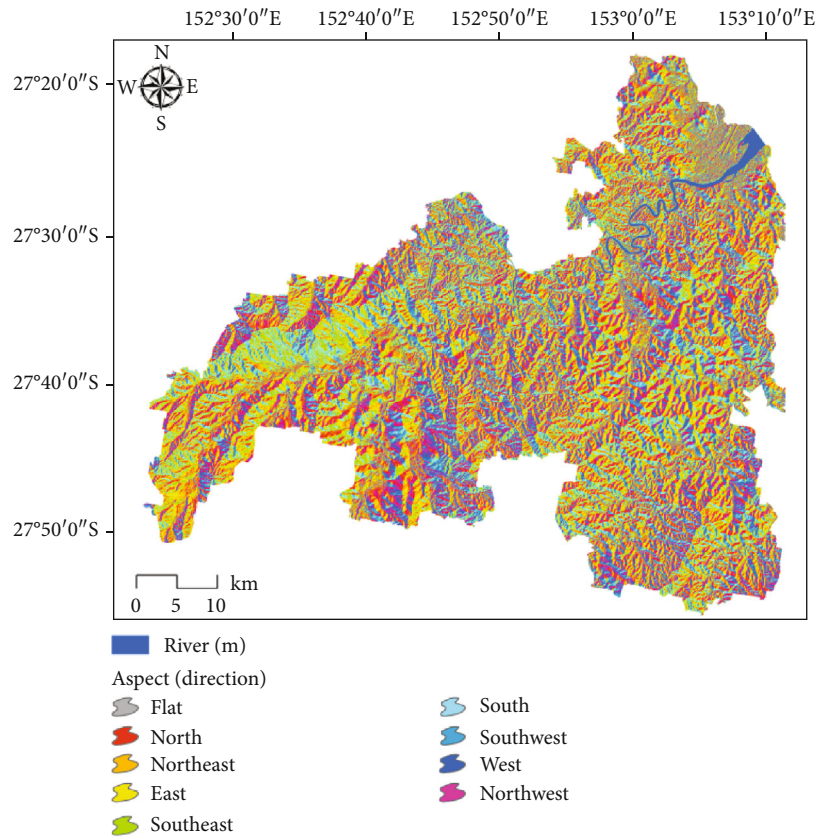


(a)

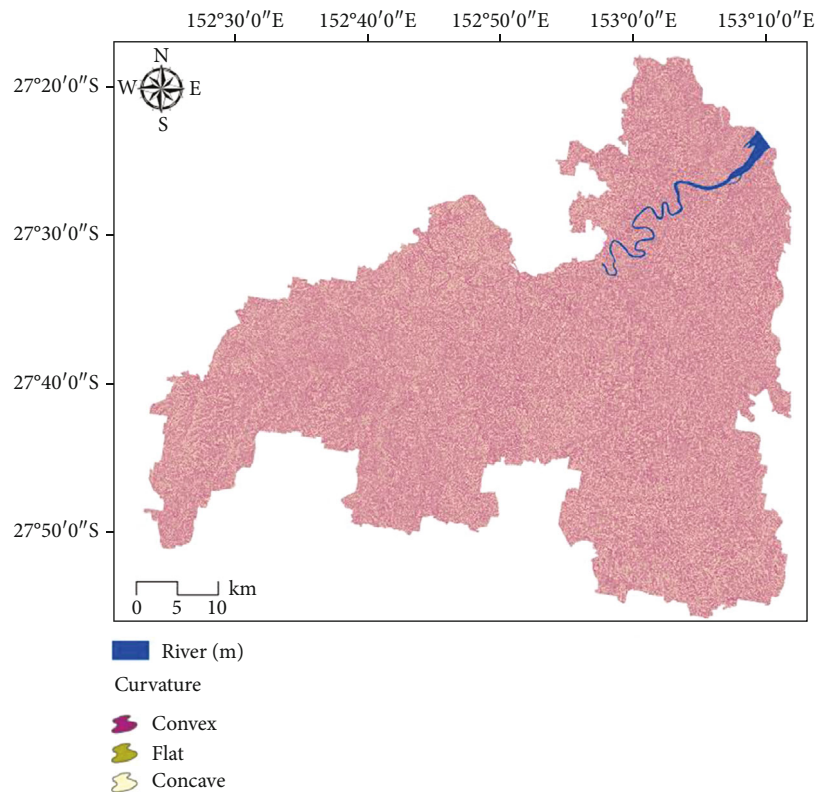


(b)

FIGURE 4: Continued.

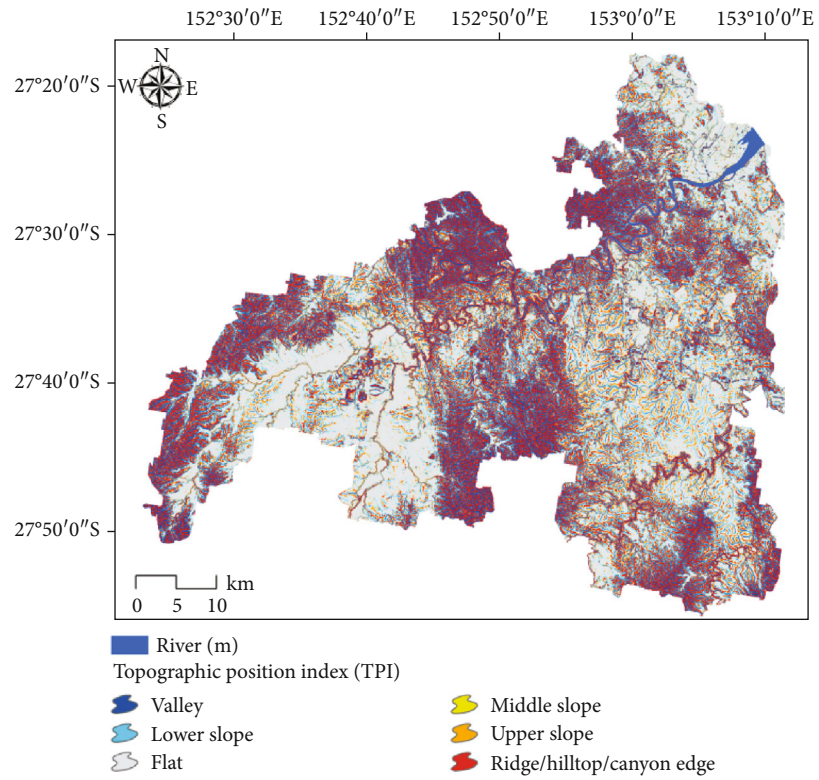


(c)

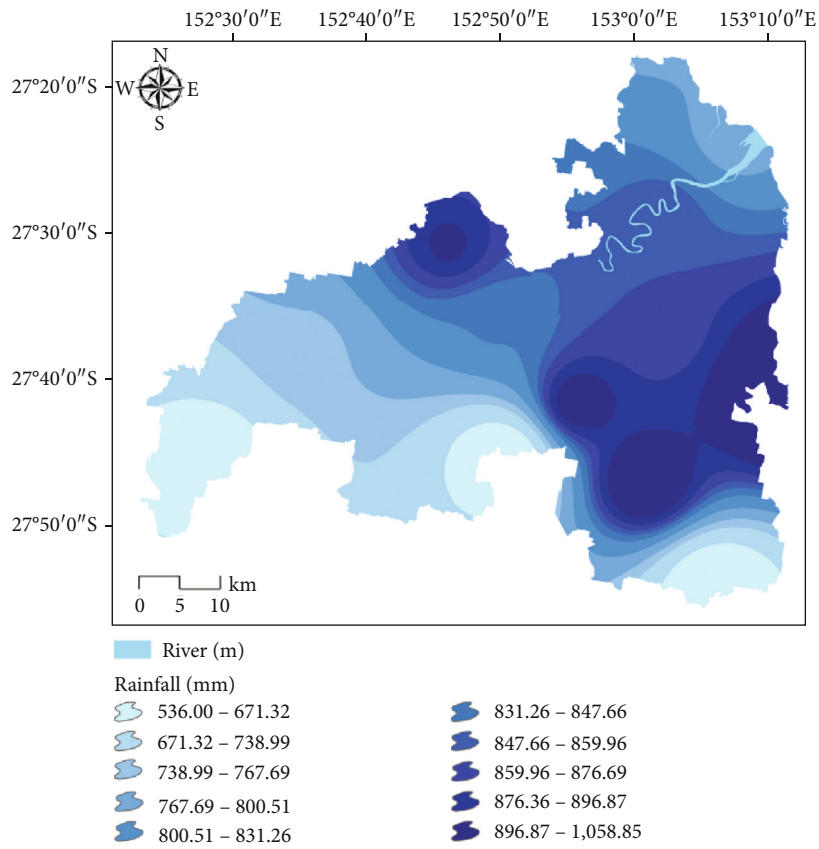


(d)

FIGURE 4: Continued.



(e)



(f)

FIGURE 4: Continued.

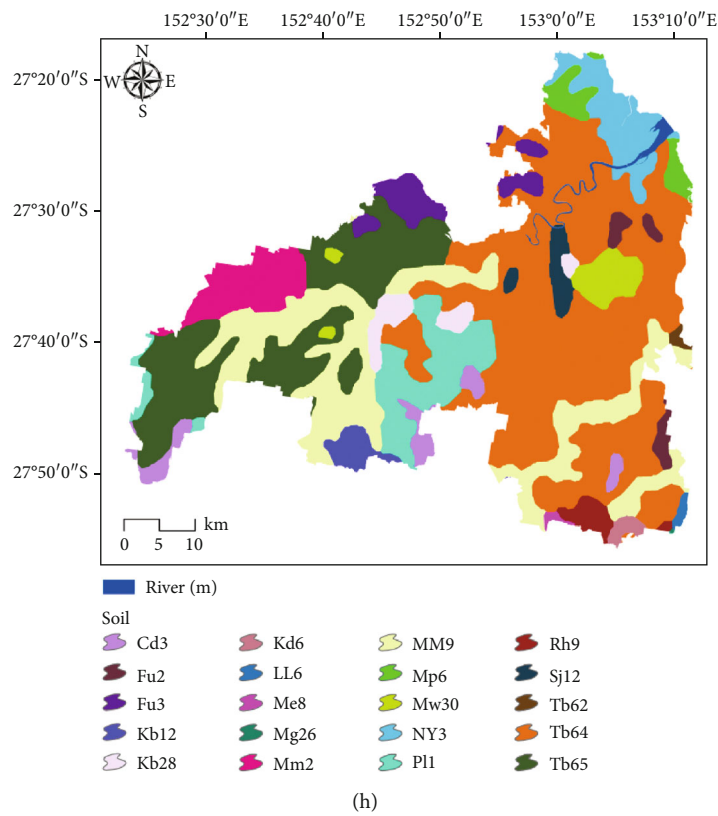
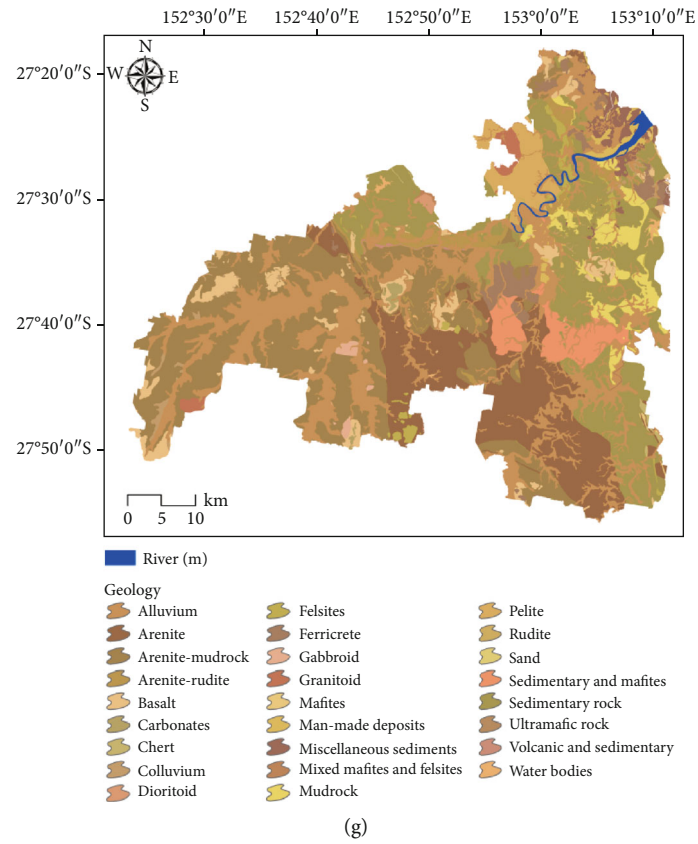
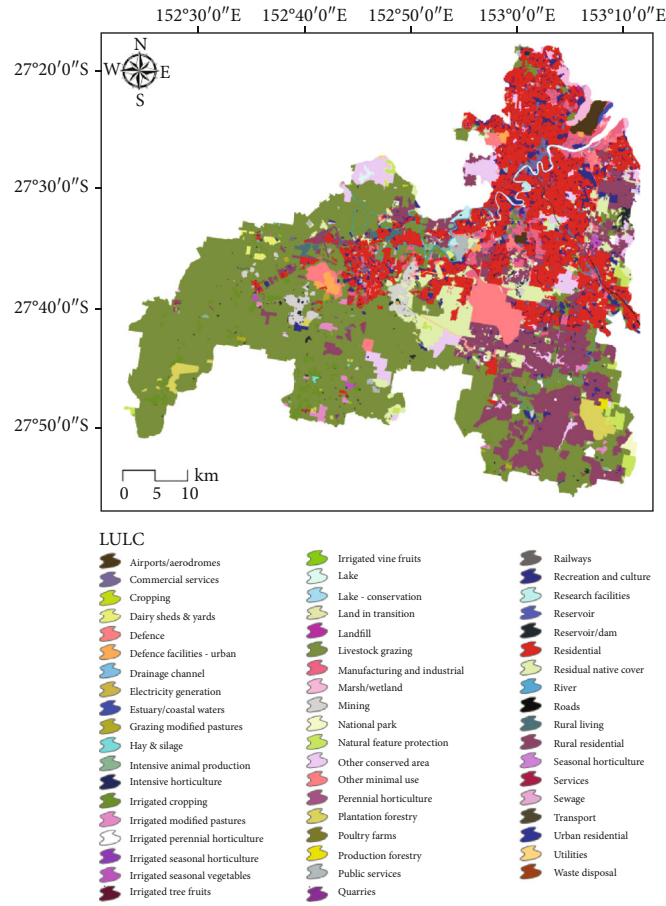
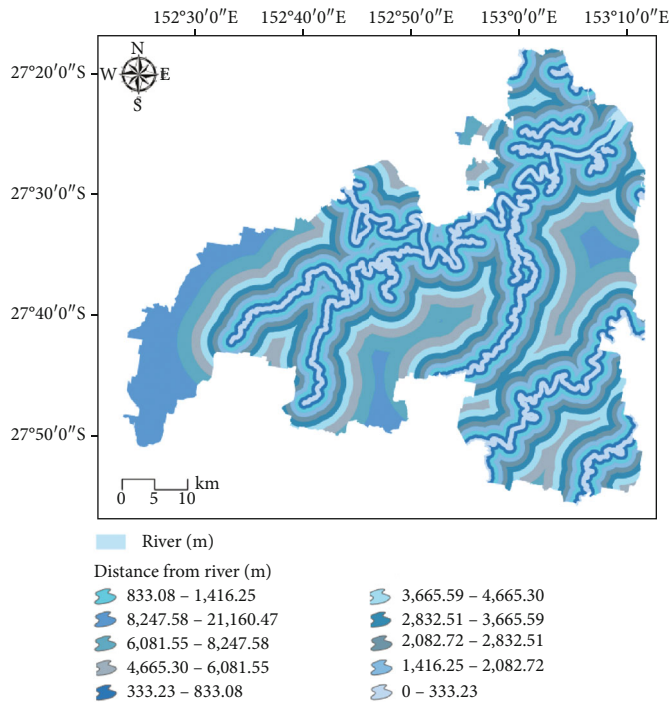


FIGURE 4: Continued.



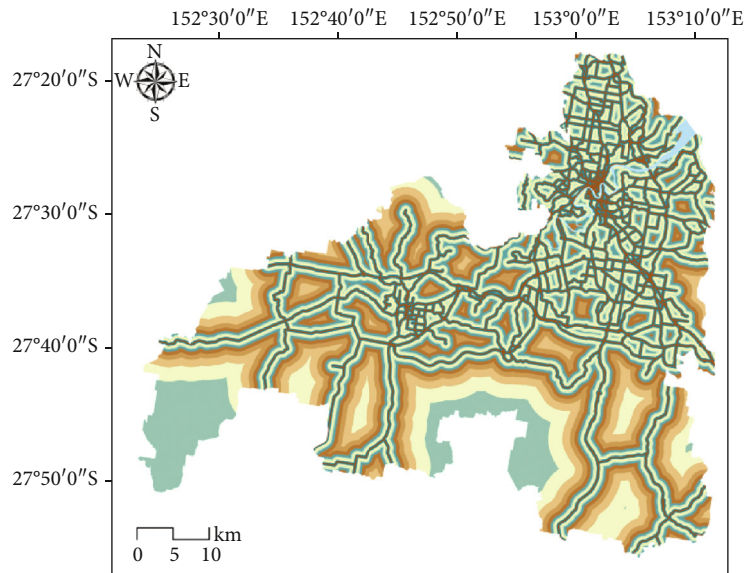


(i)

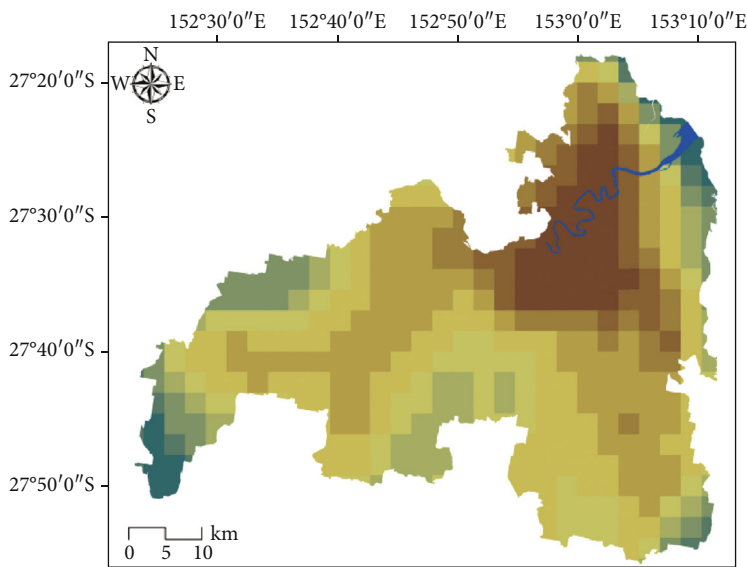


(j)

FIGURE 4: Continued.



(k)



(l)

FIGURE 4: Influencing factors consisting of (a) altitude, (b) slope, (c) aspect, (d) curvature, (e) TPI, (f) rain, (g) geology, (h) soil, (i) LULC, (j) distance from river, (k) distance from road, and (l) wind speed.

TABLE 6: Descriptive statistics of continuous parameters with respect to forest fire locations map.

Influencing factors	Minimum	Maximum	Mean	Standard deviation
Altitude	0.038	217.09	26.29	44.91
Slope	0.0012	43.62	4.02	6.71
Curvature	-31.72	37.37	0.019	2.23
Rainfall	788.84	886.45	823.07	29.12
River	0	9341.12	2273.05	1819.59
Road	0	1611.19	403.42	365.25
Wind	3.09	4.3	3.67	0.26

obtain more solar radiation and are consequently warmer, so fuels tend to dry out sooner. This may be a logical explanation for the derived weight for this aspect class. Results for the TPI factor show that the ridge landform is relatively conducive (highly susceptible) to wildfire occurrence. Wildfires on ridges can burn in any direction and by wind can move up through saddles and canyons. The steep slope runs off the water faster and keeps a smaller amount of moisture content and ridge areas acted as a steep slope. Therefore, those areas are more prone to the fire hazard if were covered by vegetation. For distance to rivers, the highest wildfire probability is within distances 1,416.25–2,832.51. In the case of distance to roads, the distance of 240.99–481.99 m to roads has the highest susceptibility. Both distances to rivers and roads were recognized as positive factors in this study, as they act like barriers towards fire spread. There are features like lakes, roads, and rivers, which act as barriers to wildfire spread [123], preventing the continuity of fire in the area. Ridges have a similar influence, acting like fuel breaks, interrupting the continuation. Some landform types can influence prevailing wind patterns by funneling air, wind speed, and, thus, fire intensity [124]. The BSA weights for soil showed clearly that the class of “Mp6” has the greatest effect on wildfire occurrence. The dominant soil types of this class are sand and clay, which usually have very low moisture content. The geology types of “Granitoid” and “Miscellaneous unconsolidated sediments” had the highest BSA weights of 0.268 and 0.231, respectively. Regarding the LULC factor, cropping received the highest weight of 0.252 among LULC types followed by residential. The class of 4.09–4.19 in wind factor had the highest value of 0.335. The highest weights were derived for the classes that have a very high influence in triggering wildfires due to clear reasons that have been stated.

Table 7 also lists information regarding the MSA. In the case of IoE, in addition to the derived BSA weights for each class, this method also provided a relevant weight for each influencing factor itself ( $W_j$ ). LR weights represent the MSA weights for each influencing factor derived from the ensemble modeling of LR. This implies that the derived weights from LR are according to the classified influencing factors imported from BSA analysis. The findings based on IoE revealed that the most important wildfire influencing factors affecting the wildfire distribution were soil (1.251) and

geology (0.623). LR ensemble MSA outcomes showed that LULC and soil received the highest weights of 0.781 and 0.653, respectively. The soil characteristics and its effect on forest fire were discussed in [83] and were consistent with our finding. Apart from the topographic and geologic factors (e.g., TPI and soil) influencing the bushfire in the region, it was obvious that LULC played a major role as triggering factors. In detail, as it was revealed by BSA weighting values and susceptibility map, cropping and residential areas gained higher weight and were more susceptible to the fire risk rather than other LULC. It highlighted that human activity contributed to that hazard as well. The influence of the residence area as an important factor was in agreement with Tien Bui et al. [32] and Kalantar et al. [35]. Therefore, more detailed investigation is desirable by the management committee to find some of the reasons (e.g., cigarettes, grinding activities, and power lines adjacency) in widening the bushfire in residential areas. Another detected human activity in the area was cropping, and it needs to be carefully explored according to the crops and process of cultivation. Some parts of the cropping process might contribute to worsen the fire in its intensity and speed such as intentional ignition for agricultural clearing or wrapping the bunch of bananas in plastic bag on the plant to reduce the ripening time, which can magnify the fire as fuel. This could improve the decision upon revising the process of cropping in those susceptible areas.

The IoE and LR methods demonstrated some similarities and differences in outcomes in the analysis of the influencing factors. TPI and soil were identified as considerable influencing factors in both models. Penman et al. [125] concluded that on ridges with higher TPI, the probability of lightning ignitions was higher which was in agreement with our outcome. In IoE, geology is the second and curvature the third most influential factor. Alternatively, in LR, after LULC, slope is the most influential factor. Parente et al. [63] found slope to be the main influencing factor. The LR outcome also showed that rainfall has a high negative correlation with wildfire occurrence for the weight of -0.326, implying that as rainfall increases, the probability of wildfire occurrence decreases. There is a conflict among the MSA weights derived from IoE and ensemble LR for aspect. The derived values were 0 and 0.781 from IoE and LR, respectively. It is well-known that aspect has a considerable influence on a region’s characteristics such as exposure to sunshine, wind direction, precipitation, drying winds, and the morphologic structure that has been associated with fire occurrences. Here, IoE failed to indicate a strong association between aspect and wildfire occurrence. This will be dealt with in the AUC analysis.

In addition, in order to have a visual view of the location of the burnt areas, a 3D map of the altitude and wildfire inventories was produced and is presented in Figure 5. It can be clearly seen that most of the burnt areas are located on the slopes and in the north and northeast of the region.

**4.3. Susceptibility Maps and Validations.** The individual IoE (Figure 6(a)) and EBF (Figure 6(b)) modeling and the ensemble LR (Figure 6(c)) modeling were implemented. Three wildfire probability index maps were generated. In order to

TABLE 7: Spatial relationship between wildfire and wildfire influencing factors by IoE, EBF, and ensemble LR models.

Influencing factors	Classes	IOE						EBF			LR
		$P_{ij}$	$(P_{ij})$	$H_j$	$H_{j\max}$	$I_j$	$W_j$	Bel	Dis	Unc	Coefficient
Slope (degree)	0–0.29	0.908	0.082					0.07	0.10	0.83	
	0.29–1.19	0.160	0.014					0.01	0.11	0.88	
	1.19–2.09	0.409	0.037					0.03	0.10	0.87	
	2.09–2.99	1.119	0.101					0.09	0.09	0.82	
	2.99–3.89	0.968	0.087	2.974	3.322	0.105	0.095	0.08	0.10	0.82	0.611
	3.89–5.09	0.796	0.072					0.06	0.10	0.84	
	5.09–6.88	0.804	0.072					0.07	0.10	0.83	
	6.88–9.58	0.838	0.075					0.07	0.10	0.83	
	9.58–14.97	3.289	0.296					0.30	0.07	0.63	
	14.97–76.38	1.826	0.164					0.16	0.09	0.75	
Rainfall	536.00–671.32	2.461	0.248					0.25	0.08	0.67	
	671.32–738.99	0.882	0.089					0.08	0.10	0.82	
	738.99–767.69	2.364	0.238					0.24	0.08	0.68	
	767.69–800.51	2.405	0.242					0.25	0.08	0.67	
	800.51–831.26	0.837	0.084	2.616	3.322	0.213	0.523	0.07	0.10	0.83	-0.326
	831.26–847.66	0.269	0.027					0.02	0.10	0.88	
	847.66–859.96	0.361	0.036					0.03	0.10	0.87	
	859.96–876.36	0.201	0.020					0.01	0.10	0.89	
	876.36–896.87	0.144	0.014					0.01	0.10	0.89	
	896.87–1,058.85	0.000	0.000					0.00	0.11	0.89	
Altitude (m)	0–10.41	0.469	0.051					0.04	0.10	0.86	
	10.41–21.61	0.858	0.093					0.08	0.10	0.82	
	21.61–29.99	0.215	0.023					0.02	0.10	0.88	
	29.99–38.38	1.580	0.171					0.16	0.09	0.75	
	38.38–46.76	1.715	0.185	2.742	3.322	0.175	0.082	0.18	0.09	0.73	0.062
	46.76–57.95	3.129	0.338					0.36	0.06	0.58	
	57.95–71.93	0.210	0.023					0.02	0.11	0.87	
	71.93–94.31	0.434	0.047					0.04	0.10	0.86	
	94.31–139.05	0.259	0.028					0.02	0.10	0.88	
	139.05–675.96	0.377	0.041					0.03	0.10	0.87	
Curvature	Concave	0.849	0.406					0.40	0.38	0.22	
	Flat	0.097	0.046	0.476	1.585	0.700	0.594	0.04	0.33	0.63	0.282
	Convex	1.146	0.548					0.54	0.28	0.18	
Aspect (direction)	Flat	0.000	0.000					0.00	0.11	0.89	
	North	1.523	0.201					0.20	0.10	0.70	
	Northeast	1.728	0.229					0.23	0.09	0.68	
	East	1.523	0.201					0.20	0.10	0.70	
	Southeast	0.129	0.017	2.579	3.170	0.186	0.001	0.01	0.12	0.87	0.303
	South	0.156	0.021					0.01	0.12	0.87	
	Southwest	0.149	0.020					0.01	0.12	0.87	
	West	1.280	0.169					0.16	0.10	0.74	
	Northwest	1.074	0.142					0.14	0.10	0.76	
TPI	Valley	1.923	0.241					0.24	0.12	0.64	
	Lower slope	0.262	0.033	2.173	2.585	0.159	0.306	0.03	0.17	0.80	0.408
	Flat slope	0.036	0.004					0.00	0.27	0.73	
	Middle slope	1.981	0.248					0.24	0.16	0.60	

TABLE 7: Continued.

Influencing factors	Classes	IOE						EBF			LR
		$P_{ij}$	$(P_{ij})$	$H_j$	$H_{j\max}$	$I_j$	$W_j$	Bel	Dis	Unc	Coefficient
	Upper slope	1.769	0.221					0.22	0.14	0.64	
	Ridge	2.023	0.253					0.25	0.12	0.63	
Distance from river	0–333.23	0.115	0.012					0.01	0.10	0.89	
	333.23–833.08	0.261	0.027					0.02	0.11	0.87	
	833.08–1,416.25	1.308	0.134					0.13	0.09	0.78	
	1,416.25–2,082.72	2.288	0.234					0.24	0.08	0.68	
	2,082.72–2,832.51	1.809	0.185					0.18	0.09	0.73	
	2,832.51–3,665.59	0.836	0.086	2.926	3.322	0.119	0.014	0.08	0.10	0.82	0.002
	3,665.59–4,665.30	0.744	0.076					0.07	0.10	0.83	
	4,665.30–6,081.55	1.520	0.156					0.15	0.09	0.76	
	6,081.55–8,247.58	0.711	0.073					0.07	0.10	0.83	
	8,247.58–21,160.47	0.169	0.017					0.01	0.10	0.89	
Distance from road	0–80.33	1.839	0.193					0.19	0.09	0.72	
	80.33–240.99	0.230	0.024					0.02	0.11	0.87	
	240.99–481.99	2.123	0.223					0.22	0.08	0.70	
	481.99–722.98	1.380	0.145					0.14	0.09	0.77	
	722.98–1,044.31	1.240	0.130					0.12	0.09	0.79	
	1,044.31–1,526.31	0.821	0.086	2.983	3.322	0.102	0.188	0.08	0.10	0.82	0.347
	1,526.31–2,168.96	0.633	0.066					0.06	0.10	0.84	
	2,168.96–3,213.27	0.808	0.085					0.08	0.10	0.82	
	3,213.27–5,141.24	0.203	0.021					0.02	0.10	0.88	
	5,141.24–20,484.65	0.261	0.027					0.02	0.10	0.88	
Soil	Fu3	2.391	0.110					0.08	0.04	0.88	
	Tb64	0.859	0.040					0.02	0.05	0.93	
	Mp6	3.316	0.153					0.11	0.04	0.85	
	NY3	11.355	0.524					0.65	0.02	0.33	
	Tb65	0.000	0.000					0.00	0.05	0.95	
	Mm2	0.000	0.000					0.00	0.05	0.95	
	MM9	0.000	0.000					0.00	0.05	0.95	
	Fu2	0.803	0.037					0.02	0.04	0.94	
	Cd3	0.000	0.000					0.00	0.05	0.95	
	Sj12	0.231	0.011					0.00	0.05	0.95	
	Mw30	2.729	0.126	2.060	4.322	0.523	1.251	0.09	0.04	0.87	0.653
	Kb28	0.000	0.000					0.00	0.05	0.95	
	Pl1	0.000	0.000					0.00	0.05	0.95	
	Tb62	0.000	0.000					0.00	0.04	0.96	
	Kb12	0.000	0.000					0.00	0.05	0.95	
	LL6	0.000	0.000					0.00	0.04	0.96	
	Rh9	0.000	0.000					0.00	0.05	0.95	
	Me8	0.000	0.000					0.00	0.04	0.96	
Kd6	0.000	0.000					0.00	0.05	0.95		
Mg26	0.000	0.000					0.00	0.04	0.96		
Geology	Alluvium	1.781	0.067					0.00	0.04	0.96	
	Sand	0.000	0.000					0.00	0.03	0.97	
	Miscellaneous unconsolidated sediments	6.171	0.231	2.811	4.322	0.350	0.623	0.25	0.03	0.72	0.008
	Sedimentary rock	0.982	0.037					0.03	0.03	0.94	

TABLE 7: Continued.

Influencing factors	Classes	$P_{ij}$	$(P_{ij})$	IOE			EBF			LR	
				$H_j$	$H_{j \max}$	$I_j$	$W_j$	Bel	Dis	Unc	Coefficient
	Basalt	0.218	0.008					0.00	0.03	0.97	
	Gabbroid	0.000	0.000					0.00	0.03	0.97	
	Granitoid	7.162	0.268					0.31	0.03	0.66	
	Arenite-mudrock	0.081	0.003					0.00	0.04	0.96	
	Felsites (lavas, clastics, and high-level intrusives)	0.170	0.006					0.00	0.03	0.97	
	Mixed volcanic and sedimentary rocks	0.000	0.000					0.00	0.03	0.97	
	Mixed sedimentary rocks and mafites	0.151	0.006					0.00	0.03	0.97	
	Mudrock	1.894	0.071					0.06	0.03	0.91	
	Chert	0.000	0.000					0.00	0.03	0.97	
	Pelite	0.619	0.023					0.01	0.03	0.96	
	Arenite	0.116	0.004					0.00	0.04	0.96	
	Colluvium	1.868	0.070					0.06	0.03	0.91	
	Mafites (lavas, clastics, and high-level intrusives)	0.000	0.000					0.00	0.03	0.97	
	Ferricrete	5.361	0.201					0.21	0.03	0.76	
	Arenite-rudite	0.159	0.006					0.00	0.03	0.97	
	Water bodies	0.000	0.000					0.00	0.03	0.97	
	Man-made deposits (tailings, land-fill, mine dumps, etc.)	0.000	0.000					0.00	0.03	0.97	
	Rudite	0.000	0.000					0.00	0.03	0.97	
	Dioritoid	0.000	0.000					0.00	0.03	0.97	
	Carbonates (limestone or dolomite)	0.000	0.000					0.00	0.03	0.97	
	Ultramafic rock	0.000	0.000					0.00	0.03	0.97	
	Mixed mafites and felsites (mainly volcanics)	0.000	0.000					0.00	0.03	0.97	
LULC	Reservoir/dam	0.000	0.000					0.00	0.03	0.97	
	Landfill	0.567	0.028					0.02	0.03	0.95	
	Sewage	0.000	0.000					0.00	0.03	0.97	
	Lake	0.000	0.000					0.00	0.03	0.97	
	Lake—conservation	0.000	0.000					0.00	0.03	0.97	
	Marsh/wetland—conservation	0.000	0.000					0.00	0.03	0.97	
	Estuary/coastal waters	0.000	0.000					0.00	0.03	0.97	
	Reservoir	0.000	0.000					0.00	0.03	0.97	
	River	0.000	0.000					0.00	0.03	0.97	
	Drainage channel/aqueduct	0.000	0.000					0.00	0.03	0.97	
	Marsh/wetland	1.282	0.063	2.956	5.833	0.493	0.000	0.04	0.03	0.93	0.781
	National park	0.000	0.000					0.00	0.03	0.97	
	Natural feature protection	0.000	0.000					0.00	0.03	0.97	
	Other conserved area	0.000	0.000					0.00	0.03	0.97	
	Other minimal use	0.211	0.010					0.00	0.03	0.97	
	Defence	0.000	0.000					0.00	0.03	0.97	
	Residual native cover	0.834	0.041					0.03	0.03	0.94	
	Livestock grazing	0.067	0.003					0.00	0.06	0.94	
	Production forestry	0.000	0.000					0.00	0.03	0.97	
	Plantation forestry	0.000	0.000					0.00	0.03	0.97	
Grazing modified pastures	0.000	0.000					0.00	0.03	0.97		
Cropping	5.171	0.252					0.30	0.03	0.67		

TABLE 7: Continued.

Influencing factors	Classes	IOE						EBF			LR
		$P_{ij}$	$(P_{ij})$	$H_j$	$H_{j \max}$	$I_j$	$W_j$	Bel	Dis	Unc	Coefficient
	Hay and silage	0.000	0.000					0.00	0.03	0.97	
	Perennial horticulture	0.000	0.000					0.00	0.03	0.97	
	Land in transition	0.000	0.000					0.00	0.03	0.97	
	Seasonal horticulture	0.000	0.000					0.00	0.03	0.97	
	Irrigated modified pastures	0.000	0.000					0.00	0.03	0.97	
	Irrigated cropping	0.000	0.000					0.00	0.03	0.97	
	Irrigated perennial horticulture	0.000	0.000					0.00	0.03	0.97	
	Irrigated tree fruits	0.000	0.000					0.00	0.03	0.97	
	Irrigated vine fruits	0.000	0.000					0.00	0.03	0.97	
	Irrigated seasonal horticulture	0.000	0.000					0.00	0.03	0.97	
	Irrigated seasonal vegetables and herbs	0.000	0.000					0.00	0.03	0.97	
	Intensive horticulture	0.459	0.022					0.01	0.03	0.96	
	Intensive animal production	0.144	0.007					0.00	0.03	0.97	
	Dairy sheds and yards	0.000	0.000					0.00	0.03	0.97	
	Poultry farms	1.074	0.052					0.03	0.03	0.94	
	Manufacturing and industrial	0.182	0.009					0.00	0.03	0.97	
	Residential	4.698	0.229					0.25	0.00	0.75	
	Urban residential	0.000	0.000					0.00	0.03	0.97	
	Rural residential	0.161	0.008					0.00	0.04	0.96	
	Rural living	0.000	0.000					0.00	0.03	0.97	
	Services	3.705	0.181					0.17	0.03	0.80	
	Commercial services	0.033	0.002					0.00	0.03	0.97	
	Public services	0.000	0.000					0.00	0.03	0.97	
	Recreation and culture	1.909	0.093					0.07	0.03	0.90	
	Defence facilities—Urban	0.000	0.000					0.00	0.03	0.97	
	Utilities	0.000	0.000					0.00	0.03	0.97	
	Fuel powered electricity generation	0.000	0.000					0.00	0.03	0.97	
	Research facilities	0.000	0.000					0.00	0.03	0.97	
	Transport and communication	0.000	0.000					0.00	0.03	0.97	
	Airports/aerodromes	0.000	0.000					0.00	0.03	0.97	
	Roads	0.000	0.000					0.00	0.03	0.97	
	Railways	0.000	0.000					0.00	0.03	0.97	
	Mining	0.000	0.000					0.00	0.03	0.97	
	Quarries	0.000	0.000					0.00	0.03	0.97	
	Waste treatment and disposal	0.000	0.000					0.00	0.03	0.97	
Wind (m/s)	3.00–3.29	0.331	0.017					0.01	0.10	0.89	
	3.29–3.40	0.173	0.009					0.00	0.10	0.90	
	3.40–3.49	0.397	0.021					0.01	0.10	0.89	
	3.49–3.59	0.488	0.026					0.02	0.11	0.87	
	3.59–3.69	0.554	0.029	2.580	3.322	0.223	0.074	0.02	0.11	0.87	0.102
	3.69–3.79	1.713	0.090					0.08	0.08	0.84	
	3.79–3.89	1.800	0.095					0.08	0.09	0.83	
	3.89–4.09	1.989	0.105					0.09	0.09	0.82	
	4.09–4.19	6.373	0.335					0.36	0.09	0.55	
4.19–5.00	5.198	0.273					0.28	0.09	0.63		

\*Names and descriptions of the soil types have been listed in Table 3.

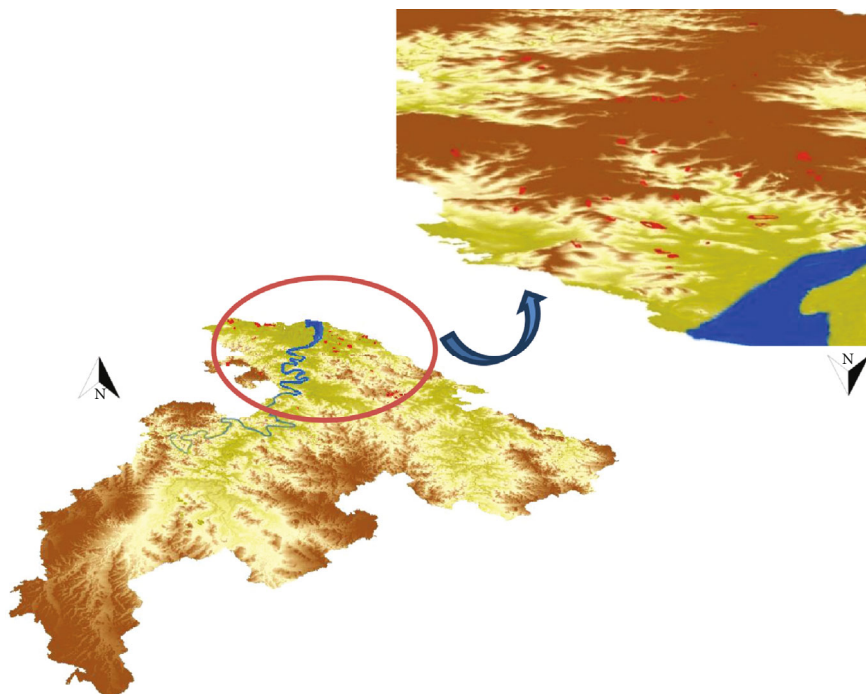


FIGURE 5: 3D view from the northeast region of the study area with the burnt locations.

create a susceptibility map, the probability index maps should be classified. In this study, the probability maps were classified using the quantile classification method and grouped into relative categories of very low, low, moderate, high, and very high susceptibilities of wildfire occurrence (Figure 6).

Table 8 shows that the IoE and EBF proportions of the very high wildfire susceptibility category are 10.25% and 13.52%, respectively, which is greater than that of LR (6.56%). This implies that the LR ensemble model produced less exaggerated outcomes, compared to the two individual methods. The wildfire susceptibility map derived from the ensemble model classified 68.34% of the total region as very low susceptibility. However, the two individual methods, IoE and EBF, detected 22.77% and 51.21%, respectively, as “very low.” Regarding the LR ensemble model, the other zones, high, moderate, low, and very low, were 3.78%, 9.23%, and 12.09%, respectively.

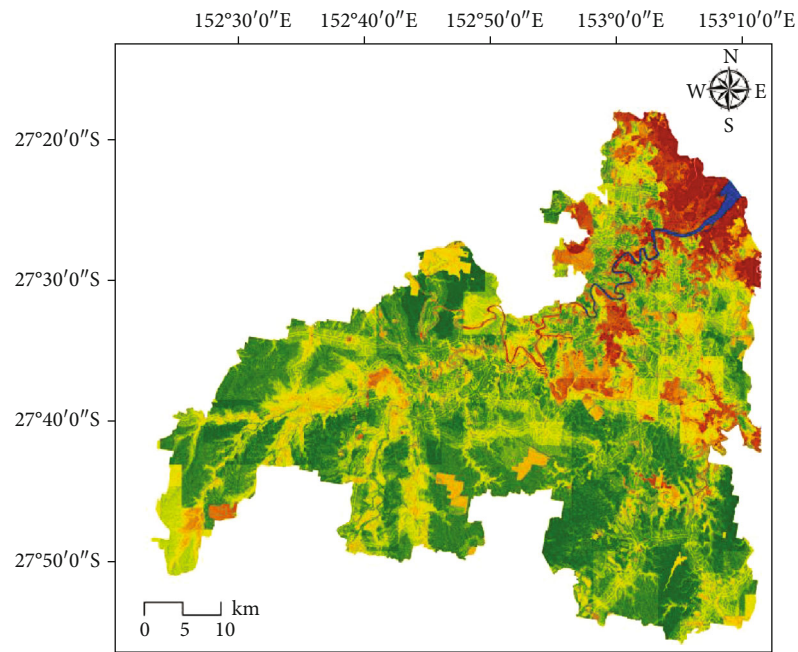
The AUC prediction accuracy of the two individual methods and final ensemble model created by LR is displayed in Figure 7. The greatest accuracy (88.51%) was recorded by the ensemble method, while the least accuracy (75.32%) was recorded by the individual IoE method. The AUC results showed that the outcome of the ensemble analysis was more reliable than that of the individual methods. Consequently, the EBF technique robustness to exploit different variables in the processing was proved. One of the advantages in the EBF model is a calculation of the degrees of uncertainty in the prediction along with belief and disbelief (Table 7) during the process of generating probability mass functions [79]. The degrees of uncertainty and plausibility of a pixel (classified as fire event) can be measured quantitatively which could not be achieved through other methods, and it is a fast algo-

rithm without heavy calculation and iteration [110]. The closer value to 0.5 is recorded, and the higher uncertainty of the class is considered. By looking at the uncertainty value in Table 7, one can find how reliable the measurement is in every single feature and evidence. Besides, the three exploited algorithms do not require the assumption of normal distribution that provides robust operation for the complex events modeling [110]. The simplicity of the EBF, IoE, and LR makes them a great choice for modeling big data rather than the iteration in ML. For instance, the LR has less parameters to fine tune, while the SVM model requires optimizing the kernel function, the penalty, and gamma parameters.

The risk and vulnerability can be performed for different characteristics. Brisbane City Plan 2014 is a huge future development plan of the Brisbane City Council that has a variety of aspects. The city planners divided the region into different zones based on specific topics. The class of “very high” of the final wildfire susceptibility map derived from ensemble modeling was extracted and overlaid on the Brisbane City Plan thematic layers. These layers illustrate the spatial distributions of a variety of important species, features, etc., in the city of Brisbane. Figure 8 illustrates different risk maps. The single upper individual map represents only the very high susceptibility zone. Subsequently, every pair of maps in each row represents the vulnerability map and its overlaid outcome with very high susceptibility zone. The seven maps relate to (a) general zoning, (b) significant trees, (c) critically endangered species, (d) heritage area, (e) industrial areas, (f) freight route, and (g) koala habitat areas.

The following maps were prepared by overlaying the aforementioned maps with the class of “very high” of the wildfire susceptibility map derived from the ensemble modeling (Figure 8). The first wildfire risk likelihood map is related

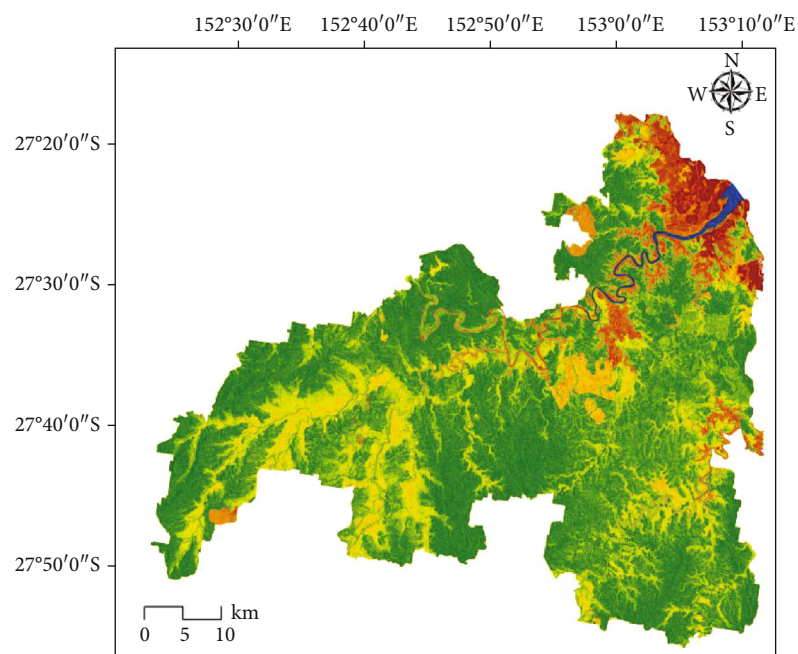




Forest fire susceptibility map (IOE)

- Very low
- Low
- Moderate
- High
- Very high
- River (m)

(a)



Forest fire susceptibility map (EBF)

- Very low
- Low
- Moderate
- High
- Very high
- River (m)

(b)

FIGURE 6: Continued.

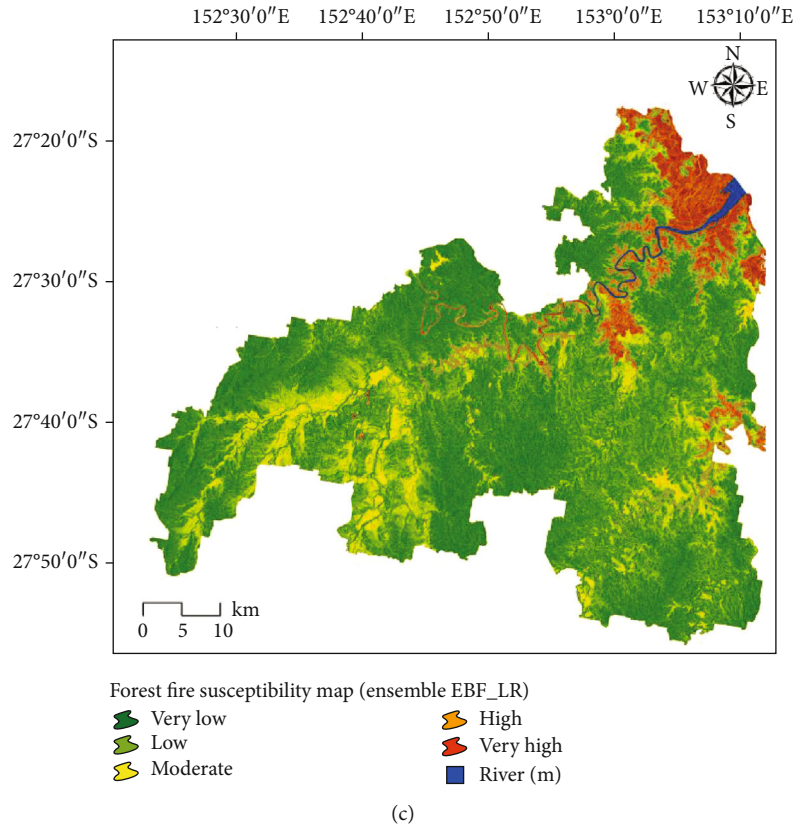


FIGURE 6: Susceptibility maps derived from three methods: (a) IoE, (b) EBF, and (c) ensemble EBF-LR.

TABLE 8: The distribution of the forest fire areas with respect to the forest fire occurrence potential zones.

Forest fire susceptibility mapping	IOE Area (%)	EBF Area (%)	Ensemble IOE + EBF Area (%)
Very high	10.25	13.52	6.56
High	16.81	12.03	3.78
Moderate	12.32	13.07	9.23
Low	37.85	10.17	12.09
Very low	22.77	51.21	68.34

to the general zoning map. As illustrated in the first row (Figure 8(a)), the very high susceptibility zone is distributed across general residential areas; consequently, it would be efficient and reasonable if fire prevention strategies and management plans were organized based on these fire-risk zones. The second row (Figure 8(b)) represents a significant tree map. The overlaid risk map shows that very few portions of those trees are located in the very high wildfire susceptibility zone. Therefore, those species are not at very high risk. In the third-row maps (Figure 8(c)), only a few of the critically endangered species are located in the very high susceptibility zone. In the case of the heritage area (Figure 8(d)) in the fourth row, there are several areas in the susceptible zone. Susceptible areas increase in the

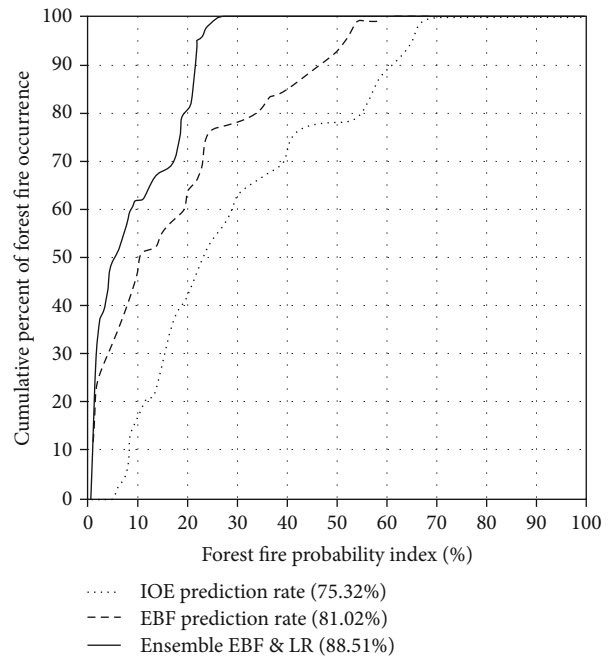


FIGURE 7: Area under curve (AUC) chart, this technique evaluates the reliability of the outcomes using the testing dataset.

industrial areas (Figure 8(e)) map in the fifth row, and many industrial regions are in the very high wildfire susceptibility zone.

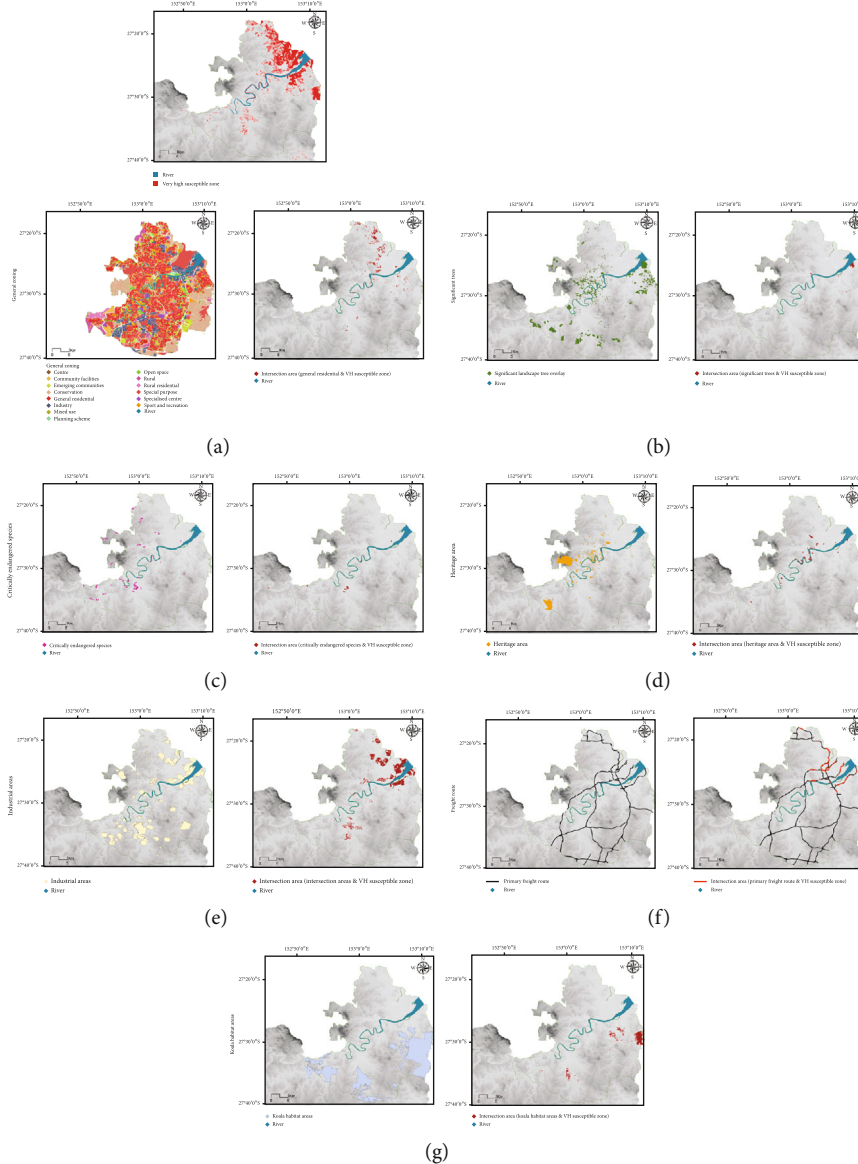


FIGURE 8: Overlaid city plan maps with the class of “very high” susceptibility of wildfire. (a) General zoning. (b) Significant trees. (c) Critically endangered species. (d) Heritage area. (e) Industrial areas. (f) Freight route. (g) Koala habitat areas.

Freight routes (Figure 8(f)) which are usually used for transportation and cargo services are presented in row six and only the red routes occur in the very high susceptible areas. The slightest disruption to such routes can have a serious impact on the total transportation of the region. The last row illustrates the koala habitat areas (Figure 8(g)). This species is very special in Australia and those areas which they inhabit are ranked as very high wildfire susceptibility zone, according to our analysis.

Our research indicates that a variety of elements are at risk when wildfires vary. In some cases, the risk map gives more information than the susceptibility map and may be of more use to government agencies, councils, insurance companies, and the inhabitants of risk areas. Wildfire management is a colossal undertaking and many aspects are impractical. Therefore, the maps like those illustrated in Figure 8 could assist organizations and individuals at risk.

The best policy strategies include preventative and mitigating measures.

### 5. Conclusion

This research has focused on increasing the accuracy of wildfire susceptibility mapping through ensemble modeling. Additionally, the importance of the application of susceptibility mapping in risk analysis was evaluated and illustrated. The mapping process was commenced with the structuring and processing of two datasets: the inventory and influencing factors. The IoE, EBF, and LR statistical methods were used to perform BSA and MSA. The process calculated the statistical weights for each wildfire influencing factor (e.g., geology map) and the classes of each influencing factor (i.e., geology types) to produce the final wildfire susceptibility map. IoE and EBF ranked each class of each influencing factor, while

the influencing factors were classified according to their BSA weights and entered into ensemble modeling using LR. The final assessment of the accuracy of susceptibility maps showed that the ensemble method produced a more reliable outcome with an 88.51% prediction capability. The AUC exceeded most of the previous research. It is a recommendation that precision in the composition of the raw datasets is crucial, to realize the full potential of the increased accuracy of an ensemble model. The selection of the most influential classes and factors has a considerable impact on the result.

Additional information extracted from the analysis and the derived weights confirmed that features such as rivers, rock outcroppings, road networks, and water bodies can act as fire barriers (fuel breaks). City planners can take advantage of these natural and manmade features in controlling and minimizing wildfires. Using the topographic map of a region, these features can be easily located. The influencing factors of slope, TPI, and soil have a significant impact on the creation and location of the wildfire susceptible areas, while land management practices have a considerable impact on the magnitude and consequences of this phenomenon. As described, fire risk analysis is an essential practice protecting forest environment, where possible. The zoning maps of a variety of demographic, topographical, and environmental aspects were overlaid onto the “very high” wildfire susceptibility map, from which produced alternative risk information. It might improve the human perception and understanding of the hazard. Managing fire is vital for the protection of human dwellings and environmental habitats. Wildfires are an annual occurrence in Queensland, and preparations for prevention and mitigation are invaluable. Hence, accurate identification of the conditioning and triggering factors in the region along with a risk map would enhance the mitigation strategies and plans, and it could pose minimum loss and damages. Some strategies could be applied to replace the wood with fire resistance lumber or metals for building and construction in susceptible areas. In this study, irrigated cropping was classified as low and very low-prone area to bushfire. This finding might be investigated as future research and discussion over the potential and effect of irrigation system to keep standard moisture in the soil preventing the fuel source. Moreover, the vulnerable wildfire zones exhibiting with dry soil could raise the attention and need more inspection in terms of the groundwater sources and their quality. Our planned future research into modeling wildfire will focus on comprehensive risk and vulnerability assessment using a time series perspective of the trend and extent of wildfire in the region.

### Data Availability

The data used to support the findings of this study are available from the corresponding author upon request.

### Conflicts of Interest

The authors declare that they have no competing interests.

### Authors' Contributions

M.S.T, H.Ö, F.S, and F.S. conceived and designed the experiments. M.S.T, F.H, and F.H. performed the experiments. M.S.T, H.Ö, F.S, and F.S. analyzed the data. M.S.T, H.Ö, M.R.H, F.S, and F.S. contributed reagents/materials/analysis tools. M.S.T, M.R.H, F.S, B.K, V.S, and F.S. wrote the paper. B.K, N.U, and V.S. edited, restructured, and professionally optimized the manuscript.

### Acknowledgments

Thanks are due to the Australian Research Council Centre of Excellence for Australian Biodiversity and Heritage. This research was done by the Australian Research Council Centre of Excellence for Australian Biodiversity and Heritage (CE170100015; <http://EpicAustralia.org/>).

### References

- [1] A. M. Gill, S. L. Stephens, and G. J. Cary, “The worldwide “wildfire” problem,” *Ecological Applications*, vol. 23, pp. 438–454, 2013.
- [2] D. E. Mercer, J. P. Prestemon, D. T. Butry, and J. M. Pye, “Evaluating alternative prescribed burning policies to reduce net economic damages from wildfire,” *American Journal of Agricultural Economics*, vol. 89, pp. 63–77, 2007.
- [3] D. R. Brown, M. T. Jorgenson, T. A. Douglas et al., “Interactive effects of wildfire and climate on permafrost degradation in Alaskan lowland forests,” *Journal of Geophysical Research: Biogeosciences*, vol. 120, pp. 1619–1637, 2015.
- [4] H. Etchells, A. J. O'Donnell, W. L. McCaw, and P. F. Grierson, “Fire severity impacts on tree mortality and post-fire recruitment in tall eucalypt forests of Southwest Australia,” *Forest Ecology and Management*, vol. 459, p. 117850, 2020.
- [5] D. C. Laughlin, J. D. Bakker, M. T. Stoddard et al., “Toward reference conditions: wildfire effects on flora in an old-growth ponderosa pine forest,” *Forest Ecology and Management*, vol. 199, pp. 137–152, 2004.
- [6] R. N. Gwinn and J. L. Koprowski, “Differential response to fire by an introduced and an endemic species complicates endangered species conservation,” *Journal of Mammalogy*, vol. 27, 2016.
- [7] V. Fernández-García, J. Miesel, M. J. Baeza, E. Marcos, and L. Calvo, “Wildfire effects on soil properties in fire-prone pine ecosystems: indicators of burn severity legacy over the medium term after fire,” *Applied Soil Ecology*, vol. 135, pp. 147–156, 2019.
- [8] J. Murphy, D. Johnson, W. Miller, R. Walker, E. Carroll, and R. Blank, “Wildfire effects on soil nutrients and leaching in a Tahoe Basin watershed,” *Journal of Environmental Quality*, vol. 35, pp. 479–489, 2006.
- [9] M. Moretti, M. K. Obrist, and P. Duelli, “Arthropod biodiversity after forest fires: winners and losers in the winter fire regime of the southern Alps,” *Ecography*, vol. 27, pp. 173–186, 2004.
- [10] T. Gallo, L. T. Stinson, and L. Pejchar, “Mitigation for energy development fails to mimic natural disturbance for birds and mammals,” *Biological Conservation*, vol. 212, pp. 39–47, 2017.

- [11] D. Stojanovic, J. W. nee Voogdt, M. Webb, H. Cook, and R. Heinsohn, "Loss of habitat for a secondary cavity nesting bird after wildfire," *Forest Ecology and Management*, vol. 360, pp. 235–241, 2016.
- [12] M. Parise and S. Cannon, "Wildfire impacts on the processes that generate debris flows in burned watersheds," *Natural Hazards*, vol. 61, pp. 217–227, 2012.
- [13] H. G. Smith, G. J. Sheridan, P. N. Lane, P. Nyman, and S. Haydon, "Wildfire effects on water quality in forest catchments: a review with implications for water supply," *Journal of Hydrology*, vol. 396, pp. 170–192, 2011.
- [14] J.-H. Son, S. Kim, and K. H. Carlson, "Effects of wildfire on river water quality and riverbed sediment phosphorus," *Water, Air, & Soil Pollution*, vol. 226, no. 3, 2015.
- [15] C. Black, Y. Tesfaigzi, J. A. Bassein, and L. A. Miller, "Wildfire smoke exposure and human health: significant gaps in research for a growing public health issue," *Environmental Toxicology and Pharmacology*, vol. 55, pp. 186–195, 2017.
- [16] I. Kochi, P. A. Champ, J. B. Loomis, and G. H. Donovan, "Valuing morbidity effects of wildfire smoke exposure from the 2007 Southern California wildfires," *Journal of Forest Economics*, vol. 25, pp. 29–54, 2016.
- [17] S. Karma, E. Zorba, G. C. Pallis et al., "Use of unmanned vehicles in search and rescue operations in forest fires: advantages and limitations observed in a field trial," *International Journal of Disaster Risk Reduction*, vol. 13, pp. 307–312, 2015.
- [18] Z. S. Pourtaghi, H. R. Pourghasemi, R. Aretano, and T. Semeraro, "Investigation of general indicators influencing on forest fire and its susceptibility modeling using different data mining techniques," *Ecological Indicators*, vol. 64, pp. 72–84, 2016.
- [19] M. Leuenberger, J. Parente, M. Tonini, M. G. Pereira, and M. Kanevski, "Wildfire susceptibility mapping: deterministic vs. stochastic approaches," *Environmental Modelling & Software*, vol. 101, pp. 194–203, 2018.
- [20] J. Verde and J. Zêzere, "Assessment and validation of wildfire susceptibility and hazard in Portugal," *Natural Hazards and Earth System Sciences*, vol. 10, pp. 485–497, 2010.
- [21] A. Massetti, C. Rüdiger, M. Yebra, and J. Hilton, "The vegetation structure perpendicular index (VSPI): a forest condition index for wildfire predictions," *Remote Sensing of Environment*, vol. 224, pp. 167–181, 2019.
- [22] S. Saatchi, K. Halligan, D. G. Despain, and R. L. Crabtree, "Estimation of forest fuel load from radar remote sensing," *IEEE Transactions on Geoscience and Remote Sensing*, vol. 45, pp. 1726–1740, 2007.
- [23] D. M. Staley, A. C. Tillery, J. W. Kean et al., "Estimating post-fire debris-flow hazards prior to wildfire using a statistical analysis of historical distributions of fire severity from remote sensing data," *International Journal of Wildland Fire*, vol. 27, pp. 595–608, 2018.
- [24] J. E. Keeley, "Fire intensity, fire severity and burn severity: a brief review and suggested usage," *International Journal of Wildland Fire*, vol. 18, pp. 116–126, 2009.
- [25] M. Kervyn, G. Ernst, A. Harris, F. Belton, E. Mbede, and P. Jacobs, "Thermal remote sensing of the low-intensity carbonite volcanism of Oldoinyo Lengai, Tanzania," *International Journal of Remote Sensing*, vol. 29, pp. 6467–6499, 2008.
- [26] M.-A. Parisien, V. Kafka, K. Hirsch, J. Todd, S. Lavoie, and P. Maczek, *Mapping Wildfire Susceptibility with the BURN-P3 Simulation Model*, Natural Resources Canada, Canadian Forest Service, Northern Forestry Centre, Information report NOR-X-405, Edmonton, AB, 2005.
- [27] H. Hong, S. A. Naghibi, M. M. Dashtpajardi, H. R. Pourghasemi, and W. Chen, "A comparative assessment between linear and quadratic discriminant analyses (LDA-QDA) with frequency ratio and weights-of-evidence models for forest fire susceptibility mapping in China," *Arabian Journal of Geosciences*, vol. 10, p. 167, 2017.
- [28] M. Tonini, M. G. Pereira, J. Parente, and C. V. Orozco, "Evolution of forest fires in Portugal: from spatio-temporal point events to smoothed density maps," *Natural Hazards*, vol. 85, pp. 1489–1510, 2017.
- [29] A. Jaafari, E. K. Zenner, and B. T. Pham, "Wildfire spatial pattern analysis in the Zagros Mountains, Iran: a comparative study of decision tree based classifiers," *Ecological Informatics*, vol. 43, pp. 200–211, 2018.
- [30] P. Jain, S. C. P. Coogan, S. G. Subramanian, M. Crowley, S. Taylor, and M. D. Flannigan, "A review of machine learning applications in wildfire science and management," *Environmental Reviews*, vol. 28, no. 4, pp. 478–505, 2020.
- [31] Z. S. Pourtaghi, H. R. Pourghasemi, and M. Rossi, "Forest fire susceptibility mapping in the Minudasht forests, Golestan province, Iran," *Environmental Earth Sciences*, vol. 73, pp. 1515–1533, 2015.
- [32] D. Tien Bui, K.-T. T. Le, V. C. Nguyen, H. D. Le, and I. Revhaug, "Tropical forest fire susceptibility mapping at the Cat Ba National Park Area, Hai Phong City, Vietnam, using GIS-based kernel logistic regression," *Remote Sensing*, vol. 8, p. 347, 2016.
- [33] H. R. Pourghasemi, M. Beheshtirad, and B. Pradhan, "A comparative assessment of prediction capabilities of modified analytical hierarchy process (M-AHP) and Mamdani fuzzy logic models using Netcad-GIS for forest fire susceptibility mapping," *Geomatics, Natural Hazards and Risk*, vol. 7, pp. 861–885, 2016.
- [34] K. Gholamnia, T. G. Nachappa, O. Ghorbanzadeh, and T. Blaschke, "Comparisons of diverse machine learning approaches for wildfire susceptibility mapping," *Symmetry*, vol. 12, no. 4, p. 604, 2020.
- [35] B. Kalantar, N. Ueda, M. O. Idrees, S. Janizadeh, K. Ahmadi, and F. Shabani, "Forest fire susceptibility prediction based on machine learning models with resampling algorithms on remote sensing data," *Remote Sensing*, vol. 12, pp. 1–24, 2020.
- [36] T. Wuest, D. Weimer, C. Irgens, and K.-D. Thoben, "Machine learning in manufacturing: advantages, challenges, and applications," *Production & Manufacturing Research*, vol. 4, pp. 23–45, 2016.
- [37] C. Brun, T. Margalef, A. Cortés, and A. Sikora, "Enhancing multi-model forest fire spread prediction by exploiting multi-core parallelism," *The Journal of Supercomputing*, vol. 70, pp. 721–732, 2014.
- [38] H. R. Podschwit, N. K. Larkin, E. A. Steel, A. Cullen, and E. Alvarado, "Multi-model forecasts of very-large fire occurrences during the end of the 21st century," *Climate*, vol. 6, p. 100, 2018.
- [39] Z.-H. Zhou, *Ensemble Methods: Foundations and Algorithms*, Chapman and Hall/CRC, 2012.
- [40] O. F. Althuwaynee, B. Pradhan, H.-J. Park, and J. H. Lee, "A novel ensemble bivariate statistical evidential belief function with knowledge-based analytical hierarchy process and

- multivariate statistical logistic regression for landslide susceptibility mapping,” *Catena*, vol. 114, pp. 21–36, 2014.
- [41] B. Kalantar, N. Ueda, V. Saeidi, and P. Ahmadi, “Application of machine learning algorithms and their ensemble for landslide susceptibility mapping,” in *Understanding and Reducing Landslide Disaster Risk Application*, Springer, 2020.
- [42] S. A. Naghibi, D. D. Moghaddam, B. Kalantar, B. Pradhan, and O. Kisi, “A comparative assessment of GIS-based data mining models and a novel ensemble model in groundwater well potential mapping,” *Journal of Hydrology*, vol. 548, pp. 471–483, 2017.
- [43] A. M. Youssef, B. Pradhan, M. N. Jebur, and H. M. El-Harbi, “Landslide susceptibility mapping using ensemble bivariate and multivariate statistical models in Fayfa area, Saudi Arabia,” *Environmental Earth Sciences*, vol. 73, pp. 3745–3761, 2015.
- [44] A. Jaafari, E. K. Zenner, M. Panahi, and H. Shahabi, “Hybrid artificial intelligence models based on a neuro-fuzzy system and metaheuristic optimization algorithms for spatial prediction of wildfire probability,” *Agricultural and Forest Meteorology*, vol. 266, pp. 198–207, 2019.
- [45] M. S. Tehrany, S. Jones, F. Shabani, F. Martínez-Álvarez, and D. T. Bui, “A novel ensemble modeling approach for the spatial prediction of tropical forest fire susceptibility using logitboost machine learning classifier and multi-source geospatial data,” *Theoretical and Applied Climatology*, vol. 137, 2018.
- [46] M. S. Tehrany, B. Pradhan, and M. N. Jebur, “Flood susceptibility mapping using a novel ensemble weights-of-evidence and support vector machine models in GIS,” *Journal of Hydrology*, vol. 512, pp. 332–343, 2014.
- [47] M. S. Tehrany, M.-J. Lee, B. Pradhan, M. N. Jebur, and S. Lee, “Flood susceptibility mapping using integrated bivariate and multivariate statistical models,” *Environmental Earth Sciences*, vol. 72, pp. 4001–4015, 2014.
- [48] M. Constantin, M. Bednarik, M. C. Jurchescu, and M. Vlaicu, “Landslide susceptibility assessment using the bivariate statistical analysis and the index of entropy in the Sibiciu Basin (Romania),” *Environmental Earth Sciences*, vol. 63, pp. 397–406, 2011.
- [49] A. Ozdemir and T. Altural, “A comparative study of frequency ratio, weights of evidence and logistic regression methods for landslide susceptibility mapping: Sultan Mountains, SW Turkey,” *Journal of Asian Earth Sciences*, vol. 64, pp. 180–197, 2013.
- [50] M. Ward, A. I. T. Tulloch, J. Q. Radford et al., “Impact of 2019–2020 mega-fires on Australian fauna habitat,” *Nature Ecology & Evolution*, vol. 4, pp. 1321–1326, 2020.
- [51] C. Bryant, “Understanding bushfire: trends in deliberate vegetation fires in Australia,” *Geophysical Research Letters*, vol. 13, 2008.
- [52] M. H. Vahidnia, A. A. Alesheikh, A. Alimohammadi, and F. Hosseinali, “A GIS-based neuro-fuzzy procedure for integrating knowledge and data in landslide susceptibility mapping,” *Computers & Geosciences*, vol. 36, pp. 1101–1114, 2010.
- [53] B. Pradhan, M. S. Tehrany, and M. N. Jebur, “A new semi-automated detection mapping of flood extent from TerraSAR-X satellite image using rule-based classification and taguchi optimization techniques,” *IEEE Transactions on Geoscience and Remote Sensing*, vol. 54, pp. 4331–4342, 2016.
- [54] L. Ayalew and H. Yamagishi, “The application of GIS-based logistic regression for landslide susceptibility mapping in the Kakuda-Yahiko Mountains, Central Japan,” *Geomorphology*, vol. 65, pp. 15–31, 2005.
- [55] S. Lee, “Application of logistic regression model and its validation for landslide susceptibility mapping using GIS and remote sensing data,” *International Journal of Remote Sensing*, vol. 26, pp. 1477–1491, 2005.
- [56] A. Yalcin, “GIS-based landslide susceptibility mapping using analytical hierarchy process and bivariate statistics in Ardesen (Turkey): comparisons of results and confirmations,” *Catena*, vol. 72, pp. 1–12, 2008.
- [57] A. E. Al-Juaidi, A. M. Nassar, and O. E. Al-Juaidi, “Evaluation of flood susceptibility mapping using logistic regression and GIS conditioning factors,” *Arabian Journal of Geosciences*, vol. 11, p. 765, 2018.
- [58] Y. Garosi, M. Sheklabadi, H. R. Pourghasemi, A. A. Besalatpour, C. Conoscenti, and K. Van Oost, “Comparison of differences in resolution and sources of controlling factors for gully erosion susceptibility mapping,” *Geoderma*, vol. 330, pp. 65–78, 2018.
- [59] Z. Umar, B. Pradhan, A. Ahmad, M. N. Jebur, and M. S. Tehrany, “Earthquake induced landslide susceptibility mapping using an integrated ensemble frequency ratio and logistic regression models in West Sumatera Province, Indonesia,” *Catena*, vol. 118, pp. 124–135, 2014.
- [60] F. C. Eugenio, A. R. dos Santos, N. C. Fiedler et al., “Applying GIS to develop a model for forest fire risk: a case study in Espirito Santo, Brazil,” *Journal of Environmental Management*, vol. 173, pp. 65–71, 2016.
- [61] X. Li and W. Magill, “Modeling fire spread under environmental influence using a cellular automaton approach,” *Complexity International*, vol. 8, pp. 1–14, 2001.
- [62] N. Nicholls and C. Lucas, “Interannual variations of area burnt in Tasmanian bushfires: relationships with climate and predictability,” *International Journal of Wildland Fire*, vol. 16, pp. 540–546, 2007.
- [63] J. Parente, M. G. Pereira, and M. Tonini, “Space-time clustering analysis of wildfires: the influence of dataset characteristics, fire prevention policy decisions, weather and climate,” *Science of the Total Environment*, vol. 559, pp. 151–165, 2016.
- [64] C. Aguilar, J. Herrero, and M. Polo, “Topographic effects on solar radiation distribution in mountainous watersheds and their influence on reference evapotranspiration estimates at watershed scale,” *Hydrology and Earth System Sciences*, vol. 14, pp. 2479–2494, 2010.
- [65] Z. A. Holden and W. M. Jolly, “Modeling topographic influences on fuel moisture and fire danger in complex terrain to improve wildland fire management decision support,” *Forest Ecology and Management*, vol. 262, pp. 2133–2141, 2011.
- [66] A. Duane, M. Piqué, M. Castellnou, and L. Brotons, “Predictive modelling of fire occurrences from different fire spread patterns in Mediterranean landscapes,” *International Journal of Wildland Fire*, vol. 24, no. 3, pp. 407–418, 2015.
- [67] J. Lecina-Diaz, A. Alvarez, and J. Retana, “Extreme fire severity patterns in topographic, convective and wind-driven historical wildfires of Mediterranean pine forests,” *PLoS One*, vol. 9, article e85127, 2014.
- [68] J. J. Sharples, “An overview of mountain meteorological effects relevant to fire behaviour and bushfire risk,” *International Journal of Wildland Fire*, vol. 18, pp. 737–754, 2009.

- [69] A. L. Sullivan, W. L. McCaw, M. G. Cruz, S. Matthews, and P. F. Ellis, "Fuel, fire weather and fire behaviour in Australian ecosystems," *Flammable Australia: Fire Regimes, Biodiversity and Ecosystems in a Changing World*, pp. 51–77, 2012.
- [70] J.-L. Dupuy and J. Maréchal, "Slope effect on laboratory fire spread: contribution of radiation and convection to fuel bed preheating," *International Journal of Wildland Fire*, vol. 20, pp. 289–307, 2011.
- [71] D. X. Viegas, "Slope and wind effects on fire propagation," *International Journal of Wildland Fire*, vol. 13, pp. 143–156, 2004.
- [72] J. M. Fernández-Alonso, J. A. Vega, E. Jiménez, A. D. Ruiz-González, and J. G. Álvarez-González, "Spatially modeling wildland fire severity in pine forests of Galicia, Spain," *European Journal of Forest Research*, vol. 136, pp. 105–121, 2017.
- [73] S. J. Prichard and M. C. Kennedy, "Fuel treatments and landform modify landscape patterns of burn severity in an extreme fire event," *Ecological Applications*, vol. 24, pp. 571–590, 2014.
- [74] D. X. Viegas and L. P. Pita, "Fire spread in canyons," *International Journal of Wildland Fire*, vol. 13, pp. 253–274, 2004.
- [75] P. Nyman, D. Metzen, P. J. Noske, P. N. Lane, and G. J. Sheridan, "Quantifying the effects of topographic aspect on water content and temperature in fine surface fuel," *International Journal of Wildland Fire*, vol. 24, pp. 1129–1142, 2015.
- [76] X. Zapata-Rios, P. D. Brooks, P. A. Troch, J. McIntosh, and Q. Guo, "Influence of terrain aspect on water partitioning, vegetation structure and vegetation greening in high-elevation catchments in northern New Mexico," *Ecohydrology*, vol. 9, pp. 782–795, 2016.
- [77] A. F. Mark, K. J. Dickinson, J. Allen, R. Smith, and C. J. West, "Vegetation patterns, plant distribution and life forms across the alpine zone in southern Tierra del Fuego, Argentina," *Austral Ecology*, vol. 26, pp. 423–440, 2001.
- [78] J. Hilton, C. Miller, J. Sharples, and A. Sullivan, "Curvature effects in the dynamic propagation of wildfires," *International Journal of Wildland Fire*, vol. 25, pp. 1238–1251, 2017.
- [79] H. R. Pourghasemi, "GIS-based forest fire susceptibility mapping in Iran: a comparison between evidential belief function and binary logistic regression models," *Scandinavian Journal of Forest Research*, vol. 31, pp. 80–98, 2016.
- [80] B. Kalantar, N. Ueda, H. A. H. Al-Najjar, V. Saeidi, M. B. A. Gibril, and A. A. Halin, "A comparison between three conditioning factors dataset for landslide prediction in the sajadrood catchment of Iran," *ISPRS Annals of the Photogrammetry, Remote Sensing and Spatial Information Sciences*, vol. 5, pp. 625–632, 2020.
- [81] H. A. H. Al-Najjar and B. Pradhan, "Spatial landslide susceptibility assessment using machine learning techniques assisted by additional data created with generative adversarial networks," *Geoscience Frontiers*, vol. 12, pp. 625–637, 2021.
- [82] Z. Liu, J. Yang, Y. Chang, P. J. Weisberg, and H. S. He, "Spatial patterns and drivers of fire occurrence and its future trend under climate change in a boreal forest of Northeast China," *Global Change Biology*, vol. 18, pp. 2041–2056, 2012.
- [83] M. N. Ndalila, G. J. Williamson, and D. M. J. S. Bowman, "Geographic patterns of fire severity following an extreme eucalyptus forest fire in southern Australia: 2013 Forcett-Dunalley fire," *Fire*, vol. 1, no. 3, p. 40, 2018.
- [84] R. Bradstock, I. Davies, O. Price, and G. Cary, "Effects of climate change on bushfire threats to biodiversity, ecosystem processes and people in the Sydney region," *Final report to the New South Wales department of environment and climate change: climate change impacts and adaptation research project*, vol. 50831, p. 65, 2008.
- [85] M. D. Flannigan, B. M. Wotton, G. A. Marshall et al., "Fuel moisture sensitivity to temperature and precipitation: climate change implications," *Climatic Change*, vol. 134, pp. 59–71, 2016.
- [86] K. Reddy, G. Veershetty, and T. S. Vikram, "Effect of wind speed and direction on convective heat losses from solar parabolic dish modified cavity receiver," *Solar Energy*, vol. 131, pp. 183–198, 2016.
- [87] F. Takakai, T. Morishita, Y. Hashidoko et al., "Effects of agricultural land-use change and forest fire on N<sub>2</sub>O emission from tropical peatlands, Central Kalimantan, Indonesia," *Soil Science and Plant Nutrition*, vol. 52, pp. 662–674, 2006.
- [88] S. E. Page and A. Hooijer, "In the line of fire: the peatlands of Southeast Asia," *Philosophical Transactions of the Royal Society B: Biological Sciences*, vol. 371, p. 20150176, 2016.
- [89] S. Cumming, "Forest type and wildfire in the Alberta boreal mixedwood: what do fires burn?," *Ecological Applications*, vol. 11, pp. 97–110, 2001.
- [90] J. K. Agee and C. N. Skinner, "Basic principles of forest fuel reduction treatments," *Forest Ecology and Management*, vol. 211, pp. 83–96, 2005.
- [91] F. Morsdorf, E. Meier, B. Kötz, K. I. Itten, M. Dobbertin, and B. Allgöwer, "LIDAR-based geometric reconstruction of boreal type forest stands at single tree level for forest and wildland fire management," *Remote Sensing of Environment*, vol. 92, pp. 353–362, 2004.
- [92] S. L. Stephens, M. I. JD, R. E. Boerner et al., "The effects of forest fuel-reduction treatments in the United States," *Bioscience*, vol. 62, pp. 549–560, 2012.
- [93] M. H. Hachmi, A. Sesbou, H. Benjelloun, N. El Handouz, and F. Bouanane, "A simple technique to estimate the flammability index of Moroccan forest fuels," *Journal of Combustion*, vol. 2011, 11 pages, 2011.
- [94] K. A. Uyeda, D. A. Stow, and P. J. Riggan, "Tracking MODIS NDVI time series to estimate fuel accumulation," *Remote sensing letters*, vol. 6, pp. 587–596, 2015.
- [95] M. S. Tehrani, S. Jones, and F. Shabani, "Identifying the essential flood conditioning factors for flood prone area mapping using machine learning techniques," *Catena*, vol. 175, pp. 174–192, 2019.
- [96] J. Hauke and T. Kossowski, "Comparison of values of Pearson's and Spearman's correlation coefficients on the same sets of data," *Quaestiones geographicae*, vol. 30, pp. 87–93, 2011.
- [97] R. M. O'brien, "A caution regarding rules of thumb for variance inflation factors," *Quality & Quantity*, vol. 41, pp. 673–690, 2007.
- [98] H. Pourghasemi, H. Moradi, and S. F. Aghda, "Landslide susceptibility mapping by binary logistic regression, analytical hierarchy process, and statistical index models and assessment of their performances," *Natural Hazards*, vol. 69, pp. 749–779, 2013.
- [99] D. T. Bui, T. A. Tuan, H. Klempe, B. Pradhan, and I. Revhaug, "Spatial prediction models for shallow landslide hazards: a comparative assessment of the efficacy of support vector

- machines, artificial neural networks, kernel logistic regression, and logistic model tree,” *Landslides*, vol. 13, pp. 361–378, 2016.
- [100] C. G. Thompson, R. S. Kim, A. M. Aloe, and B. J. Becker, “Extracting the variance inflation factor and other multicollinearity diagnostics from typical regression results,” *Basic and Applied Social Psychology*, vol. 39, pp. 81–90, 2017.
- [101] A. Ávila, F. Justino, A. Wilson, D. Bromwich, and M. Amorim, “Recent precipitation trends, flash floods and landslides in southern Brazil,” *Environmental Research Letters*, vol. 11, p. 114029, 2016.
- [102] J. Vlcko, P. Wagner, and Z. Rychlikova, “Evaluation of regional slope stability,” *Mineralia Slovaca*, vol. 12, pp. 275–283, 1980.
- [103] A. P. Dempster, “Upper and lower probabilities induced by a multivalued mapping,” in *Classic Works of the Dempster-Shafer Theory of Belief Functions*, pp. 57–72, Springer, 2008.
- [104] H. R. Pourghasemi, B. Pradhan, and C. Gokceoglu, “Remote sensing data derived parameters and its use in landslide susceptibility assessment using Shannon’s entropy and GIS,” in *Applied Mechanics and Materials*, vol. 225, pp. 486–491, Trans Tech Publications Ltd, 2012.
- [105] S. Yufeng and J. Fengxiang, “Landslide stability analysis based on generalized information entropy,” in *2009 international conference on environmental science and information application technology*, pp. 83–85, Wuhan, China, 2009.
- [106] A. P. Dempster, “Upper and lower probabilities induced by a multivalued mapping,” *The Annals of Mathematical Statistics*, vol. 38, pp. 325–339, 1967.
- [107] S. M. Mousavi, S. Roostaei, and H. Rostamzadeh, “Estimation of flood land use/land cover mapping by regional modelling of flood hazard at sub-basin level case study: Marand basin,” *Geomatics, Natural Hazards and Risk*, vol. 10, pp. 1155–1175, 2019.
- [108] W. Chen, X. Zhao, H. Shahabi et al., “Spatial prediction of landslide susceptibility by combining evidential belief function, logistic regression and logistic model tree,” *Geocarto International*, vol. 34, no. 11, pp. 1177–1201, 2019.
- [109] M. O. Idrees, V. Saeidi, B. Pradhan, H. Zulhaidi, and M. Shafri, *Maximizing Urban Features Extraction from Multi-sensor Data with Dempster-Shafer Theory and HSI Data Fusion Techniques 03*, pp. 218–228, 2015.
- [110] V. Saeidi, B. Pradhan, M. O. Idrees, and Z. A. Latif, “Fusion of airborne LiDAR with multispectral SPOT 5 image for enhancement of feature extraction using Dempster-Shafer theory,” *IEEE Transactions on Geoscience and Remote Sensing*, vol. 52, pp. 6017–6025, 2014.
- [111] G. Shafer, “A mathematical theory of evidence,” *Bulletin of the London Mathematical Society*, vol. 9, pp. 237–238, 1976.
- [112] M. N. Jebur, B. Pradhan, and M. S. Tehrani, “Manifestation of LiDAR-derived parameters in the spatial prediction of landslides using novel ensemble evidential belief functions and support vector machine models in GIS,” *IEEE Journal of Selected Topics in Applied Earth Observations and Remote Sensing*, vol. 8, pp. 674–690, 2015.
- [113] D. T. Bui, B. Pradhan, O. Lofman, I. Revhaug, and O. B. Dick, “Spatial prediction of landslide hazards in Hoa Binh province (Vietnam): a comparative assessment of the efficacy of evidential belief functions and fuzzy logic models,” *Catena*, vol. 96, pp. 28–40, 2012.
- [114] B. Pradhan and S. Lee, “Delineation of landslide hazard areas on Penang Island, Malaysia, by using frequency ratio, logistic regression, and artificial neural network models,” *Environmental Earth Sciences*, vol. 60, pp. 1037–1054, 2010.
- [115] D. Dominey-Howes and M. Papathoma, “Validating a tsunami vulnerability assessment model (the PTVA model) using field data from the 2004 Indian Ocean tsunami,” *Natural Hazards*, vol. 40, pp. 113–136, 2007.
- [116] G. Ljubomir, D. Pamučar, S. Drobnjak, and H. R. Pourghasemi, “Modeling the spatial variability of forest fire susceptibility using geographical information systems and the analytical hierarchy process,” in *Spatial Modeling in GIS and R for Earth and Environmental Sciences*, pp. 337–369, Elsevier, 2019.
- [117] S. Siahkamari, A. Haghizadeh, H. Zeinivand, N. Tahmasebipour, and O. Rahmati, “Spatial prediction of flood-susceptible areas using frequency ratio and maximum entropy models,” *Geocarto International*, vol. 33, pp. 927–941, 2018.
- [118] C. Zhou, K. Yin, Y. Cao et al., “Landslide susceptibility modeling applying machine learning methods: a case study from Longju in the Three Gorges Reservoir area, China,” *Computers & Geosciences*, vol. 112, pp. 23–37, 2018.
- [119] M. Nami, A. Jaafari, M. Fallah, and S. Nabiuni, “Spatial prediction of wildfire probability in the Hyrcanian ecoregion using evidential belief function model and GIS,” *International journal of Environmental Science and Technology*, vol. 15, pp. 373–384, 2018.
- [120] L. Ayalew, H. Yamagishi, and N. Ugawa, “Landslide susceptibility mapping using GIS-based weighted linear combination, the case in Tsugawa area of Agano River, Niigata Prefecture, Japan,” *Landslides*, vol. 1, pp. 73–81, 2004.
- [121] Z. Wu, H. S. He, J. Yang, Z. Liu, and Y. Liang, “Relative effects of climatic and local factors on fire occurrence in boreal forest landscapes of northeastern China,” *Science of the Total Environment*, vol. 493, pp. 472–480, 2014.
- [122] F. Guo, G. Wang, Z. Su et al., “What drives forest fire in Fujian, China? Evidence from logistic regression and random forests,” *International Journal of Wildland Fire*, vol. 25, pp. 505–519, 2016.
- [123] J. K. Agee, B. Bahro, M. A. Finney et al., “The use of shaded fuelbreaks in landscape fire management,” *Forest Ecology and Management*, vol. 127, pp. 55–66, 2000.
- [124] I. Mitsopoulos and G. Mallinis, “A data-driven approach to assess large fire size generation in Greece,” *Natural Hazards*, vol. 88, pp. 1591–1607, 2017.
- [125] T. D. Penman, M. Bedward, and R. A. Bradstock, *National Fire Danger Rating System Probabilistic Framework Project: Year 2 Report, Report No. 2014.008*, Bushfire & Natural Hazards CRC, Australia, 2014.